# The Petrogenesis of Angrites and Martian Meteorites Inferred from Isotope and Trace Element Systematics

by

Matthew E. Sanborn

A Dissertation Presented in Partial Fulfillment
of the Requirements for the Degree
Doctor of Philosophy

Approved October 2012 by the
Graduate Supervisory Committee:

Meenakshi Wadhwa, Chair
Richard Hervig
Thomas Sharp
Amanda Clarke
Lynda Williams
Richard Carlson

ARIZONA STATE UNIVERSITY

December 2012

ABSTRACT

The present understanding of the formation and evolution of the earliest bodies in the Solar System is based in large part on geochemical and isotopic evidences contained within meteorites. The differentiated meteorites (meteorites originating from bodies that have experienced partial to complete melting) are particularly useful for deciphering magmatic processes occurring in the early Solar System. A rare group of differentiated meteorites, the angrites, are uniquely suited for such work. The angrites have ancient crystallization ages, lack secondary processing, and have been minimally affected by shock metamorphism, thus allowing them to retain their initial geochemical and isotopic characteristics at the time of formation.

The scarcity of angrite samples made it difficult to conduct comprehensive investigations into the formation history of this unique meteorite group. However, a dramatic increase in the number of angrites recovered in recent years presents the opportunity to expand our understanding of their petrogenesis, as well as further refine our knowledge of the initial isotopic abundances in the early Solar System as recorded by their isotopic systematics.

Using a combination of geochemical tools (radiogenic isotope chronometers and trace element chemistry), I have investigated the petrogenetic history of a group of four angrites that sample a range of formation conditions (cooling histories) and crystallization ages. Through isotope ratio measurements, I have examined a comprehensive set of long- and short-lived radiogenic isotope systems ($^{26}$Al-$^{26}$Mg, $^{87}$Rb-$^{87}$Sr, $^{146}$Sm-$^{142}$Nd, $^{147}$Sm-$^{143}$Nd, and $^{176}$Lu-$^{176}$Hf) within

these four angrites. The results of these measurements provide information regarding crystallization ages, as well as revised estimates for the initial isotopic abundances of several key elements in the early Solar System. The determination of trace element concentrations in individual mineral phases, as well as bulk rock samples, provides important constraints on magmatic processes occurring on the angrite parent body. The measured trace element abundances are used to estimate the composition of the parent melts of individual angrites, examine crystallization conditions, and investigate possible geochemical affinities between various angrites.

The new geochemical and isotopic measurements presented here significantly expand our understanding of the geochemical conditions found on the angrite parent body and the environment in which these early basaltic meteorites formed.

ACKNOWLEDGEMENTS

The work of this dissertation would not have been possible without the guidance and support from a number of individuals. First, I would like to thank my entire advisory committee who have always been supportive and encouraging throughout my graduate career, in particular my advisor Meenakshi Wadhwa. I am also deeply thankful for the advice and mentorship provided to me by Rick Carlson at the Department of Terrestrial Magnetism, Carnegie Institution of Washington. Many weeks were spent in the labs at DTM and the great group of research staff and postdocs there made me feel extremely welcome during my visits. I also am deeply indebted to Nick Schmerr and Amy McAdam whom I stayed with on many occasions while working at DTM. They made me feel completely at home, which made the long days in the lab much easier. I would also like to thank Phil Janney and Rebekah Hines for all their help in the ICGL clean lab, as well as Rick Hervig and Lynda Williams for their assistance in the SIMS lab.

I have been lucky to have a great group of friends and colleagues in the Center for Meteorite Studies and the School of Earth and Exploration both past and present, including: Greg Brennecka, Lev Spivak-Birndorf, Curtis Williams, Prajkta Mane, Audrey Bouvier, Karen Rieck, Michelle Minitti, Susie Nowak, Rebekah Hines, Phil Janney, Wendy Taylor, Laurence Garvie, Melissa Morris, Amy Jurewicz, Jo-Anne Wartho, Thijs van Soest, and Lora Bleacher, plus many more people too numerous to list individually. The friendship and support from all of you definitely enhanced my graduate school experience. I also want to

thank Carleton Moore for all the historical insight provided during our conversations and Laurie Leshin and Yunbin Guan for providing my first research experience during my undergraduate years.

Finally, I would like to thank my family, especially my mother, for all the encouragement and support given to me over the years.

TABLE OF CONTENTS

Page

CHAPTER Page

CHAPTER Page

LIST OF TABLES

Table Page

LIST OF FIGURES

Figure Page

Figure Page

CHAPTER 1

# INTRODUCTION I: ANGRITES

## 1.1 INTRODUCTION

### 1.1.1 General Introduction to Angrites

Asteroidal meteorites, which range from primitive undifferentiated stones with compositions similar to the Sun's photosphere to crustal rocks from fully differentiated bodies (e.g., Weisberg et al., 2006), yield vital insights into planetary formation processes occurring in the early Solar System. A particular subgroup of asteroidal meteorites, the achondrites, sample a continuum of planetary differentiation processes and range from samples that experienced small degrees of partial melting to samples originating from parent bodies that underwent complete differentiation and core formation (e.g., Mittlefehldt et al., 1998). A rare group of these differentiated basaltic meteorites, the angrites, have become an important set of samples for deciphering the formation and evolution of differentiated bodies in the early Solar System.

The original type specimen of the angrites, Angra dos Reis, was an observed fall in 1869 (the only observed fall thus far of an angrite) (e.g., Prinz et al., 1977). From this original angrite, over 100 years elapsed before the recovery of three additional angrites in the 1980s in Antarctica (Table 1.1). Initial studies of the earliest angrites revealed unique geochemical characteristics, such as extreme depletion in moderately volatile elements (e.g., K, Na, Li, Mn, Rb, and Cs), enrichment of refractory elements (e.g., Ca and Ti), and the presence of unique mineral phases (e.g., kirschsteinite) not previously observed within

meteorites, indicating a unique formation environment (e.g., Tera et al., 1970; Prinz et al., 1977; Mittlefehldt and Lindstrom, 1990). Ancient crystallization ages (e.g., Lugmair and Marti, 1977; Wasserburg et al., 1977; Jacobsen and Wasserburg, 1984; Lugmair and Galer, 1992; Nyquist, 1994) and a primitive Sr isotopic composition (e.g., Wasserburg et al., 1977; Lugmair and Galer, 1992; Nyquist, 1994) pointed to the formation of angrites early in the evolution of the Solar System. In addition, lack of evidence for significant shock metamorphism (e.g., Mittlefehldt et al., 1998) indicated the parent body for the angrites underwent a different impact history than that observed in other differentiated meteorite parent bodies. These unique characteristics established the angrites as an intriguing set of differentiated meteorites for investigation of early Solar System processes. However, additional angrites were not recovered for almost a decade after the Antarctic samples were collected, although within the past ten years the total number of angrites recovered and identified has more than doubled. Currently, there are twelve individual angrite meteorites, and twenty when paired stones are considered in the total (Table 1.1). The rarity of angrites has hindered establishing a detailed understanding of the formation and evolution of the angrite parent body, but the rapid increase in the number of angrites presents the opportunity to expand our understanding of angrite formation through detailed geochemical analysis of newly recovered samples.

All angrites can be divided into one of two textural sub-groups: (1) coarse-grained "plutonic" angrites or (2) fine-grained "quenched" angrites corresponding to differing crystallization conditions associated with their formation. Figures 1.1

and 1.2 illustrate the typical petrographic characteristics observed in the plutonic and quenched angrites, respectively. The quenched angrites experienced relatively rapid cooling and have been proposed to form very near the surface of the angrite parent body, possibly associated with surficial lava flows, with cooling rate estimates yielding a burial depth of less than 0.5 meters (Mikouchi et al., 2001). In contrast, the plutonic angrites appear to have formed from shallow plutonic intrusive bodies at variable depth in the crust of the angrite parent body with burial depth estimates ranging from 75 to 240 meters (McKay et al., 1998; Mikouchi et al., 2011). While the crystallization depth between the two angrite textural subgroups differ, details as to the geochemical differences between the source melts of the two groups is still an open question; one which this dissertation works to address.

Table 1.1
Summary of currently identified angrites (samples analyzed in this work in bold)

| Sample | Petrographic Type | Fall/Find | Year |
|---|---|---|---|
| Angra dos Reis | Plutonic | Fall | 1869 |
| LEW 86010 | Plutonic | Find | 1986 |
| LEW 87051 | Quenched | Find | 1987 |
| Asuka 881371 | Quenched | Find | 1988 |
| Sahara 99555 | Quenched | Find | 1999 |
| **D'Orbigny** | **Quenched** | **Find** | **2001** |
| **NWA 1296** | **Quenched** | **Find** | **2001** |
| **NWA 1670** | **Quenched** | **Find** | **2003** |
| **NWA 2999** | **Plutonic** | **Find** | **2004** |
| **NWA 4590** | **Plutonic** | **Find** | **2006** |
| **NWA 4801** | **Plutonic** | **Find** | **2007** |
| NWA 7203 | Quenched | Find | 2011 |

Note: NWA 2999 is paired with 8 additional stones: NWA 3158, NWA 3164, NWA 4931, NWA 5167, and NWA 6291

Abbreviations: (LEW) Lewis Cliff and (NWA) Northwest Africa
Source: Meteoritical Bulletin Database (2012)

The magmatic activity on the angrite parent body that resulted in the formation of the quenched and plutonic angrites spanned approximately a seven million year period from ~4556 to ~4563 Ma with quenched angrites clustered around ~4563 Ma and the plutonic angrites spanning a range from ~4560 to ~4556 Ma (Amelin, 2008; Brennecka and Wadhwa, 2012). The currently observed cluster of quenched angrites around ~4563 Ma suggests that near surface activity occurred early in the evolution of the angrite parent body with protracted magmatic activity continuing at a relatively greater depth for much longer. In addition to the crystallization ages of individual angrites, further evidence suggests the rapid formation and evolution (differentiation and core formation) of the angrite parent body. Recent isotopic studies have indicated evidence for core formation on the angrite parent body occurring as early as approximately 2 million years after the formation of the first solids in the Solar System, calcium-aluminum rich inclusions (CAIs) (Kleine et al., 2012). In addition, paleomagnetism measurements have suggested evidence for a likely internally generated magnetic field on the angrite parent body as early as ~4564 Ma (Weiss et al., 2008). The early accretion and differentiation of the angrite parent body and the onset of magmatic activity within the first five million years of the formation of CAIs have made the angrites optimal sample for deciphering the formation and evolution of planetary materials in the early Solar System.

The ancient crystallization ages of angrites, the lack of secondary processing, and minimal shock metamorphism, allow angrites to retain their initial geochemical and isotopic characteristics at the time of formation. For example,

isotopic studies of these pristine meteorites have provided additional evidence for the occurrence (and estimates for initial abundances) of several short-lived radionuclides, such as $^{26}$Al, $^{53}$Mn, $^{146}$Sm, and $^{182}$Hf within the early Solar System and established the angrites as anchor points for relative age dating using short-lived radiogenic systems (e.g., Lugmair and Galer, 1992; Nyquist et al., 1994; Markowski et al., 2008; Spivak-Birndorf et al., 2009). The angrites have also provided insight into magmatic processes occurring on differentiated objects within the first five million years after CAI formation through studies of trace element systematics (e.g., Floss et al., 2003). While the angrites thus far have provided vital information into early Solar System processes, the increasing number of recovered angrites has the potential to provide important new insight into the evolution of differentiated objects and initial isotopic abundances in the early Solar System.

## 1.2 MOTIVATION AND OBJECTIVES

The recent influx of new angrites within the past decade (particularly the rapid increase in plutonic angrites) provides a unique opportunity to further refine our understanding of the petrogenesis of this unique and important meteorite group. The goal of the first part of this thesis is to utilize several geochemical tools (e.g., radiogenic isotope and trace element systematics) to investigate the formation processes and associated timescales of a suite of plutonic and quenched angrites. Understanding the formation of these unique basaltic meteorites not only aid in deciphering the magmatic processes occurring on the early differentiated bodies, but also place important constraints on the initial isotopic

composition, as well as elucidate wide scale processes occurring in the early Solar System.

In Chapter 2, a combination of short- and long-lived radiogenic isotope systems ($^{147}$Sm-$^{143}$Nd, $^{146}$Sm-$^{142}$Nd, $^{176}$Lu-$^{176}$Hf, $^{87}$Rb-$^{87}$Sr, and $^{26}$Al-$^{26}$Mg) are utilized to investigate the formation history of the angrites and the evolution of the angrite parent body including petrologic activity recorded in the resetting of isotope systems within individual angrites. The initial isotopic compositions determined through these measurements are used to consider early Solar System conditions and processes, such as previously proposed irradiation of the angrite parent body, timing of volatile loss in the angrites, and extrapolated initial Solar System isotopic abundances.

Chapter 3 investigates the trace element geochemistry in a suite of recently recovered plutonic (NWA 2999, NWA 4590, and NWA 4801) and quenched angrites (NWA 1296 and NWA 1670). These newly recovered angrites provide an opportunity to investigate the magmatic history of the angrite group, with particular interest in the plutonic angrites that, until recently, were only comprised of two samples. The trace element systematics of the individual angrites are used to investigate their petrogenetic history, such as composition of their parent melt, redox conditions at the time of crystallization, as well as possible petrogenetic relationships to other angrites. The results of these measurements are used to discuss the possibility of a complex petrogenetic history of the plutonic angrites.

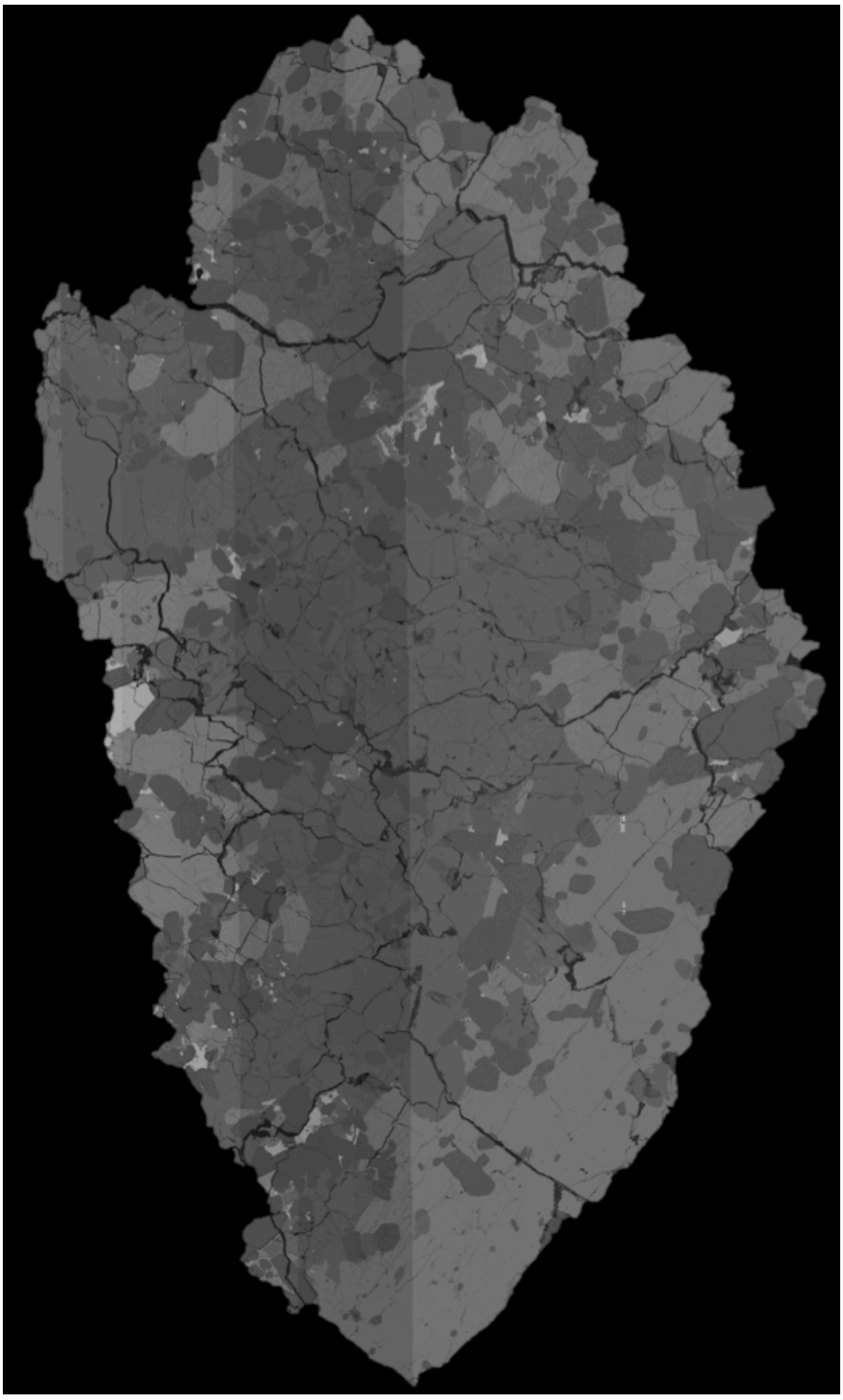

*Figure 1.1*- Back-scattered electron image mosaic map of plutonic angrite Northwest Africa 4590 (image is 2.5 cm long in the vertical direction). Dark gray: plagioclase, gray: pyroxene, light gray: olivine/kirschsteinite, white: spinel. For more detailed image, see Figure 3.1b.

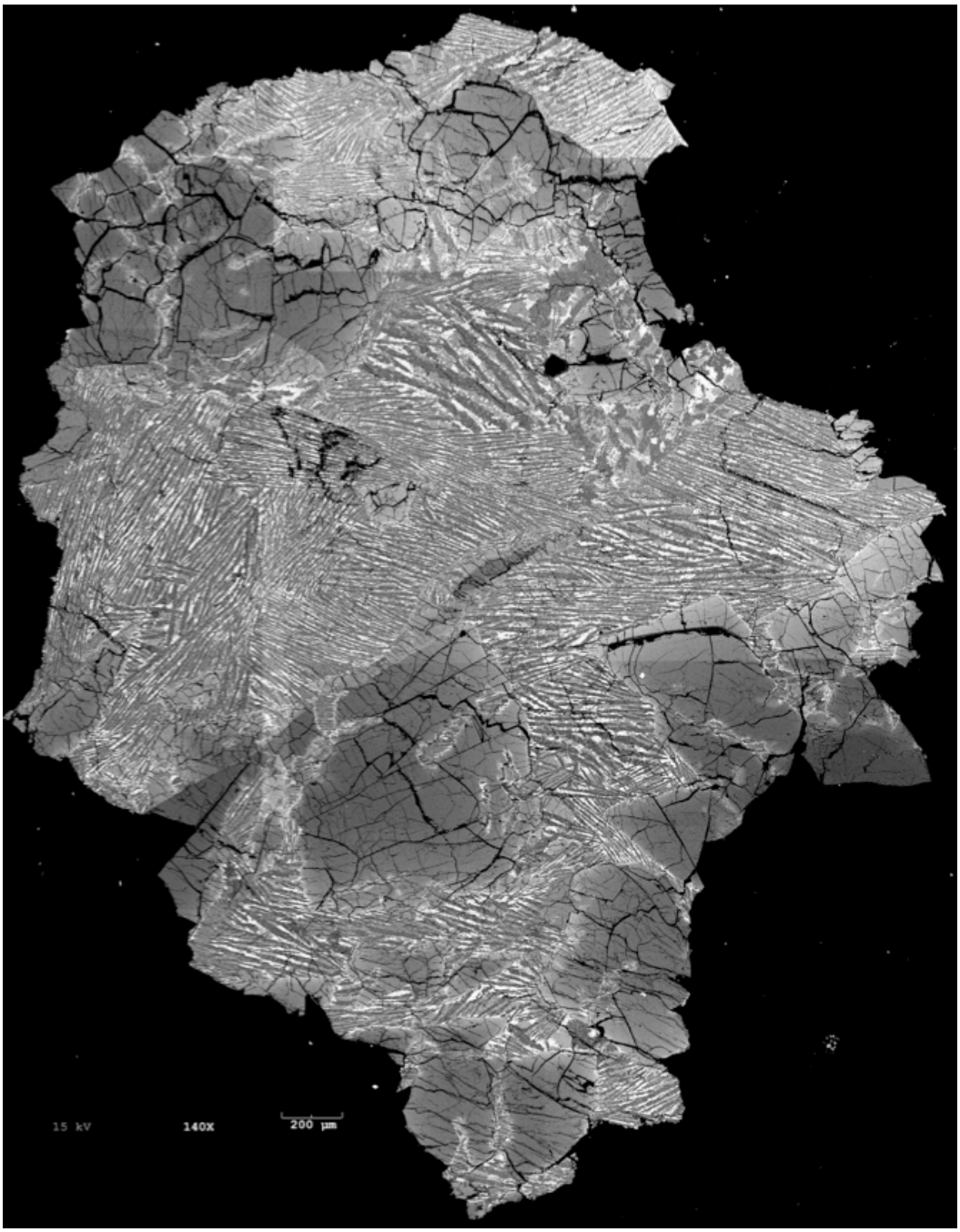


*Figure 1.2*- Back-scattered electron image mosaic map of quenched angrite Northwest Africa 1670. For a more detailed image, see Figure 3.2b.

# CHAPTER 2

# ISOTOPE SYSTEMATICS OF ANGRITES: IMPLICATIONS FOR EARLY SOLAR SYSTEM CHRONOLOGY AND PROCESSES ON THE ANGRITE PARENT BODY

## 2.1 INTRODUCTION

The isotopic evidence preserved in meteorites can provide important insight into the planetary formation and differentiation processes, and their associated timescales, occurring in the early Solar System. The angrites, a unique basaltic achondrite subgroup, have become an invaluable resource for investigating such processes due to their ancient crystallization ages, unique geochemical characteristics, and their pristine nature with the absence of shock metamorphism (Mittlefehldt et al., 1998).

The angrites are a relatively small achondrite subgroup comprised of only twelve distinct samples with a majority of these samples having been only recently recovered. These meteorites encompass a range of petrologic types from slowly cooled, plutonic rocks to samples with quenched textures that indicate rapid cooling close to surface of their parent body (e.g., Mikouchi et al., 2001). High-precision absolute radiometric ages of angrites, determined using the Pb-Pb isotope system, indicate that the magmatic activity on the angrite parent body spanned over seven million years from ~4563 Ma to ~4556 Ma (e.g., Amelin, 2008; Brennecka and Wadhwa, 2012). The diversity of petrologic types and the range of crystallization ages make angrites particularly suitable for deciphering processes in the early Solar System through the determination and understanding

of their isotopic composition. Several recent studies have investigated the isotope systematics of the long-lived Pb-Pb system (e.g., Amelin, 2008), as well as a suite of short-lived chronometers such as $^{182}$Hf-$^{182}$W, $^{53}$Mn-$^{53}$Cr, and $^{26}$Al-$^{26}$Mg (e.g., Markowski et al., 2007; Shukolyukov and Lugmair, 2008; Shukolyukov et al., 2009; Spivak-Birndorf et al., 2009; Kleine et al., 2012) within the angrites. However, there has been a paucity of studies of several radiogenic isotope systems important to developing a detailed understanding of planetary formation and evolution timescales, in particular $^{147}$Sm-$^{143}$Nd ($t_{1/2}$ ~106 Gyr), $^{146}$Sm-$^{142}$Nd ($t_{1/2}$ ~68 Myr), $^{176}$Lu-$^{176}$Hf ($t_{1/2}$ ~37.8 Gyr), and $^{87}$Rb-$^{87}$Sr ($t_{1/2}$ ~48.8 Gyr). Investigations of the $^{147}$Sm-$^{143}$Nd, $^{146}$Sm-$^{142}$Nd, and $^{87}$Rb-$^{87}$Sr isotope systems have been limited to a handful of studies of only two plutonic angrites, Lewis Cliff (LEW) 86010 and Angra dos Reis (Jacobsen and Wasserburg, 1984; Lugmair and Marti, 1977; Lugmair and Galer, 1992; Nyquist et al., 1994), while measurements of the $^{176}$Lu-$^{176}$Hf isotope system in angrites are limited to a single isotopic study of the quenched angrite Sahara 99555 (Bizzarro et al., 2012).

The plutonic angrites are particularly valuable samples for use in deciphering the isotope systematics of the angrite parent body with the mineralogy of the plutonic angrites providing a wide spread in the parent-daughter ratio among the various mineral phases. Until recently, isotopic studies of these angrites were limited to just two available samples LEW 86010 and Angra dos Reis (e.g., Lugmair and Galer, 1992; Nyquist et al., 1994). However, the recent identification of several new angrites (Northwest Africa (NWA) 4590, NWA 4801, and NWA 2999) has more than doubled the number of plutonic

samples available, providing the opportunity to expand the range of isotopic investigations. Prior to the recent increase in the plutonic angrites, the quenched angrites were far more prevalent in number. The higher proportion of quenched angrites available allowed for more expansive set of isotopic studies (e.g., Suguira et al., 2005; Markowski et al., 2007; Amelin et al., 2008; Spivak-Birndorf et al., 2009; Kleine et al., 2012); however, these studies have still only focused on a select few angrites: D'Orbigny, Sahara 99555, Asuka 881371, and NWA 1670. Some quenched angrites (e.g., D'Orbigny) have become vital chronological anchor points for short-lived chronometers (e.g., Spivak-Birndorf et al., 2009). As such, it is critical to develop a detailed understanding of various isotopes systems (both long- and short-lived) to fully understand the evolution of such a sample. The variation in crystallization ages and petrologic settings (e.g., burial depths) between the plutonic and quenched angrites provides the opportunity to further understand the petrogenesis and evolution of the angrite parent body in terms of both a temporal and spatial interpretation.

In this study, we report comprehensive isotopic composition measurements of the coupled $^{147,146}$Sm-$^{143,142}$Nd, $^{176}$Lu-$^{176}$Hf, and $^{87}$Rb-$^{87}$Sr systematics for a suite of plutonic (NWA 4590, NWA 4801, and NWA 2999) and quenched (D'Orbigny) angrites. In addition, new measurements of the $^{26}$Al-$^{26}$Mg isotope system in NWA 2999 are presented. Results of the coupled $^{147,146}$Sm-$^{143,142}$Nd systematics are used to discuss the evolution of angrite through their $^{147}$Sm-$^{143}$Nd ages, as well as new estimates of the initial Solar System $^{146}$Sm/$^{144}$Sm ratio. The $^{87}$Rb-$^{87}$Sr systematics measured in the four angrites are

used to calculate the initial $^{87}Sr/^{86}Sr$ isotope composition of the angrite body in order to estimate the timing of volatile loss among the angrites. New measurements of the $^{176}Lu$-$^{176}Hf$ isotope system in the angrites are utilized in evaluating prior evidence for intense irradiation events in the early Solar System, in addition to providing new estimates of the initial $^{176}Hf/^{177}Hf$ ratio of the Solar System. Finally, the new determination of an upper-limit $^{26}Al$-$^{26}Mg$ age for NWA 2999 is used to place further constraints on its formation age.

## 2.2 ANALYTICAL METHODS

### 2.2.1 Sample Preparation and Mineral Separation

Four angrites (three plutonic and one quenched) were analyzed in this study: NWA 4590, NWA 4801, NWA 2999, and D'Orbigny. Sample processing and mineral separation was completed under clean lab conditions in the Isotope Cosmochemistry and Geochronology Laboratory (ICGL) at Arizona State University (ASU). Mineral separates were obtained using interior pieces of each of the four angrites (total amount of material processed ~1 to 1.5 g). Each interior piece was initially washed with Milli-Q deionized water in an ultrasonic bath to remove any surface contaminants. The washed interior pieces were then crushed in an agate mortar and pestle reserved exclusively for meteoritic material. The crushed material was separated according to grain size and the material between 150 and 75 μm was further processed using a Frantz magnetic separator. Fractions processed using the Frantz separator were then purified through extensive handpicking with particular emphasis on removing grains with observed

inclusions. Fine-grained material (< 53 μm) that could not be processed using magnetic separation or handpicking was reserved as a separate composite fraction for analysis. In addition, a separate aliquot of material from each sample that was not processed any further other than gently crushing was reserved as whole-rock samples.

### 2.2.2 Sample Dissolution and Column Chemistry

The dissolution of samples for isotopic composition measurements was completed in three separate sessions. Dissolution of samples and subsequent column chemistry for Sm, Nd, Lu, Hf, Rb, and Sr isotope analysis described below were completed in the clean laboratory in the Department of Terrestrial Magnetism (DTM) at the Carnegie Institution of Washington. Samples for Al and Mg isotopic composition measurements were processed in the clean laboratory of the ICGL at Arizona State University.

#### *2.2.2.1 Sm, Nd, Rb, and Sr Separation*

All samples, with the exception of phosphate separates and whole-rock fractions, were leached in 2.5 N HCl for approximately 30 minutes using an ultrasonic bath. The leaching procedure was reduced to 10 minutes for the olivine samples. Leaching of the phosphate and whole-rock fractions was avoided to prevent the dissolution of the phosphates, a main rare earth element carrier, during the leaching process. After leaching, samples (with the exception of one whole-rock of each sample) were spiked with $^{149}$Sm-$^{150}$Nd, $^{87}$Rb, and $^{84}$Sr to measure the concentrations of each element using isotope dilution. Isotope spiking was made on the total sample prior to dissolution rather than an aliquot to maximize the

amount of the elements of interest available for mass spectrometry and to ensure spike-sample equilibration. Dissolution acids were added and each sample was ultrasonicated for 30 minutes. After the ultrasonic treatment, the samples were placed on a 95° C hotplate overnight in sealed Teflon beakers. Samples containing pyroxene and plagioclase, as well as whole-rock samples, were dissolved using a mixture of concentrated ultra-clean HF and $HNO_3$ in a 2:1 ratio with samples containing phosphates and olivine dissolved using a 6N HCl solution. The olivine dissolution was accomplished using preferential dissolution where the olivine grains were dissolved from a non-pure mixture of olivine and pyroxene. Preferential dissolution was necessary to obtain enough olivine material to analyze due to the low abundances of rare earth elements (REE), Sr, and Rb in the angrite olivine and the difficulty in separation of olivine from pyroxene. Samples were treated after dissolution first with concentrated $HNO_3$ to ensure complete removal of fluorides, then with 6N HCl until the sample solution was clear. Samples were then dried down and dissolved in 5 mL of 1N HCl-0.1N HF.

Each sample was initially processed using a 20 cm x 6 mm ID primary cation exchange column (referred to hereafter as the primary column) filled with AGW50x8 resin (200-400 mesh) to separate out the light rare earth elements (LREEs), Rb, Sr, Lu, and Hf. The columns were conditioned with 20 mL of 1 N HCl-0.1 N HF prior to the loading of the samples. The samples, dissolved in the 5 mL 1N HCl-0.1N HF solution, were loaded onto the columns with an additional 5 mL of 1N HCl-0.1N HF subsequently added to the column. The Hf was

collected from this 10 mL fraction. The eluent was then switched to 2.5N HCl with Rb and Sr collected from the elution 34 mL of 2.5N HCl. The eluent was then switched a final time to 4N HCl and the REE collected in 28 mL of 4N HCl (Lu fraction collected in the first 12 mL and the LREE fraction collected in the remaining 16 mL).

Samarium and neodymium were separated from the LREE fraction from the primary column using a nitrogen pressurized 20 cm x 0.2 cm quartz column filled with AG50W-X8 cation exchange resin (200-400 mesh) and 2-methyllatctic acid (α-hydroxyisobutyric acid) following the methods described by Boyet and Carlson (2005). The 2-methyllactic acid columns were repeated a total of three times on the neodymium cut of each sample to decrease the level of $^{142}$Ce present, in order to reduce the potential interference on $^{142}$Nd. Total procedural blanks in this study for Sm and Nd were 3 pg and 12 pg, respectively.

Strontium and rubidium fractions obtained using the primary cation exchange column also contain a range of major and trace elements that co-elute (e.g., Ca, Mg, and Ti). Removal of these matrix elements was accomplished by passing the Sr and Rb fractions through additional clean-up columns. The Sr fractions from the primary column was dried down and re-dissolved using 1.5 mL of 2N $HNO_3$. The sample was loaded onto a column containing approximately 100 μL of Sr-resin conditioned using 3 mL of 2N $HNO_3$. After eluting 2 mL of 2N $HNO_3$, the Sr was collected in 2mL of 0.05N $HNO_3$. Rubidium fractions collected from the primary column were dried down and re-dissolved in 0.5 mL of 0.5N HCl and added to a 10.5 cm x 0.6 cm ID column filled with AG50Wx8 resin

(200-400 mesh) that was previously backwashed with Milli-Q water and conditioned using 20 mL of 0.5N HCl. The columns were washed with 51 mL of 0.5N HCl and the Rb collected from an additional 20 mL of 0.5N HCl. Total procedural blanks for Sr and Rb from this chemistry was 305 pg and 7 pg, respectively.

*2.2.2.2 Lu and Hf Separation*

Samples dedicated for Lu and Hf isotope analysis were prepared from distinct mineral and whole-rock separates from those used in the sample preparation described in section 2.2.2.1, although Lu and Hf were also collected from these previous samples. Samples were not leached prior to dissolution. Each sample was spiked prior to dissolution with a mixed $^{176}$Lu-$^{180}$Hf spike for concentration determination by isotope dilution. Spiked samples were then dissolved using a 2:1 mixture of ultra-pure concentrated HF-$HNO_3$ in a Parr acid digestion vessel overnight in an oven at 150° C. Dissolved samples were treated with 6N HCl and concentrated $HNO_3$ until the samples produced a precipitate free solution. Samples were then dried down and re-dissolved in 5 mL of a 1N HCl-0.1N HF solution.

Lutetium and hafnium were separated from each sample using the same primary column procedure described previously. Removal of Ti and a portion of Zr from the primary column Hf fraction was accomplished using a 3.8 cm x 0.6 cm ID column filled with Eichrom LN-spec resin (100-150 μ m, $H^+$ form) following the Hf separation chemistry described by Münker et al (2001). Lutetium was further separated from Yb in the HREE primary column fraction

using a 72 mm x 4 mm ID quartz column filled with LN-spec resin. Total procedural blanks for Lu and Hf were 6 pg and 42 pg, respectively.

*2.2.2.3 Al and Mg Separation*

Sample dissolution and chemistry for Al and Mg separation was completed in the ICGL at Arizona State University. Each sample was dissolved in a mixture of ultra-pure HF and $HNO_3$ in a 2:1 ratio in sealed Teflon beakers on hot plate at 120°C for two days. The dissolved samples were evaporated to dryness and re-dissolved in alternating ultra-pure concentrated $HNO_3$ and 6N HCl until the sample solutions were free of precipitates. After obtaining a clear solution, the samples were dried down and re-dissolved in 1N $HNO_3$. Approximately 10% of the dissolved sample solution was reserved for Al/Mg ratio measurements. The remaining sample solution was dried down a final time and re-dissolved in 100 μL of 1M $HNO_3$. Separation of Mg from the sample matrix was accomplished using pressurized quartz columns filled with AG50-X8 cation exchange resin (200-400 mesh) and Bio-Rad Poly-Prep columns filled with AG1-X8 anion exchange resin (200-400 mesh) following the chemical separation procedures described by Spivak-Birndorf et al. (2009). Each sample was passed through the Mg separation column a total of three times to ensure adequate separation of Mg from other matrix elements. Total procedural blanks for Mg from this chemistry was <2 ng.

## 2.3 MASS SPECTROMETRY

### 2.3.1 TIMS (Nd, Sm, and Sr)

Isotopic measurements of Sm, Nd, and Sr were performed using a Thermo Finnigan Triton thermal ionization mass spectrometer at DTM. Neodymium samples were loaded onto refined Re filaments in 1μL of 3N HCl. Isotope analysis of Nd was made using a double filament configuration with measurement of the $Nd^+$ ion. Measurements were completed in static mode for all samples with samples having abundant Nd present also analyzed in dynamic mode. Runs were comprised, when possible, of 18 blocks of 20 ratios with 8-second integration times for static runs and 16-second integration times for dynamic runs. Correction for instrumental mass fractionation was made using the exponential law and the normalization ratio $^{146}Nd/^{144}Nd = 0.7219$. Neodymium data are reported relative to the JNdi standard ($^{143}Nd/^{144}Nd = 0.512115$; Tanaka et al. (2000)). During the analytical sessions, the average measured $^{143}Nd/^{144}Nd$ value for the JNdi standard was $^{143}Nd/^{144}Nd = 0.512104 \pm 0.000005$ ($\pm 2\sigma$) in static mode and $^{143}Nd/^{144}Nd = 0.512090 \pm 0.000002$ in dynamic mode (10 ppm and 5 ppm external reproducibility, respectively). The average measured value for $^{142}Nd/^{144}Nd$ in the JNdi standard during the analytical sessions was $1.141840 \pm 0.000009$ in static mode and $1.141839 \pm 0.000004$ in dynamic mode (8 ppm and 3 ppm external reproducibility, respectively).

Samarium samples were loaded onto single zone-refined Re filaments for isotope analysis. Isotope ratio measurements were collected in 6 blocks of 20 ratios with 8-second integration times. The $^{149}Sm/^{152}Sm$ ratios in unspiked whole-

rock samples were monitored for anomalies due to neutron capture resulting from cosmic ray exposure. Corrections for deficits in the $^{149}Sm/^{152}Sm$ ratio were included in the isotope dilution calculations used for determining Sm concentrations.

Strontium samples were loaded onto single Re filaments with a maximum sample load of approximately 500 ng. Each sample was loaded onto the filaments in ~1 μL of 4N $HNO_3$ with 0.5 μL of $Ta_2O_5$ slurry loaded on the filament to increase Sr ionization efficiency. Analytical runs typically consisted of 20 blocks of 20 ratios and 8 second integration times. Correction for mass fractionation was made using the exponential law and normalization to $^{86}Sr/^{88}Sr = 0.1194$. Strontium data are reported relative to the NBS 987 standard ($^{87}Sr/^{86}Sr = 0.71025$) with an average $^{87}Sr/^{86}Sr$ ratio measured in NBS 987 throughout the analytical sessions of 0.710240±0.000006.

**2.3.2 MC-ICPMS (Hf, Lu, Rb, Al, and Mg)**

Isotopic composition measurements of Hf, Lu, and Rb were performed using the Nu Instruments multicollector inductively coupled plasma mass spectrometer (MC-ICPMS) located at DTM. Hafnium isotopic measurements were made using a CETAC MCN-6000 desolvating microcentric nebulizer for sample introduction to increase analytical sensitivity. Samples were run using a mixture of 0.08N $HNO_3$-0.06N HF. Each analytical run consisted of 2 blocks of 40 ratios with 8-second integration times. A washout of the sample introduction system using a solution of 0.4N $HNO_3$-0.1N HF was completed between each sample analysis until the Hf signal was below the detection limit, followed by a

rinse out using the 0.08N $HNO_3$-0.06N HF running acid. This washout procedure was used to suppress the memory effect of Hf in the sample introduction system. Correction for mass fractionation was made using the exponential law and the normalization ratio $^{179}Hf/^{177}Hf$= 0.7325. All Hf isotope ratios were corrected for Yb and Lu interferences and are reported relative to the JMC 475 Hf standard ($^{176}Hf/^{177}Hf$ = 0.282160). The average $^{176}Hf/^{177}Hf$ value for the JMC 475 standard during the three analytical sessions was 0.282159±0.000022, 0.282125±0.000053, and 0.282169±0.000078 (2σ), respectively. Lutetium isotopic measurements were made using a glass spray chamber. Standards consisting of pure Lu and Lu doped with a small amount of Yb (6:1 Lu to Yb) were run throughout the analytical session. Instrument runs consisted of a single block of 25 ratios with 8-second integration times. Correction for mass fractionation using Lu isotopes is not possible with only two naturally present isotopes, $^{175}Lu$ and $^{176}Lu$. However, a correction for mass fraction during the analyses can be accomplished using Yb still present in the samples after the secondary Lu separation column. Using the measured Yb isotopic composition in the samples, a mass fraction correction was determined using the exponential law and the normalization ratio of $^{173}Yb/^{172}Yb$ = 0.73889. The mass fraction correction was then applied to the measured Lu isotope ratios. In all samples used in the subsequent data regressions, Yb was present at concentrations that allowed for the determination of a robust mass fractionation correction. Rubidium isotope ratio measurements were made in analytical runs consisting of a single block of 20 ratios and 8-second integration times. For Rb analyses, sample-standard

bracketing was employed with a 50 ppb Rb standard solution analyzed after every third sample to correct for instrumental mass fractionation.

Magnesium isotopic compositions and the Al/Mg ratios of NWA 2999 were measured using the Thermo Finnigan Neptune MC-ICPMS in the ICGL at Arizona State University. The $^{27}Al/^{24}Mg$ ratios were measured using aliquot solutions of the dissolved sample that were not subjected to separation chemistry that were redissolved in 3% $HNO_3$. SPEX Mg and Al elemental standard solutions were used to generate a six-point calibration curve spanning a range of Al/Mg ratios from 0.1 to 200. The calibration standards were measured a total of three times bracketing the samples and two terrestrial rock standards (BCR-2 and JR-2). The external reproducibility ($2\sigma$) of the $^{27}Al/^{24}Mg$ ratio measurements of the standards was ±2 %. Magnesium samples purified through column chemistry were re-dissolved in a 3% solution of twice distilled $HNO_3$. Sample introduction was made using an ESI APEX desolvating nebulizer. Each sample was bracketed using the DSM-3 Mg isotope standard. Magnesium-26 excesses (i.e., $^{26}Mg^*$) due to decay of $^{26}Al$ were calculated by applying an exponential law mass fractionation correction and a normalization ratio of $^{25}Mg/^{24}Mg = 0.12663$ to the measured $^{26}Mg/^{24}Mg$ ratio and comparing the measured deviation of the mass fractionation corrected $^{26}Mg/^{24}Mg$ ratios of the samples with the corresponding bracketed standard. External reproducibility ($2\sigma_m$) of standards during this analytical session was ± 0.05 ‰ per amu for $\delta^{25}Mg$ and $\delta^{26}Mg$ and ± 0.03 ‰ for $\delta^{26}Mg^*$.

## 2.4 RESULTS

The following sections report the results of the isotope ratio measurements of the NWA 4590, NWA 4801, NWA 2999, and D'Orbigny angrites. Regression line fitting and associated error determination of slopes and ages were completed using the Isoplot (version 3.75) analysis program (Ludwig, 1991). For isochrons comprised of four or more data points, errors reported are the 2σ standard deviation (95% confidence limit). Uncertainties for isochrons with only three data points are calculated using the 2σ standard deviation from observed scatter alone due to the disproportionately large errors (i.e., errors significantly larger than expected given the uncertainty of individual data points and scatter in the data) provided by Isoplot using the 95% confidence-limit error in the case of three-point isochrons.

### 2.4.1 Sm-Nd Systematics

Neodymium isotopic compositions and concentrations of Sm and Nd in each sample are presented in Table 2.1. Certain values presented below are expressed in epsilon notation where $\varepsilon^{14X}Nd = [((^{14X}Nd/^{144}Nd)_{Sample}/(^{14X}Nd/^{144}Nd)_{Standard} -1) \times 10^4]$. $^{143}Nd/^{144}Nd$ values expressed in epsilon notation are reported relative to modern average bulk chondrite values (CHUR; $^{143}Nd/^{144}Nd = 0.512630$ and $^{147}Sm/^{144}Nd = 0.1960$ (Bouvier et al., 2008)) and $^{142}Nd/^{144}Nd$ ratios are reported relative to average measured value of the JNdi standard of $^{142}Nd/^{144}Nd = 1.141840 \pm 0.000009$. Present-day initial $^{143}Nd/^{144}Nd$ and $^{142}Nd/^{144}Nd$ values calculated relative to CHUR (i.e., $\varepsilon^{14X}Nd$) were calculated using the regression procedures of Fletcher and Rosman (1982).

*2.4.1.1 NWA 4590*

The $^{147}$Sm-$^{143}$Nd and $^{146}$Sm-$^{142}$Nd isochrons for NWA 4590 are defined by four points (phosphate, whole-rock, pyroxene, and olivine) and are shown in Figure 2.1. The plagioclase fraction from NWA 4590 does not fall on the isochrons and is not used in the regression line calculations. The slope of the regression line of the $^{147}$Sm-$^{143}$Nd isochron is 0.03032±0.00018 (2σ, MSWD = 6.6) with an initial $^{143}$Nd/$^{144}$Nd ratio (i.e., the isochron intercept) of 0.506682±0.000052 (initial $\varepsilon^{143}Nd_{CHUR}$ = -0.08±0.49). The regression line slope yields an age of 4568±27 Ma using a decay constant of $\lambda^{147}Sm = 6.54\times10^{-12}$ yr$^{-1}$. The slope of the regression line of the $^{146}$Sm-$^{142}$Nd isochron (as calculated using a $^{144}$Sm/$^{144}$Nd - $^{142}$Nd/$^{144}$Nd isotope diagram) corresponds to the initial $^{146}$Sm/$^{144}$Sm ratio of the sample at the time of the last closure of the Sm-Nd system. Using this relationship, the $^{146}$Sm-$^{142}$Nd isochron yields an initial $^{146}$Sm/$^{144}$Sm ratio in NWA 4590 of 0.00745±0.00021 (MSWD = 0.50) and an initial $\varepsilon^{142}$Nd of -2.75±0.09. This initial $\varepsilon^{142}$Nd ratio corresponds to a present-day initial $\varepsilon^{142}$Nd = -0.13±0.03 at a chondritic$^{144}$Sm/$^{144}$Nd ratio.

*2.4.1.2 NWA 4801*

Four data points (phosphate, plagioclase, whole-rock, and pyroxene) define the $^{147}$Sm-$^{143}$Nd and $^{146}$Sm-$^{142}$Nd isochrons of NWA 4801 (Fig. 2.2). Olivine lies slightly off the isochrons and is not used the regression calculations. The slope of the $^{147}$Sm-$^{143}$Nd isochron 0.03025±0.00055 (MSWD = 4.4) corresponds to an age of 4556±82 Ma and initial $^{143}$Nd/$^{144}$Nd ratio of 0.50669±0.00010 (initial $\varepsilon^{143}Nd_{CHUR}$ = -0.17±0.51). The slope of the $^{146}$Sm-$^{142}$Nd

isochron corresponds to an initial $^{146}Sm/^{144}Sm$ of 0.00846±0.00075 (MSWD = 1.7) and an initial $\varepsilon^{142}Nd$ = -2.32±0.4 ($\varepsilon^{142}Nd$ = -0.26±0.04 at a chondritic Sm/Nd).

*2.4.1.3 D'Orbigny*

The plagioclase, whole-rock, and pyroxene data points define both the $^{147}Sm$-$^{143}Nd$ and $^{146}Sm$-$^{142}Nd$ isochrons of D'Orbigny (Fig. 2.3). As observed in NWA 4801, the olivine data point lies off the isochrons and is not used in the regression calculations. The three data points yield a best-fit line with a slope of 0.0299±0.0010 (MSWD = 13) with an initial $^{143}Nd/^{144}Nd$ ratio of 0.50677±0.00006 (initial $\varepsilon^{143}Nd_{CHUR}$ = 0.20±0.18) yielding an age of 4507±89 Ma. The $^{146}Sm$-$^{142}Nd$ isochron of D'Orbigny yields a $^{146}Sm/^{144}Sm$ ratio of 0.00618±0.0010, a ratio lower than that observed in both NWA 4590 and NWA 4801. The initial $\varepsilon^{142}Nd$ of -2.32±0.04 obtained from the $^{146}Sm$-$^{142}Nd$ isochron corresponds to a present-day initial $\varepsilon^{142}Nd$ of -0.14±0.05 at a chondritic Sm/Nd value.

*2.4.1.4 NWA 2999*

Three points define the $^{147}Sm$-$^{143}Nd$ isochron of NWA 2999: pyroxene, plagioclase, and the whole-rock (Fig. 2.4). The concentration of Nd in the plagioclase phase and the minor occurrence of the phase in the whole-rock prevented the acquisition of high-precision $^{142}Nd/^{144}Nd$ ratios. Therefore, the results of the Nd isotope ratio measurements of NWA 2999 are limited to only the long-lived $^{147}Sm$-$^{143}Nd$ system. The $^{147}Sm$-$^{143}Nd$ isochron yields a regression line slope of 0.0260±0.0011 (MSWD = 19) and an initial $^{143}Nd/^{144}Nd$ ratio of

0.50770±0.00024 (initial $\varepsilon^{143}Nd_{CHUR}$ = 2.93±0.78) corresponding to an age of 3925±165 Ma.

### 2.4.2 Lu-Hf Systematics

The hafnium isotopic composition and concentrations of Lu and Hf in each sample are presented in Table 2.2. Three mineral phases (pyroxene, plagioclase, and olivine), a fine-grained fraction, and whole-rock sample were analyzed in each of the angrite discussed individually below. All samples (with the exception of D'Orbigny Px-2 and WR-2) were dissolved using the Parr acid digestion vessel (see section 2.2.2). The D'Orbigny samples denoted as Px-2 and WR-2 are pyroxene and whole-rock fractions that underwent sample dissolution following the hot plate dissolution method described in section 2.2.2.

#### *2.4.2.1 NWA 4590*

Pyroxene and olivine separates, the finest-grained size fraction and the whole-rock fraction define the $^{176}Lu$-$^{176}Hf$ isochron of NWA 4590 (Fig. 2.5). The plagioclase, Px-2, and WR-2 fractions falls off the isochron and were not used in regression line fitting. The mineral and whole-rock fractions of NWA 4590 span an exceptionally wide range of $^{176}Lu/^{177}Hf$ ratios with values ranging from 0.012 to 0.483. The regression line fitting through the data points of NWA 4590 yields a line with a slop of 0.08704±0.00048 (MSWD = 1.6) and an initial $^{176}Hf/^{177}Hf$ ratio of 0.279939±0.000036. Using a $^{176}Lu$ decay constant of $^{176}\lambda = 1.867\times10^{-11}$ $yr^{-1}$ (Söderlund et al., 2004), the NWA 4590 regression line corresponds to age of 4470±23 Ma.

*2.4.2.2 NWA 4801*

Four points define the $^{176}$Lu-$^{176}$Hf isochron of NWA 4801: pyroxene and olivine separates, the finest-grained size fraction, and the whole-rock fraction (Fig. 2.6). These data points span a moderate range of $^{176}$Lu/$^{177}$Hf ratios from 0.020 to 0.119. As with NWA 4590, plagioclase, Px-2 and WR-2 fall off the isochron and are not used in the regression line fitting. The regression line through the four points of the isochron yields a slope of 0.08916±0.0010 (MSWD = 1.7) with an initial $^{176}$Hf/$^{177}$Hf ratio of 0.279768±0.000046, corresponding to an age of 4575±50 Ma.

*2.4.2.3 D'Orbigny*

The D'Orbigny $^{176}$Lu-$^{176}$Hf isochron is comprised of six data points: two pyroxene mineral separates (Px and Px-2), the fine-grain fraction, two whole-rock fractions (WR and WR-2), and an olivine separate (Fig. 2.7). The plagioclase mineral separate falls off the single isochron line defined by the other six D'Orbigny data points and is not used in subsequent regression line fitting. The data points of the D'Orbigny angrite span a more narrow range of $^{176}$Lu/$^{177}$Hf ratios (0.014 to 0.048) than that observed in NWA 4590 and NWA 4801. The regression through the D'Orbigny data (with the exception of plagioclase) yields a best-fit line with a slope of 0.08810±0.0020 (MSWD = 1.9) with an initial $^{176}$Hf/$^{177}$Hf ratio of 0.279775±0.000043. The isochron slope corresponds to an age of 4520±97 Ma.

### 2.4.3 Rb-Sr Systematics

Strontium isotope ratio measurements and the concentration of Rb and Sr are summarized in Table 2.3 and shown in Figure 2.8.

The pyroxene, olivine, plagioclase, and whole-rock fractions from NWA 4590, NWA 4801, and D'Orbigny are highly depleted in Rb (0.009 – 0.075 ppm) with a narrow spread in the $^{87}Rb/^{86}Sr$ ratio from <0.001 to 0.004. The phosphates have marginally higher Rb concentrations than those observed in the silicates (0.171 – 1.916 ppm) with $^{87}Rb/^{86}Sr$ ratios ranging from 0.001 to 0.023. In contrast, the silicate phases of NWA 2999 have Rb concentrations ranging from 0.203 to 0.644 ppm and $^{87}Rb/^{86}Sr$ ratios ranging from 0.001 to 0.017.

Analyses of the plagioclase fractions indicate this phase yields among the least radiogenic Sr isotopic compositions and the lowest $^{87}Rb/^{86}Sr$ ratios of any of the fractions measured in these samples. Pyroxene, olivine, and whole-rock fractions display a range of $^{87}Sr/^{86}Sr$ isotopic from 0.698993±0.000003 to 0.700429±0.000062 with a significant amount of scatter among the phases in a single angrite. The nominal spread in the $^{87}Rb/^{86}Sr$ ratios among the constituent phases and whole-rock fractions and the scatter in the data prevent the calculation of a robust isochron regression line for a given individual sample.

### 2.4.4 Al-Mg Systematics of NWA 2999

Magnesium isotopic composition and $^{27}Al/^{24}Mg$ ratios were determined in the mineral separate samples (plagioclase and pyroxene) and whole-rock sample of NWA 2999 and are presented in Table 2.4. Magnesium isotope ratios are presented in delta-notation ($\delta^{x}Mg = [((^{x}Mg/^{24}Mg)_{Sample}/(^{x}Mg/^{24}Mg)_{Standard} - 1) \times$

$10^3$]) with samples reported relative to the DSM-3 Mg standard. Radiogenic excesses ($\delta^{26}Mg^*$) are calculated using the mass fractionation corrected $^{26}Mg/^{24}Mg$ ratio for the sample and bracketed standard (see section 2.2.3 for details). The reported errors on the $\delta^{26}Mg^*$ values are 2 standard deviation of the mean or standard error ($2\sigma_m$) based on repeat measurements of each sample. The pyroxene and whole-rock samples of NWA 2999 have a normal Mg isotopic composition (i.e., no resolvable excesses of radiogenic $^{26}Mg^*$ from the standard) with $\delta^{26}Mg^*$ values of -0.004±0.010 and -0.003±0.010 for the whole-rock and pyroxene, respectively. Plagioclase, with a significantly higher $^{27}Al/^{24}Mg$ ratio of 181, also shows no resolvable excesses of $^{26}Mg^*$ with $\delta^{26}Mg^* = 0.013\pm0.023$. The regression line slope of the $^{26}Mg^*/^{24}Mg$-$^{27}Al/^{24}Mg$ plot corresponds to the $^{26}Al/^{27}Al$ ratio at the time of the last equilibration for Mg isotopes. The calculated slope of the regression line through the NWA 2999 separates is not resolvable from zero with an upper limit of $3.07\times10^{-8}$ (Fig. 2.9). The upper limit $^{26}Al/^{27}Al$ ratio corresponds to an upper limit $^{26}Al$-$^{26}Mg$ age for NWA 2999 of $T \leq 4560.46$ Ma calculated with the D'Orbigny angrite as an anchor using a $^{27}Al/^{26}Al$ ratio of $5.06\pm0.92\times10^{-7}$ (Spivak-Birndorf et al., 2009) and a U-isotope adjusted Pb-Pb age of 4563.37±0.25 Ma (Amelin, 2008; Brennecka and Wadhwa, 2012).

Table 2.1
Samarium-neodymium isotope measurements of NWA 4590, NWA 4801, D'Orbigny, and NWA 2999.

| Sample | Fraction[a] | Mass (mg) | Sm (ppm) | Nd (ppm) | Mode[b] | $^{147}Sm/^{144}Nd$ | $^{142}Nd/^{144}Nd$ (±2σ)[c] | $\varepsilon^{142}Nd$ (±2σ)[d] | $^{143}Nd/^{144}Nd$ (±2σ)[e] |
|---|---|---|---|---|---|---|---|---|---|
| **NWA 4590** | PX | 96.10 | 3.035 | 7.756 | Static | 0.2365 | 1.141882±15 | 0.36 ± 0.13 | 0.513845±5 |
| | PL | 76.08 | 0.068 | 0.261 | Static | 0.1574 | 1.141732±17 | -0.95 ± 0.14 | 0.511494±6 |
| | OL | 56.03 | 0.161 | 0.193 | Static | 0.5037 | 1.142297±15 | 4.00 ± 0.13 | 0.521962±6 |
| | P | 0.369 | 187.11 | 765.97 | Dynamic | 0.1473 | 1.141751±6 | -0.77 ± 0.05 | 0.511157±2 |
| | WR | 49.47 | 2.491 | 6.665 | Dynamic | 0.2260 | 1.141868±6 | 0.25 ± 0.05 | 0.513531±2 |
| **NWA 4801** | PX | 101.90 | 4.044 | 11.023 | Dynamic | 0.2218 | 1.141855±6 | 0.14 ± 0.05 | 0.513407±2 |
| | PL | 64.38 | 0.155 | 0.689 | Static | 0.1361 | 1.141710±13 | -1.15 ± 0.11 | 0.510800±5 |
| | OL | 70.59 | 0.033 | 0.076 | Static | 0.2623 | 1.141924±43 | 0.73 ± 0.38 | 0.514754±20 |
| | P | 0.062 | 24.87 | 118.96 | Static | 0.1264 | 1.141654±44 | -1.64 ± 0.39 | 0.510528±16 |
| | WR | 59.82 | 2.532 | 7.169 | Static | 0.2135 | 1.141837±8 | -0.03 ± 0.07 | 0.513145±3 |
| **D'Orbigny** | PX | 52.84 | 2.165 | 5.581 | Dynamic | 0.2345 | 1.141871±6 | 0.28 ± 0.05 | 0.513797±2 |
| | PL | 104.83 | 0.076 | 0.296 | Static | 0.1556 | 1.141782±38 | -0.51 ± 0.33 | 0.511437±16 |
| | OL | 120.32 | 0.683 | 0.225 | Dynamic | 0.1831 | 1.141801±9 | -0.33 ± 0.08 | 0.512406±3 |
| | WR | 54.14 | 1.988 | 6.033 | Dynamic | 0.1993 | 1.141826±6 | -0.11 ± 0.05 | 0.512723±2 |
| **NWA 2999** | PX | 50.36 | 0.995 | 2.707 | Static | 0.2220 | | - | 0.513477±5 |
| | PL | 16.75 | 0.037 | 0.170 | Static | 0.1307 | | - | 0.511078±91 |
| | WR | 48.60 | 0.548 | 2.237 | Static | 0.2323 | | - | 0.513712±9 |
| JNdi Standard | | | | | Static | | 1.141840±9 | | 0.512104±5 |
| | | | | | Dynamic | | 1.141839±4 | | 0.512090±3 |

[a] Fraction abbreviations: (PX) pyroxene, (PL) plagioclase, (OL) olivine, (P) phosphate, and (WR) whole-rock

[b] Analysis mode during data colleciton for reported values.

[c] Uncertainties are 2 standard deviation in the last decimal places.

[d] $^{142}Nd/^{144}Nd$ ratio at chondritic Sm/Nd ratio (Bouvier et al., 2008) relative to average Jndi standard. See text for explanation of epsilon notation.

[e] Uncertainties are 2 standard deviation in the last decimal places.

Table 2.2

Lutetium-hafnium isotope measurements of NWA 4590, NWA 4801, and D'Orbigny.

| Sample | Fraction[ab] | Mass (mg) | Lu (ppm) | Hf (ppm) | Session[c] | $^{176}Lu/^{177}Hf$ | $^{176}Hf/^{177}Hf$ (±2σ) |
|---|---|---|---|---|---|---|---|
| **NWA 4590** | PX | 79.45 | 0.422 | 4.869 | (S2) | 0.0123 | 0.280996 ± 0.000010 |
| | PX-2 | 96.10 | 0.420 | 4.902 | (S1) | 0.0122 | 0.280835 ± 0.000004 |
| | PL | 73.50 | 0.021 | 0.162 | (S3) | 0.0187 | 0.281923 ± 0.000023 |
| | OL | 85.26 | 0.668 | 0.197 | (S3) | 0.4832 | 0.321997 ± 0.000023 |
| | F | 75.58 | 0.496 | 3.010 | (S3) | 0.0235 | 0.281942 ± 0.000013 |
| | WR | 63.01 | 0.407 | 3.110 | (S2) | 0.0187 | 0.281599 ± 0.000009 |
| | WR-2 | 49.47 | 0.462 | 2.965 | (S1) | 0.0226 | 0.281745 ± 0.000006 |
| **NWA 4801** | PX | 50.03 | 0.469 | 3.398 | (S2) | 0.0197 | 0.281533 ± 0.000009 |
| | PX-2 | 101.90 | 0.462 | 3.411 | (S1) | 0.0195 | 0.281554 ± 0.000004 |
| | PL | 57.94 | 0.043 | 0.322 | (S3) | 0.0189 | 0.282356 ± 0.000014 |
| | OL | 78.43 | 0.265 | 2.824 | (S3) | 0.1185 | 0.290332 ± 0.000018 |
| | F | 68.22 | 0.336 | 1.978 | (S3) | 0.0243 | 0.281979 ± 0.000012 |
| | WR | 52.13 | 0.438 | 2.824 | (S2) | 0.0221 | 0.281704 ± 0.000009 |
| | WR-2 | 59.82 | 0.335 | 1.892 | (S1) | 0.0257 | 0.282030 ± 0.000005 |
| **D'Orbigny** | PX | 39.58 | 0.590 | 3.219 | (S2) | 0.0261 | 0.282093 ± 0.000007 |
| | PX-2 | 52.84 | 0.369 | 3.791 | (S1) | 0.0140 | 0.281018 ± 0.000005 |
| | PL | 74.91 | 0.036 | 0.173 | (S3) | 0.0296 | 0.283027 ± 0.000025 |
| | OL | 66.46 | 0.384 | 1.131 | (S3) | 0.0484 | 0.284070 ± 0.000012 |
| | F | 70.90 | 0.283 | 1.254 | (S3) | 0.0321 | 0.282630 ± 0.000016 |
| | WR | 59.21 | 0.280 | 1.984 | (S2) | 0.0201 | 0.281584 ± 0.000011 |
| | WR-2 | 54.14 | 0.305 | 1.882 | (S1) | 0.0235 | 0.281824 ± 0.000004 |
| *Hf standard* JMC 475 | Session 1 (S1) | | | | | | 0.282159 ± 0.000022 |
| | Session 2 (S2) | | | | | | 0.282125 ± 0.000053 |
| | Session 3 (S3) | | | | | | 0.282169 ± 0.000078 |

[a] Fraction abbreviations: (PX) pyroxene, (PL) plagioclase, (OL) olivine, (F) fine-size fraction ≤53 μm, and (WR) whole-rock

[b] Samples denoted as PX-2 and WR-2 are samples dissolved without a Parr bomb.

[c] Analytical session (S1, S2, and S3) in which sample was analyzed. $^{176}Hf/^{177}Hf$ ratio reported relative to JMC 745 standard analyzed during the same analytical session.

Table 2.3
Rubidium-strontium isotope measurements of NWA 4590, NWA 4801, D'Orbigny, and NWA 2999

| Sample | Fraction[a] | Mass (mg) | Rb (ppm) | Sr (ppm) | $^{87}Rb/^{86}Sr$ | $^{87}Sr/^{86}Sr$ (±2σ)[b] |
|---|---|---|---|---|---|---|
| **NWA 4590** | PX | 96.10 | 0.009 | 37.12 | 0.0007 | 0.698993 ± 0.000003 |
| | PL | 76.08 | 0.063 | 418.12 | 0.0004 | 0.699002 ± 0.000003 |
| | OL | 56.03 | 0.016 | 9.781 | 0.0047 | 0.699929 ± 0.000004 |
| | P | 0.369 | 0.373 | 801.33 | 0.0013 | 0.699073 ± 0.000014 |
| | WR | 49.47 | 0.075 | 111.03 | 0.0019 | 0.699379 ± 0.000003 |
| **NWA 4801** | PX | 101.90 | 0.013 | 52.26 | 0.0007 | 0.699039 ± 0.000003 |
| | PL | 64.38 | 0.075 | 632.89 | 0.0003 | 0.698999 ± 0.000002 |
| | OL | 70.59 | 0.017 | 13.11 | 0.0037 | 0.700070 ± 0.000007 |
| | P | 0.062 | 1.916 | 239.43 | 0.0231 | 0.700429 ± 0.000062 |
| | WR | 59.82 | 0.040 | 168.02 | 0.0007 | 0.699148 ± 0.000003 |
| **D'Orbigny** | PX | 52.84 | 0.012 | 30.06 | 0.0012 | 0.699039 ± 0.000004 |
| | PL | 104.83 | 0.042 | 246.49 | 0.0005 | 0.699019 ± 0.000003 |
| | OL | 120.32 | 0.171 | 76.03 | 0.0063 | 0.699161 ± 0.000004 |
| | WR | 54.14 | 0.013 | 41.66 | 0.0005 | 0.699180 ± 0.000003 |
| **NWA 2999** | PX | 50.36 | 0.203 | 78.31 | 0.0076 | 0.699674 ± 0.000006 |
| | PL | 16.75 | 0.308 | 504.77 | 0.0018 | 0.699099 ± 0.000007 |
| | WR | 48.60 | 0.644 | 108.65 | 0.0174 | 0.699674 ± 0.000007 |
| *Sr Standard* | | | | | | |
| NBS 987 | | | | | | 0.710243 ± 0.000007 |

[a] Fraction abbreviations: (PX) pyroxene, (PL) plagioclase, (P) phosphate, and (OL) olivine

[b] Values reported normalized to NBS 987 ($^{87}Sr/^{86}Sr = 0.71025$)

Table 2.4
Aluminum-magnesium isotope measurements of NWA 2999.

| Sample | Fraction | $^{27}Al/^{24}Mg$ | $\delta^{25}Mg$ ($\pm 2\sigma_m$) | $\delta^{26}Mg$ ($\pm 2\sigma_m$) | $\delta^{26}Mg^*$ ($\pm 2\sigma_m$) | *n* |
|---|---|---|---|---|---|---|
| **NWA 2999** | PX | 0.57 | -0.206 ± 0.008 | -0.403 ± 0.016 | -0.003 ± 0.006 | 8 |
| | PL | 180.89 | -0.138 ± 0.021 | -0.260 ± 0.044 | 0.013 ± 0.023 | 7 |
| | WR | 0.27 | -0.205 ± 0.030 | -0.410 ± 0.046 | -0.004 ± 0.009 | 8 |
| *Mg Solution Standard* | | | | | | |
| SPEX | | | -1.046 ± 0.037 | -2.031 ± 0.068 | 0.013 ± 0.026 | 8 |
| *Mineral/Rock Standards* | | | | | | |
| San Carlos Olivine | | - | -0.364 ± 0.051 | -0.719 ± 0.108 | -0.005 ± 0.019 | 8 |
| USGS BCR-2 | | 3.61 | - | - | - | 5 |
| USGS JR-2 | | 314.2 | - | - | - | 5 |

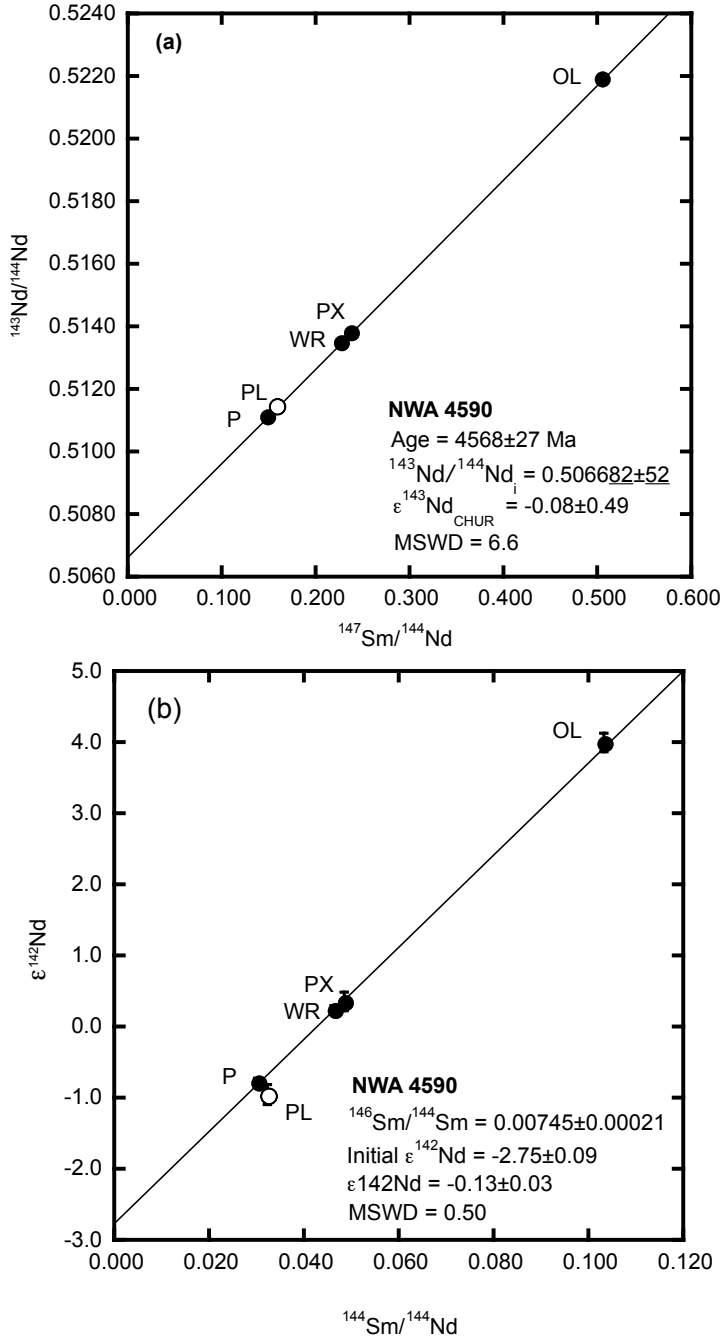


*Figure 2.1* – Internal Sm-Nd systematics of NWA 4590. (a) $^{147}Sm$-$^{143}Nd$ isochron. (b) $\varepsilon^{142}Nd$ versus $^{144}Sm/^{144}Nd$ proxy diagram of the $^{146}Sm$-$^{142}Nd$ isotope system. Fraction abbreviations: (P) Phosphate, (PL) plagioclase, (WR) whole-rock, (PX) pyroxene, and (OL) olivine. Data points that have been omitted from regression calculations are represented by open symbols. Error bars are 2SD with some error bars smaller than the data points.

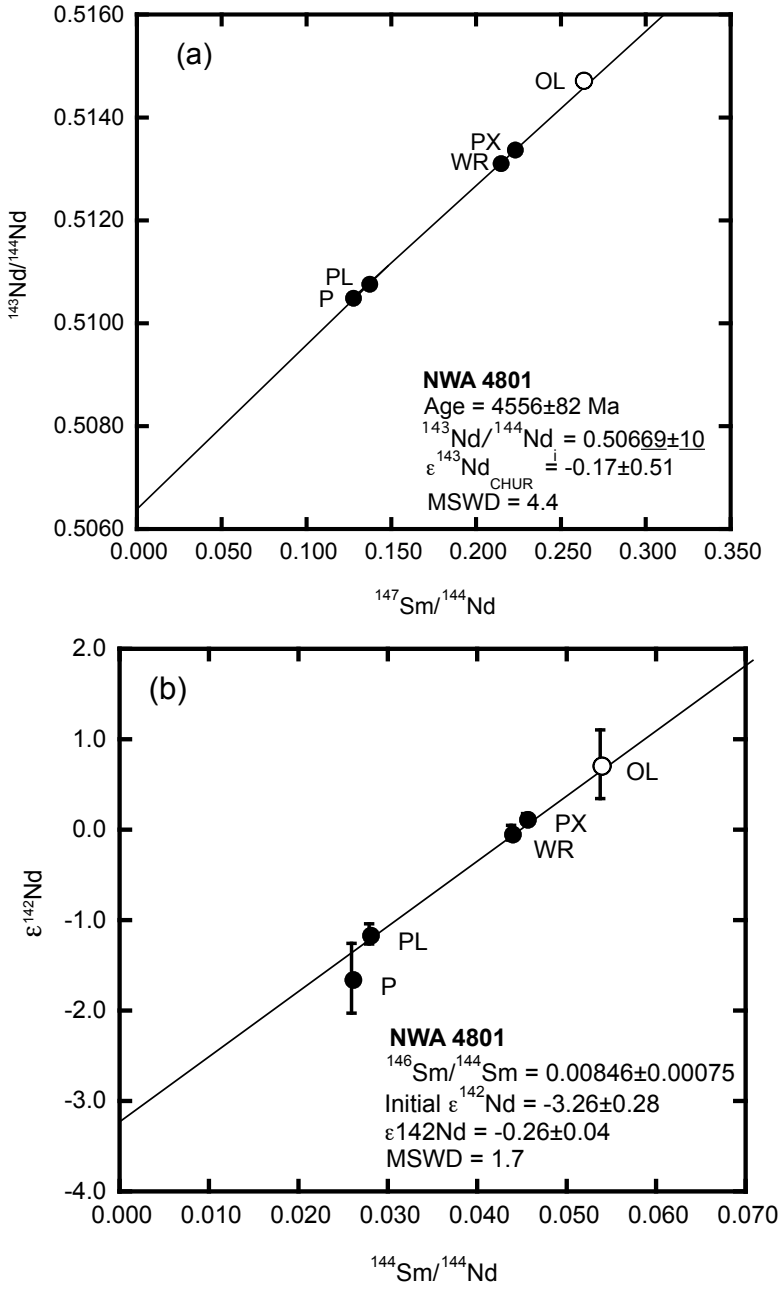


*Figure 2.2* – Internal Sm-Nd systematics of NWA 4801. (a) $^{147}Sm$-$^{143}Nd$ isochron. (b) $\varepsilon^{142}Nd$ versus $^{144}Sm/^{144}Nd$ proxy diagram of the $^{146}Sm$-$^{142}Nd$ isotope system. Fraction abbreviations are the same as Fig 2.1. Data points that have been omitted from regression calculations are represented by open symbols. Error bars are 2SD with some error bars smaller than the data points.

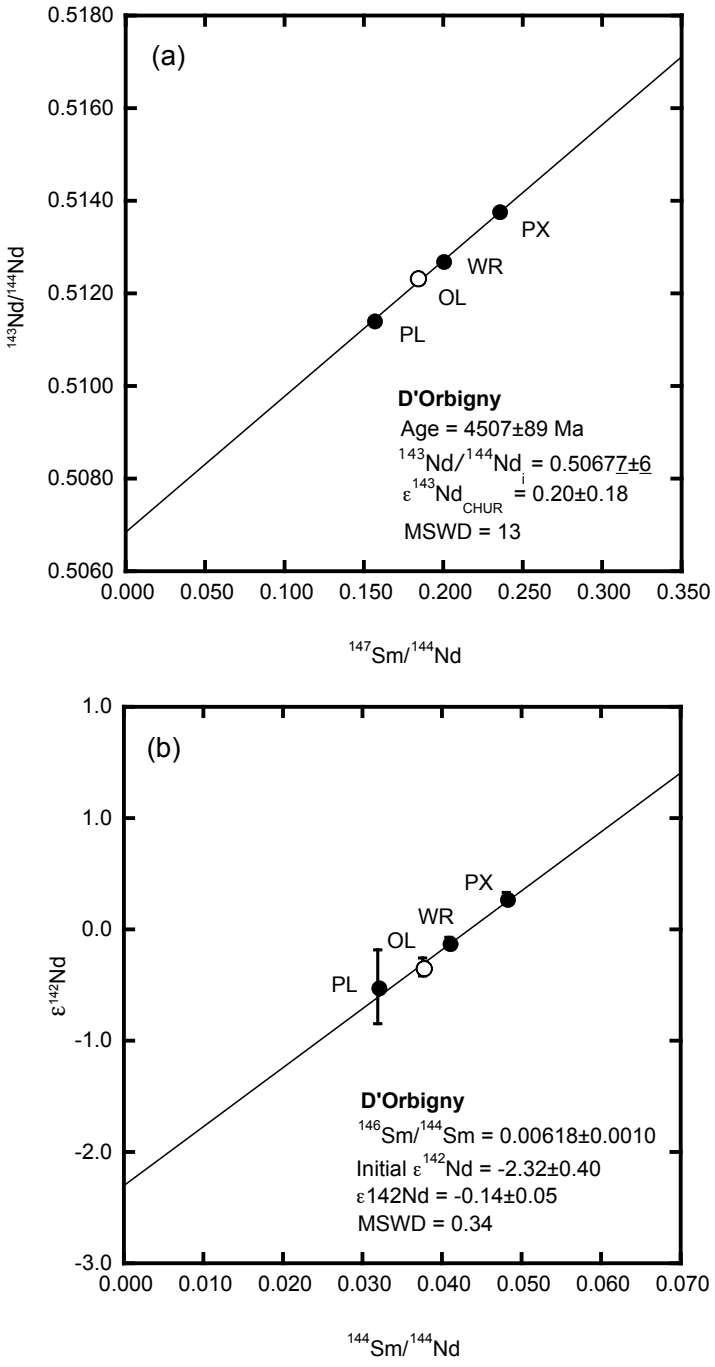


*Figure 2.3* – Internal Sm-Nd systematics of D'Orbigny. (a) $^{147}Sm$-$^{143}Nd$ isochron. (b) $\varepsilon^{142}Nd$ versus $^{144}Sm/^{144}Nd$ proxy diagram of the $^{146}Sm$-$^{142}Nd$ isotope system. Fraction abbreviations are the same as Fig. 2.1. Data points that have been omitted from regression calculations are represented by open symbols. Error bars are 2SD with some error bars smaller than the data points.

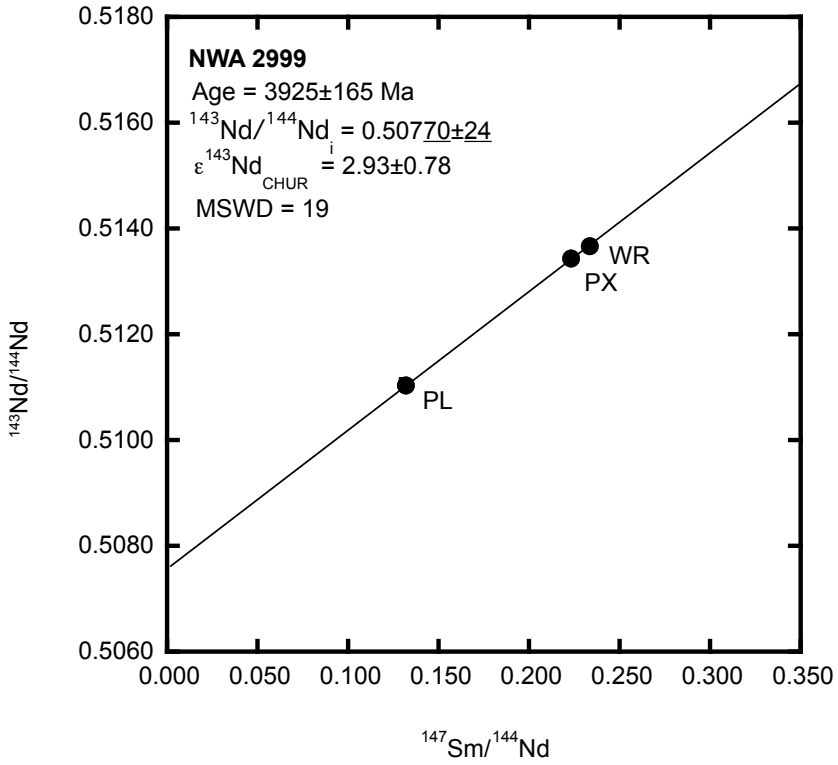


*Figure 2.4* – Internal Sm-Nd systematics ($^{147}$Sm-$^{143}$Nd isochron) of NWA 2999. Fraction abbreviations are the same as Fig 2.1. Error bars are 2SD with some error bars smaller than the data points.

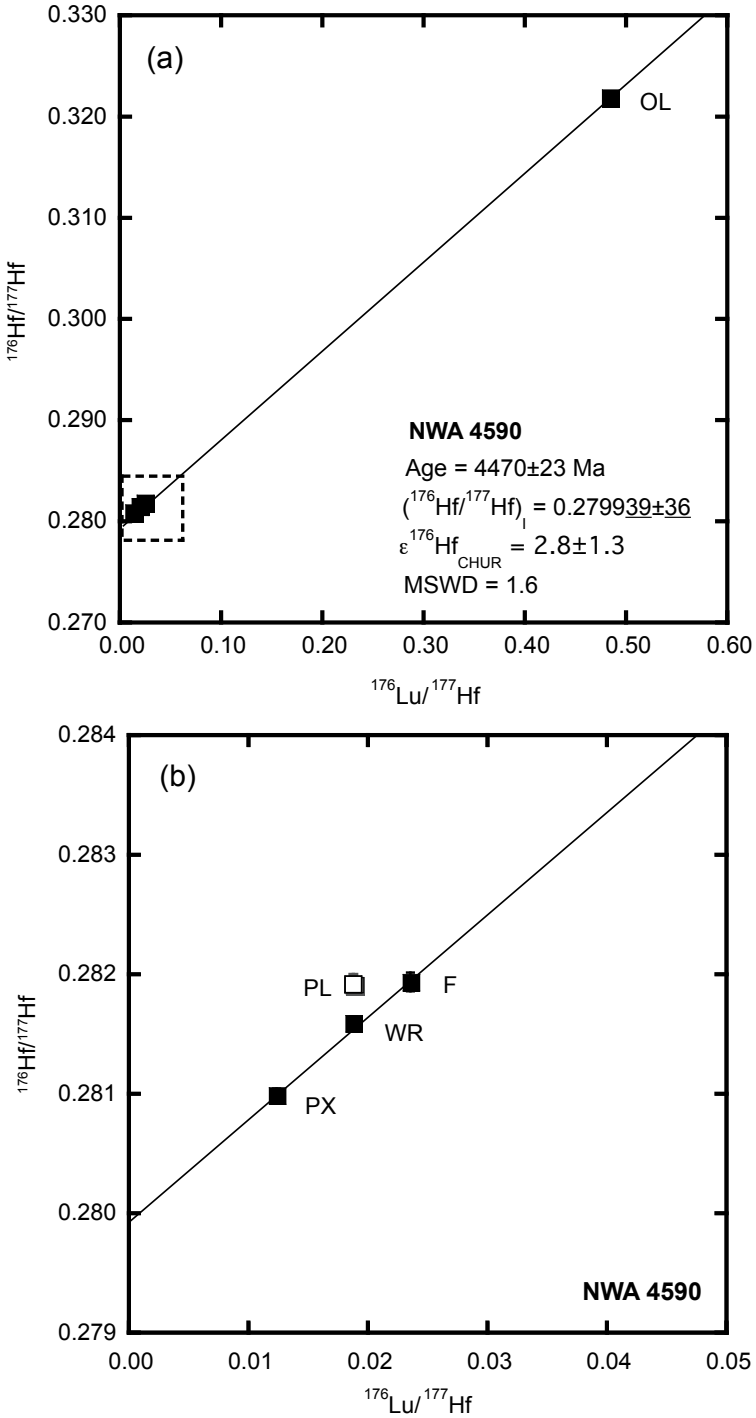


*Figure 2.5* – Internal Lu-Hf systematics of NWA 4590. (a) $^{176}$Lu-$^{176}$Hf isochron. (b) Emphasis of low $^{176}$Lu/$^{177}$Hf fractions. Fraction abbreviations: (PL) plagioclase, (WR) whole-rock, (PX) pyroxene, and (OL) olivine. Data points that have been omitted from regression calculations are represented by open symbols. Error bars are 2SD with some error bars smaller than the data points.

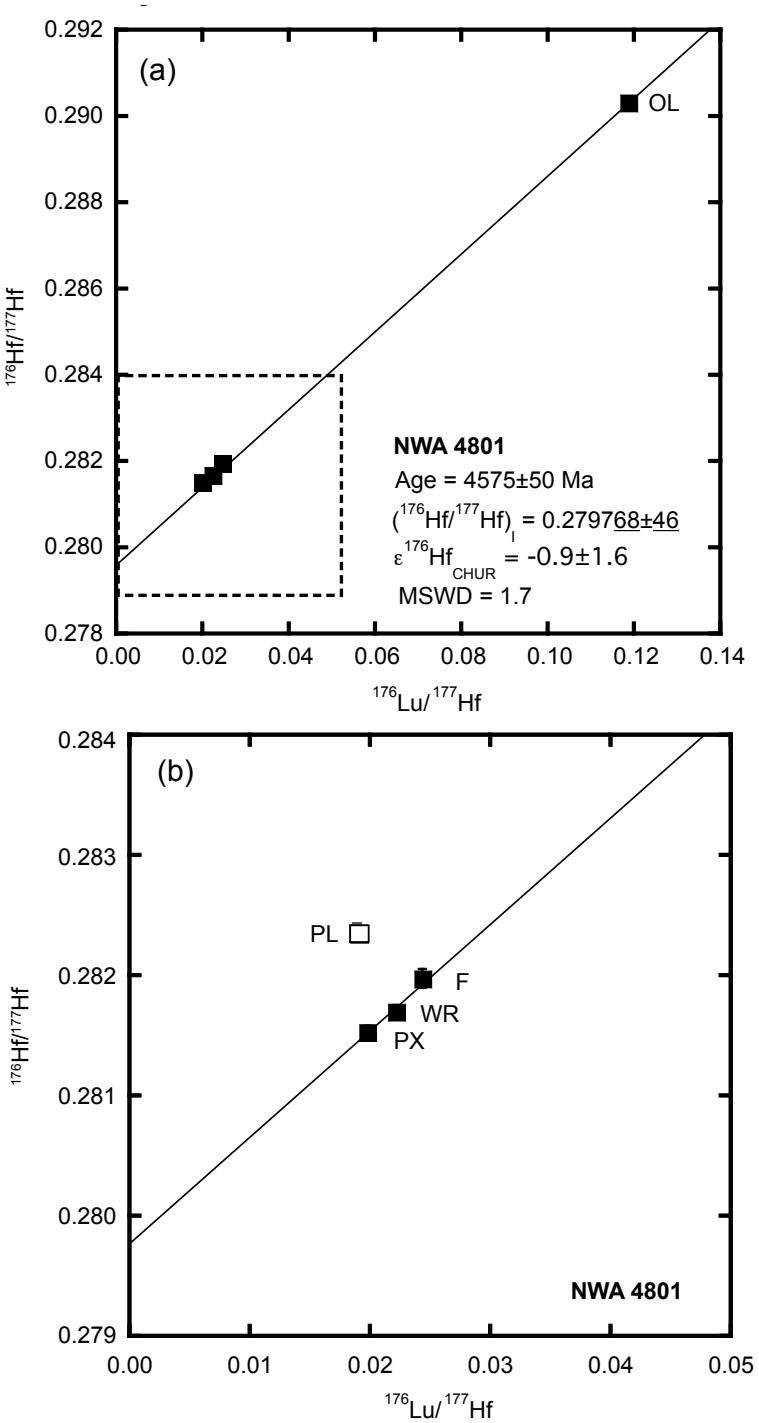


*Figure 2.6* – Internal Lu-Hf systematics of NWA 4801. (a) $^{176}$Lu-$^{176}$Hf isochron. (b) Emphasis of low $^{176}$Lu/$^{177}$Hf fractions. Fraction abbreviations are the same as Fig. 2.5. Data points that have been omitted from regression calculations are represented by open symbols. Error bars are 2SD with some error bars smaller than the data points.

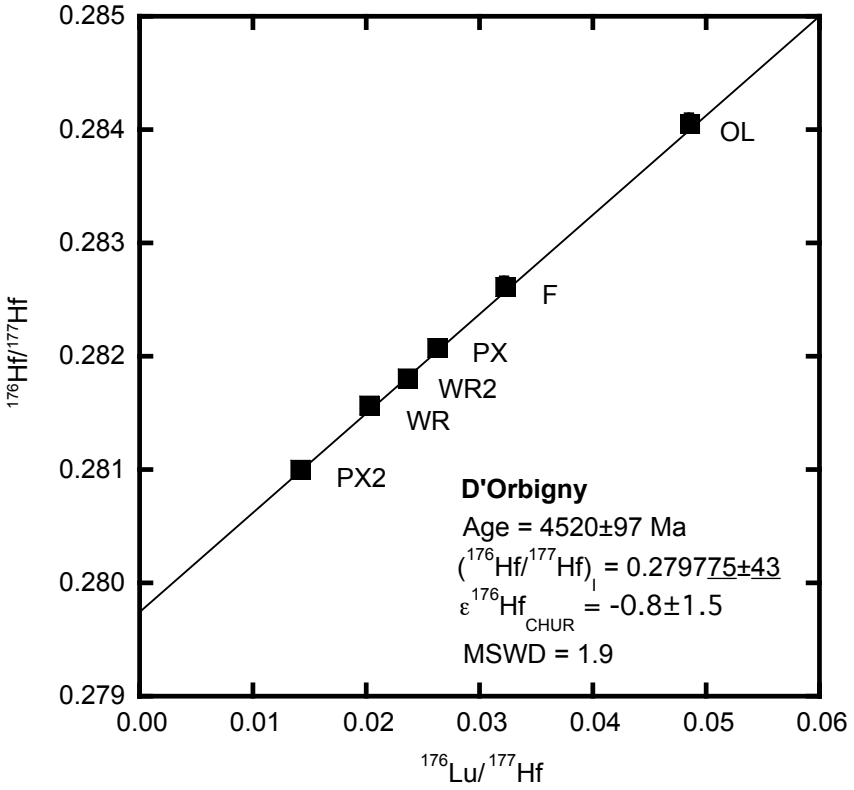


*Figure 2.7* – Internal Lu-Hf systematics ($^{176}$Lu-$^{176}$Hf isochron) of D'Orbigny. Fraction abbreviations: (PL) plagioclase, (WR, WR-2) whole-rock, (PX, PX-2) pyroxene, and (OL) olivine. Error bars are 2SD with some error bars smaller than the data points.

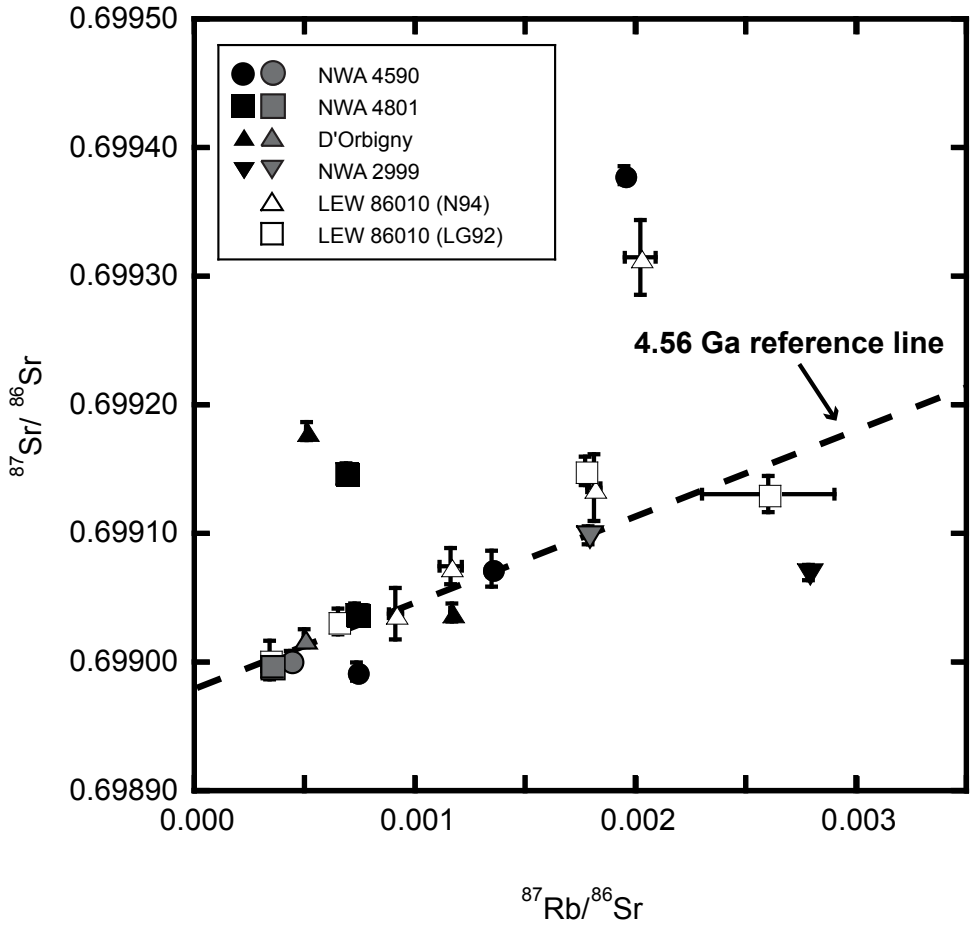


*Figure 2.8* – $^{87}Rb$-$^{87}Sr$ systematics of NWA 4590, NWA 4801, NWA 2999, and D'Orbigny. Gray data points denote the plagioclase fractions. Open symbols are literature data for angrite LEW 86010 (LG92: Lugmair and Galer, 1992; N94: Nyquist et al., 1994). The 4.56 Ga reference line from the average angrite initial $^{87}Sr/^{86}Sr$ is represented by the dashed line. Error bars are 2SD with some error bars smaller than the data points.

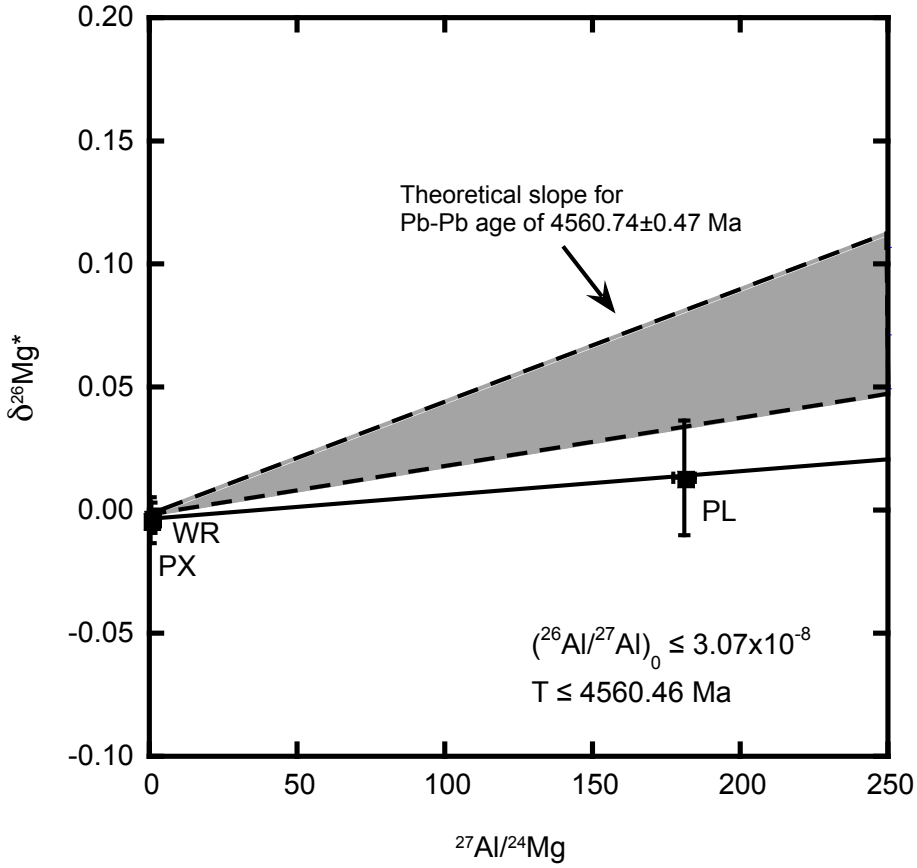


*Figure 2.9* – $\delta^{26}Mg^{*}$ versus $^{27}Al/^{24}Mg$ diagram for NWA 2999. Fraction abbreviations: (PX) Pyroxene, (WR) whole-rock, and (PL) plagioclase. Error bars are 2SE. Shaded region indicates the theoretical slope of an $\delta^{26}Mg^{*}$ versus $^{27}Al/^{24}Mg$ diagram for an age of 4560.74±0.47 Ma.

## 2.5 DISCUSSION

### 2.5.1 Coupled $^{147}$Sm-$^{143}$Nd and $^{146}$Sm-$^{142}$Nd Systematics of Angrites

Knowledge of the long-lived $^{147}$Sm-$^{143}$Nd and short-lived $^{146}$Sm-$^{142}$Nd isotope systems in angrites has been hindered by the paucity of detailed isotopic studies. Studies of the Sm-Nd systematics in angrites have been limited primarily to two samples, LEW 86010 and Angra dos Reis, with LEW 86010 the only sample exhibiting evidence of coupled $^{147}$Sm-$^{143}$Nd and $^{146}$Sm-$^{142}$Nd isotope systematics that appear undisturbed (Lugmair and Marti, 1977; Jacobson and Wasserburg, 1984; Lugmair and Galer, 1992; Nyquist et al., 1994). The $^{147}$Sm-$^{143}$Nd and $^{146}$Sm-$^{142}$Nd isotope systematics of NWA 2999, NWA 4590, NWA 4801, and D′Orbigny which represent a range of crystallization ages, burial depths, and cooling histories can provide new insight into their evolution on the angrite parent body.

The $^{147}$Sm-$^{143}$Nd age of 4568±27 Ma determined for NWA 4590 is concordant with its U-isotope corrected Pb-Pb age of 4557.81±0.37 Ma (Amelin et al., 2011; Brennecka and Wadhwa, 2012). In addition, the $^{147}$Sm-$^{143}$Nd systematics yields an age that is in agreement with the age obtained using the Hf-W relative chronometer (Kleine et al., 2012). The present-day initial $\varepsilon^{143}Nd_{CHUR}$ value of -0.08±0.49 obtained from the NWA 4590 systematics is indistinguishable from the average chondrite composition. The agreement between the Sm-Nd, Pb-Pb, and Hf-W ages coupled with the $\varepsilon^{143}Nd_{CHUR}$ value suggests the Sm-Nd systematics are isotopically undisturbed in NWA 4590. Furthermore, the $^{146}$Sm-

$^{142}$Nd isochron of NWA 4590 currently provides the highest precision $^{146}$Sm/$^{144}$Sm ratio measured in an angrite of 0.00745±0.00021.

As with NWA 4590, the $^{147}$Sm-$^{143}$Nd age of 4556±82 Ma of NWA 4801 is in full agreement with its U-isotope corrected Pb-Pb age of 4557.01±27 Ma (Amelin and Irving, 2006; Brennecka and Wadhwa, 2012), as well as the Hf-W and Mn-Cr chronometers (Shukolyukov et al., 2009; Kleine et al., 2012). The $^{146}$Sm/$^{144}$Sm ratio of 0.00846±0.00075 of NWA 4801, while not as precise as NWA 4590, provides an additional, robust estimate of the angrite initial $^{146}$Sm/$^{144}$Sm ratio.

In contrast with the isotopically undisturbed nature of the Sm-Nd system observed in NWA 4590 and NWA 4801, both D'Orbigny and NWA 2999 provide evidence for subsequent resetting of their Sm-Nd systematics. While the D'Orbigny $^{147}$Sm-$^{143}$Nd age of 4507±89 Ma overlaps the absolute Pb-Pb age of 4563.37±0.25 Ma (Amelin, 2008; Brennecka and Wadhwa, 2012), the overlap is largely due to the significant uncertainty in the age associated with scatter about the regression line coupled with the narrow Sm/Nd ratio range encompassed by the data. The apparent disturbance is further evident in the $\varepsilon^{143}Nd_{CHUR}$ value of D'Orbigny. The $\varepsilon^{143}Nd_{CHUR}$ value of +0.20±0.18 is elevated compared to the values obtained from NWA 4590 and NWA 4801 that are unresolvable from the average chondrite values. Additional evidence for disturbance of the Sm-Nd system can be observed in the D'Orbigny $^{146}$Sm/$^{144}$Sm ratio of 0.00618±0.0010 obtained from the $^{146}$Sm-$^{142}$Nd isochron. This $^{146}$Sm/$^{144}$Sm ratio is significantly lower than the ratio observed in NWA 4590 and NWA 4801. The lower $^{147}$Sm-

$^{143}$Nd age, positive $\varepsilon^{143}Nd_{CHUR}$ value, and lower $^{146}$Sm/$^{144}$Sm ratio suggests a substantial disturbance in the Sm-Nd system of D'Orbigny. The apparent resetting of the Sm-Nd system is particularly important given the previously concordant nature observed in a suite of short-lived chronometers in D'Orbigny and its use as a relative time anchor.

A similar disturbance of the $^{147}$Sm-$^{143}$Nd system is seen in NWA 2999. From the isotopic results, an absolute $^{147}$Sm-$^{143}$Nd age of 3925±125 Ma is estimated. The young age is well resolved from the U-isotope corrected Pb-Pb age (Amelin and Irving, 2006; Brennecka and Wadhwa 2012) and the short-lived, relative Hf-W and Mn-Cr chronometers (Shukolyukov and Lugmair, 2008; Kleine et al., 2012). The large positive $\varepsilon^{143}Nd_{CHUR}$ value for NWA 2999 of +2.93±0.78, a value significantly higher than that of NWA 4590, NWA 4801, and D'Orbigny, further suggests a disturbance of the $^{147}$Sm-$^{143}$Nd system later in the evolution of the angrite parent body.

The coupled $^{147}$Sm-$^{143}$Nd and $^{146}$Sm-$^{142}$Nd systematics of these angrites indicates a more complex isotopic history compared to that inferred from the short-lived Al-Mg, Hf-W, and Mn-Cr chronometers commonly utilized. The exact cause of an isotopic resetting event in the NWA 2999 and D'Orbigny is not easily discernable. Contrary to other achondrite groups that contain samples that exhibit disturbed Sm-Nd systematics (e.g., eucrites), angrites provide no evidence for widespread shock metamorphism and most lack evidence of thermal metamorphism events (Mittlefehldt et al., 1998). However, there are a few pieces of evidence suggesting NWA 2999 experienced some degree of thermal

metamorphism. These lines of evidence include the homogenous composition of the clinopyroxene and the presence of petrographic textures (i.e., symplectites and coronas) analogous to metamorphic textures in terrestrial rocks (Kuehner et al., 2006). Therefore, the disturbance of the Sm-Nd systematics may be recording further evidence of metamorphism of NWA 2999. D'Orbigny, however, presents no petrographic or chemical evidence for thermal metamorphism (Mittlefehldt et al., 2002), one reason for its use as a relative time anchor. The older Pb-Pb, Hf-W, and Mn-Cr ages obtained in both NWA 2999 and D'Orbigny indicate that the cause of the Sm-Nd resetting did not reach an intensity or duration that allowed a resetting of all the isotope systems. The observed resetting of the Sm-Nd systematics appears to be independent of the burial depth, with resetting occurring in both D'Orbigny and NWA 2999, and not correlated to a single episode with a 500 Ma time difference between the resetting events in these two angrites.

### 2.5.2 Determination of solar system initial $^{146}Sm/^{144}Sm$ ratio from angrites: Comparison to other planetary materials

A detailed understanding of the initial isotopic composition of the Solar System (e.g., the initial abundance of short-lived radionuclides such as $^{146}Sm$) is essential for fully elucidating the formation and subsequent evolution of the early Solar System (e.g., isotopic homogeneity or heterogeneity) and timescales associated with Solar System formation (e.g., the free decay interval). A recent Solar System initial $^{146}Sm/^{144}Sm$ ratio (i.e., $(^{146}Sm/^{144}Sm)_0$) was reported by Boyet et al. (2010) based on the calculated average of the $^{146}Sm/^{144}Sm$ ratios from a suite of achondrites (four eucrites, one angrite, and one mesosiderite)

extrapolated from their Sm-Nd closure age to 4568 Ma (i.e., the initial Solar System). This estimate of $(^{146}Sm/^{144}Sm)_0$= 0.0085±0.0007 from Boyet et al. (2010) was calculated based using a $^{146}Sm$ half-life of ~103 Myr. However, the recent experimental work by Kinoshita et al. (2012) has estimated a revised half-life for $^{146}Sm$ of 68 Myr, a value considerably shorter than the previous estimates. The magnitude of the difference between the two half-lives has significant implications for estimates of the Solar System initial $^{146}Sm/^{144}Sm$ ratio. Using the previously reported data of Boyet et al. (2010), the new half-life corresponds to a Solar System initial $^{146}Sm/^{144}Sm$ ratio of 0.0094±0.0005 (Kinoshita et al., 2012). However, this value is only based on six achondrites with only one of those an angrite. The results of $^{146}Sm$-$^{142}Nd$ isotope systematics analyses in NWA 4590, NWA 4801, and D'Orbigny present the opportunity to further refine our understanding of the Solar System initial $^{146}Sm/^{144}Sm$ ratio with three additional angrites.

Using the measured $^{146}Sm/^{144}Sm$ ratio measured at the closure time of the Sm-Nd system, the $^{146}Sm/^{144}Sm$ ratios of NWA 4590, NWA 4801, and D'Orbigny were extrapolated to the ratio at 4568 Ma using the revised $^{146}Sm$ half-life (68 Myr) of Kinoshita et al. (2012). Given the undisturbed nature of NWA 4590 and NWA 4801, the more precise Pb-Pb from each meteorite (Amelin and Irving, 2006; Brennecka and Wadhwa, 2012) was used for the initial Solar System $^{146}Sm/^{144}Sm$ ratio calculation. The $^{147}Sm$-$^{143}Nd$ age (i.e., 4507 Ma) was used for D'Orbigny due to the apparent disturbance of the Sm-Nd system. Table 2.5 shows the calculated initial Solar System $^{146}Sm/^{144}Sm$ ratio for each of the

angrites. NWA 4590 yields the best estimate of the Solar System initial $^{146}Sm/^{144}Sm$ from this study with a $(^{146}Sm/^{144}Sm)_0$ ratio of 0.0084±0.0003. A Solar System initial $^{146}Sm/^{144}Sm$ ratio of 0.0086±0.0008 is obtained when averaging all reported undisturbed angrites (This study; Lugmair and Galer, 1992). Expanding the included ratios to all undisturbed angrite and eucrites (This study; Lugmair et al., 1991; Lugmair and Galer, 1992; Wadhwa and Lugmair, 1996; Boyet et al., 2010) an average Solar System initial $^{146}Sm/^{144}Sm$ ratio of 0.0089±0.0005 is calculated. The two undisturbed angrites in this study (i.e., NWA 4590 and NWA 4801) yield consistent initial Solar System $^{146}Sm/^{144}Sm$ ratios, within error, of each other and the previously measured angrite LEW 86010 (Lugmair and Galer, 1992; Nyquist et al., 1994). Furthermore, the Solar System initial $^{146}Sm/^{144}Sm$ ratio calculated from the new angrites overlap, within error, the values calculated using eucrites (Fig. 2.10). The indistinguishable Solar System initial $^{146}Sm/^{144}Sm$ ratio observed in a range of achondrites further supports the homogenous distributions of Sm isotopes in the source region(s) for the achondrite parent bodies in the early Solar System as suggested previously by Boyet et al. (2010).

### 2.5.3 Initial $^{87}Sr/^{86}Sr$ Ratio of the Angrites and Inferred Timing of Volatile Loss

A notable characteristic of angrites is the relative extreme depletion of alkali and moderately volatile elements such as Na, Rb, and Cs (e.g., Tera et al., 1970), which results in extremely low $^{87}Rb/^{86}Sr$ ratios. The associated minimal spread in the $^{87}Rb/^{86}Sr$ ratios precludes the acquisition of high precision ages from

internal $^{87}$Rb-$^{87}$Sr isochrons. In addition, terrestrial weathering can be problematic for certain phases, such as olivine and pyroxene, not only due to the low Rb content, but also relatively low Sr content. Nevertheless, the extremely low $^{87}$Rb/$^{86}$Sr ratios of phases, such as plagioclase with $^{87}$Rb/$^{86}$Sr <0.0005, are useful in the determination of high-precision model initial $^{87}$Sr/$^{86}$Sr values with a minimal amount of extrapolation. The calculation of model initial $^{87}$Sr/$^{86}$Sr values has been utilized in previous angrite Rb-Sr studies (e.g., Lugmair and Galer, 1992; Nyquist et al. 1994) and is accomplished using the measured $^{87}$Sr/$^{86}$Sr value, the corresponding $^{87}$Rb/$^{86}$Sr ratio, a model age of 4.56 Ga, and a $^{87}$Rb decay constant of $1.402\times10^{11}$ yr$^{-1}$ (Minster et al., 1982). While this model initial calculation can be applied to any phase, plagioclase is the most resistant to the effects of terrestrial Sr contamination (due to the high Sr content) and has among the lowest $^{87}$Rb/$^{86}$Sr ratio, requiring a minimal adjustment for radiogenic ingrowth of $^{87}$Rb. The calculated model initial $^{87}$Sr/$^{86}$Sr using the plagioclase from each angrite is presented in Table 2.7. The model initial $^{87}$Sr/$^{86}$Sr of all four angrites are in agreement with each other and correspond to an average initial $^{87}$Sr/$^{86}$Sr of 0.698978±0.000003.

The exact timing of the volatile loss on the angrite parent body is still an open question with important implications for early Solar System processes. Utilizing the method described by Gray et al. (1973), the timing of volatile loss on the angrite parent body can be estimated by the comparison of the angrite parent body initial $^{87}$Sr/$^{86}$Sr ratio (as calculated through the model initial $^{87}$Sr/$^{86}$Sr of the plagioclase samples) with a time-evolution curve of the $^{87}$Sr/$^{86}$Sr isotope ratio

from an initial point representative of the initial bulk Solar System composition. An optimal approximation of the Solar System initial isotopic composition has been proposed to be the refractory calcium-aluminum rich inclusions, particularly the Allende CV3 chondrite, that yield that most primitive (i.e., lowest) $^{87}Sr/^{86}Sr$ compositions measured (e.g., Grey et al., 1973). However, the application of this method using Allende CAIs is slightly complicated by conflicting initial $^{87}Sr/^{86}Sr$ compositions. Two values are presently reported for the Allende CAI initial $^{87}Sr/^{86}Sr$ composition, 0.698808±0.000020 for the Allende 3529-Z CAI (Podosek et al., 1991) and 0.698774±0.000022 for the Allende D7 CAI (Gray et al., 1973). Since there is no clear reason to choose the $^{87}Sr/^{86}Sr$ estimates of one CAI (3529-Z or D7) over another, it is necessary to utilize both values when inferring the timing of volatile loss on the angrite parent body.

Figure 2.11 shows the $^{87}Sr/^{86}Sr$ isotopic evolution from each of these initial values, assuming a solar photosphere $^{87}Rb/^{86}Sr$ ratio of 1.5 (Anders and Grevasse, 1989), in relation to the average angrite model initial $^{87}Sr/^{86}Sr$. The intersection of the $^{87}Sr/^{86}Sr$ evolution line with the $^{87}Sr/^{86}Sr$ initial ratio of the angrite parent body indicates the point at which the loss of Rb occurred from the angrite source reservoir. The results indicate that the timing of volatile loss in the angrites occurred at a point approximately 3-5 Ma after CAI formation, a value that does not significantly differ from earlier estimates of volatile loss from Nyquist et al. (1994). This time range would place the volatile loss event after the angrite parent body accretion and core formation that occurred in the initial ~2 Myr after CAI formation (Kleine et al., 2012) and contemporaneous with the

formation of the quenched angrites (e.g., Amelin 2008; Brennecka and Wadhwa, 2012). It is important to note that recent reports have indicated the presence of Sr isotopic anomalies in Allende CAIs (e.g., Monyier et al., 2010; Patton et al., 2011; Hans et al., 2011; Brennecka et al., 2012); the exact nature of the isotopic anomaly is still ambiguous. If the isotopic anomaly were present on one of the isotopes used for mass fractionation normalization in the previous Allende studies (e.g., excesses in $^{88}Sr$), it would have implications in terms the measured $^{87}Sr/^{86}Sr$ ratio with broader implication on the initial Solar System composition used in the volatile loss timing estimates (Hans et al., 2011). However, it is not currently possible to determine exactly which Sr isotope or isotopes is experiencing a nucleosynthetic anomaly. Until the ambiguity of the CAI initial Sr isotopic compositions are clarified, the estimate of volatile loss in the angrite source material 3-5 Myr after CAI formation (made using the assumption that any nucleosynthetic anomalies are not affecting $^{88}Sr$) can be considered a lower-limit estimate for the time at which volatiles were removed from the angrite source material.

### 2.5.4 Lu-Hf Systematics of the Angrites and the Implications of Early Solar System Irradiation Models

The long-lived $^{176}Lu$-$^{176}Hf$ isotope system has the potential to be an important chronometer for understanding planetary differentiation processes and evolution. However, the utilization of the $^{176}Lu$-$^{176}Hf$ system requires: (1) knowledge of the $^{176}Lu$ decay constant (i.e., $\lambda^{176}Lu$), (2) knowledge of the initial Solar System $^{176}Hf/^{177}Hf$ isotopic composition, and (3) an understanding of

potential mechanisms that can alter the $^{176}$Lu-$^{176}$Hf isotope systematics. The investigation of the $^{176}$Lu-$^{176}$Hf isotope system in meteoritic samples to address these constraints has almost solely focused on whole-rock eucrite and chondrite samples (e.g., Patchett and Tatsumoto, 1980, Blichert-Toft et al., 2002, Bizzarro et al., 2003; and Patchett et al., 2004). Early estimates of the $^{176}$Lu decay constant made by measuring the $^{176}$Lu-$^{176}$Hf systematics in samples with accompanying U-Pb ages provided conflicting values depending on whether the material was a terrestrial or meteoritic sample (e.g., Patchett and Tatsumoto, 1980; Scherer et al., 2001). An analysis of specifically chosen terrestrial samples by Söderlund et al. (2004) yielded a $\lambda^{176}$Lu value of $1.867\times10^{-11}$ yr$^{-1}$. Amelin (2005) subsequently verified the $\lambda^{176}$Lu value from Söderlund et al. (2004) using phosphates from the Richardton and Acapulco meteorites, confirming the applicability of the decay constant to both terrestrial and meteoritic samples. The previously anomalous $\lambda^{176}$Lu values from chondrite and eucrite whole-rock samples appear to have arisen from excess in $^{176}$Hf correlated to the $^{176}$Lu/$^{177}$Hf ratio (i.e., an increased slope of the $^{176}$Lu-$^{176}$Hf isochron). To account for the apparent excess $^{176}$Hf, Albarède et al. (2006) proposed a $\gamma$-ray irradiation model that results in excess $^{176}$Hf by the formation of a short-lived $^{176}$Lu isomer. The observed excess of $^{176}$Hf was limited to the whole-rock eucrite and chondrite $^{176}$Lu-$^{176}$Hf isochrons (e.g., Patchett and Tatsumoto, 1980, Blichert-Toft et al., 2002, Bizzarro et al., 2003; and Patchett et al., 2004), until the recent measurement of an internal $^{176}$Lu-$^{176}$Hf isochron of the angrite Sahara 99555 by Bizzarro et al. (2012). From the Sahara 99555 internal isochron, Bizzarro et al. (2012) determined a $^{176}$Lu-$^{176}$Hf

age of 4869±34 Myr with an initial $^{176}Hf/^{177}Hf$ of 0.279685±0.000019. This implausibly old age is approximately 300 Ma older than the commonly accepted age of the Solar System at 4568 Ma (Bouvier and Wadhwa, 2010). According to Thrane et al. (2010), the excess $^{176}Hf$ observed in Sahara 99555 could not be explained using the gamma-ray irradiation model of Albarède et al. (2006) due to the predicted burial depth (i.e., less than 0.5 m) on the angrite parent body being greater than the penetration depth of gamma-ray irradiation. To account the observed excess of $^{176}Hf$ in Sahara 99555, Thrane et al. (2010) proposed a mechanism involving cosmic ray irradiation of the angrite parent body for the generation of a short-lived $^{176}Lu$ isomer that rapidly decays to $^{176}Hf$ in a similar fashion to the γ-ray irradiation model of Albarède et al. (2006). However, this interpretation and model is complicated by the subsequent determination of an angrite whole-rock $^{176}Lu$-$^{176}Hf$ isochron by Amelin et al. (2011) that yielded an age of 4576±49 Ma, suggesting the absence of an irradiation event, such as that proposed by Thrane et al. (2010). The three new internal $^{176}Lu$-$^{176}Hf$ isochrons determined for NWA 4590, NWA 4801, and D'Orbigny allow for the further testing of the cosmic-ray irradiation model of Thrane et al. (2010) and further constraining the initial $^{176}Hf/^{177}Hf$ ratio with its implications for the evolution of $^{176}Hf/^{177}Hf$ ratio over time.

D'Orbigny provides an optimal sample for a direct comparison to the Sahara 99555 angrite analyzed by Bizzarro et al. (2012) to evaluate the proposed intense irradiation event. D'Orbigny and Sahara 99555 have identical Pb-Pb ages indicating contemporaneous crystallization (Amelin, 2008; Amelin and Irving,

2007; Brennecka and Wadhwa, 2012) and comparable burial depths on the angrite parent body obtained from cooling rates of the quenched angrites (Mikouchi et al., 2001). As such, both angrites should have the same potential for exposure to any irradiation events affecting the angrite parent body. The D'Orbigny internal isochron obtained in this study yields an age of 4520±97 Ma, an age indistinguishable from its Pb-Pb age of 4563.37±0.25 Ma (Amelin, 2008; Brennecka and Wadhwa, 2012), in direct contrast with the implausibly old $^{176}$Lu-$^{176}$Hf age obtained by Bizzarro et al. (2012) for Sahara 99555. Furthermore, the internal $^{176}$Lu-$^{176}$Hf isochron of NWA 4801, with a greater burial depth than the quenched angrites, yields a $^{176}$Lu-$^{176}$Hf age of 4575±50 Ma that is consistent with its previously determined Pb-Pb age of 4557.01±0.27 Ma (Amelin and Irving, 2006; Brennecka and Wadhwa, 2012). The concordant $^{176}$Lu-$^{176}$Hf age of D'Orbigny and NWA 4801 obtained in this study do not require the invocation of a cosmic-ray irradiation event of the angrite parent body and indicate these two angrites have not experienced any post-closure isotopic disturbance, providing the first examples of undisturbed internal Lu-Hf isochrons from an achondrite. In contrast, the internal isochron of NWA 4590 provides a nominally younger $^{176}$Lu-$^{176}$Hf age and a slightly higher initial $^{176}$Hf/$^{177}$Hf ratio, suggesting a significant disturbance of the $^{176}$Lu-$^{176}$Hf system after its initial closure.

With the occurrence of a high-energy irradiation event not evident in D'Orbigny and NWA 4801, the initial $^{176}$Hf/$^{177}$Hf ratios obtained from the internal $^{176}$Lu-$^{176}$Hf isochrons of these samples can be used to determine a robust initial $^{176}$Hf/$^{177}$Hf ratio of the Solar System. Previous studies that have estimated

the initial $^{176}Hf/^{177}Hf$ ratio from internal isochrons (e.g., Bizzarro et al., 2012) have relied on isochrons that have yielded anomalous $^{176}Lu$-$^{176}Hf$ ages, making the reliability of the initial ratios uncertain. Averaging the initial $^{176}Hf/^{177}Hf$ ratio of D'Orbigny and NWA 4801, which agree within error of each other, provides a best estimate of the angrite parent body initial $^{176}Hf/^{177}Hf$ ratio of 0.279772±0.000031 (2σ). This value is indistinguishable from the initial $^{176}Hf/^{177}Hf$ ratio obtained from angrite whole-rocks (Amelin et al., 2011) and chondrite whole-rocks (Bouvier et al., 2008), but is in stark contrast with the initial value ~ 3 epsilon units lower estimated by Bizzarro et al. (2012) using the Sahara 99555 angrite (Fig. 2.12). The "normal" internal isochrons (i.e., no evidence of excess $^{176}Hf$) of D'Orbigny and NWA 4801 and the consistent nature between these samples and the recent whole-rock studies of angrites and chondrites suggest these values yield the current best estimates for the Solar System initial $^{176}Hf/^{177}Hf$. The estimate of the initial $^{176}Hf/^{177}Hf$ ratio provides further constraints to assist in the full utilization of the $^{176}Lu$-$^{176}Hf$ isotope system in investigations of other planetary materials. However, while a cosmic-ray irradiation mechanism for alteration of the $^{176}Lu$-$^{176}Hf$ systematics now appears doubtful given the pristine nature of the system in D'Orbigny, the cause of the anomalous results in Sahara 99555 are still uncertain and need further investigation.

### 2.5.5 Al-Mg Systematics and Additional Constraints on the Age of NWA 2999

The ages of angrites, as determined using Pb-Pb chronometry, encompass a time span of approximately seven million years from ~4563 Ma to ~4556 Ma (Amelin, 2008; Brennecka and Wadhwa, 2012, and references therein). Among the sixteen presently known angrites, all but NWA 2999 (and its paired stones) fall into one of two chronological groupings: (1) the quenched, fine-grained angrites that have Pb-Pb ages clustered around 4563 Ma and (2) plutonic, course-grained angrites that yield ages of approximately 4557 Ma. NWA 2999 is presently the only angrite with an "intermediate" Pb-Pb age that does not fall into one of the two chronological groups based on the quenched and plutonic angrites (Amelin and Irving, 2007; Brennecka and Wadhwa, 2012). Furthermore, the unique Pb-Pb age of NWA 2999 is complicated by the short-lived Mn-Cr and Hf-W systems, which have been measured within the sample. The Hf-W system yields an age of 4559.8±0.9 Ma that overlaps, within error, the Pb-Pb age (Kleine et al., 2012). However, the Mn-Cr system provides a younger, discordant age of 4557.9±1.1 Ma (Shukolyukov and Lugmair, 2008). The unique Pb-Pb age and the lack of agreement among the short-lived chronometers have made the formation age of NWA 2999 particularly difficult to constrain.

The short half-life of $^{26}Al$ ($t_{1/2}$ ~ 0.72 Myr), compared to the other relative chronometers, limits its utility for objects much younger than ~4560 Ma due to the analytical precision currently available for determining radiogenic $^{26}Mg^{*}$ excess; however, the $^{26}Al$-$^{26}Mg$ system can be used to determine an upper-limit

$^{26}Al/^{27}Al$ ratio and age. The $^{26}Al$-$^{26}Mg$ systematics of NWA 2999 provides an upper-limit age ≤ 4560.46 Ma, which is within the error of the Pb-Pb age of 4560.74±0.47 Ma (Amelin and Irving, 2007; Brennecka and Wadhwa, 2012). While the $^{26}Al$-$^{26}Mg$ age can only place an upper-limit to the age of NWA 2999, it does provide yet another chronometer that is in agreement, although marginally, with the unique Pb-Pb age. Although the Mn-Cr age still provides at least one relative chronometer that is not in agreement with the Pb-Pb age, additional support of an intermediate Pb-Pb age for NWA 2999 indicates that the petrogenesis of the plutonic, coarse-grained angrites occurred over a time span of approximately three million years. Furthermore, NWA 2999 provides the first evidence for magmatic activity on the angrite parent body outside of the periods indicated by the previous chronology groups of the plutonic and quenched angrites.

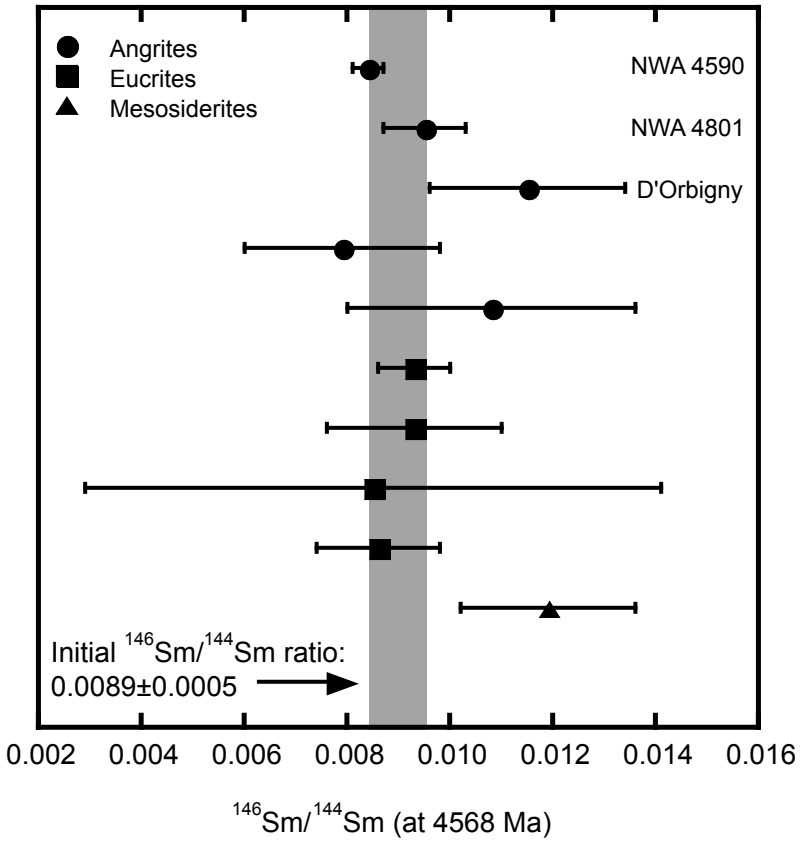


*Figure 2.10* – Initial Solar System $^{146}Sm/^{144}Sm$ ratio (i.e., at 4568 Ma) for NWA 4590, NWA 4801, and D'Orbigny. Also shown are the calculated Solar System initial $^{146}Sm/^{144}Sm$ ratios from previously reported angrite, eucrite, and mesosiderite $^{146}Sm/^{144}Sm$ data (Lugmair et al., 1991; Lugmair and Galer, 1992; Stewart et al., 1994; Wadhwa and Lugmair, 1996; Boyet et al., 2010). Shaded region indicates the calculated initial Solar System $^{146}Sm/^{144}Sm$ ratio from angrites and eucrites (see text for details).

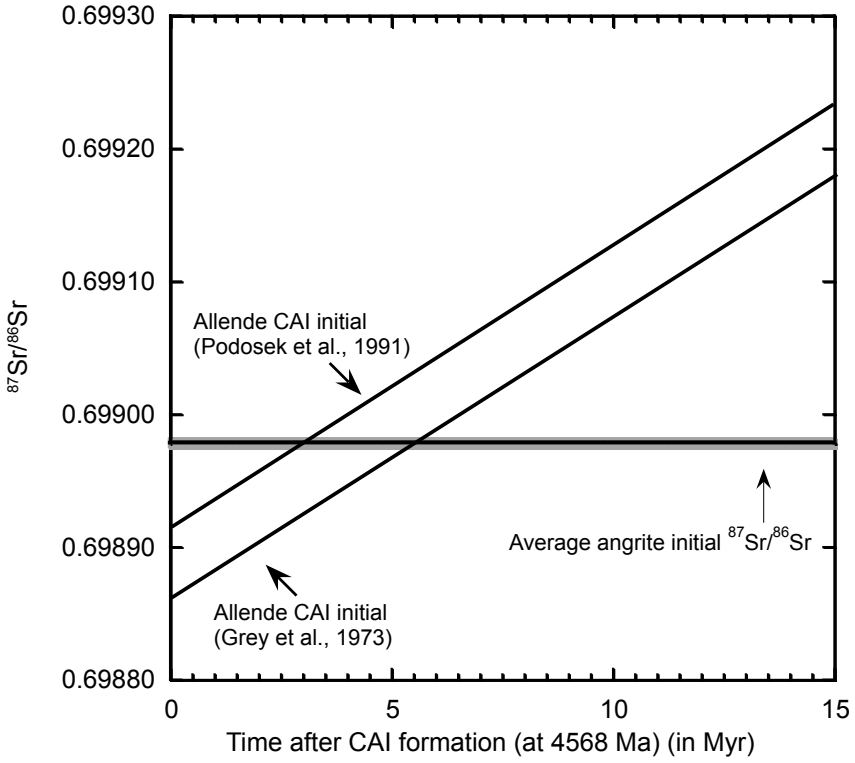


*Figure 2.11* – Average angrite initial $^{87}Sr/^{86}Sr$ in comparison with the Sr isotopic evolution from Allende CAI initial (Grey et al., 1973; Podosek et al., 1991) assuming an $^{87}Rb/^{86}Sr$ ratio of 1.5 based on Solar photosphere estimates (Anders and Grevasse, 1989).

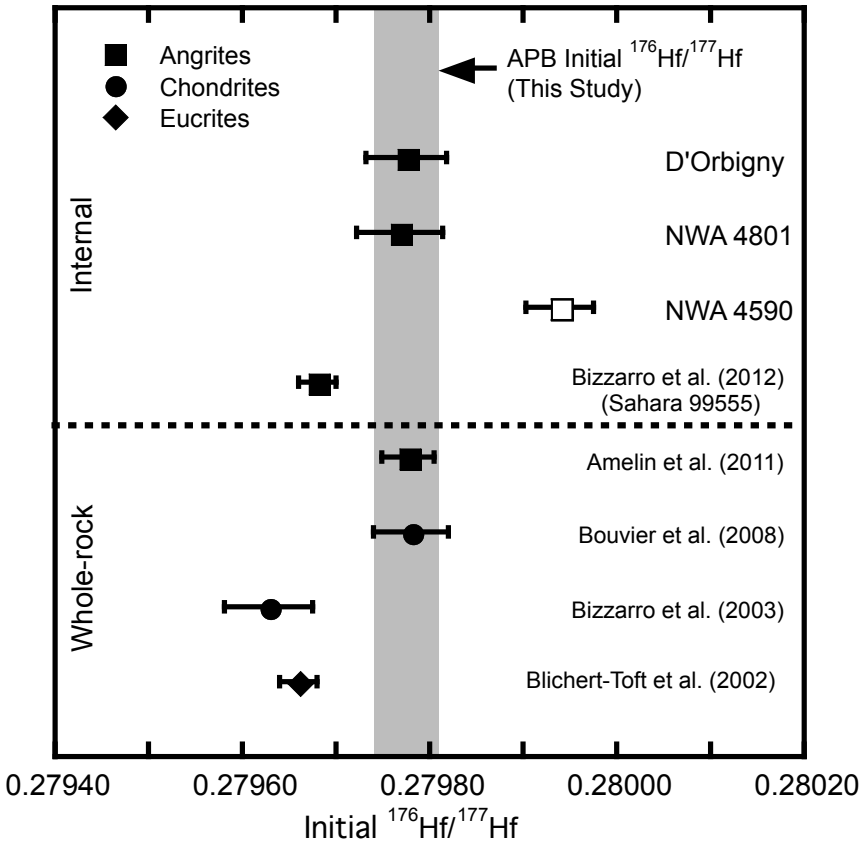


*Figure 2.12* – Initial $^{176}Hf/^{177}Hf$ ratio from internal (angrite) and whole-rock isochrons (angrite, eucrite, and chondrite) isochrons. Shaded region indicates angrite parent body initial $^{176}Hf/^{177}Hf$ calculated from NWA 4801 and D'Orbigny.

Table 2.5
Summary of $^{147}Sm$-$^{143}Nd$ and $^{146}Sm$-$^{142}Nd$ systematics

| Sample | $^{147}Sm$-$^{143}Nd$ Age (Ma) | $\varepsilon^{143}Nd_{CHUR}$ [a] | MSWD | $^{146}Sm/^{144}Sm_T$ [b] | $\varepsilon^{142}Nd$ [c] | MSWD | $^{146}Sm/^{144}Sm_0$ [d] |
|---|---|---|---|---|---|---|---|
| NWA 4590 | 4568±27 | -0.08±0.49 | 6.6 | 0.00745±0.00021 | -0.13±0.03 | 0.5 | 0.0084±0.0003 |
| NWA 4801 | 4556±82 | -0.17±0.51 | 4.4 | 0.00846±0.00075 | -0.26±0.04 | 1.7 | 0.0095±0.0008 |
| D'Orbigny | 4507±89 | 0.20±0.18 | 13 | 0.00618±0.00100 | -0.14±0.05 | 0.3 | 0.0115±0.0019 |
| NWA 2999 | 3925±165 | 2.93±0.78 | 19 | - | - | - | - |

[a] $^{143}Nd/^{144}Nd$ ratio at chondritic Sm/Nd ratio reported relative to the CHUR value of Bouvier et al. (2008)
[b] $^{146}Sm/^{144}Sm$ ratio at time of isotopic closure
[c] $^{142}Nd/^{144}Nd$ ratio at chondritic Sm/Nd ratio (Bouvier et al., 2008) relative to the average $^{142}Nd/^{144}Nd$ ratio of the JNdi standard
[d] $^{146}Sm/^{144}Sm$ ratio extrapolated back to T=4568 Ma using isotopic closure ages as described in text

Table 2.6
Summary of $^{176}Lu$-$^{176}Hf$ systematics

| Sample | $^{176}Lu$-$^{176}Hf$ Age (Ma) | $(^{176}Hf/^{177}Hf)_0$ | MSWD |
|---|---|---|---|
| NWA 4590 | 4470±23 | 0.279939±0.000036 | 1.6 |
| NWA 4801 | 4575±50 | 0.279768±0.000046 | 1.7 |
| D'Orbigny | 4520±97 | 0.279775±0.000043 | 1.9 |

Table 2.7
Model initial $^{87}Sr/^{86}Sr$ ratios calculated from plagioclase

| Sample | Measured $^{87}Sr/^{86}Sr$ | Measured $^{87}Rb/^{86}Sr$ | Initial $^{87}Sr/^{86}Sr$[a] |
|---|---|---|---|
| NWA 4590 | 0.699002±0.000003 | 0.00043 | 0.698973±0.000005 |
| NWA 4801 | 0.698999±0.000002 | 0.00034 | 0.698976±0.000005 |
| D'Orbigny | 0.699019±0.000003 | 0.00050 | 0.698986±0.000005 |
| NWA 2999 | 0.699099±0.000007 | 0.00178 | 0.698980±0.000007 |

[a]Calculated using a model age of 4.56 Ga

## 2.6 CONCLUSION

The systematics of a suite of long- and short-lived isotope systems (i.e., $^{147}$Sm-$^{143}$Nd, $^{146}$Sm-$^{142}$Nd, $^{176}$Lu-$^{176}$Hf, $^{87}$Rb-$^{87}$Sr, and $^{26}$Al-$^{26}$Mg) were investigated in three plutonic angrites (NWA 4590, NWA 4801, and NWA 2999) and one quenched angrite (D'Orbigny). These results have yielded several important observations on the evolution of angrites and the angrite parent body.

The coupled $^{147,146}$Sm-$^{143,142}$Nd systematics indicate a complex history of the angrites in terms of this isotope system on the angrite parent body. Among the four samples analyzed, two of the plutonic angrites, NWA 4590 and NWA 4801, appear isotopically undisturbed with $^{147}$Sm-$^{143}$Nd ages concordant with numerous other radiometric ages and initial isotopic compositions (e.g., $\varepsilon^{143}Nd_{CHUR}$) indistinguishable from a chondritic composition. High precision $^{146}$Sm/$^{144}$Sm ratios determined from the $^{146}$Sm-$^{142}$Nd systematics of NWA 4590 and NWA 4801 have provided additional constraints on the estimated initial Solar System $^{146}$Sm/$^{144}$Sm ratio. Averaging the ratios extrapolated from NWA 4590 and NWA 4801 with estimates based on eucrites and angrites from previous studies yields an initial Solar System $^{146}$Sm/$^{144}$Sm ratio of 0.0089±0.0005 (or 0.0086±0.0008 using the estimates based on angrites only). However, two other angrites in this study, NWA 2999 and D'Orbigny, indicate evidence for significant disturbances to the isotope systematics with younger $^{147}$Sm-$^{143}$Nd ages and elevated initial $^{143}$Nd/$^{144}$Nd ratios. These disturbances provide evidence of significant resetting events on the angrite parent body not recorded in the Pb-Pb, Hf-W, Al-Mg, and Mn-Cr systematics of both plutonic and quenched angrites.

The measured $^{176}$Lu-$^{176}$Hf systematics in D'Orbigny and NWA 4801 provide the first examples of angrites (and of achondrites in general) that do not yield implausibly old $^{176}$Lu-$^{176}$Hf ages, such as the recent age of Sahara 99555 reported by Bizzarro et al. (2012). The "normal" $^{176}$Lu-$^{176}$Hf systematics of these two angrites do not support the occurrence of intense cosmic ray irradiation of the angrite parent body. Therefore, a re-evaluation of the mechanism generating the anomalously old age observed in Sahara 99555 may be necessary. The $^{176}$Lu-$^{176}$Hf systematics of D'Orbigny and NWA 4801 provide the current best estimate of the angrite parent body initial $^{176}$Hf/$^{177}$Hf of 0.279772±0.000031.

Inferred initial $^{87}$Sr/$^{86}$Sr ratios obtained in this study indicate a possible timing of loss of volatiles from the angrite source material of between 3 and 5 Myr after CAI formation. However, the possibility of nucleosynthetic anomalies makes this timeframe only an upper limit estimate with the possibility of earlier volatile loss not completely excluded.

The new measurements of the $^{26}$Al-$^{26}$Mg isotope system in NWA 2999 have provided additional constraints on the formation age of the enigmatic angrite. The upper-limit $^{26}$Al-$^{26}$Mg age of 4560.46 Ma is concordant with the $^{182}$Hf-$^{182}$W age and within the uncertainty of its intermediate Pb-Pb age. While disagreement still exists between these chronometers and the Mn-Cr system, the upper-limit age calculated using the $^{26}$Al-$^{26}$Mg systematics has provided additional constraints towards determining the crystallization history of NWA 2999.

# CHAPTER 3

# TRACE ELEMENT SYSTEMATICS OF PLUTONIC AND QUENCHED ANGRITES

## 3.1 INTRODUCTION

Angrites are basaltic achondrites that are characterized by distinctive mineralogical and geochemical features (Mittlefehldt et al., 1998). This rare group is currently composed of approximately twelve unique members (twenty when paired stones are included), which can be divided primarily into two subgroups based on their textural features: (1) coarse-grained "plutonic" angrites and (2) fine-grained "quenched" angrites. Among the already limited number of angrites, over half have only been recovered within the past ten years. As such, research into the understanding their petrogenetic history of these meteorites is still an evolving area.

The extremely old crystallization ages of angrites, one of their key characteristics, makes these meteorites (and understanding their formation history) of particular interest for understanding differentiation processes in the early Solar System. Almost all angrites have crystallization ages that fall into one of two age clusters: (1) ~4556 Ma for the plutonic angrites or (2) ~4563 Ma for the quenched angrites (Amelin, 2008; Amelin et al., 2008; Brennecka and Wadhwa, 2012). Notable exceptions to this are the paired Northwest Africa (NWA) 2999/6291 angrites (Meteoritical Bulletin). These two angrites have textural features that are distinct from those of the other angrites (both quenched and plutonic). Northwest Africa 2999 has an overall coarse-grained texture but is

characterized by a significant amount (~8% modal abundance) of metal, the highest modal metal content observed in any angrite thus far. In contrast, NWA 6291 is comprised of a mixture of fine- and coarse-grained domains. The crystallization ages inferred from the Pb-Pb isotope system are also unique with both angrites yielding an age of ~4560 Ma, intermediate between the age clusters observed for the other angrites (Amelin and Irving, 2008; Bouvier et al., 2011, Brennecka and Wadhwa, 2012).

Prior to the recent recovery of the angrites NWA 2999, NWA 4590, and NWA 4801, trace element studies of the plutonic angrites had been restricted to two samples, Lewis Cliff (LEW) 86010 and Angra dos Reis (e.g., Crozaz and McKay, 1990; Mittlefehldt and Lindstrom, 1990; Floss et al., 2003). These few studies inferred that LEW 86010 and Angra dos Reis formed from distinct geochemical sources from each other and from the known quenched angrites. However, deciphering much more into the petrogenesis of the plutonic angrites has been complicated by the paucity of sample, as well as the anomalous mineralogical composition of Angra dos Reis (e.g., Mittlefehldt et al., 2002). Fortunately, the recent recovery of NWA 2999, NWA 4590 and NWA 4801 has more than doubled the total number of plutonic angrites available for study, providing a renewed opportunity to investigate the formation history and evolution of this rare angrite subgroup.

While relatively more abundant than the plutonic angrites, the quenched angrites are still limited in number, and interpretations into their petrogenetic history are restricted to a handful of studies (e.g., Floss et al., 2003) focusing on

essentially four samples (Sahara 99555, D'Orbigny, Asuka 881371, and LEW 87051). As with the plutonic angrites the recent influx of newly recovered samples, such as NWA 1296 and NWA 1670, provides the opportunity to develop an expanded interpretation as to their formation and relationship to other angrites in the quenched angrite textural subgroup.

In this study, we report the rare earth element (REE) and other selected trace element abundances in individual mineral grains, as well as the whole-rock REE abundances in bulk samples of the newly recovered plutonic (NWA 2999, NWA 4590, and NWA 4801) and quenched (NWA 1296 and NWA 1670) angrites. These geochemical measurements are used to infer conditions at the time of formation (i.e., parent melt composition and oxygen fugacity at crystallization), as well as investigate possible petrogenetic relationships among the angrites.

## 3.2 ANALYTICAL METHODS

### 3.2.1 Petrographic Documentation and Electron Microprobe Analyses

Initial documentation and characterization of polished thick sections of NWA 2999 (130.8 $mm^2$), NWA 4590 (117.4 $mm^2$), NWA 4801 (208.7 $mm^2$), NWA 1296 (20 $mm^2$), and NWA 1670 (6 $mm^2$) was completed using a combination of a JEOL JSM-845 and FEI XL-30 scanning electron microscopes at Arizona State University (ASU). Back-scattered electron images and elemental mapping (using energy dispersive X-ray spectroscopy) were utilized to identify phases present within each sample. After initial sample characterization, the major element chemistry of various mineral phases was determined using a JEOL JXA-

8600 electron probe microanalyzer (EPMA) at ASU. Measurements were performed using a 15 kV accelerating voltage and a 25 nA beam current. Initial calibrations were completed using a set of natural mineral standards. Elemental abundances were determined using wave dispersive spectrometry (WDS) and measurements were corrected using ZAF (PAP) correction procedures. Typical detections limits for the elements analyzed by EPMA within these samples are 0.03 wt.% for $SiO_2$, $TiO_2$, $Al_2O_3$, MgO, CaO, $Na_2O$, and $P_2O_5$, and 0.05 wt.% for FeO, MnO, and $Cr_2O_3$.

### 3.2.2 *In situ* and Bulk Trace Element Measurements

Rare earth elements (REE) and other selected trace elements were measured *in situ* using a Cameca IMS-6f secondary ion mass spectrometer at ASU, utilizing procedures similar to those previously described by Zinner and Crozaz (1986). Analyses were performed using an O– primary beam with a 3-7 nA current and a primary accelerating voltage of –12.5 kV. Secondary ions were accelerated at +10 kV for a total impact energy of 21.5 k. A –75 V offset on the sample voltage avoids interferences from molecular ions (Zinner and Crozaz, 1986). Secondary ions were collected using an electron multiplier in peak jumping mode. Depending on the REE abundances, analysis times for individual mineral phases typically ranged from 1 to 2.5 hours.

In addition to the individual *in situ* mineral analyses, bulk, whole-rock REE abundances were determined for NWA 2999, NWA 4590, NWA 4801, and NWA 1296. Interior chips of each angrite (0.6131 g, 0.7375 g, 0.6112 g, and 0.0995g of NWA 2999, NWA 4590, NWA 4801, and NWA 1296, respectively)

were crushed in an agate mortar and pestle and then digested in a 3:1 HF-$HNO_3$ acid mixture using a Parr digestion vessel, and then brought into final solution in 3% $HNO_3$. The REE composition of the whole-rock solution were determined using a Thermo X-series quadrupole inductively coupled plasma mass spectrometer (ICPMS) ($2\sigma$ external reproducibility = ±5%) with samples bracketed with USGS terrestrial rock standards BCR-2 and BIR-2.

## 3.3 RESULTS

### 3.3.1 Mineral Chemistry and Petrography

Details on the petrology and mineral chemistry of the plutonic angrites NWA 2999, NWA 4590, and NWA 4801, have been limited primarily to abstracts (e.g., Irving et al., 2005, 2006; Irving and Kuehner, 2007), while the mineral chemistry and petrography of the quenched angrites NWA 1296 and NWA 1670 have previously been examined in detail (e.g., Jambon et al., 2005, 2008). The following section provides general descriptions of the thick sections specifically analyzed in this study with an overview of the mineral chemistry of the REE-bearing phases analyzed in section 3.3.2. Representative major element abundances in the various mineral phases of the plutonic angrites (NWA 2999, NWA 4590, and NWA 4801) and quenched angrites (NWA 1296 and NWA 1670) are provided in Tables 3.1 and 3.2, respectively.

*3.3.1.1 Northwest Africa 2999*

Northwest Africa 2999 is a coarse-grained, allotriomorphic-granular stone that displays evidence of brecciation. The section is composed primarily of Al,Ti-pyroxene, olivine, plagioclase, oxides, and Fe-Ni metal. Compositionally, the

pyroxenes within NWA 2999 are Al, Ti-rich clinopyroxene. Major element variation within the clinopyroxene is limited with compositions ranging from $En_{37.8}Fs_{10.1}Wo_{52.1}$ to $En_{34.6}Fs_{10.6}Wo_{54.8}$ ((En) enstatite, (Fs) ferrosilite, (Wo) wollastonite) (Fig. 3.1). The olivine is relatively Ca-rich with a nearly homogenous composition in terms of fayalite content ($Fa_{40.7}Fo_{57.9}La_{1.9}$ - $Fa_{39.8}Fo_{58.3}La_{1.9}$) ((Fa) fayalite, (Fo) forsterite, (La) larnite). Plagioclase is a trace phase within NWA 2999 and is essentially pure anorthite in composition. Fe-Ni metal is abundant and occurs sporadically throughout the sample. Veins of iron hydroxides are prevalent throughout NWA 2999 appearing to coincide with cracks and grain boundaries. An example of the typical texture observed in NWA 2999 is shown in Figure 3.2a.

*3.3.1.2 Northwest Africa 4590*

Northwest Africa 4590 has an overall coarse-grained hypidiomorphic-granular texture (Fig. 3.2b). The sample is composed primarily of pyroxene (Al, Ti-rich clinopyroxene), olivine (with extensive exsolution lamellae of kirschsteinite), plagioclase with lesser abundant spinel and accessory phases such as phosphate (merrillite). Clinopyroxenes in NWA 4590 exhibit a strong variation in Fe and Mg content, including zonation within individual grains from core to rim. Clinopyroxene compositions range from $En_{35.5}Fs_{12.2}Wo_{52.3}$ to $En_{21.0}Fs_{23.8}Wo_{55.1}$. Olivine grains in NWA 4590 are observed to have widespread occurrence of kirschsteinite exsolution lamellae with the average width of the lamellae around 20-25 μm. The olivines range in Mg-content from $Fo_{25.3}Fa_{70.3}Ln_{4.4}$ to $Fo_{19.6}Fa_{75.0}Ln_{5.4}$. Kirschsteinite exsolution lamellae present

within the olivine span a compositional range of $Fo_{10.5}Fa_{52.3}Ln_{37.1}$ to $Fo_{7.9}Fa_{46.1}Ln_{46.0}$. Plagioclase is homogenous and nearly pure anorthite in composition occurring as subheadral to euhedral grains. Phosphates occur sporadically as merrillite with larger grains ranging in size up to 400 μm.

*3.3.1.3 Northwest Africa 4801*

Northwest Africa 4801 has a coarse-grained, granular texture with large (mm-size) Al, Ti-rich clinopyroxene grains with substantially smaller anhedral plagioclase and anhedral to subhedral olivine grains (Fig. 3.2c). Clinopyroxene is the most abundance phase within the sample with sub-equal amounts of olivine and plagioclase and minor occurrence of spinel and phosphate. Minor variation in the Fe and Mg content of the clinopyroxene is observed with compositions ranging from $En_{33.8}Fs_{11.9}Wo_{54.2}$ to $En_{31.9}Fs_{11.5}Wo_{56.6}$. Olivines in NWA 4801 have only slight variation in Fe content from $Fo_{53.8}Fa_{43.4}Ln_{2.8}$ to $Fo_{53.1}Fa_{44.6}Ln_{2.3}$ with no kirschsteinite observed within the sample. Plagioclase is homogenous in composition with all nearly $An_{100}$ in composition. Phosphates observed in this section of NWA 4801 are merrillite in composition and occur in small fine-grained regions.

*3.3.1.4 Northwest Africa 1296*

In contrast to the plutonic angrites, NWA 1296 has an overall fine-grained texture (Fig. 3.3a). The pyroxenes span a compositional range from $En_{14.9}Fs_{31.5}Wo_{53.5}$ in the most Mg-rich end-member to $En_{0.6}Fs_{48.9}Wo_{50.5}$ in the Fe-rich end-member. Plagioclase is nearly pure anorthite in composition. The

primary occurrence of the olivine as a dendritic texture prevents clean analyses of the mineral composition using EPMA.

*3.3.1.5 Northwest Africa 1670*

Northwest Africa 1670 is composed of numerous large olivine subhedral to euhedral macrocrysts (up to 0.6 mm in size) set within a fine-grained matrix (Fig. 3.3b). The fine-grained material between the olivine is comprised of needle-like laths of plagioclase with olivine and pyroxene microcrysts between the laths. Larger olivine and pyroxene phenocrysts also occur within the interstitial matrix. Clinopyroxenes span a compositional range from $En_{28.3}Fs_{15.4}Wo_{56.3}$ to $En_{2.8}Fs_{45.1}Wo_{52.1}$. The large olivine macrocryst are less compositionally variable ranging from $Fa_{18.4}Fo_{80.8}La_{0.08}$ to $Fa_{22}$ $Fo_{77.1}La_{0.09}$.

**3.3.2 Rare Earth Element Microdistributions**

Rare earth element abundances were measured *in situ* within grains of pyroxene, olivine (including kirschsteinite, when present), plagioclase, and phosphate. Representative REE abundances in these minerals are given in Tables 3.3, 3.4, 3.5, and 3.6, while whole-rock (or bulk) REE abundances for all five angrites are shown in Table 3.7.

*3.3.2.1 Pyroxene*

Representative REE abundances in the cores and rims of the pyroxene in NWA 2999, NWA 4590, NWA 4801, NWA 1296, and NWA 1670 are shown in Figs. 3.4a-c. The range of REE concentrations in pyroxenes of NWA 2999 are rather restricted (La ~5.4-6.4 × CI chondrite abundance) compared to that in pyroxene of the other angrites (La ~2.5-12.7, 3.5-8.6, 6.2-10.8, and 8.5-11.4 × CI

in NWA 4590, NWA 4801, NWA 1296, and NWA 1670, respectively). The pyroxenes in all five angrites have light rare earth element (LREE)-depleted patterns (CI-normalized Sm/La~2.2-3.4) with moderate negative Eu anomalies ($Eu/Eu^{*}$~ 0.5-0.7, where $Eu^{*}$ represents the interpolated value between the CI-normalized Sm and Gd abundances). The main variation in the pyroxene REE composition of the five angrites occurs among the heavy rare earth element (HREE) patterns. The three plutonic angrites (NWA 2999, NWA 4590, and NWA 4801) have what appear to be three distinct HREE patterns: (1) a rather flat HREE pattern in NWA 2999 with a CI-normalized Gd/Lu ratio (i.e., $[Gd/Lu]_{CI}$) of ~1.1, (2) a HREE depleted pattern in NWA 4590 with a $[Gd/Lu]_{CI}$ of ~ 1.9, and (3) a variation in the HREE pattern from a flat pattern in the cores of NWA 4801 ($[Gd/Lu]_{CI}$ ~1.2) to a moderately HREE depleted rim ($[Gd/Lu]_{CI}$ ~1.6). In contrast, the two quenched angrites (NWA 1296 and NWA 1670) have flat HREE patterns that display almost no variation between samples with a $[Gd/Lu]_{CI}$ ~ 0.96 and $[Gd/Lu]_{CI}$ ~ 0.98 in NWA 1296 and NWA 1670, respectively.

In addition to the REE, additional selected trace element abundances were also measured in the pyroxenes of all five angrites. Figure 3.5 shows the abundance of Zr plotted versus Ti concentrations in pyroxene of NWA 2999, NWA 4590, NWA 4801, NWA 1296, and NWA 1670. As expected for these highly incompatible, high field strength elements, they are positively correlated in pyroxene of all five angrites. Analogous to the abundance range observed in the REE, the range of these trace elements is the most restricted in NWA 2999 and spans the largest range in NWA 4590.

*3.3.2.2 Plagioclase*

Figure 3.6 shows representative REE abundance in the angrite plagioclase (with the exception of NWA 1670 in which plagioclase grains were too fine-grained for *in situ* analyses). In both the plutonic and quenched angrites, plagioclase has an LREE-enriched pattern ($[La/Sm]_{CI}$ ~4.3-5.5) with a large positive Eu anomaly ($Eu/Eu^{*}$ ~50 for NWA 2999, ~40 for NWA 4590, ~38 for NWA 4801, and ~45 for NWA 1296). Only minor variation in absolute REE abundances is observed in different plagioclase grains within each of the samples. In all the angrites investigated in this study, HREEs heavier than Er were present in concentrations below the analytical detection limit of the ion microprobe.

*3.3.2.3 Olivine and Kirschsteinite*

Figure 3.7 shows representative REE abundances in olivine of NWA 2999, NWA 4801, and NWA 1670, and in olivine/kirschsteinite of NWA 4590. Olivine phenocrysts in NWA 2999 have the HREE-enrichment that is characteristic of this mineral ($[Lu/Tb]_{CI}$ ~4.8). However, the olivine also exhibits a slight enrichment in the LREE ($[La/Sm]_{CI}$ ~1.3). Olivine grains in NWA 4590 include prevalent kirschsteinite exsolution lamellae. Due to the fine spatial scale of the exsolution lamellae within the olivine, it was not possible to analyze the host olivine and the kirschsteinite lamellae separately and the reported analyses are for a "bulk" olivine composition that includes both phases. The olivine/kirschsteinite in NWA 4590 has a HREE-enriched pattern ($[Lu/Tb]_{CI}$ ~3.8), but with absolute abundances that are substantially higher than in olivine of NWA 2999. Olivine in NWA 4801 is HREE-enriched ($[Lu/Tb]_{CI}$ ~6.7) and has

absolute REE abundances that are higher than olivines of NWA 2999, but not as high as those in the olivine/kirschsteinite of NWA 4590. The REE patterns of both the olivine macrocrysts and interstitial olivine in NWA 1670 have nearly identical HREE-enriched patterns ($[Lu/Tb]_{CI}$ ~8.3) with the lowest absolute REE abundances among the angrites analyzed (Lu ~0.95 × CI).

*3.3.2.4 Phosphate*

Phosphate (i.e., merrillite) grains were only observed directly in two angrites in this study, NWA 4590 and NWA 4801. In both NWA 4590 and NWA 4801, individual merrillite grains were relatively large (up to 400 $\mu$m in diameter), which allowed multiple analyses to be performed on single grains without contamination from adjacent phases. Figure 3.8 shows representative REE abundances in merrillite of NWA 4590 and NWA 4801. This mineral, in both of these angrites, has high REE concentrations (La ~3000 × CI and ~3500 × CI in merrillites of NWA 4590 and NWA 4801, respectively). Merrillite in NWA 4590 has a LREE-enriched pattern (CI-normalized La/Lu ~85) and a small negative Eu anomaly ($Eu/Eu^*$ ~0.7). Whereas, merrillite in NWA 4801 is somewhat less LREE-enriched (CI-normalized La/Lu ~19), but has a similar negative Eu anomaly ($Eu/Eu^*$ ~ 0.7).

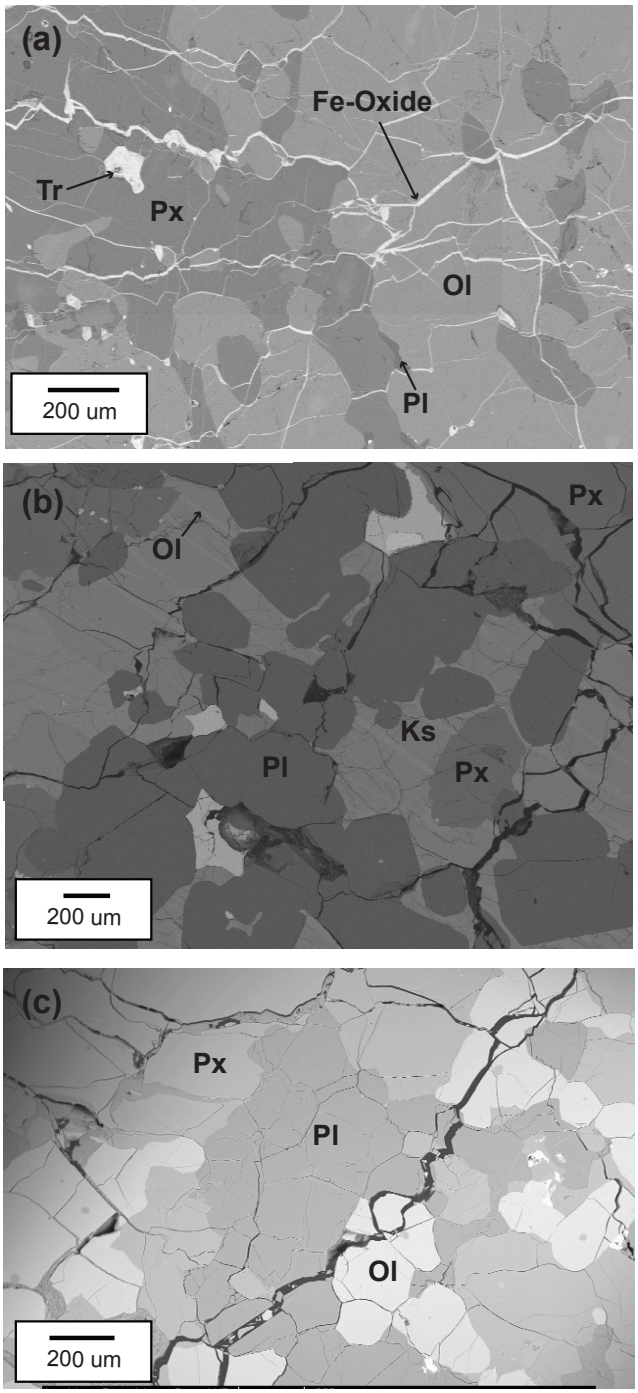


*Figure 3.1*- Back-scattered electron images of (a) Northwest Africa (NWA) 2999, (b) NWA 4590, and (c) NWA 4801 showing representative mineral assemblages (Px: pyroxene, Ol: olivine, Pl: plagioclase, Ks: Kirschsteinite, Tr: troilite).

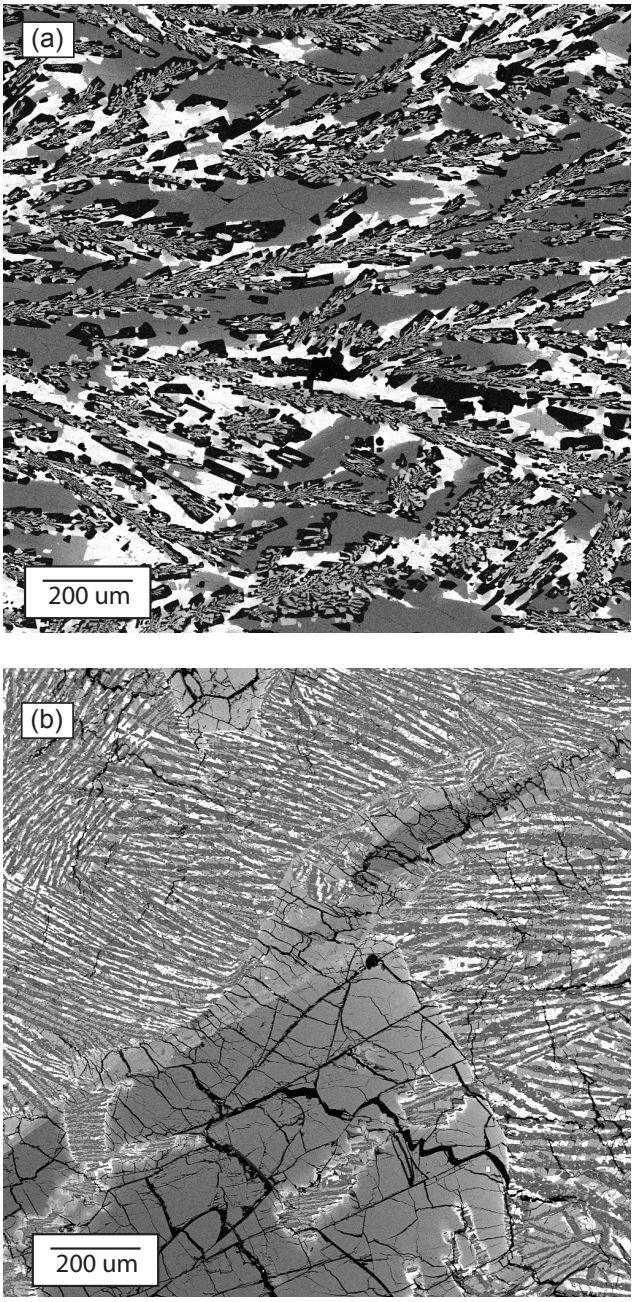


*Figure 3.2*- Back-scattered electron images indicating typical textures observed in (a) Northwest Africa 1296 (NWA) and (b) NWA 1670.

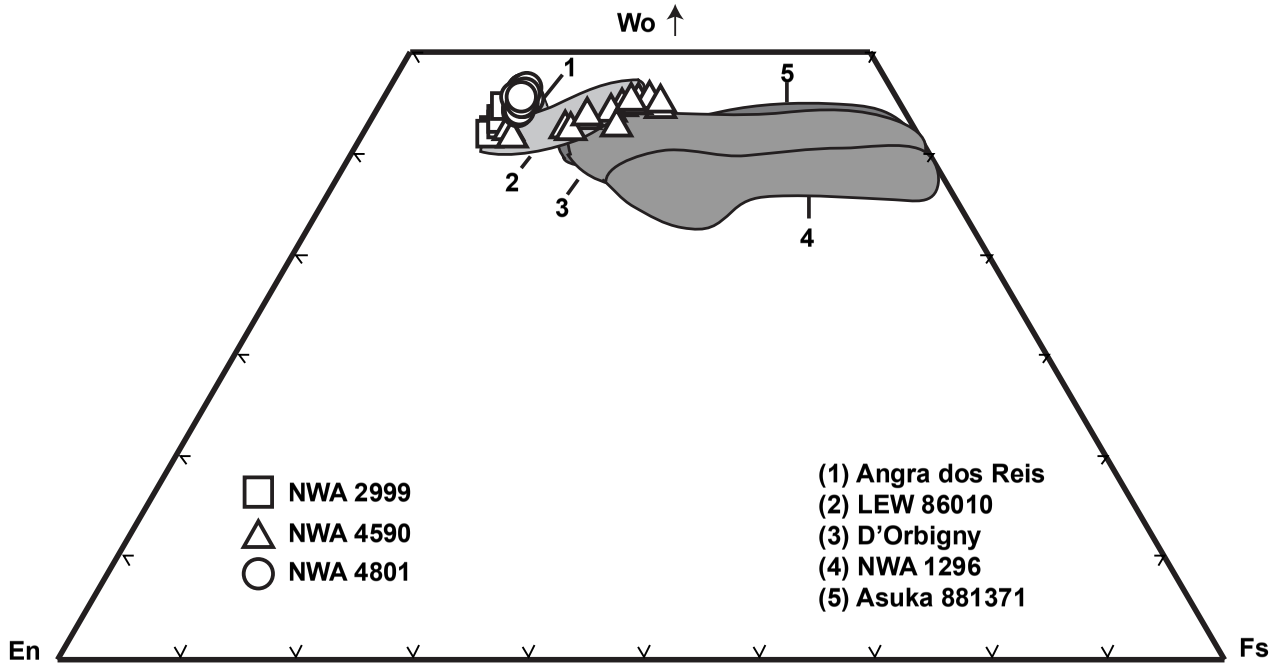


*Figure 3.3*- Pyroxene compositions of NWA 2999, NWA 4590, and NWA 4801. For comparison, the pyroxene compositional ranges observed in the fine- and coarse-grained angrites are shown (after Prinz et al. 1977; Crozaz and McKay, 1990; Yanai, 1994; Mikouchi et al., 1996; Mittlefehldt et al., 2002; Jambon et al., 2005).

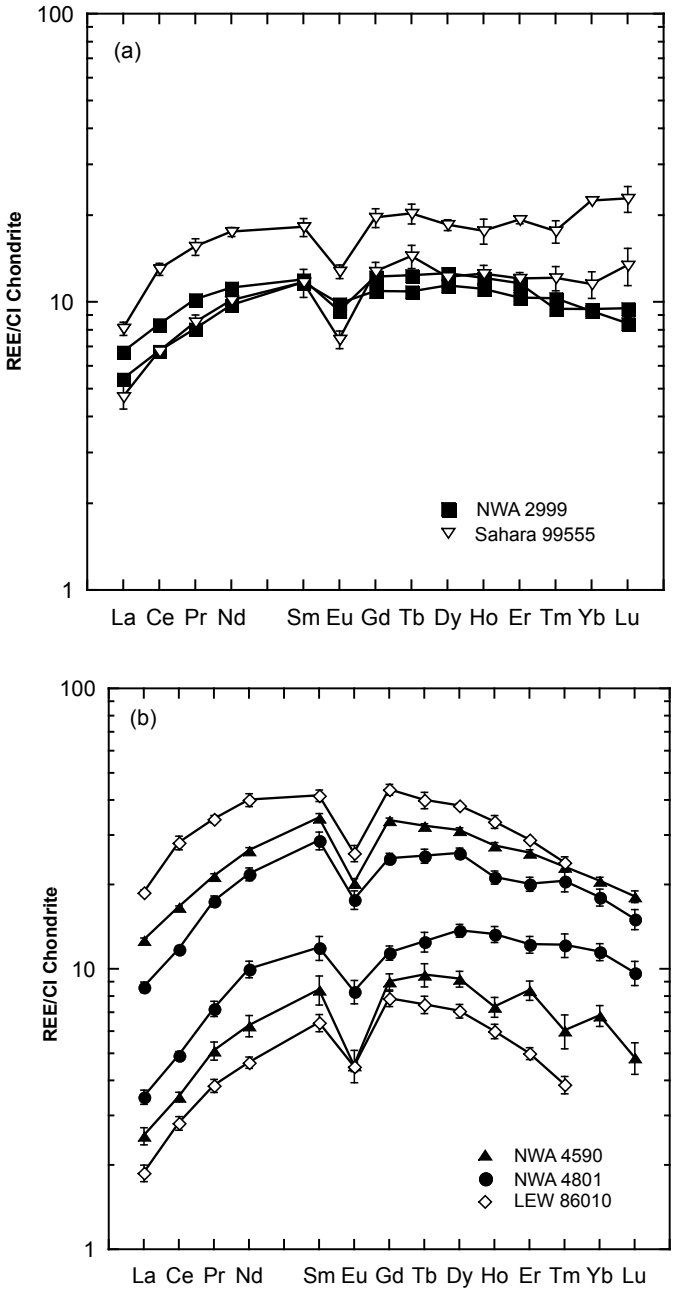


*Figure 3.4*- Range of chondrite-normalized REE abundances in clinopyroxenes of (a) Northwest Africa (NWA) 2999, (b) NWA 4590 and NWA 4801, and (c, next page) NWA 1296 and NWA 1670. For comparison, ranges of REE concentrations in clinopyroxenes of the quenched angrite Sahara 99555 and the plutonic angrite LEW 86010 are shown (after Floss et al., 2003). Chondritic REE abundances used for normalization in this figure, as well as Figs. 3.6-3.10, are from Palme and Beer (1993).

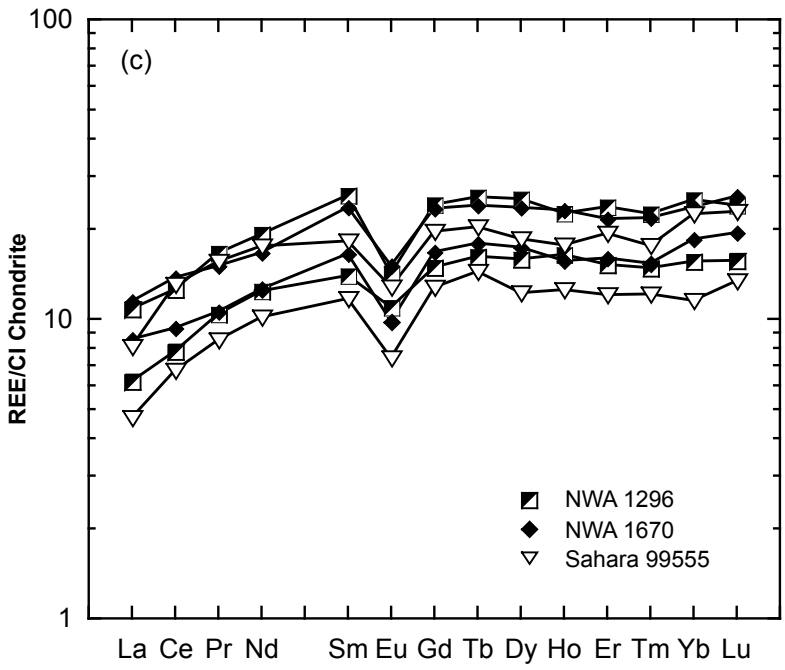


*Figure 3.4 (continued)*- Range of chondrite-normalized REE abundances in clinopyroxenes of (a, previous page) Northwest Africa (NWA) 2999, (b, previous page) NWA 4590 and NWA 4801, and (c) NWA 1296 and NWA 1670. For comparison, ranges of REE concentrations in clinopyroxenes of the quenched angrite Sahara 99555 and the plutonic angrite LEW 86010 are shown (after Floss et al., 2003). Chondritic REE abundances used for normalization in this figure, as well as Figs. 3.6-3.11, are from Palme and Beer (1993).

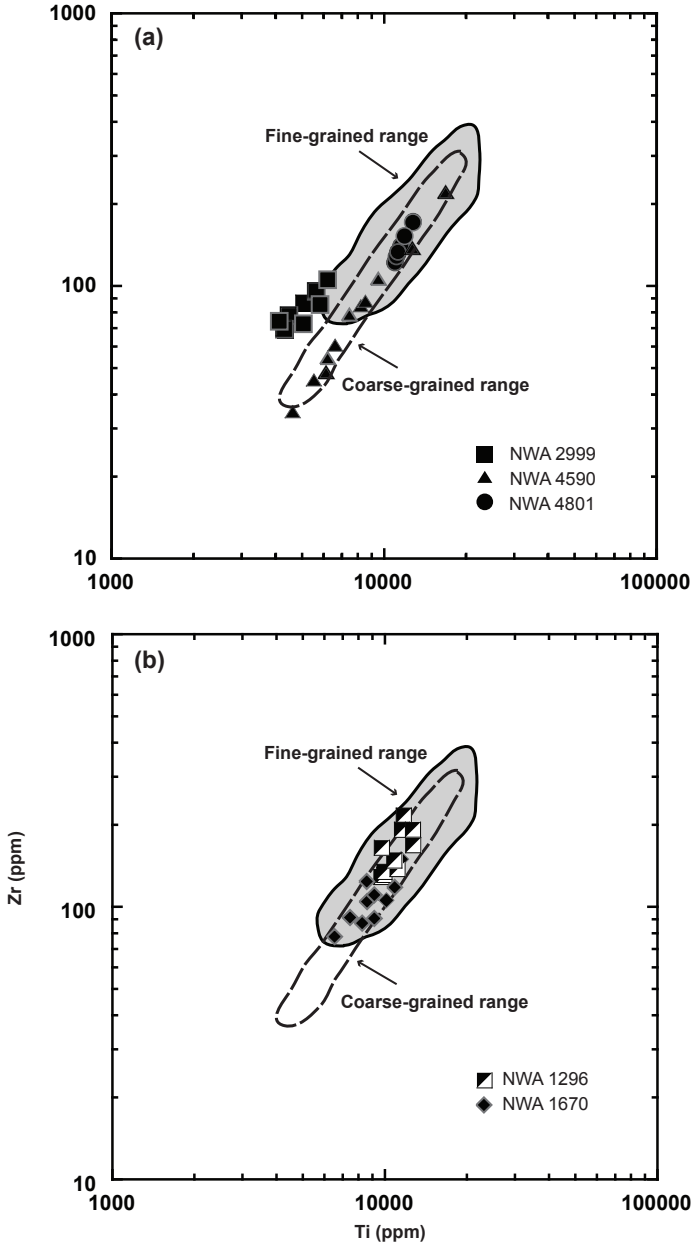


*Figure 3.5*- Plot of Ti versus Zr concentrations in clinopyroxenes of (a) Northwest Africa (NWA) 2999, NWA 4590, and NWA 4801, and (b) NWA 1296 and NWA 1670; for comparison, the compositional ranges of clinopyroxenes in the quenched angrites D'Orbigny, Asuka 881371, Sahara 99555, and LEW 87051 (light gray shaded region) and in the plutonic angrite LEW 86010 (region outlined with dashed line) are also shown (after Floss et al., 2003).

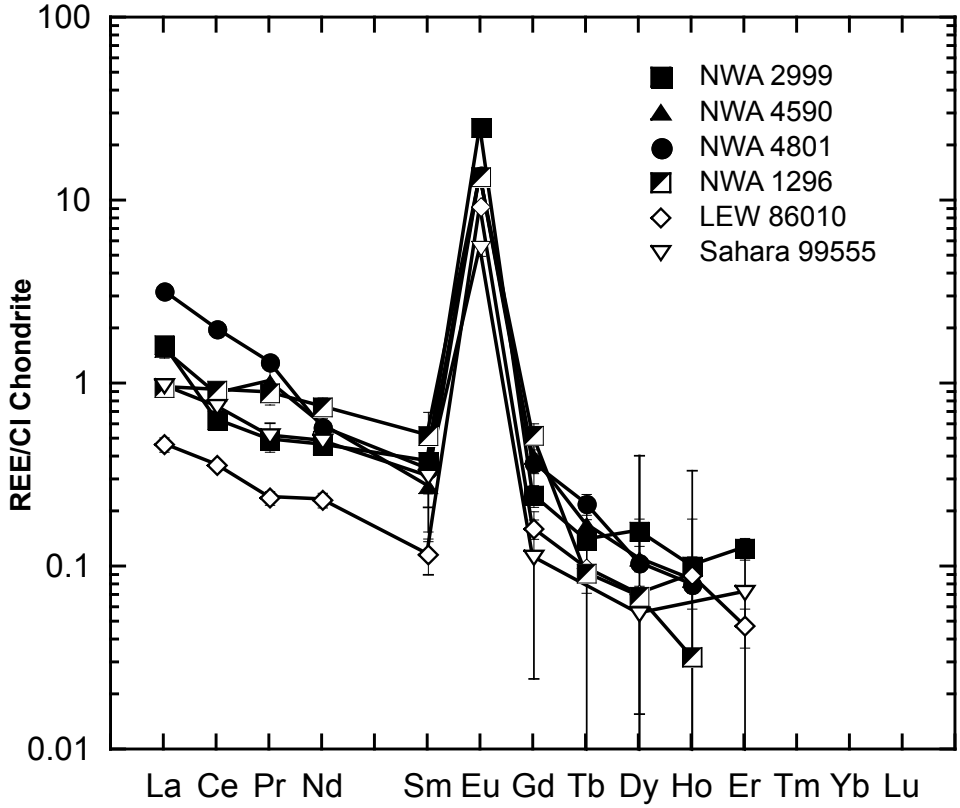


*Figure 3.6*- Representative chondrite-normalized REE abundances in plagioclase (anorthite) of Northwest Africa (NWA) 2999, NWA 4590, NWA 4801, and NWA 1296. Also shown for comparison are REE abundances in plagioclase of the Sahara 99555 quenched angrite and the LEW 86010 plutonic angrite (after Floss et al., 2003).

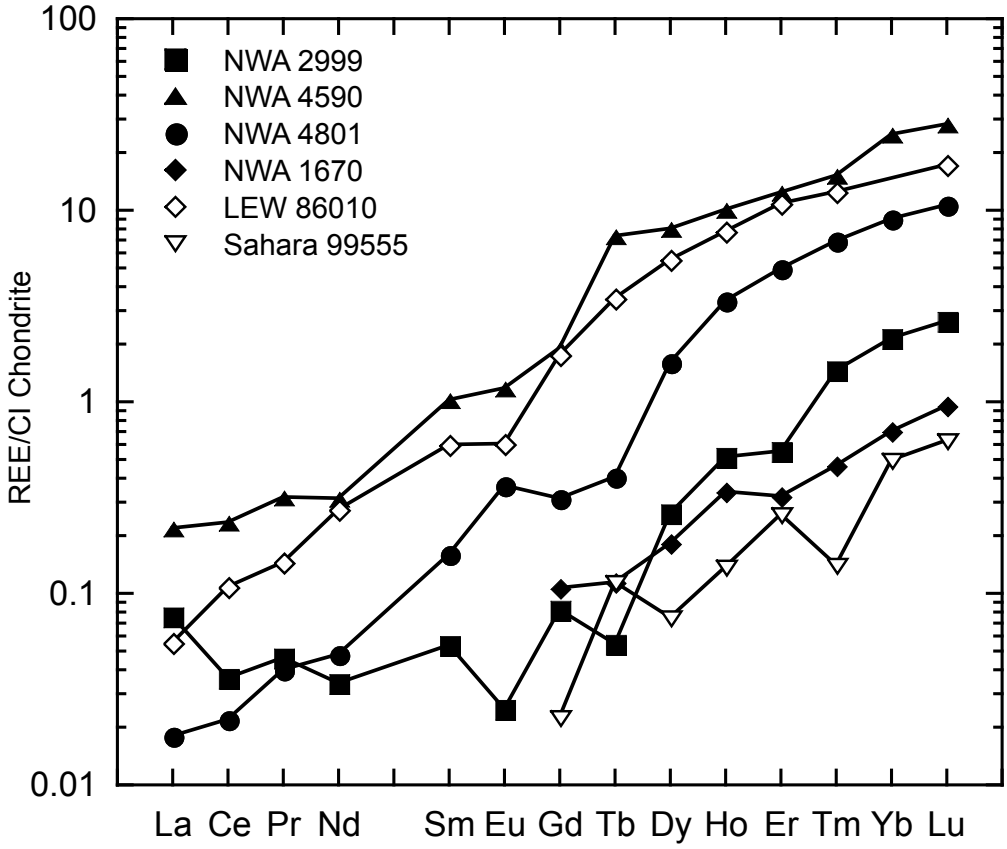


*Figure 3.7*- Representative chondrite-normalized REE abundances in olivine (including kirschsteinite, when present) of Northwest Africa (NWA) 2999, NWA 4590, NWA 4801, and NWA 1670. Also shown for comparison are the REE abundances in olivines of the Sahara 99555 quenched angrite and the LEW 86010 plutonic angrite (after Floss et al., 2003).

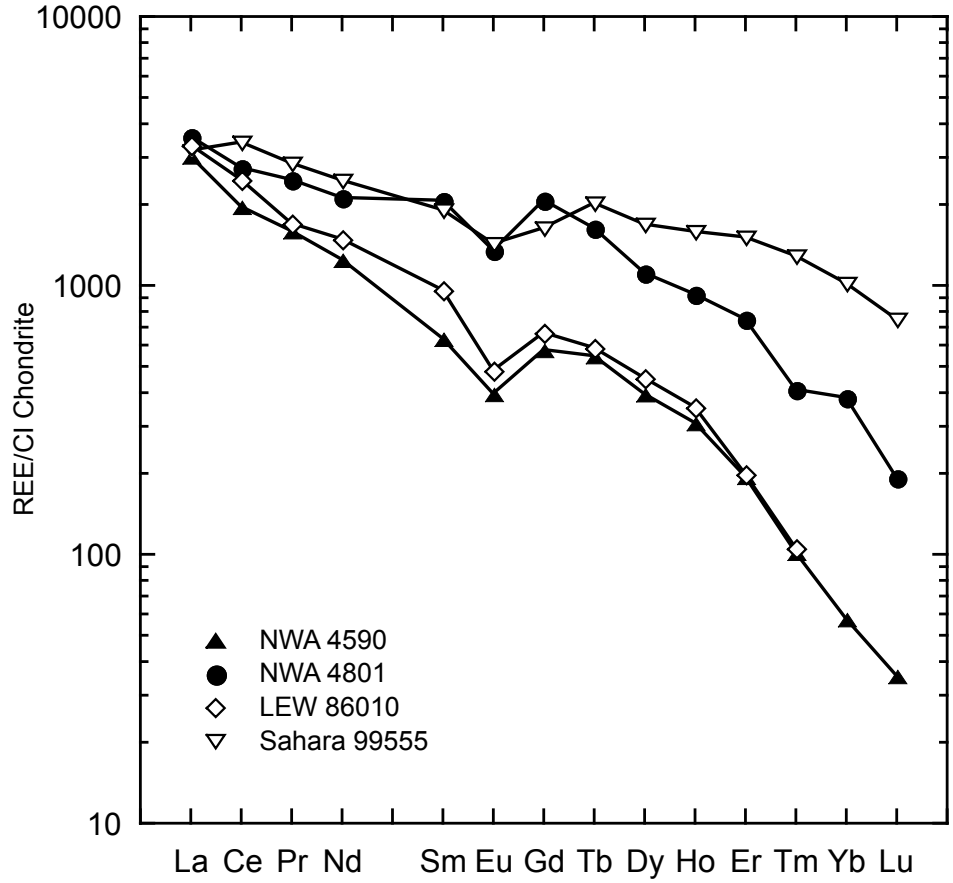


*Figure 3.8*- Representative chondrite-normalized REE abundances in phosphate (merrillite) of Northwest Africa (NWA) 4590 and NWA 4801. Also shown for comparison are REE abundances in phosphates of the Sahara 99555 quenched angrite (Floss et al., 2003) and of the LEW 86010 plutonic angrite (Crozaz and McKay, 1990).

Table 3.1
Representative electron microprobe analyses in coarse-grained angrites NWA 2999, NWA 4590, and NWA 4801 (in wt. %)

| | **NWA 2999** | | | **NWA 4590** | | | | **NWA 4801** | | | |
|---|---|---|---|---|---|---|---|---|---|---|---|
| | Plagioclase | Pyroxene | Olivine | Plagioclase | Pyroxene | Olivine [1] | Phosphate | Plagioclase | Pyroxene | Olivine | Phosphate |
| $SiO_2$ | 42.01 | 48.13 | 35.64 | 42.91 | 48.88 | 32.20 | 0.66 | 42.50 | 44.98 | 35.43 | 0.73 |
| $TiO_2$ | 0.04 | 0.71 | <0.03 | <0.03 | 0.83 | <0.03 | n.d. | <0.03 | 2.62 | <0.03 | n.d. |
| $Al_2O_3$ | 35.96 | 7.69 | 1.05 | 36.17 | 5.58 | 0.83 | n.d. | 36.17 | 9.83 | 0.97 | n.d. |
| FeO | 0.30 | 6.54 | 33.58 | 0.18 | 7.45 | 39.83 | 2.12 | 0.04 | 6.55 | 35.88 | 1.73 |
| MgO | <0.03 | 11.42 | 27.61 | <0.03 | 12.15 | 5.50 | 2.31 | <0.03 | 10.53 | 25.66 | 3.04 |
| CaO | 20.80 | 24.75 | 1.48 | 20.70 | 24.95 | 22.07 | 48.73 | 20.48 | 25.39 | 1.84 | 50.20 |
| MnO | <0.05 | 0.12 | 0.13 | <0.05 | 0.08 | 0.22 | n.d | <0.05 | 0.11 | 0.17 | n.d. |
| $Cr_2O_3$ | <0.05 | 0.24 | 0.07 | <0.05 | 0.11 | 0.14 | n.d. | <0.05 | 0.18 | <0.05 | n.d. |
| $P_2O_5$ | <0.03 | <0.03 | <0.03 | <0.03 | <0.03 | <0.03 | 44.20 | <0.03 | <0.03 | <0.03 | 43.56 |
| Total | 99.11 | 99.60 | 99.56 | 99.96 | 100.03 | 100.79 | 98.02 | 99.19 | 100.19 | 99.95 | 99.26 |

n.d. = not determined.
[1] Olivine analyses include kirschteinite

Table 3.2
Representative electron microprobe analyses in fine-grained angrites NWA 1296 and NWA 1670 (in wt. %)

| | **NWA 1296** | | | **NWA 1670** | | |
|---|---|---|---|---|---|---|
| | Plagioclase | Pyroxene | Olivine | Plagioclase | Pyroxene | Olivine |
| $SiO_2$ | 43.51 | 41.95 | 34.31 | 42.40 | 44.52 | 38.53 |
| $TiO_2$ | <0.03 | 4.20 | <0.03 | <0.03 | 2.46 | 0.05 |
| $Al_2O_3$ | 35.38 | 6.10 | 1.87 | 34.88 | 7.57 | 0.12 |
| FeO | 1.28 | 24.20 | 41.32 | 1.84 | 14.68 | 20.05 |
| MgO | <0.03 | 1.14 | 18.83 | <0.03 | 6.74 | 39.70 |
| CaO | 19.69 | 21.50 | 3.16 | 19.95 | 22.71 | 0.60 |
| MnO | <0.05 | 0.15 | <0.05 | <0.05 | 0.10 | 0.26 |
| $Cr_2O_3$ | <0.05 | <0.05 | 0.41 | <0.05 | 0.37 | 0.09 |
| $P_2O_5$ | n.d. | n.d. | n.d. | n.d. | n.d. | n.d. |
| Total | 99.86 | 99.23 | 99.90 | 99.07 | 99.16 | 99.39 |

n.d. = not determined.

Table 3.3
Representative REE abundances (in ppm) in minerals of NWA 2999.

| | Clinopyroxene (l) | Clinopyroxene (h) | Plagioclase | Olivine |
|---|---|---|---|---|
| La | 1.5618 ± 0.0275 | 1.4607 ± 0.0307 | 0.4005 ± 0.0127 | 0.0185 ± 0.0023 |
| Ce | 4.0902 ± 0.0429 | 4.6330 ± 0.0635 | 0.4060 ± 0.0134 | 0.0231 ± 0.0029 |
| Pr | 0.9287 ± 0.0196 | 0.8960 ± 0.0233 | 0.0477 ± 0.0041 | 0.0044 ± 0.0011 |
| Nd | 4.6147 ± 0.0660 | 5.0377 ± 0.0912 | 0.2195 ± 0.0133 | 0.0161 ± 0.0034 |
| Sm | 1.5944 ± 0.0526 | 1.6726 ± 0.0716 | 0.0581 ± 0.0194 | 0.0083 ± 0.0041 |
| Eu | 0.5714 ± 0.0227 | 0.4031 ± 0.0162 | 0.9068 ± 0.0247 | 0.0014 ± 0.0004 |
| Gd | 2.4545 ± 0.0493 | 2.2552 ± 0.0575 | 0.0502 ± 0.0068 | 0.0167 ± 0.0040 |
| Tb | 0.4566 ± 0.0123 | 0.4362 ± 0.0147 | 0.0053 ± 0.0016 | 0.0020 ± 0.0007 |
| Dy | 3.0792 ± 0.0610 | 3.4252 ± 0.0884 | 0.0398 ± 0.0067 | 0.0664 ± 0.0086 |
| Ho | 0.7589 ± 0.0180 | 0.7478 ± 0.0304 | 0.0057 ± 0.0007 | 0.0293 ± 0.0031 |
| Er | 1.7652 ± 0.0417 | 2.1709 ± 0.0688 | 0.0210 ± 0.0029 | 0.0920 ± 0.0097 |
| Tm | 0.2628 ± 0.0098 | 0.2952 ± 0.0143 | n.d. | 0.0373 ± 0.0037 |
| Yb | 1.7081 ± 0.0441 | 1.9181 ± 0.0986 | n.d. | 0.3538 ± 0.0298 |
| Lu | 0.2630 ± 0.0103 | 0.3194 ± 0.0164 | n.d. | 0.0670 ± 0.0056 |

n.d. = not detected. Errors are 1σ from counting statists only.
"l" and "h" refer to clinopyroxene analyses with the lowest and highest REE abundances.
Number of analyses: clinopyroxene (9), plagioclase (2), and olivine (3)

Table 3.4
Representative REE abundances (in ppm) in minerals of NWA 4590.

| | Clinopyroxene (l) | Clinopyroxene (h) | Plagioclase | Olivine[1] | Phosphate |
|---|---|---|---|---|---|
| La | 0.6223 ± 0.0434 | 3.1032 ± 0.0578 | 0.3771 ± 0.0368 | 0.0537 ± 0.0071 | 740.709 ± 0.721 |
| Ce | 2.2343 ± 0.0874 | 10.6055 ± 0.1129 | 0.5614 ± 0.0427 | 0.1499 ± 0.0128 | 1253.415 ± 0.699 |
| Pr | 0.4929 ± 0.0368 | 2.0655 ± 0.0447 | 0.0991 ± 0.0228 | 0.0307 ± 0.0052 | 153.835 ± 0.084 |
| Nd | 2.9772 ± 0.2574 | 12.5411 ± 0.3143 | 0.2839 ± 0.0687 | 0.1484 ± 0.0322 | 591.552 ± 1.062 |
| Sm | 1.2993 ± 0.1542 | 5.3321 ± 0.1834 | 0.0425 ± 0.0213 | 0.1574 ± 0.0303 | 97.701 ± 0.469 |
| Eu | 0.3627 ± 0.0345 | 1.1755 ± 0.0439 | 0.8014 ± 0.0481 | 0.0682 ± 0.0081 | 22.963 ± 0.316 |
| Gd | 1.8374 ± 0.1214 | 6.9144 ± 0.1397 | 0.0818 ± 0.0290 | 0.3905 ± 0.0341 | 117.694 ± 1.193 |
| Tb | 0.3577 ± 0.0338 | 1.2125 ± 0.0246 | 0.0064 ± 0.0026 | 0.2750 ± 0.0203 | 20.522 ± 0.219 |
| Dy | 2.3424 ± 0.1532 | 7.9314 ± 0.1689 | 0.0282 ± 0.0749 | 2.0371 ± 0.0841 | 100.406 ± 0.595 |
| Ho | 0.4153 ± 0.0337 | 1.5616 ± 0.0420 | 0.0048 ± 0.0143 | 0.5721 ± 0.0245 | 17.483 ± 0.134 |
| Er | 1.3941 ± 0.1109 | 4.3037 ± 0.1162 | n.d. | 2.0606 ± 0.0762 | 32.299 ± 0.715 |
| Tm | 0.1543 ± 0.0214 | 0.5924 ± 0.0254 | n.d. | 0.3898 ± 0.0180 | 2.601 ± 0.154 |
| Yb | 1.1253 ± 0.0962 | 3.4018 ± 0.1005 | n.d. | 4.1189 ± 0.1264 | 9.488 ± 0.927 |
| Lu | 0.1228 ± 0.0158 | 0.4605 ± 0.0217 | n.d. | 0.7139 ± 0.0330 | 0.897 ± 0.279 |

n.d. = not detected. Errors are 1σ from counting statists only.
l and "h" refer to clinopyroxene analyses with the lowest and highest REE abundances.
[1]Olivine analyses include kirschteinite.
Number of analyses: clinopyroxene (10), plagioclase (5), phosphate (3), and olivine (3)

Table 3.5
Representative REE abundances (in ppm) in minerals of NWA 4801.

| | Clinopyroxene (l) | Clinopyroxene (h) | Plagioclase | Olivine[1] | Phosphate |
|---|---|---|---|---|---|
| La | 0.8568 ± 0.0500 | 2.1117 ± 0.0899 | 0.7855 ± 0.0292 | 0.0044 ± 0.0007 | 876.390 ± 3.193 |
| Ce | 3.1383 ± 0.1021 | 7.5010 ± 0.1806 | 1.2734 ± 0.0389 | 0.0140 ± 0.0019 | 1745.632 ± 4.747 |
| Pr | 0.6964 ± 0.0432 | 1.6810 ± 0.0769 | 0.1268 ± 0.0111 | 0.0039 ± 0.0012 | 238.291 ± 1.575 |
| Nd | 4.7334 ± 0.3200 | 10.3289 ± 0.5413 | 0.2754 ± 0.0465 | 0.0228 ± 0.0052 | 1003.790 ± 8.522 |
| Sm | 1.8338 ± 0.1806 | 4.4180 ± 0.3214 | 0.0527 ± 0.0199 | 0.0246 ± 0.0092 | 318.734 ± 4.762 |
| Eu | 0.4820 ± 0.0462 | 1.0246 ± 0.0774 | 0.8991 ± 0.0548 | 0.0212 ± 0.0017 | 78.422 ± 1.183 |
| Gd | 2.3303 ± 0.1353 | 5.0482 ± 0.2281 | 0.0755 ± 0.0094 | 0.0639 ± 0.0082 | 423.320 ± 4.110 |
| Tb | 0.4692 ± 0.0382 | 0.9475 ± 0.0545 | 0.0083 ± 0.0011 | 0.0152 ± 0.0017 | 61.208 ± 0.994 |
| Dy | 3.4831 ± 0.1844 | 6.5715 ± 0.2888 | 0.0267 ± 0.0094 | 0.4074 ± 0.0244 | 282.981 ± 3.243 |
| Ho | 0.7545 ± 0.0496 | 1.2037 ± 0.0638 | 0.0045 ± 0.0012 | 0.1912 ± 0.0104 | 52.592 ± 0.839 |
| Er | 2.0307 ± 0.1391 | 3.3356 ± 0.1897 | n.d. | 0.8242 ± 0.0354 | 124.357 ± 2.019 |
| Tm | 0.3117 ± 0.0301 | 0.5269 ± 0.0444 | n.d. | 0.1774 ± 0.0088 | 10.482 ± 0.332 |
| Yb | 1.9011 ± 0.1322 | 2.9738 ± 0.2064 | n.d. | 1.4867 ± 0.0450 | 63.073 ± 1.383 |
| Lu | 0.2462 ± 0.0244 | 0.3825 ± 0.0313 | n.d. | 0.2715 ± 0.0125 | 4.897 ± 0.175 |

n.d. = not detected. Errors are 1σ from counting statists only.
"l" and "h" refer to clinopyroxene analyses with the lowest and highest REE abundances.
Number of analyses: clinopyroxene (9), plagioclase (5), phosphate (2), and olivine (3)

Table 3.6
Representative REE abudnances (in ppm) in NWA 1296 and NWA 1670

| | NWA 1296 | | | NWA 1670 | | |
|---|---|---|---|---|---|---|
| | Clinopyroxene (l) | Clinopyroxene (h) | Plagioclase | Clinopyroxene (l) | Clinopyroxene (h) | Olivine |
| La | 1.4565 ± 0.0669 | 2.5418 ± 0.0936 | 0.2242 ± 0.0193 | 2.0149 ± 0.0513 | 2.6886 ± 0.0524 | 0.0745 ± 0.0100 |
| Ce | 4.9823 ± 0.1341 | 8.0054 ± 0.1800 | 0.5897 ± 0.0391 | 5.9564 ± 0.0992 | 8.7765 ± 0.1025 | 0.1057 ± 0.0151 |
| Pr | 0.9997 ± 0.0533 | 1.6002 ± 0.0714 | 0.0859 ± 0.0115 | 1.0187 ± 0.0364 | 1.4515 ± 0.0358 | 0.0214 ± 0.0055 |
| Nd | 5.8742 ± 0.2493 | 9.0984 ± 0.3377 | 0.3546 ± 0.0450 | 5.9589 ± 0.1700 | 7.8874 ± 0.1581 | 0.0896 ± 0.0211 |
| Sm | 2.1470 ± 0.1993 | 1.5013 ± 0.1064 | 0.0800 ± 0.0283 | 2.5436 ± 0.1469 | 3.6304 ± 0.1463 | 0.0042 ± 0.0021 |
| Eu | 0.4815 ± 0.0455 | 0.8205 ± 0.0720 | 0.7865 ± 0.0487 | 0.5690 ± 0.0324 | 0.8743 ± 0.0403 | 0.0058 ± 0.0033 |
| Gd | 3.0344 ± 0.1563 | 4.9081 ± 0.2108 | 0.1066 ± 0.0173 | 3.4153 ± 0.1110 | 4.7700 ± 0.1105 | 0.0217 ± 0.0072 |
| Tb | 0.6063 ± 0.0410 | 0.9585 ± 0.0549 | 0.0234 ± 0.0057 | 0.6708 ± 0.0294 | 0.8982 ± 0.0271 | 0.0043 ± 0.0019 |
| Dy | 4.0298 ± 0.2118 | 6.3939 ± 0.2662 | 0.0734 ± 0.0184 | 4.4083 ± 0.1507 | 5.9827 ± 0.1393 | 0.0464 ± 0.0101 |
| Ho | 0.9315 ± 0.0565 | 1.2784 ± 0.0697 | 0.0238 ± 0.0066 | 0.8872 ± 0.0372 | 1.3090 ± 0.0385 | 0.0192 ± 0.0042 |
| Er | 2.5214 ± 0.1543 | 3.9334 ± 0.2042 | 0.0824 ± 0.0200 | 2.6483 ± 0.1070 | 3.5860 ± 0.1057 | 0.0534 ± 0.0103 |
| Tm | 0.3786 ± 0.0375 | 0.5742 ± 0.0466 | 0.0102 ± 0.0021 | 0.3927 ± 0.0244 | 0.5569 ± 0.0256 | 0.0119 ± 0.0027 |
| Yb | 2.5694 ± 0.1652 | 4.1327 ± 0.2219 | 0.0733 ± 0.0203 | 3.0425 ± 0.1219 | 4.0690 ± 0.1198 | 0.1160 ± 0.0175 |
| Lu | 0.3981 ± 0.0368 | 0.6087 ± 0.0505 | 0.0140 ± 0.0053 | 0.4930 ± 0.0294 | 0.6527 ± 0.0294 | 0.0242 ± 0.0077 |

n.d. = not detected. Errors are 1σ from counting statistics only.
"l" and "h" refer to clinopyroxene analyses with the lowest and highest REE abundances.

Table 3.7
Whole-rock (or bulk) REE concentrations (in ppm) in NWA 2999, 4590, 4801, 1296, and 1670

| | NWA 2999 | NWA 4590 | NWA 4801 | NWA 1296 | NWA 1670[a] |
|---|---|---|---|---|---|
| La | 0.6145 ± 0.0307 | 1.6516 ± 0.0826 | 2.1993 ± 0.1100 | 3.1529 ± 0.0400 | 3.2045 ± 0.0251 |
| Ce | 2.1332 ± 0.1067 | 5.0340 ± 0.2517 | 6.6645 ± 0.3332 | 7.9285 ± 0.0846 | 8.3209 ± 0.0439 |
| Pr | 0.3545 ± 0.0177 | 0.8824 ± 0.0441 | 1.1163 ± 0.0558 | 1.2627 ± 0.0231 | 1.2266 ± 0.0149 |
| Nd | 1.9896 ± 0.0995 | 4.7852 ± 0.2393 | 6.1313 ± 0.3066 | 6.3336 ± 0.0954 | 6.3617 ± 0.0657 |
| Sm | 0.6485 ± 0.0324 | 1.5113 ± 0.0756 | 2.2326 ± 0.1116 | 2.0979 ± 0.0446 | 2.1599 ± 0.0506 |
| Eu | 0.2380 ± 0.0119 | 0.5792 ± 0.0290 | 0.7164 ± 0.0358 | 0.7952 ± 0.0123 | 1.0932 ± 0.0197 |
| Gd | 0.9250 ± 0.0462 | 2.1999 ± 0.1100 | 2.6824 ± 0.1341 | 2.7008 ± 0.0446 | 2.0920 ± 0.0267 |
| Tb | 0.1657 ± 0.0083 | 0.3982 ± 0.0199 | 0.5332 ± 0.0267 | 0.5214 ± 0.0046 | 0.5366 ± 0.0096 |
| Dy | 1.1267 ± 0.0563 | 2.7874 ± 0.1394 | 3.4155 ± 0.1708 | 3.3452 ± 0.0415 | 3.5866 ± 0.0499 |
| Ho | 0.2524 ± 0.0126 | 0.6244 ± 0.0312 | 0.7331 ± 0.0367 | 0.7275 ± 0.0123 | 0.7761 ± 0.0130 |
| Er | 0.7534 ± 0.0377 | 1.9819 ± 0.0991 | 2.0993 ± 0.1050 | 2.2009 ± 0.0308 | 2.2114 ± 0.0363 |
| Tm | 0.1103 ± 0.0055 | 0.2986 ± 0.0149 | 0.2832 ± 0.0142 | 0.3076 ± 0.0062 | 0.3471 ± 0.0084 |
| Yb | 0.7868 ± 0.0393 | 2.0724 ± 0.1036 | 1.8827 ± 0.0941 | 2.0902 ± 0.0323 | 2.4821 ± 0.0416 |
| Lu | 0.1234 ± 0.0062 | 0.3258 ± 0.0163 | 0.2666 ± 0.0133 | 0.3153 ± 0.0046 | 0.3486 ± 0.0092 |

Errors are 2σ (±5%, based on the external reproducibility of terrestrial standards) for all except NWA 1670.
[a]NWA 1670 abundances are in situ bulk analyses from a large area raster of the fine-grained region. NWA 1670 errors 1σ from counting statistics only.

## 3.4 DISCUSSION

### 3.4.1 Rare Earth Element Budget and the Effects of Terrestrial Alteration

Merrillite is the phase that contains the highest concentrations of REE within the angrites analyzed in this study. The merrillite REE pattern is particularly LREE-enriched making it the main contributor of LREE to the overall REE budget. Plagioclase is additionally a major reservoir of LREE in the angrites. While REE concentrations are several orders of magnitude lower, plagioclase in NWA 4590 and NWA 4801 has a significantly higher modal abundance than merrillite and is, therefore, a significant contributor to the LREE budget. The large positive Eu anomalies in angritic plagioclase make this phase a significant reservoir of Eu. The HREE-enriched nature of pyroxene and olivine/kirschsteinite make these phases the main contributors to the HREE budget. Other minerals such as Fe-Ni metal, oxides, and sulfides in these angrites contribute negligibly to the whole rock REE budget as these phases contain extremely low REE concentrations and typically also have low modal abundances.

Mass balance calculations using the average REE concentrations measured *in situ* in this study in the mineral phases of each of the three angrites studied here were undertaken to assess whether we have included all phases in our analyses that contribute significantly to the REE budget of these angrites. Calculations were made iteratively by changing the abundances of each phase until the differences between the measured whole-rock REE concentrations and the calculated whole-rock REE concentration from mineral analyses in this study

were minimized. In the case of NWA 2999, mass balance calculations indicate that the measured whole-rock REE concentrations (particularly those of the LREE) cannot be reproduced without a trace amount of LREE-rich phase such as merrillite, although no grains of this mineral were seen in the polished section studied here. Therefore, for the mass balance calculation to adequately reproduce the REE abundances in the NWA 2999 whole-rock, we had to assume a merrillite composition similar to that measured in other angrites, such as Sahara 99555 and LEW 86010 (representative of the quenched and plutonic angrites, respectively). Of these two end-member angrite merrillite compositions, that from Sahara 99555 appears to best reproduce the LREE pattern in the measured NWA 2999 whole-rock. Specifically, mass balance calculations suggest the following modal abundances of: ~64% olivine, ~30% clinopyroxene, ~1% anorthite, ~0.04% merrillite, and ~15% phases with negligible REE abundances (e.g., metal, oxides and sulfides) (Fig. 3.9a). These mineral modal abundances are generally similar to those reported for NWA 2999 by Kuehner et al. (2006) (although no merrillite was reported by these authors). Therefore, our mass balance calculations suggest that trace amounts of merrillite (of a composition similar to the merrillite observed in Sahara 99555) are likely present in NWA 2999 even though this mineral has not been documented thus far by petrographic investigations of this meteorite.

In contrast with NWA 2999, merrillite has been reported previously in both NWA 4590 and NWA 4801 (Kuehner and Irving, 2007; Irving, personal communication). Mass balance calculations for NWA 4590 show that the whole-

rock REE composition of this angrite can be matched with the assumption of the following mineral modal abundances: ~35% clinopyroxene, ~23% anorthite, ~35% olivine/kirschsteinite, ~0.2% merrillite, and ~7% of phases with negligible REE abundances (Fig. 3.9b). These modal abundances do not agree with those reported by Kuehner and Irving (2007). However, given the coarse-grained texture of NWA 4590 and possible heterogeneity in the mineral abundances (especially in trace phases such as merrillite), significant variations in the mineral modal abundances may be expected based on the sizes of the samples under consideration. Similarly, mass balance calculations for NWA 4801 indicate that its whole-rock REE abundances can be matched with the following modal abundances: ~57% clinopyroxene, ~22% anorthite, ~20% olivine, ~0.2% merrillite, ~0.8% of negligible REE-bearing phases (e.g., oxides) (Fig. 3.9c). These modal abundances are similar to those estimated for this angrite based on a petrographic investigation (Irving, personal communication). In the quenched angrites, the complication in obtaining *in situ* analyses in each mineral phase limits the ability to complete mass balance calculations in the same manner for these samples.

The above mass balance calculations demonstrate the significant affect of merrillite on the whole-rock REE budget of the angrites. Heterogeneity on the mm-scale in the modal abundances of minerals in the angrites, particularly that of merrillite, indicates that relatively large (gram-sized or larger) bulk rock samples are required to obtain representative whole-rock REE concentrations for the plutonic angrites.

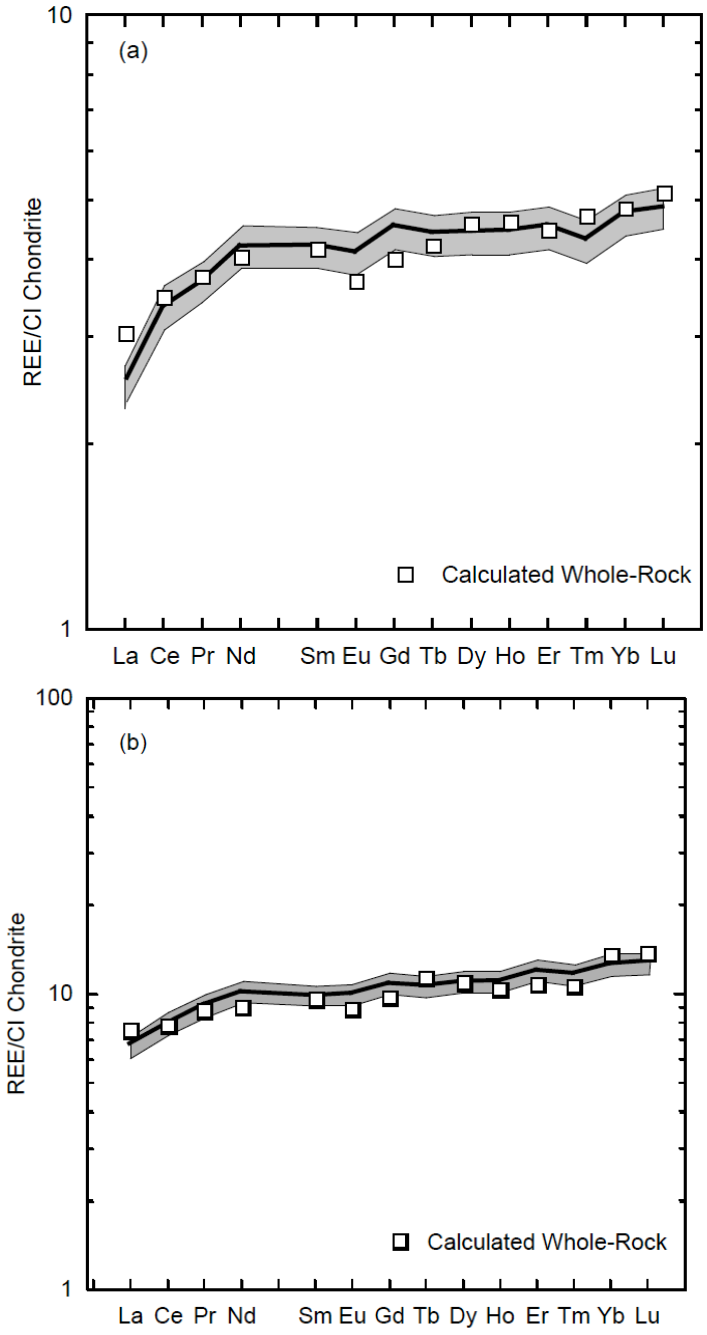


*Figure 3.9*- Comparison of measured and calculated whole-rock REE abundances in (a) Northwest Africa (NWA) 2999, (b) NWA 4590, and (c, next page) NWA 4801. Solid line is the measured whole-rock composition determined in this study with the shaded region indicating the measurement uncertainty. Squares indicate the calculated whole-rock composition (see text for details of the calculations).

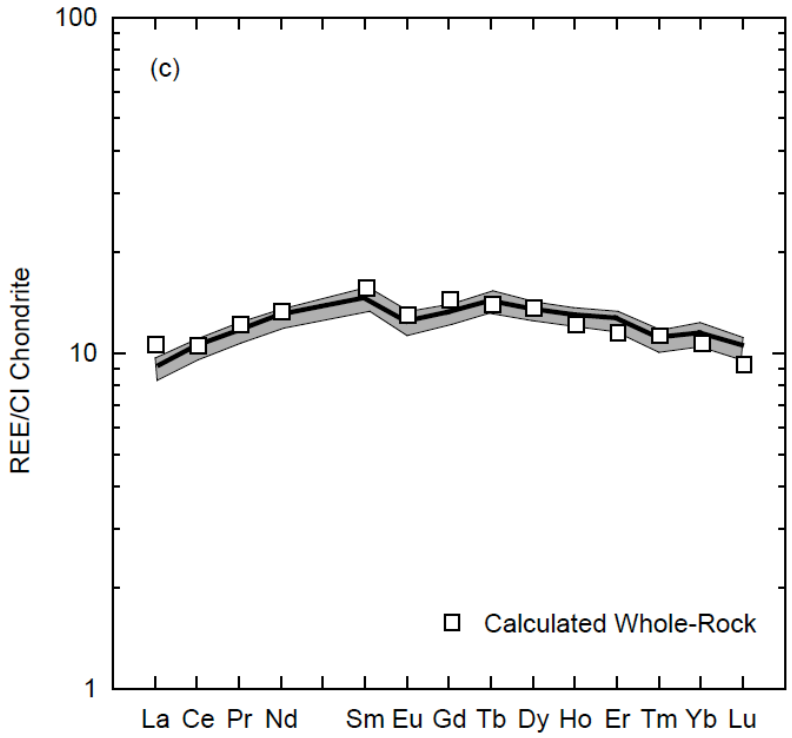


*Figure 3.9 (continued)*- Comparison of measured and calculated whole-rock REE abundances in (a, previous page) Northwest Africa (NWA) 2999, (b, previous page) NWA 4590, and (c) NWA 4801. Solid line is the measured whole-rock composition determined in this study with the shaded region indicating the measurement uncertainty. Squares indicate the calculated whole-rock composition (see text for details of the calculations).

The five angrites in this study are all finds from the hot desert region of Northwest Africa. As such, it is possible that these meteorites have undergone significant weathering in the terrestrial environment. Terrestrial alteration has been shown to affect the LREE abundances in minerals of other hot desert meteorites (Crozaz et al., 2003). Among the angrites in this study, only NWA 2999 appears to have significant geochemical evidence of weathering. In particular, the olivine of NWA 2999 (Fig. 3.7) exhibits a V-shaped REE pattern that has been observed in olivines of other hot desert meteorites, including the angrite Sahara 99555, due to the mobilization of LREE (Crozaz et al., 2003). Another common feature of terrestrial weathering reported by Crozaz et al. (2003) is the presence of Ce anomalies in pyroxenes. However, pyroxenes in the angrites investigated here do not exhibit any Ce anomalies, suggesting that these meteorites have undergone only minimal terrestrial weathering.

### 3.4.2 Parent Melt Compositions

Rare earth element compositions of individual minerals, such as pyroxene and plagioclase, have been used previously to determine the geochemical characteristics of melts in equilibrium with these phases (e.g., McKay et al., 1994; Floss et al., 2003). The determination of the geochemical composition of the melt in equilibrium with the pyroxene and plagioclase cores of an angrite can be used to: (1) determine the trace element composition of the parent melt of individual angrites and (2) investigate whether an angrite crystallized in a geochemically closed system after the formation of the earliest phases. In the inferred crystallization sequence of the angrites, pyroxene is one of the earliest phases to

crystallize containing significant amounts of REEs (Mittlefehldt et al., 2002). As such, the calculated melt in equilibrium with the pyroxene would be most representative of the composition of the parent melt. Furthermore, the calculation of the melt in equilibrium with other phases (e.g., plagioclase) can indicate when phases crystallized in equilibrium with the same melt and, therefore, experienced a geochemically closed system during formation.

The melt in equilibrium with a given phase can be calculated using the geochemical relationship:

$$D_{REE} = \frac{C_x}{C_L} \qquad \text{Eq. (3.1)}$$

where $D_{REE}$ is the mineral/melt partition coefficient for a particular REE in a given mineral phase, $C_X$ is the measured concentration of the REE in the mineral phase, and $C_L$ is the concentration of the REE in the melt in equilibrium with the phase. Mineral/melt partition coefficients are determined experimentally and are highly dependent on the bulk chemistry of the melt and the formation conditions (e.g., oxygen fugacity). The mineral/melt partition coefficients used to calculate the melt in equilibrium with the pyroxene and plagioclase are from McKay et al. (1994) that were determined using a bulk angrite starting composition. The REE abundances calculated in the melt in equilibrium with the pyroxene and plagioclase in NWA 2999, NWA 4590, NWA 4801, and NWA 1296 are shown in Figs. 3.10a-d.

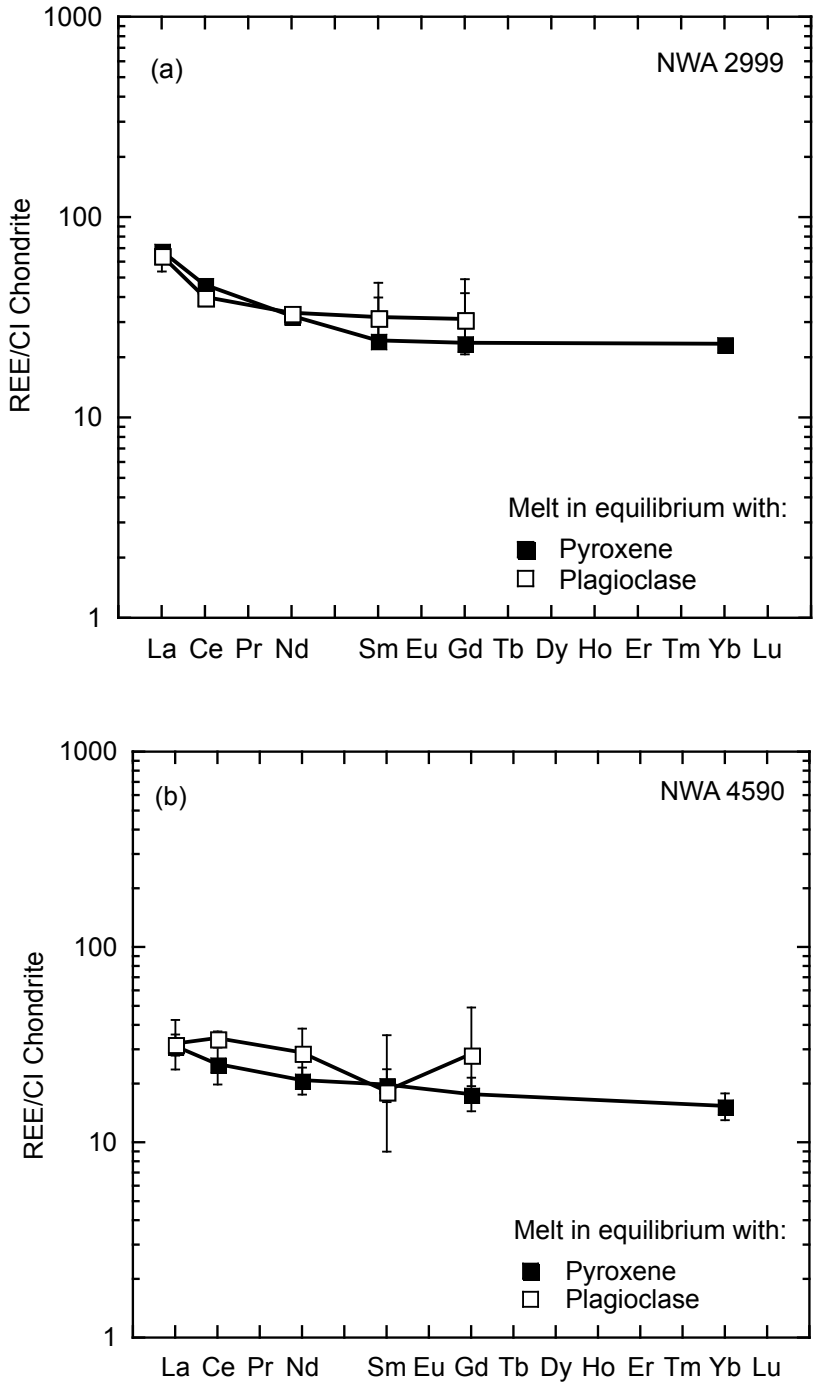


*Figure 3.10*- Calculated chondrite-normalized REE concentrations in the melts in equilibrium with the pyroxene cores and plagioclase of (a) Northwest Africa (NWA) 2999, (b) NWA 4590, (c, next page) NWA 4801, and (d, next page) NWA 1296. See text for details of the calculations.

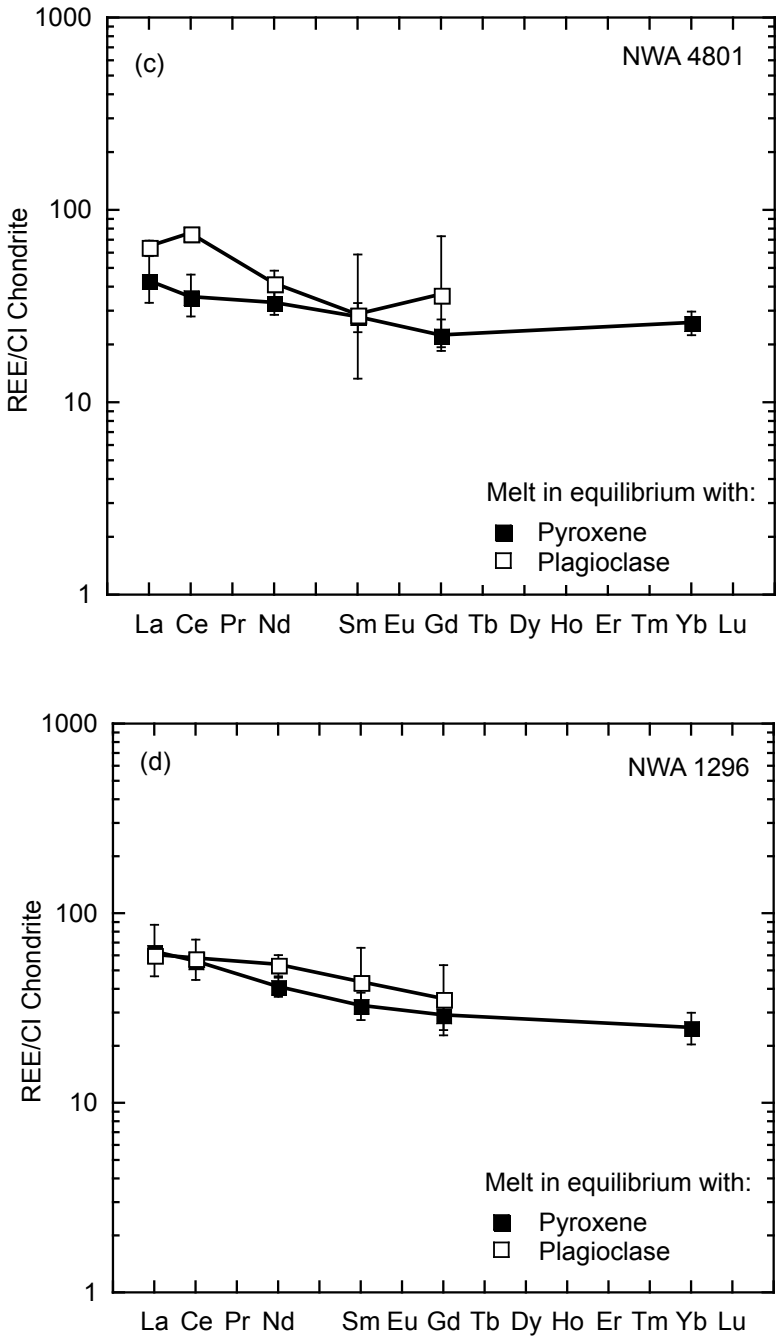


*Figure 3.10 (continued)*- Calculated chondrite-normalized REE concentrations in the melts in equilibrium with the pyroxene cores and plagioclase of (a, previous page) Northwest Africa (NWA) 2999, (b, previous page) NWA 4590, (c) NWA 4801, and (d) NWA 1296. See text for details of the calculations.

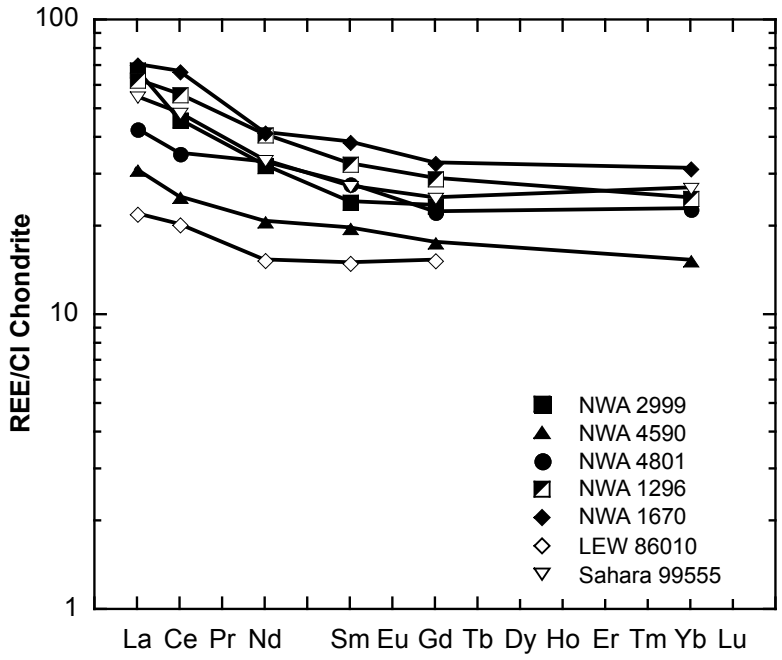


*Figure 3.11*- Calculated chondrite-normalized REE concentrations in melts in equilibrium with the clinopyroxene cores of NWA 2999, NWA 4590, NWA 4801, NWA 1296, and NWA 1670. For comparison, calculated melts in equilibrium with the clinopyroxene cores of LEW 86010 and Sahara 99555 (after Floss et al., 2003) are also shown. See text for details of the calculations.

The melt in equilibrium with the pyroxene and plagioclase cores has REE patterns that are parallel and generally in agreement with each other in NWA 2999, NWA 4590, and NWA 1296. This agreement appears to indicate the both of these phases crystallized in equilibrium with the same melt. The melt in equilibrium with the pyroxene and plagioclase of NWA 4801 is also generally in good agreement with the exception of Ce, although the REE pattern of the melts still broadly parallel each other. Additionally, the REE composition of the parent melts calculated in all the analyzed angrites are generally similar to each other and to the parent melts calculated for the other known angrites (Fig. 3.10e). These similarities indicate that all angrites crystallized from source reservoirs with broadly similar REE characteristics. However, the inherent uncertainties (e.g., uncertainties in the measured concentration and mineral/melt partition coefficients) in the parent melt composition calculations prevent the elucidation of minor differences in multiple source reservoirs using only the parent melt composition.

### 3.4.3 Oxygen Fugacity Conditions During Angrite Formation

Constraining the redox conditions on the angrite parent body (APB) is important for obtaining a greater understanding of the petrogenetic history of angrites and characteristics of their source material. Previous studies have attempted to ascertain the redox conditions at the time of angrite crystallization, and the mantle source composition on the APB, by partial melting experiments of CV chondrite composition material under varying oxygen fugacities in an attempt to generate bulk compositions similar to those of the previously identified angrites

(e.g., Jurewicz et al., 1993). These studies were able to produce bulk compositions similar, but not identical, to those of the quenched angrites under oxygen fugacity conditions of approximately 1 to 2 log units above the iron-wustite (IW) buffer (i.e., ~IW+1 to ~IW+2; Jurewicz et al., 1991, 1993). Subsequently, McKay et al. (1994) experimentally developed a calibration that allowed the determination of the oxygen fugacity at crystallization based on the partitioning of Eu and Gd in the pyroxene and plagioclase in the angrites. As discussed by McKay et al. (1994), the partitioning values are directly related to the measured abundances of Eu and Gd in the clinopyroxene and plagioclase (i.e., $K_{D_{Eu/Gd}^{Pl/Px}} = (\mathrm{Eu/Gd})_{\mathrm{Pl}}/(\mathrm{Eu/Gd})_{\mathrm{Px}}$). However, the acquisition of accurate oxygen fugacity estimates using the Eu/Gd oxybarometer requires that both phases crystallized in equilibrium with the same melt. As demonstrated in section 3.4.2, the parallel nature of the melt in equilibrium with the pyroxene and plagioclase cores indicates that the three plutonic angrites (NWA 2999, NWA 4590, and NWA 4801) and the quenched angrite NWA 1296 satisfy this requirement. Using the oxygen fugacity calibration from McKay et al. (1994) and the Eu and Gd concentrations determined in this study in the cores of the pyroxene and plagioclase, it is estimated that NWA 2999, NWA 4590, NWA 4801, and NWA 1296 crystallized at oxygen fugacity conditions of ~IW$+0.8^{+0.3}_{-0.3}$, ~IW$+1.6^{+0.8}_{-0.6}$, ~IW$+1.3^{+0.4}_{-0.3}$, and IW$+1.4^{+0.2}_{-0.2}$, respectively (errors on these oxygen fugacity estimates are based on the errors in the elemental concentrations determined by SIMS). All four of these angrites yield $fO_2$ estimates similar to those estimated for the plutonic angrite Lewis Cliff (LEW) 86010 and quenched angrites LEW

87051, Asuka 881371, D'Orbigny, and Sahara 99555 (Floss et al., 2003; Wadhwa, 2008). Therefore, it appears that all angrites (both plutonic and quenched) identified thus far crystallized under similar (constant), relatively oxidizing conditions of $fO_2 \sim$ IW+1. For comparison, the oxygen fugacity conditions during formation of the differentiated eucrite meteorites have been estimated to be more reducing at $fO_2 \sim$ IW-1.5 (Jurewicz et al., 1993).

### 3.4.4 Comparative Angrite Geochemistry

The results of the *in situ* trace element analyses and the parent melt calculations of the angrites NWA 2999, NWA 4590, NWA 4801, NWA 1296, and NWA 1670 provide important insight into possible petrogenetic similarities among the various angrites. The study by Floss et al. (2003) of the quenched angrites (e.g., Sahara 99555 and D'Orbigny) noted similarities in the geochemical characteristics of their source reservoirs. Furthermore, this study demonstrated that the quenched angrites originated from a source reservoir that was geochemically distinct from that of the plutonic angrite LEW 86010. Prior to the recent recovery of NWA 2999, NWA 4590, and NWA 4801, only two other plutonic angrites (LEW 86010 and Angra dos Reis) were available for geochemical analysis. The limited trace element investigations of these two angrites (e.g., Crozaz and McKay, 1990) indicated that Angra dos Reis and LEW 86010 were unlikely to be petrogenetically related. Therefore, the comparative trace element geochemistry of NWA 2999, NWA 4590, and NWA 4801 in comparison with the other known plutonic and quenched angrites enables the further investigation for possible petrogenetic relationships between the members

of the two angrite textural subgroups. In addition, the analyses of the quenched angrites NWA 1296 and NWA 1670 expands the available data set to elucidate any variation in the composition of the quenched angrite source reservoir(s).

Northwest Africa 2999 has been an enigmatic sample since its discovery in 2004. The absolute ages of NWA 2999 and one of its paired stones, NWA 6291, obtained through the Pb-Pb isotope radiogenic isotope system indicate a crystallization age that is intermediate to the previously reported ages for the quenched and plutonic angrites (Amelin and Irving, 2007; Bouvier et al., 2011; Brennecka and Wadhwa, 2012). While coarse-grained petrographically, the unique crystallization age compared to the other known angrites raises the possibility that its petrogenetic origin may be from a distinct source region on the APB. However, the trace element abundances reported in this study for NWA 2999 minerals demonstrate that this angrite exhibits some geochemical similarities to the quenched angrites (e.g., Sahara 99555). For example, the pyroxene REE patterns in NWA 2999 are very similar to those of this mineral in Sahara 99555, but quite distinct from those in the plutonic angrite LEW 86010 (Fig. 3.4a). Furthermore, Ti and Zr abundances in NWA 2999 pyroxenes lie off the compositional trend defined by pyroxenes of the plutonic angrite LEW 86010, but plot on the edge of the compositional region defined by pyroxenes of the quenched angrites (Fig. 3.5a). These characteristics, coupled with the unique crystallization age of NWA 2999, suggest that while this angrite may belong a subgroup distinct from the currently known angrites, it may indeed have some

petrogenetic affinities to the quenched angrites (possibly originating from a similar source reservoir) despite its coarse-grained texture.

Trace element characteristics of the whole-rock and individual mineral phases of NWA 4590 are similar to those of the previously studied plutonic angrite LEW 86010. In particular, REE patterns of the pyroxene, olivine/kirschsteinite, and merrillite in NWA 4590 closely parallel those of these minerals in LEW 86010 (Figs 3.4b, 3.5a and 3.8). Interestingly, the olivine phenocrysts of NWA 4590 include prominent and extensive kirschsteinite exsolution lamellae, a unique mineralogical feature also observed in LEW 86010 (Prinz et al., 1988). The similarity between NWA 4590 and LEW 86010 extends to the additional trace elements in their pyroxene (i.e., Ti and Zr). Specifically, in a plot of Ti versus Zr abundances, NWA 4590 and LEW 86010 pyroxenes define overlapping trends (Fig. 3.5a). Further evidence of a possible petrogenetic relationship between NWA 4590 and LEW 86010 can be seen in their crystallization ages as determined using the Pb-Pb isotope system, which are the same within error (Amelin and Irving, 2007; Brennecka and Wadhwa, 2012). The strong petrographic and geochemical similarities, in addition to the crystallization ages, suggest that both NWA 4590 and the angrite LEW 86010 were co-magmatic, having originated from the same partial melting event of their mantle source reservoir on the APB.

In contrast to the lines of evidence observed in NWA 4590, the evidence for any petrogenetic relationship between NWA 4801 and the other plutonic angrites is more ambiguous. The young crystallization age of NWA 4801 is

similar to that of both NWA 4590 and LEW 86010 (Amelin and Irving, 2007; Brennecka and Wadhwa, 2012). However, the range of REE and other trace elements (e.g., Ti and Zr) in the pyroxene of NWA 4801 is substantially narrower than both NWA 4590 and LEW 86010, but generally falls within the range observed in the quenched angrites (Figs. 3.4b and 3.5). Additionally, merrillite in NWA 4801 has a LREE pattern that is distinctly similar to that of merrillite in the quenched angrites (e.g., Sahara 99555), whereas the overall slope of the HREE pattern is more like the pattern observed for this mineral in the plutonic angrites, NWA 4590 and LEW 86010 (Fig. 3.8). Therefore, unlike NWA 4590, which shows clear and unambiguous geochemical similarities to the plutonic angrite LEW 86010, NWA 4801 has some unique geochemical characteristics that suggest that it may have affinities to both the plutonic and quenched angrites. Consequently, it may be that the parent melt of NWA 4801 represents some degree of interaction between partial melts from the source reservoirs of the plutonic, as well as quenched angrites.

In contrast to the varying geochemical relationships observed among the various plutonic angrites, the quenched angrites NWA 1296 and NWA 1670 show strong similarities to all other quenched angrites. The pyroxenes of both angrites have nearly parallel REE patterns with a similar range of abundances (although core values of both are slightly higher than the other quenched angrites). In addition, further trace and minor element abundances (e.g., Ti and Zr) plot within the compositional field defined by the quenched angrites (Fig. 3.5b). The similarity in geochemical characteristics of NWA 1296 and NWA 1670 with the

other quenched angrites provide further evidence for the proposed common origin of the quenched angrites with differing textures resulting from slightly different crystallization histories from a common geochemical reservoir (Floss et al., 2003).

**3.5 CONCLUSIONS**

The geochemical investigation of the plutonic angrite NWA 2999, NWA 4590, and NWA 4801 and the quenched angrites NWA 1296 and NWA 1670 have provided several new insights into the petrogenesis of the angrite meteorite group:

(1) NWA 2999 appears to have originated from a mantle source reservoir on the APB with geochemical affinities to the source reservoir of the quenched angrites (e.g., Sahara 99555). In particular, REE and other trace element abundances in pyroxenes of this angrite exhibit similarities to those in pyroxene of the quenched angrites.

(2) NWA 4590 shows strong geochemical similarities to the plutonic angrite LEW 86010, suggesting that these two meteorites are likely to be co-magmatic. The REE patterns of the various minerals in NWA 4590 (e.g., pyroxene and merrillite) closely parallel those of these minerals in LEW 86010. Moreover, additional trace elements (such as Ti and Y) in NWA 4590 pyroxenes define compositional trends that overlap those defined by LEW 86010 pyroxene.

(3) The possible geochemical relationship, if any, of NWA 4801 to other angrites is less clear. Specifically, REE (and other trace elements) in various minerals of NWA 4801 show affinities to both the plutonic and quenched angrites. This may

suggest that the petrogenetic history of NWA 4801 is more complicated than that of NWA 4590, and offers the possibility that this angrite may represent a petrogenetic linkage between the plutonic and quenched angrites.

(4) Both NWA 1296 and NWA 1670 indicate strong geochemical similarities to the other quenched angrites. The trace element composition of both *in situ* analyses of phases, such as pyroxene, and whole-rock abundances indicate a likely common geochemical source reservoir.

The variations among the various plutonic and quenched angrites investigated in this study indicate the occurrence of complex petrogenetic processes on the angrite parent body. While broadly similar in terms of trace element chemistry, evidence from *in situ* analyses suggests that multiple geochemical source reservoirs may have existed, including the possibility of partial interaction between melts from distinct reservoirs. The existence of multiple geochemical reservoirs, some of which produced melts over a period of several million years (e.g., similar melts producing both quenched and plutonic angrites) should be included in any subsequent models to explain the petrogenetic evolution of the angrite parent body.

# CHAPTER 4

# BROADER IMPLICATIONS FOR THE EVOLUTION OF THE ANGRITE PARENT BODY

## 4.1 CHRONOLOGY OF THE ANGRITE PARENT BODY

The development of a comprehensive understanding of the formation and evolution of the angrite parent body (APB) relies on the interpretation of chronological and petrologic information. The isotopic and trace element results in Chapters 2 and 3 can be combined with previous studies to establish a broad picture of the petrogenetic history of the APB. In particular, these results provide an opportunity to: (1) further characterize the composition of the angrite source material and the initial conditions at the time of formation and (2) expand and refine the presently inferred timeline for major processes occurring during the formation and evolution of the APB (Fig. 4.1).

Knowledge of the composition of the precursor (source) material and the conditions present at the time of melting to generate angritic melts can provide important constraints to understand variability in conditions in the early Solar System. Initial constraints of the chemical composition of the angrite source material were previously inferred through partial melting experiments of bulk chondrite samples under varying oxygen fugacity (redox) conditions (e.g., Jurewicz et al., 1991). The result of the Jurewicz et al. (1991) experiments indicated that melts similar, but not identical, to the composition of bulk angrites could be generated by melting of source material similar in composition to a CV3-type chondrite under relatively oxidizing conditions (i.e., 1 log unit above

the iron-wustite buffer; ~IW+1). While these experiments placed important initial constraints on the composition of the source material and estimates and the $fO_2$ needed to generate the proper melts to form angrites, the limited number of angrites at the time hindered a more comprehensive study of the redox conditions at the time of angrite formation. The development of the Eu-oxybarometer calibration for angrites (McKay et al., 1994) and the application to a range of quenched angrites (e.g., Floss et al., 2003; Wadhwa, 2008) provided additional evidence for a relatively oxidizing environment at the time of angrite formation at $fO_2$~IW+1. The expanded data from a range of plutonic and quenched angrites in Chapter 3 provide an opportunity to broaden the range of $fO_2$ estimates to include multiple plutonic angrites, as well as additional quenched angrites. Incorporating the new *f*O2 estimates from the angrites in this study, we observe that redox conditions experienced by the entire range of angrites (plutonic and quenched) are consistent with relatively oxidizing conditions at $fO_2$~IW+1, similar to the earliest estimates from the partial melting experiments. The relatively oxidizing condition of the APB at ~IW+1 is in contrast with other achondrite groups for which estimates of the redox conditions have been made, such as the eucrites and aubrites that experienced redox conditions ranging from ~IW-1 (eucrites) to ~IW-5 (aubrites) (e.g., Wadhwa, 2008). The range in $fO_2$ suggests significant variation in the local redox environments during the accretion and melting of the achondrite parent bodies within the first several million years of the Solar System.

Following the accretion of the precursor material to form the angrite parent body, widespread melting and core formation occurred rapidly, on the

order of ~3 Ma after CAI formation at 4568 Ma (e.g., Kleine et al., 2012). The Rb-Sr isotope systematics (Chapter 2) of a suite of plutonic and quenched angrites (i.e., NWA 2999, NWA 4590, NWA 4801, and D'Orbigny) suggest a significant volatile loss event on the APB occurred approximately 3-5 Ma after CAI formation and, according to the suggested early and rapid accretion and core formation timescales of Kleine et al. (2012), likely coincided with the formation of a global magma ocean. Evidence using the Mn-Cr isotope system suggests that the cooling and solidification of this magma ocean was rapid with mantle differentiation occurring ~4-5 Ma after CAI formation (Shukolyukov and Lugmair, 2007; Kleine et al., 2012). The earliest evidence of magmatic activity on the APB at ~4563 Ma (Brennecka and Wadhwa, 2012; references therein) appears to have occurred very shortly after the end of solidification of the magma ocean. Based on the extended range of angrite crystallization ages determined using the high-precision Pb-Pb isotope system (Brennecka and Wadhwa, 2012; references therein), as well as the absolute Sm-Nd and Lu-Hf isotope systems (Chapter 2), it appears that magmatic activity continued for approximately 7-8 Ma.

The crystallization ages of the presently known angrites indicate that the initial magmatic activity ceased by ~4556 Ma (Brennecka and Wadhwa, 2012; references therein). Apparent disturbance and possible resetting of the Sm-Nd and Lu-Hf isotope systematics (Chapter 2) after the initial period of magmatic activity in several angrites is indicative of later episodes of post-crystallization equilibration. The exact nature of the mechanisms (e.g., thermal or shock

metamorphism) resulting in the isotopic re-equilibration of the disturbed samples is not readily discernable. However, the isotopic results do indicate that the post-crystallization equilibration affected both shallow, quenched angrites, as well as the more deeply originating plutonic angrites. Furthermore, the apparent reset ages of the Sm-Nd and Lu-Hf systems indicate the episodes of post-crystallization equilibration may have extended from ~4.5 to ~3.9 Ga, indicating a complex petrologic history for the APB not previously observed after the initial period of magmatic activity between 4563 and 4556 Ma.

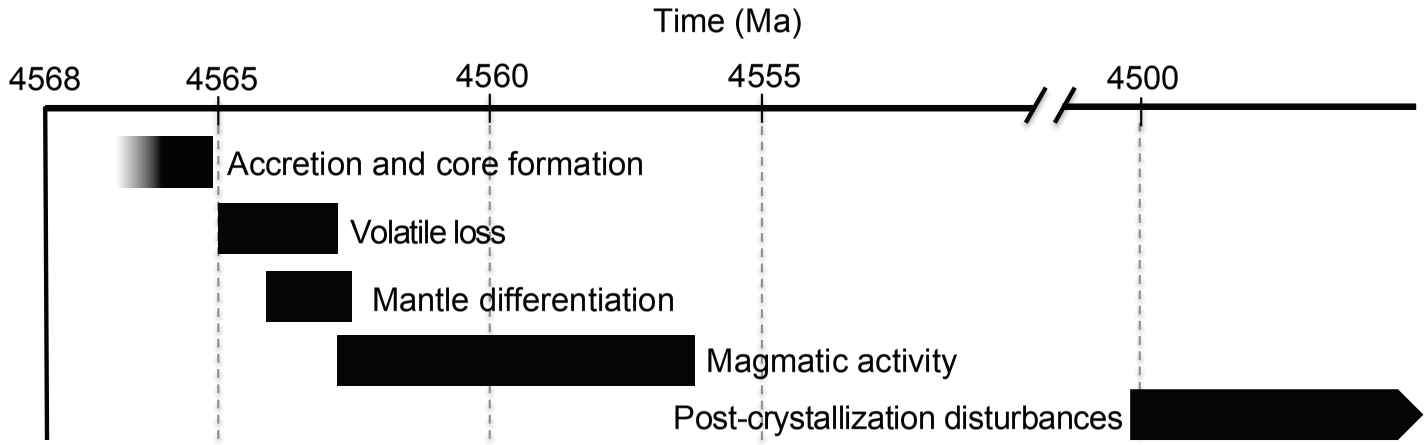


*Figure 4.1* – Chronology of processes during the formation and evolution of the angrite parent body. Data from this study, Kleine et al. (2012), and Brennecka and Wadhwa (2012) and references therein.

# CHAPTER 5

# INTRODUCTION II: SHERGOTTITES AND NAKHLITES

## 5.1 INTRODUCTION

### 5.1.1 Overview of SNC Meteorites

The shergottite-nakhlite-chassignite (SNC) meteorite group is a suite of basaltic and ultramafic rocks, commonly accepted to have formed on Mars based on a wide range of geochemical and isotopic evidence, that were subsequently launched from the martian surface by large impact events (e.g., Nyquist et al., 2001; references therein). As a result, these unique meteorites provide physical samples of the martian lithology to understand the magmatic processes occurring on Mars through detailed geochemical analyses. There are currently 68 distinct SNC meteorites (approximately 108 when paired stones are included in the total). A majority of the SNC meteorite group consists of shergottites (57 meteorites), with nakhlites (8 meteorites), chassignites (2 meteorites) and Allan Hills 84001 (an orthopyroxenite) comprising the remaining members of the meteorite group. The various subgroups of SNC meteorites sample varying formation conditions from cumulates forming within magma chambers (lherzolitic shergottites) to a thick surficial lava flow (nakhlites) (e.g., McSween, 1994; Treiman, 2005; references therein). As such, geochemical investigation into the SNC meteorites provides an opportunity to investigate a wide range of magmatic processes occurring on Mars. The following sections provide a general overview of the characteristics of the two most abundant SNC meteorite subgroups: shergottites and nakhlites.

Constituting the largest subgroup of the SNC meteorites, the shergottites display the most variation in petrographic and geochemical characteristics of any of the SNC subgroups. In terms of petrography and mineral composition, the shergottites can be classified into one of three petrographic subgroups: lherzolitic (or peridotitic), olivine-phyric, or basaltic (Bridges and Warren, 2006). Lherzolitic shergottites are interpreted as having a cumulate origin while olivine-phyric and basaltic shergottites likely represent a basaltic lava flow or a shallow intrusion (e.g., McSween, 1994; Nyquist et al., 2001; McSween, 2006). Based on a range of geochemical studies, the diverse shergottite petrographic subgroups appear to have sampled two distinct geochemical source reservoirs: (1) a depleted reservoir with significant LREE-depletion and reducing conditions, or (2) an enriched reservoir with only slight LREE-depletion and relatively oxidizing conditions (Wadhwa, 2001; Borg et al., 2002; Wadhwa, 2006; Bridges and Warren, 2006). Interestingly, the crystallization ages of the shergottites show a correlation with the geochemical source reservoir they originated from with depleted shergottites yielding relatively old ages of 300-600 Ma and enriched (and intermediate) shergottites with relatively younger crystallization ages between 165 and 185 Ma (Bridges and Warren, 2006; references therein).

Cosmic ray exposure ages suggest the ejection of shergottites from Mars occurred in multiple episodes with estimates ranging from 2 to 6 separate ejection events, occurring between ~1 and 19 Ma (Nyquist et al., 2001; references therein). Petrologic evidence (e.g., the presence of phases such as maskelynite) suggests the ejection events for the shergottites generated strong shock pressures on the

order of ~30-40 GPa for the basaltic and olivine-phyric shergottites (Stöffler et al., 2000; Nyquist et al., 2001) and ~45 GPa for the lherzolitic shergottites (Stöffler et al., 2000).

In contrast with the shergottites that sampled a range of petrologic lithologies on Mars, the nakhlites appear to have originated from a single petrologic unit, inferred to be a thick surficial lava flow with all nakhlites exhibiting an overall cumulate texture with pyroxene and olivine cumulus phases and a fine-grained quenched mesostasis (Treiman, 2005).

Unlike the shergottites that have a relatively broad range of crystallization ages, the nakhlites appear to have formed from a common formation event approximately 1.3 Ga (Nyquist et al., 2001; Treiman, 2005; references therein). The ejection of the nakhlites from the martian surface appear to have occurred as a single impact episode based on consistent ejection ages inferred through cosmic ray exposure ages, within error, of approximately 11 Ma (Eugster et al., 1997; Marty et al., 2001; Okazaki et al., 2003). Mineralogical evidence suggests that the shock pressures experienced by the nakhlites during the impact events were notably less severe than those experienced by the shergottites with shock pressure estimates of 15-25 GPa (e.g., Stöffler, 2000).

## 5.2 MOTIVATION AND OBJECTIVES

In recent years, there have been several SNC meteorites recovered that have unique characteristics, based on initial investigations, that indicate they may provide exciting new insight into the petrogenetic processes occurring on Mars.

The second part of this dissertation focuses on the geochemical investigation of three of these new SNC meteorites: the lherzolitic shergottites Roberts Massif (RBT) 04261 and 04262 and the nakhlite Northwest Africa (NWA) 5790.

Chapter 6 investigates the petrology and trace element geochemistry of two recently recovered lherzolitic shergottites from Antarctica, Roberts Massif 04261 and 04262. The initial classification of these two meteorites provided conflicting results as to whether they were representative of enriched olivine-phyric shergottites or possibly a previously unobserved shergottite subgroup, an enriched lherzolitic shergottite based on bulk geochemical measurements and petrographic observations (e.g., Mikouchi et al., 2008). The occurrence of an enriched lherzolitic shergottite has implications for our understanding of the petrogenetic processes on Mars by revising our understanding of the processes leading to the formation of the enriched shergottites. Chapter 6 works to address the questions as to the geochemical relationship of RBT 04261 and 04262 to the lherzolitic shergottites, as well as the enriched basaltic shergottite group through a study of their petrographic, major element, and trace element characteristics. The work of Chapter 6 represents a collaborative research effort between myself, M. Wadhwa (ASU), T. Usui (University of Tennessee-Knoxville), and H. Y. McSween Jr. (UTK). I was responsible for acquisition of the trace element measurements and T. Usui was responsible for major element chemistry determination and initial petrographic characterization. All four collaborators jointly participated in the interpretation of the results with primary responsibility

for the interpretation of the trace element results mine and major element results the responsibility of T. Usui.

Chapter 7 focuses on examining the petrography and geochemistry of the most recently recovered nakhlite, NWA 5790. With only 8 distinct nakhlites recovered and identified, developing an understanding of the petrogenetic processes leading to the formation of this unique SNC subgroup has been hindered. Initial characterization of NWA 5790 (e.g., Jambon et al., 2010) suggested distinctive crystallization conditions for the sample within the nakhlite cumulate pile. The unique characteristics of NWA 5790 indicate that an understanding of its petrogenetic history may provide new information about the formation conditions at a different depth of the nakhlite cumulate pile not previously sampled. To investigate the petrogenetic history of NWA 5790 and its implications for the general petrogenesis of the nakhlites, Chapter 7 examines the major and trace element geochemistry of individual phases within NWA 5790. The work of Chapter 7 represents a collaborative research effort between myself, M. Wahdwa (ASU), J. B. Balta (UTK), and H. Y. McSween Jr. (UTK). J. B. Balta acquired the major element chemistry and petrographic observations used in the discussion in Chapter 7 at UTK while I was responsible for the acquisition of the trace element data and interpretation of the results.

# CHAPTER 6

# PETROLOGY AND TRACE ELEMENT GEOCHEMISTRY OF ROBERTS MASSIF 04261 AND 04262 METEORITES: THE FIRST EXAMPLES OF GEOCHEMICALLY ENRICHED LHERZOLITIC SHERGOTTITES

## 6.1 INTRODUCTION

Shergottites have provided information about differentiation processes in the Martian mantle and crust as well as the nature of Martian magmatism. They are petrographically classified into three sub-groups: basaltic, olivine-phyric and lherzolitic shergottites (Goodrich, 2002). Basaltic and olivine-phyric shergottites are interpreted to have originated as surficial flows, whereas lherzolitic shergottites represent plutonic cumulates (McSween, 2006). The parental magmas for the three shergottite groups sampled two distinct geochemical reservoirs, producing correlations in their magmatic oxidation states, oxygen and radiogenic isotope compositions, and trace element abundances. These correlations have been interpreted as indicating the presence of a reduced, low-$\delta^{18}O$, less radiogenic, incompatible element-depleted reservoir and an oxidized, high-$\delta^{18}O$, more radiogenic, incompatible element-rich reservoir on Mars (e.g., Borg et al., 1997; Herd et al., 2002). The former is clearly a mantle source, but the identity of the latter as a distinct mantle source or assimilated crust is controversial (e.g., Wadhwa, 2001; Borg et al. 2002; Herd et al., 2002; Borg and Draper, 2003; Treiman, 2003; Symes et al. 2008; Sarbadhlikari et al. 2009). Both basaltic and olivine-phyric shergottites individually exhibit two distinct

geochemical signatures that represent the geochemically enriched and depleted reservoirs, respectively (e.g. Symes et al. 2008). In contrast, lherzolitic shergottites show an intermediate signature that is interpreted to result from the mixing of the two geochemical end-member reservoirs (Borg 2002; Barrat et al. 2002).

Roberts Massif (RBT) 04261 and RBT 04262 (likely paired) were collected by the 2004-2005 ANSMET (Antarctic Search for Meteorites) expedition. They were initially classified as olivine-phyric shergottites (Satterwhite and Righter, 2007), but subsequently, Anand et al. (2008) suggested that RBT 04262 be classified as an enriched basaltic shergottite based on its geochemical characteristics. However, Mikouchi et al. (2008) argued that RBT 04262 is petrographically similar to the lherzolitic shergottites. No petrographic or geochemical data for RBT 04261 have been reported except for a trace element study of olivine (Shearer et al., 2008).

In this study, we present petrographic and geochemical investigations of RBT 04261 and RBT 04262, based on optical microscope, electron microprobe and ion microprobe analyses. The goals of these investigations are to (1) evaluate the pairing relationship between these meteorites, (2) determine their magmatic history, and (3) estimate their parent melt composition(s). Our results demonstrate that RBT 04621 and RBT 04262 are the first examples of geochemically enriched lherzolitic shergottites. We propose that by combining petrographic and geochemical observations for shergottites with their chronological datasets (crystallization and Mars ejection ages), new constraints

may be obtained regarding the spatial distribution of the geochemical reservoirs sampled by shergottites.

## 6.2 ANALYTICAL METHODS

Polished thin sections of RBT 04261 (‘21) and RBT 04262 (‘23) were examined to study their petrographic characteristics by optical microscope and electron probe microanalyzers (EPMA, Cameca SX-50 & SX-100) at the University of Tennessee. Modal proportions of minerals were determined by phase distribution analysis (PDA) using energy dispersive spectrometry (Oxford EXL-II) equipped on the EPMA. Mineral and glass compositions were determined using wavelength dispersive spectrometry (WDS), with an accelerating potential of 15 kV, a 20 nA beam current (10 nA for glasses), 1 μm beam diameter (5 μm for glasses), and standard ZAF (PAP) correction procedures for all silicate minerals. Peak and background counting times were 20-30 s, and data quality was verified by analyzing a combination of synthetic oxide and natural mineral standards. Drift was within counting error throughout every analytical session. Analytical errors (1σ) are due to counting statistics. Detection limits (3σ background) are typically <0.03 wt.% for $SiO_2$, $TiO_2$, $Al_2O_3$, MgO, CaO, $Na_2O$, $K_2O$ and $P_2O_5$, and <0.05-0.1 wt.% for FeO, MnO, $Cr_2O_3$, NiO and $V_2O_5$.

Concentrations of rare earth elements (REE) and additional selected trace elements were measured *in situ* using a Cameca IMS-6f ion microprobe at the Arizona State University, utilizing the energy filtering technique previously

described by Zinner and Crozaz (1986). Analyses were performed using an $O^-$ primary beam with currents in the range of 3-7 nA with an accelerating voltage of -12.5 KeV. Secondary ions were accelerated using a +10 KeV accelerating voltage with a -75 eV offset to avoid interferences from molecular ions. Secondary ions were collected using an electron multiplier in peak jumping mode. Depending on the mineral phase being analyzed, analysis times for the measurements varied from ~1 hour to ~3.5 hours. The REE and other trace element concentrations were determined by comparison of the desired element to a reference element (silicon for silicates and calcium for phosphates) and the use of previously determined sensitivity factors (Zinner and Crozaz, 1986; Hsu, 1995). Appropriate standards (i.e., NIST-610, NIST-612, NIST-614, and Durango apatite) were measured at the beginning and periodically throughout the analytical sessions. While energy filtering reduces the interferences due to molecular ions, the presence of isobaric interferences by monoxides can still occur, particularly the interferences of light rare earth element (LREE) oxides on the heavy rare earth element (HREE) masses (Zinner and Crozaz, 1986). Using previously determined monoxide to element ratios at our particular energy filtering conditions and the ion signals of the LREE measured on the ion microprobe during the analytical sessions, deconvolution of the LREE-oxide interferences on the HREE masses was completed using procedures similar to those described previously (Zinner and Crozaz, 1986; Hinton, 1990).

## 6.3 RESULTS

### 6.3.1 Petrography and Major Element Compositions

Both RBT 04261 and RBT 04262 exhibit regions with two distinct textures: poikilitic and non-poikilitic. Studied polished thin sections (PTS) of RBT 04261 and RBT 04262 contain pyroxene oikocrysts enclosing olivine, and chromite chadacrysts, producing the poikilitic textures (Figs. 6.1 and 6.2). The pyroxene oikocrysts are distinctly larger than any minerals in the non-poikilitic areas. The poikilitic textures in both meteorites only occur within individual separated grains of the oikocrystic pyroxene megacrysts, whereas the non-poikilitic textures occur only in the matrix. Olivine chadacrysts are anhedral and rounded (Figs. 6.2 and 6.3). Some olivine chadacrysts contain inclusions of pyroxenes, spinels and glasses (Fig. 6.3e, f). Glass and plagioclase (transformed into maskelynite by shock) inclusions also occur rarely in the pyroxene oikocrysts. These maskelynite inclusions occur only in the rims and near cracks in the pyroxene oikocrysts.

In the non-poikilitic areas, olivine, pyroxene and maskelynite occur interstitially to each other, and minor amounts of merrillite, chromite and ilmenite are present (Figs. 6.2 and 6.3). Olivine in the non-poikilitic areas has subhedral and angular outlines, in contrast to rounded olivine chadacrysts. Merrillite and ilmenite occur only in the non-poikilitic area (Fig. 6.3b). Glass inclusions containing daughter crystals of pyroxene (Fig. 6.3d) are abundant in olivine grains but rarely occur in pyroxenes and maskelynites. The combined poikilitic and non-poikilitic lithologies observed in RBT 04261 and RBT 04262 are typical for

lherzolitic shergottites (Harvey et al., 1993; Treiman et al., 1994; Lin et al., 2005; Mikouchi, 2005).

The modal (volume) proportions of minerals in the thin sections of RBT 04261 and RBT 04262 determined here (Table 6.1) are slightly different from those of another section of RBT 04262 (Mikouchi et al., 2008). The discrepancy is probably due to heterogeneous distribution of large pyroxene oikocrysts. The modal proportions of poikilitic areas in our sections of RBT 04261 and RBT 04262 are also given in Table 6.1.

*6.3.1.1 Olivine*

Olivine in the poikilitic areas has distinctly higher forsterite content ($Fo_{60-70}$) than that in the non-poikilitic areas (hereafter non-poikilitic olivine, $Fo_{57-62}$) (Fig. 6.4 and Table 6.2). Moreover, olivine chadacrysts have more variable Fo contents than do non-poikilitic olivines. The Fo variation of the olivine chadacrysts is not due to the core-to-rim zoning of single olivine grains but corresponds to chemical variations among different homogeneous grains; higher-Fo olivine chadacrysts are located closer to the cores of pyroxene oikocrysts. No systematic trends in minor elements (e.g., Ca, Cr and Ni) are observed between the chadacrystic and non-poikilitic olivines, although some olivine chadacrysts ($Fo_{>67}$) have higher $Cr_2O_3$ contents than others (Fig. 6.4).

Olivines in RBT 04261 and RBT 04262 have almost identical major and minor element compositions. The olivine Fo contents in these meteorites (60-70 and 57-62 for chadacrystic and non-poikilitic olivines, respectively) are the lowest

among those in the lherzolitic shergottites (Fig. 6.5). A similar result was reported for another section of RBT 04262 by Mikouchi et al. (2008).

Table 6.1
Modal compositions of RBT 04261 and RBT 04262

| | RBT 04261 | RBT 04262 |
|---|---|---|
| vol. % | | |
| Olivine | 42.1 | 39.4 |
| Low-Ca pyroxene | 21.5 | 28.0 |
| High-Ca pyroxene | 10.7 | 12.4 |
| Maskelynite | 20.2 | 15.9 |
| Glass | 1.6 | 1.1 |
| Spinel | 1.6 | 1.5 |
| Ilmenite | 0.2 | 0.2 |
| Merrillite | 1.8 | 1.1 |
| Sulfide | 0.3 | 0.3 |
| | | |
| vol. % | | |
| Poikilitic area | 11.8 | 21.0 |
| Non-poikilitic area | 88.2 | 79.0 |

Table 6.2

Representative microprobe analyses of olivines in RBT 04261 and RBT 04262

| | RBT 04261 | | | | RBT 04262 | | | |
|---|---|---|---|---|---|---|---|---|
| | chadacryst in pigeonite (core) | chadacryst in pigeonite (rim) | chadacryst in augite | non-poikilitic | chadacryst in pigeonite (core) | chadacryst in pigeonite (rim) | chadacryst in augite | non-poikilitic |
| *Oxide wt%* | | | | | | | | |
| $SiO_2$ | 37.0 | 36.4 | 36.5 | 35.8 | 38.0 | 37.2 | 36.9 | 35.6 |
| $Cr_2O_3$ | 0.22 | 0.03 | 0.06 | 0.01 | 0.04 | 0.03 | 0.00 | 0.02 |
| FeO[a] | 26.6 | 30.1 | 32.7 | 35.1 | 27.2 | 29.3 | 33.4 | 34.9 |
| MnO | 0.53 | 0.61 | 0.68 | 0.64 | 0.59 | 0.61 | 0.72 | 0.73 |
| MgO | 35.5 | 32.6 | 29.9 | 28.3 | 34.8 | 32.5 | 29.5 | 28.3 |
| CaO | 0.09 | 0.16 | 0.09 | 0.18 | 0.14 | 0.17 | 0.18 | 0.31 |
| NiO | 0.10 | 0.12 | 0.12 | 0.09 | 0.12 | 0.07 | 0.05 | 0.00 |
| Total | 100.1 | 100.0 | 100.0 | 100.0 | 100.9 | 99.9 | 100.7 | 99.8 |
| *Atoms per 4 oxygen* | | | | | | | | |
| Si | 0.986 | 0.989 | 1.001 | 0.995 | 1.003 | 1.004 | 1.008 | 0.992 |
| Cr | 0.005 | 0.001 | 0.001 | 0.000 | 0.001 | 0.001 | 0.000 | 0.001 |
| $Fe^{2+}$ | 0.593 | 0.683 | 0.752 | 0.816 | 0.601 | 0.662 | 0.763 | 0.814 |
| Mn | 0.012 | 0.014 | 0.016 | 0.015 | 0.013 | 0.014 | 0.017 | 0.017 |
| Mg | 1.410 | 1.318 | 1.223 | 1.172 | 1.372 | 1.308 | 1.199 | 1.175 |
| Ca | 0.003 | 0.005 | 0.003 | 0.005 | 0.004 | 0.005 | 0.005 | 0.009 |
| Ni | 0.002 | 0.003 | 0.003 | 0.002 | 0.003 | 0.001 | 0.001 | 0.000 |
| Total | 3.011 | 3.011 | 2.998 | 3.005 | 2.996 | 2.996 | 2.992 | 3.008 |
| *Molar compositions* | | | | | | | | |
| Fo | 69.8 | 65.2 | 61.3 | 58.3 | 68.9 | 65.7 | 60.4 | 58.3 |

[a] Total Fe as FeO. Fo, forsterite.

Table 6.3
Representative microprobe analyses of pyroxenes in RBT 04261 and RBT 04262

| | RBT 04261 | | | | | | RBT 04262 | | | | | |
|---|---|---|---|---|---|---|---|---|---|---|---|---|
| | oikocryst | | | | non-poikilitic | | oikocryst | | | | non-poikilitic | |
| | pigeonite (core) | pigeonite (mantle) | pigeonite (near | augite (rim) | pigeonite | augite | pigeonite (core) | pigeonite (mantle) | pigeonite (near crack) | augite (rim) | pigeonite | augite |
| Oxide wt% | | | | | | | | | | | | |
| $SiO_2$ | 54.8 | 53.3 | 52.5 | 51.7 | 52.4 | 52.2 | 55.4 | 53.6 | 54.1 | 51.9 | 53.1 | 52.4 |
| $TiO_2$ | 0.08 | 0.25 | 0.39 | 0.36 | 0.37 | 0.34 | 0.09 | 0.19 | 0.24 | 0.38 | 0.28 | 0.39 |
| $Al_2O_3$ | 0.42 | 1.28 | 0.51 | 1.76 | 0.77 | 1.66 | 0.51 | 1.03 | 0.86 | 2.11 | 0.86 | 1.93 |
| $Cr_2O_3$ | 0.35 | 0.39 | 0.20 | 0.76 | 0.31 | 0.83 | 0.45 | 0.35 | 0.26 | 0.87 | 0.33 | 0.89 |
| FeO[a] | 16.2 | 16.8 | 20.1 | 11.2 | 19.1 | 11.3 | 16.0 | 17.3 | 19.2 | 10.6 | 19.5 | 10.1 |
| MnO | 0.53 | 0.64 | 0.70 | 0.35 | 0.64 | 0.46 | 0.55 | 0.57 | 0.63 | 0.41 | 0.68 | 0.39 |
| MgO | 25.7 | 22.1 | 21.0 | 16.0 | 21.0 | 16.5 | 26.2 | 21.8 | 22.2 | 15.9 | 21.1 | 15.2 |
| CaO | 2.03 | 5.01 | 3.86 | 16.7 | 4.51 | 16.1 | 2.06 | 4.43 | 3.61 | 17.6 | 4.12 | 18.4 |
| $Na_2O$ | 0.03 | 0.09 | 0.07 | 0.19 | 0.06 | 0.22 | 0.03 | 0.09 | 0.06 | 0.20 | 0.06 | 0.22 |
| Total | 100.2 | 99.9 | 99.3 | 99.0 | 99.1 | 99.5 | 101.3 | 99.4 | 101.2 | 100.0 | 100.0 | 100.0 |
| Atoms per 6 oxygens | | | | | | | | | | | | |
| Si | 1.989 | 1.968 | 1.972 | 1.943 | 1.966 | 1.948 | 1.985 | 1.993 | 1.982 | 1.931 | 1.977 | 1.953 |
| Ti | 0.002 | 0.007 | 0.011 | 0.010 | 0.010 | 0.010 | 0.002 | 0.005 | 0.007 | 0.011 | 0.008 | 0.011 |
| Al(IV)[b] | 0.011 | 0.032 | 0.028 | 0.057 | 0.034 | 0.052 | 0.015 | 0.007 | 0.018 | 0.069 | 0.023 | 0.047 |
| Al(VI) | 0.007 | 0.024 | 0.000 | 0.021 | 0.001 | 0.021 | 0.007 | 0.038 | 0.019 | 0.023 | 0.015 | 0.038 |
| Cr | 0.010 | 0.011 | 0.006 | 0.023 | 0.009 | 0.024 | 0.013 | 0.010 | 0.008 | 0.026 | 0.010 | 0.026 |
| $Fe^{2+}$ | 0.492 | 0.519 | 0.631 | 0.352 | 0.599 | 0.352 | 0.481 | 0.537 | 0.590 | 0.330 | 0.607 | 0.316 |
| Mn | 0.016 | 0.020 | 0.022 | 0.011 | 0.020 | 0.015 | 0.017 | 0.018 | 0.020 | 0.013 | 0.022 | 0.012 |
| Mg | 1.392 | 1.215 | 1.175 | 0.897 | 1.175 | 0.920 | 1.400 | 1.208 | 1.211 | 0.884 | 1.170 | 0.846 |
| Ca | 0.079 | 0.198 | 0.155 | 0.671 | 0.181 | 0.642 | 0.079 | 0.177 | 0.142 | 0.699 | 0.164 | 0.735 |
| Na | 0.002 | 0.007 | 0.005 | 0.014 | 0.004 | 0.016 | 0.002 | 0.007 | 0.004 | 0.014 | 0.005 | 0.016 |
| Total | 4.000 | 4.000 | 4.005 | 4.000 | 4.000 | 4.000 | 4.000 | 4.000 | 4.000 | 4.000 | 4.000 | 4.000 |
| Molar compositions | | | | | | | | | | | | |
| Mg# | 73.9 | 70.1 | 65.1 | 72.2 | 66.5 | 72.4 | 74.4 | 69.2 | 67.2 | 73.6 | 65.8 | 72.8 |
| En | 71.3 | 63.9 | 60.8 | 48.3 | 61.4 | 49.4 | 72.0 | 63.1 | 62.9 | 48.3 | 61.0 | 45.7 |
| Wo | 3.5 | 8.8 | 6.6 | 33.1 | 7.7 | 31.7 | 3.3 | 8.8 | 6.4 | 34.4 | 7.4 | 37.2 |
| Fs | 25.2 | 27.3 | 32.6 | 18.6 | 30.9 | 18.8 | 24.7 | 28.1 | 30.6 | 17.3 | 31.6 | 17.1 |

[a] Total Fe as FeO. [b] Tetrahedrally coordinated aluminum, Al (IV), is obtained by assuming that Si and Al (IV) occupy the tetrahedral site.
En, enstatite; Wo, wollastonite; Fs ferrosilite

Table 6.4
Representative microprobe analyses of plagioclase and glass in RBT 04261 and RBT 04262

| | Plagioclase | | | | | Glass | | | |
|---|---|---|---|---|---|---|---|---|---|
| | RBT 04261 | | RBT 04262 | | | RBT 04261 | | RBT 04262 | |
| | An-rich | An-poor | An-rich | An-poor | Or-rich | Si-Al-rich | P-rich | Si-Al-rich | P-rich |
| Oxide wt% | | | | | | | | | |
| $SiO_2$ | 54.5 | 57.7 | 53.8 | 63.7 | 63.8 | 66.9 | 42.2 | 67.2 | 41.3 |
| $TiO_2$ | 0.12 | 0.13 | 0.08 | 0.11 | 0.11 | 0.40 | 2.77 | 0.38 | 0.55 |
| $Al_2O_3$ | 27.9 | 25.0 | 27.6 | 22.6 | 21.2 | 18.5 | 5.73 | 16.4 | 7.53 |
| $Cr_2O_3$ | 0.08 | 0.00 | 0.02 | 0.10 | 0.00 | 0.05 | 0.14 | 0.02 | 0.14 |
| FeO[a] | 0.49 | 0.38 | 0.42 | 0.60 | 0.34 | 0.84 | 15.9 | 0.92 | 12.2 |
| MnO | 0.06 | 0.00 | 0.00 | 0.00 | 0.02 | 0.00 | 0.49 | 0.03 | 0.37 |
| MgO | 0.10 | 0.05 | 0.11 | 0.04 | 0.00 | 0.06 | 12.92 | 0.11 | 11.56 |
| CaO | 11.2 | 7.49 | 11.5 | 4.54 | 3.10 | 0.67 | 8.03 | 1.36 | 12.8 |
| $Na_2O$ | 4.79 | 6.46 | 4.81 | 8.32 | 7.12 | 6.45 | 1.68 | 3.47 | 2.78 |
| $K_2O$ | 0.38 | 0.97 | 0.34 | 0.57 | 3.53 | 5.54 | 2.06 | 7.27 | 0.29 |
| $P_2O_5$ | 0.06 | 0.06 | 0.12 | 0.06 | 0.04 | 0.23 | 5.90 | 0.19 | 9.62 |
| Total | 99.7 | 98.2 | 98.8 | 100.6 | 99.3 | 99.6 | 97.7 | 97.4 | 99.2 |
| | | | | | | | | | |
| Atoms per 8 oxygens | | | | | | | | | |
| Si | 2.474 | 2.635 | 2.467 | 2.805 | 2.865 | | | | |
| Ti | 0.004 | 0.005 | 0.003 | 0.004 | 0.004 | | | | |
| Al | 1.493 | 1.344 | 1.490 | 1.174 | 1.123 | | | | |
| Cr | 0.003 | 0.000 | 0.001 | 0.003 | 0.000 | | | | |
| $Fe^{2+}$ | 0.019 | 0.015 | 0.016 | 0.022 | 0.013 | | | | |
| Mn | 0.002 | 0.000 | 0.000 | 0.000 | 0.001 | | | | |
| Mg | 0.007 | 0.003 | 0.007 | 0.002 | 0.000 | | | | |
| Ca | 0.544 | 0.366 | 0.566 | 0.214 | 0.149 | | | | |
| Na | 0.422 | 0.572 | 0.428 | 0.710 | 0.620 | | | | |
| K | 0.022 | 0.057 | 0.020 | 0.032 | 0.202 | | | | |
| P | 0.002 | 0.002 | 0.005 | 0.002 | 0.002 | | | | |
| Total | 4.992 | 4.999 | 5.002 | 4.970 | 4.978 | | | | |
| | | | | | | | | | |
| Molar compositions | | | | | | | | | |
| An | 55.1 | 36.8 | 55.9 | 22.4 | 15.3 | | | | |
| Ab | 42.7 | 57.5 | 42.2 | 74.2 | 63.8 | | | | |
| Or | 2.2 | 5.7 | 1.9 | 3.4 | 20.9 | | | | |

[a] Total Fe as FeO. An, anorthite; Ab, albite; Or, orthoclase.

Table 6.5
Representative microprobe analyses of spinel and ilmenite in RBT 04261 and RBT 04262

| | RBT 04261 | | | | RBT 04262 | | | | RBT 04261 | RBT 04262 |
|---|---|---|---|---|---|---|---|---|---|---|
| | contact with ol. chadacryst | inclusion of pig. oikocryst | non-poikilitic Chr-rich | non-poikilitic Ulv-rich | contact with ol. chadacryst | inclusion of pig. oikocryst | non-poikilitic Chr-rich | non-poikilitic Ulv-rich | ilmenite | ilmenite |
| *Oxide wt%* | | | | | | | | | | |
| $SiO_2$ | 0.23 | 0.13 | 0.12 | 0.05 | 0.14 | 0.27 | 0.05 | 0.08 | 0.05 | 0.06 |
| $TiO_2$ | 1.24 | 1.04 | 0.75 | 14.0 | 3.30 | 1.16 | 6.73 | 13.4 | 52.5 | 52.5 |
| $Al_2O_3$ | 10 | 6.80 | 5.58 | 5.23 | 16.1 | 7.23 | 6.43 | 6.06 | 0.04 | 0.06 |
| $Cr_2O_3$ | 49.8 | 54.8 | 55.7 | 22.8 | 38.4 | 54.2 | 40.0 | 23.2 | 0.5 | 0.6 |
| $Fe_2O_3$ [a] | 3.89 | 4.09 | 4.29 | 12.7 | 5.72 | 3.30 | 8.11 | 12.5 | - | - |
| FeO [a] | 27.8 | 25.9 | 28.8 | 41.6 | 29.3 | 26.7 | 34.9 | 41.0 | 42.3 | 42.6 |
| MnO | 0.46 | 0.45 | 0.51 | 0.60 | 0.52 | 0.53 | 0.59 | 0.56 | 0.76 | 0.82 |
| MgO | 4.03 | 4.91 | 2.84 | 2.37 | 5.04 | 4.45 | 2.60 | 2.50 | 3.29 | 3.53 |
| CaO | 0.01 | 0.04 | 0.00 | 0.01 | 0.06 | 0.02 | 0.00 | 0.01 | 0.01 | 0.01 |
| $V_2O_3$ [b] | 0.56 | 0.60 | 0.62 | 0.85 | 0.63 | 0.68 | 0.65 | 0.90 | 0.32 | 0.35 |
| Total | 98.2 | 98.7 | 99.2 | 100.3 | 99.2 | 98.6 | 100.0 | 100.1 | 99.8 | 100.5 |
| *Atoms per 4 oxygen (spinel)* | | | | | | | | | *Atoms per 3 oxygen (ilmenite)* | |
| Si | 0.008 | 0.005 | 0.004 | 0.002 | 0.005 | 0.010 | 0.002 | 0.003 | 0.001 | 0.001 |
| Ti | 0.033 | 0.027 | 0.020 | 0.378 | 0.083 | 0.031 | 0.180 | 0.360 | 0.979 | 0.972 |
| Al | 0.420 | 0.282 | 0.235 | 0.221 | 0.637 | 0.301 | 0.269 | 0.255 | 0.001 | 0.002 |
| Cr | 1.381 | 1.525 | 1.579 | 0.646 | 1.021 | 1.513 | 1.125 | 0.654 | 0.011 | 0.012 |
| $Fe^{3+}$ | 0.103 | 0.108 | 0.116 | 0.343 | 0.145 | 0.088 | 0.217 | 0.335 | - | - |
| $Fe^{2+}$ | 0.814 | 0.764 | 0.863 | 1.246 | 0.824 | 0.788 | 1.037 | 1.222 | 0.876 | 0.876 |
| Mn | 0.014 | 0.014 | 0.016 | 0.018 | 0.015 | 0.016 | 0.018 | 0.017 | 0.016 | 0.017 |
| Mg | 0.211 | 0.258 | 0.152 | 0.126 | 0.253 | 0.234 | 0.138 | 0.133 | 0.122 | 0.130 |
| Ca | 0.000 | 0.001 | 0.000 | 0.000 | 0.002 | 0.001 | 0.000 | 0.000 | 0.000 | 0.000 |
| $V^{3+}$ | 0.016 | 0.017 | 0.018 | 0.027 | 0.018 | 0.020 | 0.020 | 0.028 | 0.006 | 0.007 |
| Total | 3.000 | 3.002 | 3.002 | 3.006 | 3.003 | 3.000 | 3.005 | 3.005 | 2.012 | 2.017 |
| *Molar compositions* | | | | | | | | | | |
| Ulv | 3.3 | 2.8 | 2.1 | 38.5 | 8.5 | 3.1 | 18.3 | 36.7 | | |
| Chr | 70.1 | 77.4 | 80.1 | 32.9 | 51.8 | 77.1 | 57.1 | 33.3 | | |
| Spn | 21.4 | 14.3 | 12.0 | 11.2 | 32.4 | 15.3 | 13.7 | 13.0 | | |
| Mag | 5.2 | 5.5 | 5.9 | 17.5 | 7.3 | 4.5 | 11.0 | 17.1 | | |
| Mg# | 20.6 | 25.2 | 14.9 | 9.2 | 23.5 | 22.9 | 11.7 | 9.8 | | |
| Cr# | 76.7 | 84.4 | 87.0 | 74.5 | 61.6 | 83.4 | 80.7 | 72.0 | | |

[a] Calculate from stoichiometry (Carmichael, 1967). [b] Total V as $V_2O_3$.
Ulv, ulvöspinel; Chr, chromite; Spn, spinel; Mag; magnetite.

Table 6.6

Representative microprobe analyses of merrillites in RBT 04261 and RBT 04262

| | RBT 04261 | RBT 04262 |
|---|---|---|
| Oxide wt% | | |
| $SiO_2$ | 0.18 | 0.75 |
| $TiO_2$ | 0.02 | - |
| $Al_2O_3$ | 0.04 | - |
| $Cr_2O_3$ | - | - |
| FeO[a] | 1.17 | 1.21 |
| MnO | 0.05 | 0.03 |
| MgO | 3.18 | 3.37 |
| CaO | 46.6 | 47.1 |
| $Na_2O$ | 1.94 | 1.90 |
| $K_2O$ | 0.09 | 0.08 |
| $P_2O_5$ | 44.7 | 45.1 |
| Total | 98.8 | 99.6 |
| | | |
| Atoms per 56 oxygens | | |
| Si | 0.065 | 0.266 |
| Ti | 0.006 | - |
| Al | 0.016 | - |
| Cr | - | - |
| $Fe^{total}$ | 0.350 | 0.356 |
| Mn | 0.014 | 0.010 |
| Mg | 1.701 | 1.773 |
| Ca | 17.95 | 17.83 |
| Na | 1.35 | 1.30 |
| K | 0.04 | 0.03 |
| P | 14.05 | 13.93 |
| Total | 35.54 | 35.06 |
| | | |
| Mg# | 82.9 | 83.3 |

[a] Total Fe as FeO.

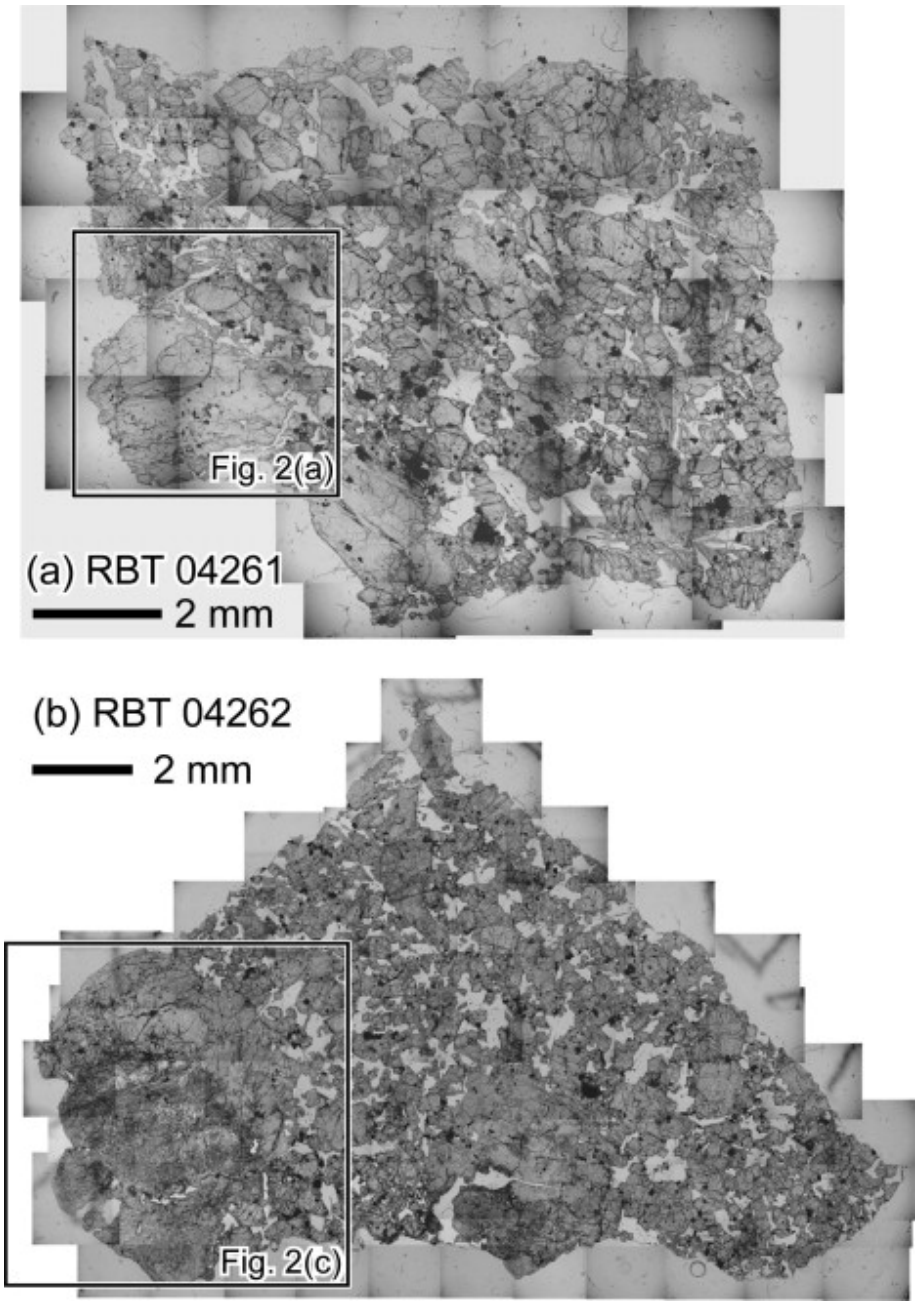


*Figure 6.1*- Photomicrographs (plane-polarized light) of (a) RBT 04261 and (b) RBT 04262 showing large pyroxene crystals (oikocrysts; see Fig. 6.2) and relatively fine-grained matrix. Transparent phases are maskelynites, and dark phases are spinel, ilmenites and sulfides. Boxes outline pyroxene megacrysts shown in more detail in Fig. 6.2.

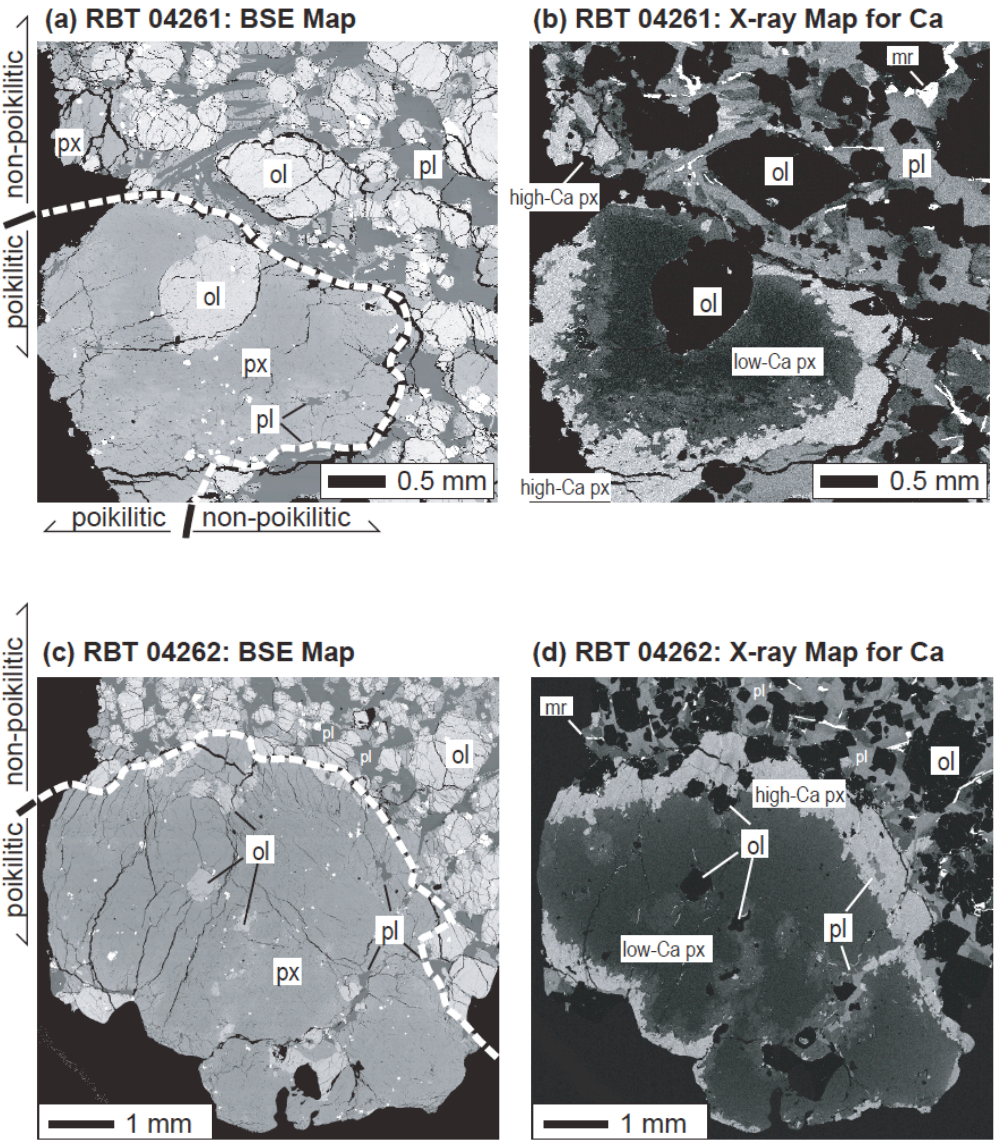


*Figure 6.2*- Electron microprobe maps of the pyroxene oikocrysts in RBT 04261 and RBT 04262 shown in Fig. 6.1. (a), (c): Back-scattered electron (BSE) images. (b), (d): X-ray maps for Ca. Brighter areas indicate higher Ca contents than darker areas. Pyroxene oikocrysts have Ca-rich (augite) rims. The pyroxene oikocrysts and the matrix show poikilitic and non-poikilitic textures, respectively. The boundaries between the two textures are delineated by white dotted lines. Abbreviations: ol = olivine; px = pyroxene; pl = plagioclase (maskelynite); mr = merrillite.

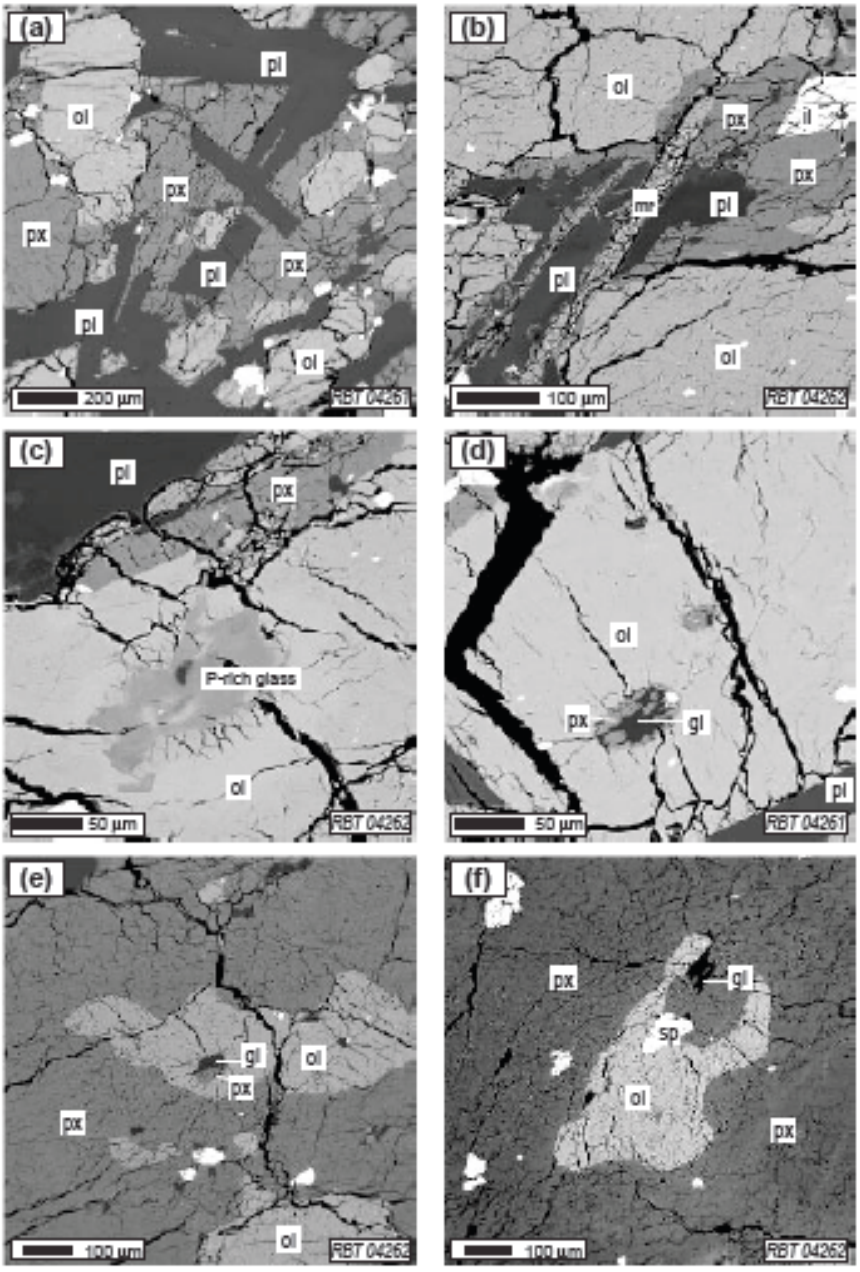


*Figure 6.3*- BSE images of non-poikilitic areas (a-d) and poikilitic areas (e-f) of RBT 04261 and RBT 04262. (a) Maskelynite retains the shapes of the original plagioclase grains. (b) Merrillite, ilmenite and Ab-rich plagioclase are closely associated with each other in a narrow interstitial space. (c) P-rich glass inclusion in olivine. (d) Magmatic inclusion in olivine. The glass inclusion is rich in Si and Al. (e, f) Anhedral olivines enclosed in pyroxene oikocrysts. Abbreviations: ol = olivine; px = pyroxene; pl = plagioclase (maskelynite); gl = glass; mr = merrillite; sp = spinel; il = ilmenite.

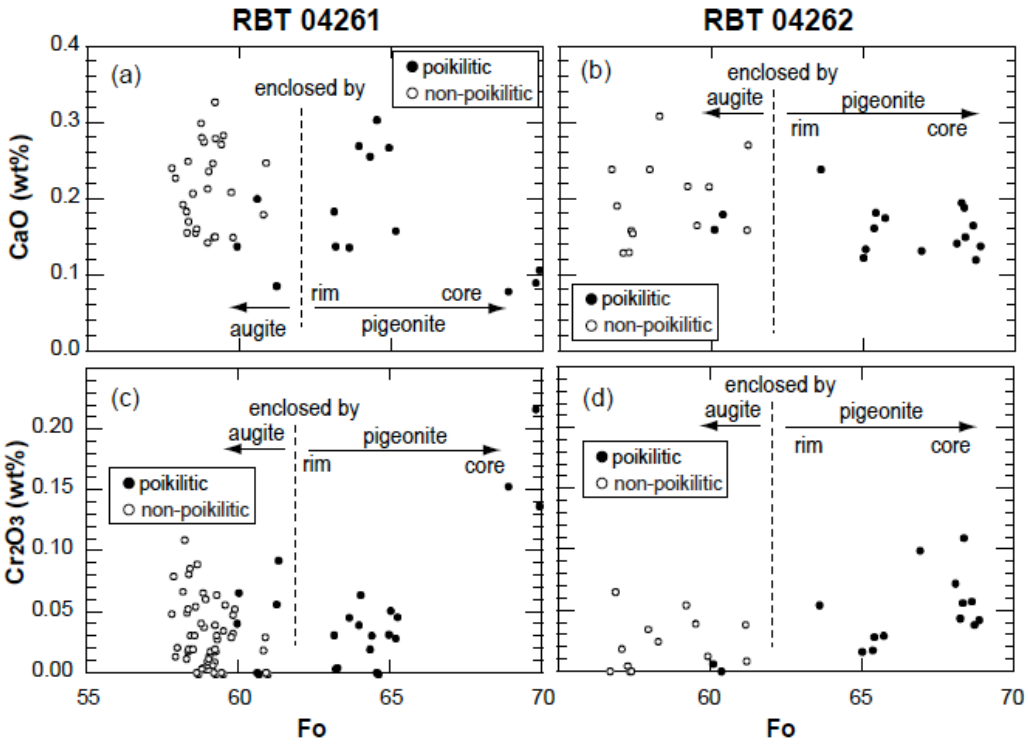


*Figure 6.4*- CaO or $Cr_2O_3$ versus Fo contents of olivines in (a, c) RBT 04261 and (b, d) RBT 04262. Olivines enclosed by cores of poikilitic pigeonites have Fo>67, while those enclosed by, or partially in contact with, the rims of poikilitic augites have Fo<67.

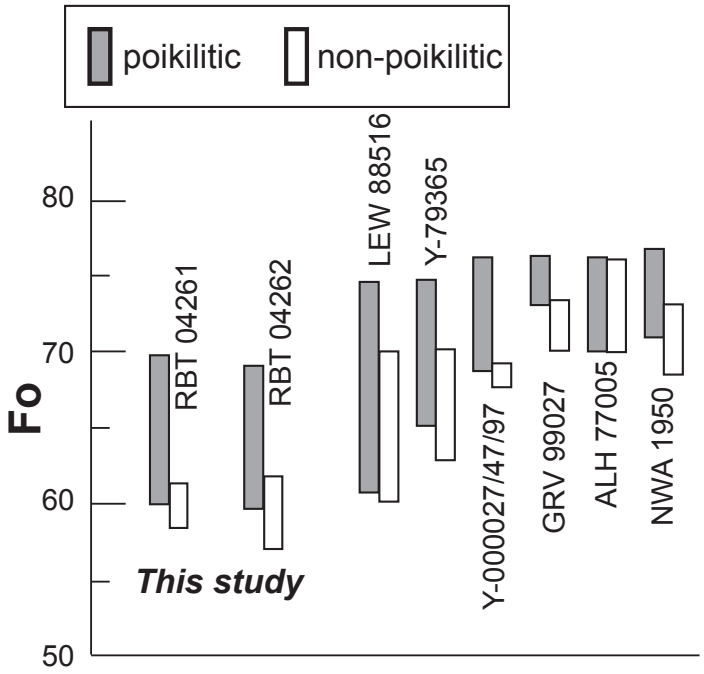


*Figure 6.5*- Comparison of Fo contents of olivines in RBT 04261 and RBT 04262 with those in the other lherzolitic shergottites. Olivine data for the other lherzolitic shergottites are from Mikouchi et al. (2008).

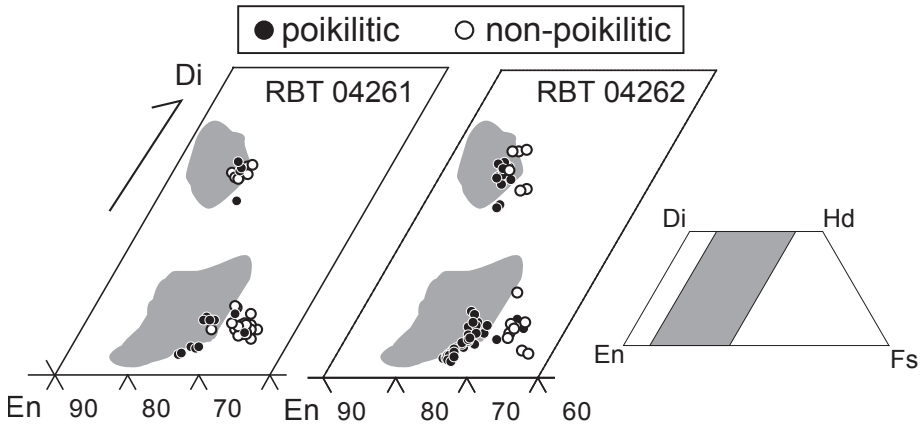


*Figure 6.6*- Compositions of pyroxenes in RBT 04261 and RBT 04262 plotted in the En-Wo-Fs system. Shaded areas show compositional fields of pyroxenes in the other lherzolitic shergottites (ALHA77005, LEW 88516, Y-793605 and NWA 1950) (Mikouchi, 2005).

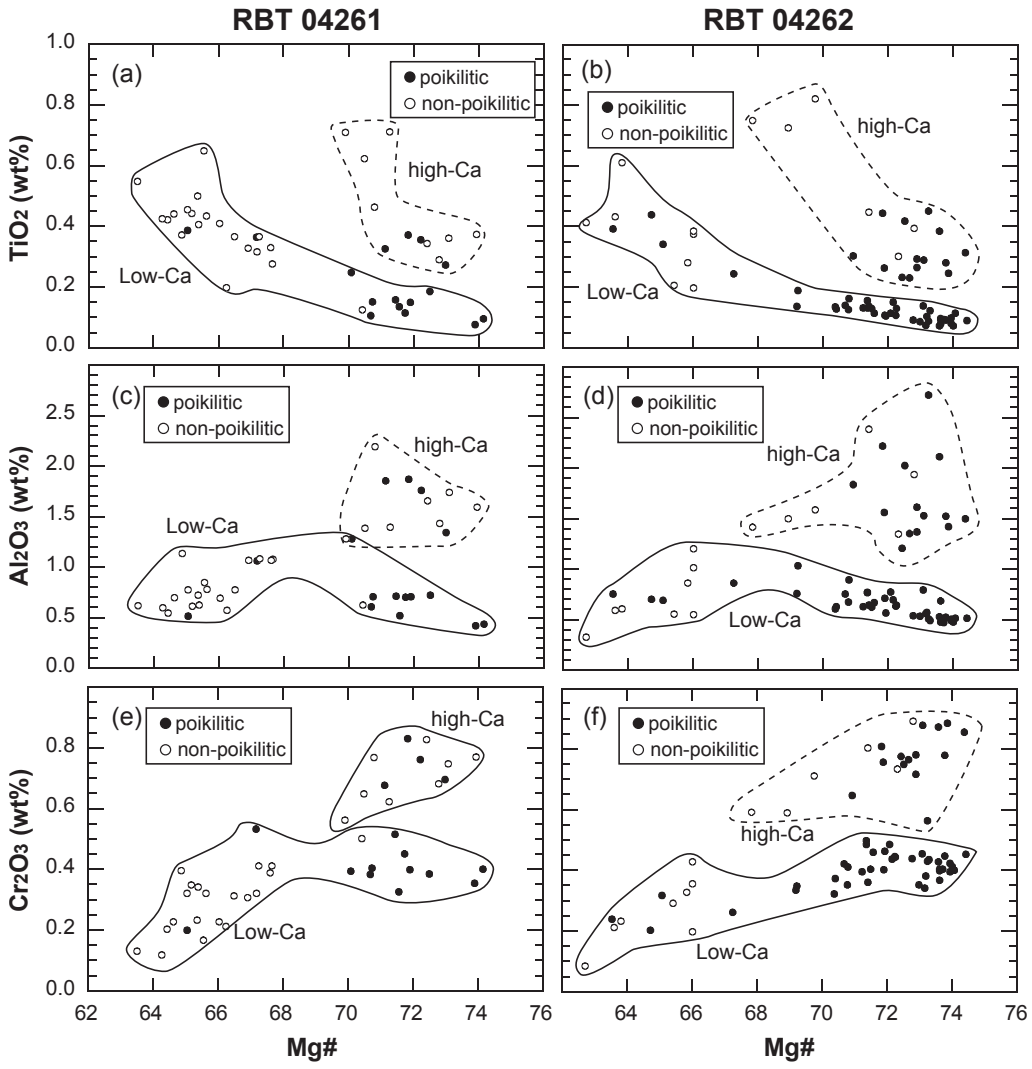


*Figure 6.7*- Variations of $TiO_2$, $Al_2O_3$ and $Cr_2O_3$ contents of pyroxenes in (a, c, e) RBT 04261 and (b, d, f) RBT 04262 as a function of Mg#.

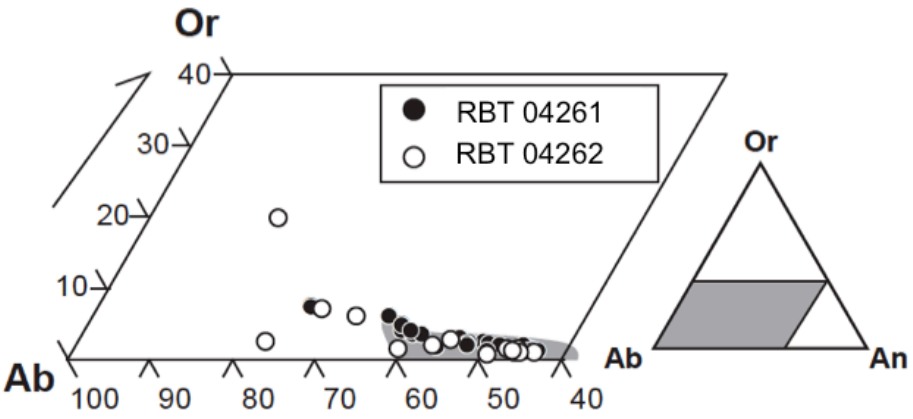


*Figure 6.8*- Maskelynite compositions in RBT 04261 and RBT 04262 in the Ab-Or-An system. Shaded areas show compositional fields of maskelynite in other lherzolitic shergottites (ALHA77005, LEW 88516, Y-793605 and NWA 1950) (Harvey et al., 1993; Mikouchi and Miyamoto, 1997; Mikouchi, 2005).

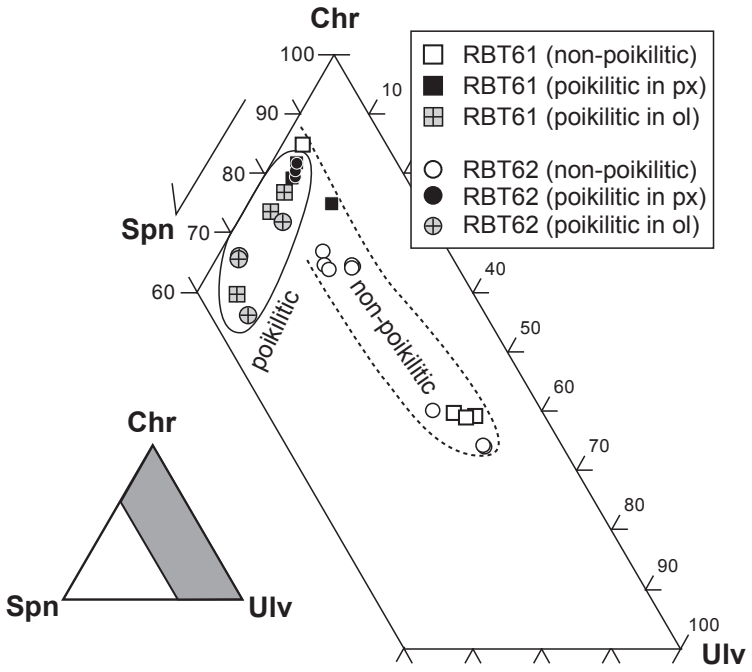


*Figure 6.9*- Compositions of spinel-group minerals in RBT 04261 and RBT 04262 in the Spn-Chr-Ulv system. Chromites in the poikilitic areas show the Chr-Spn substitution, whereas those in the non-poikilitic area show the Chr-Ulv substitution. These trends are typical for chromites in the other lherzolitic shergottites.

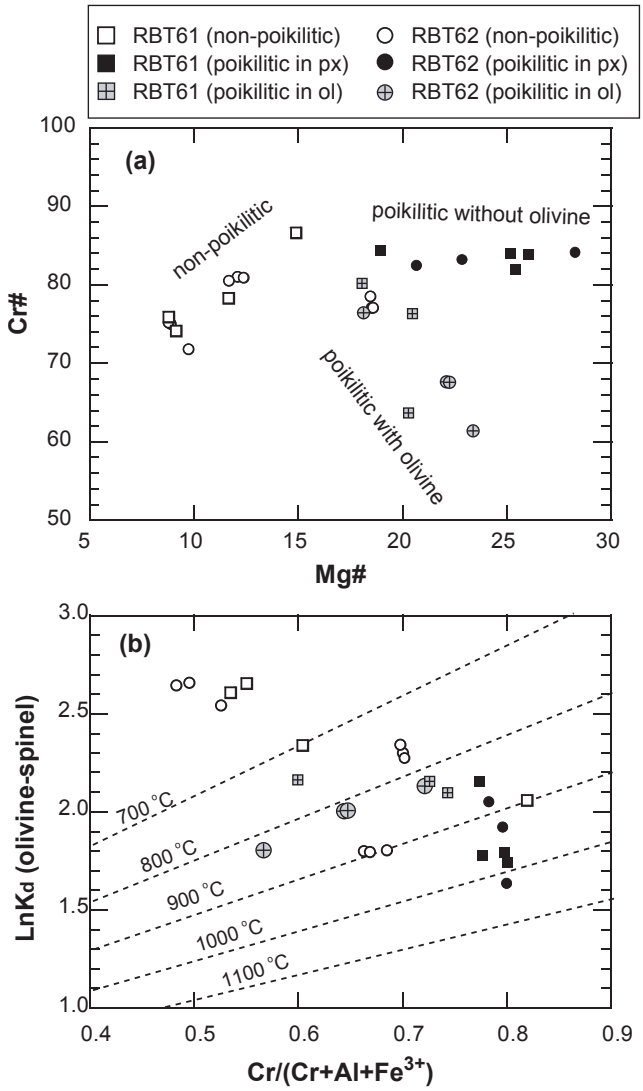


*Figure. 6.10*- (a) Cr# versus Mg# of spinels in RBT 04261 and RBT 04262. (b) The Fe-Mg exchange partition coefficients between olivine and spinel ($K_{Fe-Mg}^{ol\text{-}spinel}$) as a function of molar ratio of Cr/(Cr+Al+$Fe^{3+}$) in spinels. $K_{Fe-Mg}^{ol\text{-}spinel} = \left(X_{Mg}^{ol} / X_{Fe}^{ol}\right)\left(X_{Mg}^{sp} / X_{Fe}^{sp}\right)$, where $X_i^{\alpha}$ is the mole fraction of component *i* in phase $\alpha$. The $K_{Fe-Mg}^{ol\text{-}spinel}$ values for spinels within olivine chadacrysts (shaded circle/square with cross) are calculated based on the compositions of the adjacent spinels and olivine pairs. The $K_{Fe-Mg}^{ol\text{-}spinel}$ values for spinels completely enclosed by pyroxene oikocrysts (poikilitic without olivine, shown as filled circle/square) are calculated using a representative Fo content of olivine chadacryst ($Fo_{67}$), while those for spinels in the non-poikilitic area (open circle/square) are calculated using a representative Fo content of non-poikilitic olivine ($Fo_{57}$). Broken lines indicate isotherms based on the thermodynamic model for olivine-spinel geothermometry (Fabries, 1979).

*6.3.1.2 Pyroxene*

Pyroxene oikocrysts mainly consist of low-Ca pyroxene (>90% by volume) (Fig. 6.2). The low-Ca pyroxene is comprised of orthopyroxene and pigeonite with compositions approximately $En_{61-72}$ (enstatite), $Wo_{3-10}$ (wollastonite) and $Fs_{25-30}$ (ferrosilite). The low-Ca pyroxene oikocrysts are rimed by high-Ca pyroxene (augite with composition approximately $En_{45-50}Wo_{30-35}Fs_{17-20}$) (Fig. 6.6 and Table 6.3). There is a distinct compositional gap between the high- and low-Ca pyroxenes, exhibited as sharp and vermiculate boundaries in Ca X-ray maps (Fig. 6.2). In the non-poikilitic areas, low- and high-Ca pyroxenes are distributed randomly; they do not exhibit the core-to-rim relationship seen in the pyroxene oikocrysts. Low- and high-Ca pyroxenes in the non-poikilitic areas have pigeonite ($En_{56-62}Wo_{5-14}Fs_{32-35}$) and augite ($En_{44-50}Wo_{31-37}Fs_{17-22}$) compositions, respectively.

Figure 6.7 shows variations of minor elements (Ti, Al and Cr) in pyroxenes as a function of Mg# (molar ratio of Mg/[Mg + Fe] × 100). Low-Ca pyroxenes in the poikilitic areas have Mg# >70, consistently higher than those in the non-poikilitic areas (<68). The low-Ca pyroxenes in the poikilitic and non-poikilitic areas exhibit distinct chemical trends for these minor elements. With decreasing Mg#, $TiO_2$ and $Al_2O_3$ increase but $Cr_2O_3$ remains almost constant for the poikilitic low-Ca pyroxenes, whereas $TiO_2$ increases but $Al_2O_3$ and $Cr_2O_3$ decrease for the non-poikilitic low-Ca pyroxenes. Some poikilitic low-Ca pyroxenes have Mg# similar to the non-poikilitic ones; they occur near cracks in the oikocrysts where plagioclase is occasionally present (Fig. 6.2c). These

poikilitic low-Ca pyroxenes plot within the field of the non-poikilitic low-Ca pyroxenes (Fig. 6.7).

High-Ca pyroxenes in the non-poikilitic areas have slightly lower Mg# than those in the poikilitic areas, although their compositions almost overlap. The high-Ca pyroxenes are enriched in $TiO_2$, $Al_2O_3$ and $Cr_2O_3$ and show small variations in Mg# relative to the low-Ca pyroxenes. $TiO_2$ increases but $Cr_2O_3$ decreases with decreasing Mg# for the high-Ca pyroxenes; no systematic trend is observed for $Al_2O_3$.

Both low- and high-Ca pyroxenes have almost identical major and minor element compositions in RBT 04261 and RBT 04262. Both have distinctly lower En components than those in the other lherzolitic shergottites (Fig. 6.6). A similar result was reported for another section of RBT 04262 by Mikouchi et al. (2008).

*6.3.1.3 Maskelynite and Glass*

Plagioclase grains in RBT 04261 and RBT 04262 have been converted to maskelynite by shock. Most maskelynites retain the elongated lath forms of the original plagioclase crystals, although some irregular grains occur interstitially to cumulus grains (Fig. 6.3a, b). Maskelynite typically has a plagioclase composition in the range of $An_{22-56}Ab_{42-75}Or_{<10}$ (Fig. 6.8). However, maskelynite with the composition of K-rich alkali feldspar ($An_{15}Ab_{64}Or_{21}$) is also observed. Maskelynite in RBT 04261 and RBT 04262 is more enriched in the Ab component than that in the other lherzolitic shergottites (Fig. 6.8). The major and minor element compositions of maskelynite are listed in Table 6.4.

In addition to the feldspathic glass (maskelynite), two distinct magmatic glasses are present in the samples. One is a Si- and Al-rich glass (>65 wt% $SiO_2$ and ~18 wt% $Al_2O_3$) that commonly occurs as inclusions in olivine with daughter crystals (Fig. 6.3d). It is also enriched in $K_2O$ (>5 wt%) and $Na_2O$ (>3 wt%). The Si-Al-rich glass has compositions similar to alkali feldspar, but its stoichiometry is inconsistent with that of feldspar. The other is P-rich glass, which occurs as inclusions in olivine and in the matrix of the non-poikilitic area (Fig. 6.3c). The glass compositions are given in Table 6.4.

*6.3.1.4 Spinel Group*

Spinel occurs both in the poikilitic and non-poikilitic areas. Spinel grains are commonly rounded, but some in the non-poikilitic areas are euhedral. Spinels in poikilitic and non-poikilitic areas show distinct chemical trends. Chromite grains in the poikilitic areas vary from $Spn_{32}$ (spinel), $Chr_{52}$ (chromite), $Ulv_9$ (ulvöspinel), and $Mag_7$ (magnetite) to $Spn_{15}Chr_{77}Ulv_3Mag_5$, suggesting relatively linear chromite to spinel substitution (Fig. 6.9). The chromite chadacrysts are generally homogeneous; the compositional variation is related to their occurrence either within olivine chadacrysts or within pyroxene oikocrysts. Chromites within olivine chadacrysts have compositions more Spn-rich than those hosted by pyroxene oikocrysts. In contrast, spinel in the non-poikilitic areas vary from chromite ($Spn_{12}Chr_{80}Ulv_2Mag_6$) to chromian ulvöspinel ($Spn_{13}Chr_{33}Ulv_{37}Mag_{17}$), suggesting relatively linear chromite to ulvöspinel substitution. Some spinel grains are slightly zoned from Chr-rich cores to Ulv-rich rims. The Chr-Ulv

substitution strongly correlates with V contents. Ulvöspinel-rich spinels have ~0.9 wt% $V_2O_3$, whereas ulvöspinel-poor spinels have ~0.6 wt% $V_2O_3$ (Table 6.5). Such a signature for V contents was reported for spinels in shergottites (Herd et al. 2006) and terrestrial and lunar basalts (Papike et al. 2004). Moreover, the two distinct chemical trends (observed as the Chr-Spn and Chr-Ulv substitutions) are typical for spinels in the lherzolitic shergottites, although Mg# is lower for RBT 04261 and RBT 04262 spinels (~10-30) than for the other lherzolitic shergottites (e.g. ~15-35 for ALHA77005) (Ikeda, 1997; Goodrich et al. 2003; Lin et al., 2005).

Spinel exhibits three distinct features in a Cr# (molar ratio of Cr/[Cr + Al] × 100) versus Mg# diagram; the features are clearly correlated with their occurrences (Fig. 6.10). Spinels in the non-poikilitic area show positive correlation (decreasing Cr# with decreasing Mg#). The positive trend is a typical magmatic trend commonly seen in spinels in basalts (e.g., Barnes and Roeder, 2001); the composition of each spinel grain in the non-poikilitic area is interpreted to reflect that of its coexisting melt. In contrast, spinels associated with olivine chadacrysts show a negative trend in the Cr# vs Mg# diagram (Fig. 6.10). The negative trend is commonly seen in mafic plutonic rocks (e.g., Barnes and Roeder, 2001) and is interpreted to result from olivine-spinel Fe/Mg equilibration. Spinels completely hosted by pyroxene oikocrysts have almost constant Cr# with variable Mg#. These spinels probably did not reach Fe/Mg equilibration with olivine. The spinels associated with olivine chadacrysts plot along an ~830 °C isotherm, whereas the other two exhibit trends that cross isotherms (Fig. 6.10b).

Ilmenite occurs only in the non-poikilitic area. Some ilmenite grains abut Ulv-rich chromites, whereas others are not associated with chromites grains. The latter ilmenite commonly has a needle-like shape and is smaller (Fig. 6.3b).

Chemical compositions of spinel group minerals are listed in Table 6.5. Each spinel phase has almost identical major and minor element compositions in RBT 04261 and RBT 04262.

*6.3.1.5 Merrillite*

Merrillite occurs as an accessory mineral with a needle- or stick-like outline in the non-poikilitic areas (Fig. 6.3b). Merrillite has a relatively homogeneous major element composition and is characterized by high Na values of ~1.3 pfu. (per formula unit, O = 56, Table 6). Its Mg# (~83) is lower than those in the other lherzolitic shergottites but distinctly higher than those in the basaltic shergottites (Jolliff et al., 2006).

### 6.3.2 Rare Earth Element Compositions

REE abundances were measured *in situ* in individual grains of olivine chadacrysts, low- and high-Ca pyroxenes (both poikilitic and non-poikilitic), maskelynite and merrillite. Representative REE concentrations in minerals of RBT 04261 and RBT 04262 are given in Tables 6.7 and 6.8, respectively.

Table 6.7

Representative REE abundances from ion microprobe analyses (in ppm) in RBT 04261.

| | Poikilitic Lithology | | | | Non-Poikilitic Lithology | | | | | | |
|---|---|---|---|---|---|---|---|---|---|---|---|
| | Pigeonite (l) | Pigeonite (h) | Augite (l) | Augite (h) | Pigeonite (l) | Pigeonite (h) | Augite (l) | Augite (h) | Maskelynite | Merrillite | Olivine |
| La | 0.009 ± 0.001 | 0.018 ± 0.001 | 0.057 ± 0.007 | 0.088 ± 0.011 | 0.033 ± 0.003 | 0.051 ± 0.004 | 0.052 ± 0.003 | 0.145 ± 0.004 | 0.245 ± 0.012 | 152.5 ± 2.9 | n. d. |
| Ce | 0.022 ± 0.002 | 0.056 ± 0.004 | 0.224 ± 0.019 | 0.392 ± 0.031 | 0.135 ± 0.009 | 0.185 ± 0.011 | 0.279 ± 0.008 | 0.930 ± 0.015 | 0.365 ± 0.016 | 358.4 ± 4.8 | n. d. |
| Pr | 0.004 ± 0.001 | 0.013 ± 0.002 | 0.063 ± 0.008 | 0.153 ± 0.017 | 0.041 ± 0.005 | 0.050 ± 0.006 | 0.081 ± 0.004 | 0.236 ± 0.007 | 0.042 ± 0.005 | 53.8 ± 1.7 | n. d. |
| Nd | 0.031 ± 0.006 | 0.098 ± 0.014 | 0.518 ± 0.061 | 1.297 ± 0.143 | 0.376 ± 0.045 | 0.514 ± 0.057 | 0.808 ± 0.043 | 2.412 ± 0.072 | 0.190 ± 0.018 | 269.2 ±10.6 | n. d. |
| Sm | 0.012 ± 0.003 | 0.037 ± 0.007 | 0.310 ± 0.044 | 0.633 ± 0.084 | 0.132 ±0.015 | 0.177 ± 0.022 | 0.275 ± 0.021 | 0.877 ± 0.036 | 0.042 ± 0.534 | 109.2 ± 6.2 | n. d. |
| Eu | 0.003 ± 0.001 | 0.019 ± 0.002 | 0.090 ± 0.012 | 0.175 ± 0.022 | 0.061 ± 0.007 | 0.090 ± 0.010 | 0.116 ± 0.007 | 0.362 ± 0.012 | 0.534 ± 0.021 | 40.8 ± 1.9 | n. d. |
| Gd | 0.031 ± 0.004 | 0.112 ± 0.009 | 0.474 ± 0.039 | 0.833 ± 0.065 | 0.500 ± 0.030 | 0.610 ± 0.036 | 0.712 ± 0.023 | 2.107 ± 0.039 | 0.054 ± 0.006 | 163.1 ± 4.6 | 0.003 ± 0.002 |
| Tb | 0.007 ± 0.001 | 0.028 ± 0.002 | 0.103 ± 0.009 | 0.137 ± 0.012 | 0.129 ± 0.008 | 0.152 ± 0.010 | 0.156 ± 0.006 | 0.417 ± 0.009 | 0.012 ± 0.002 | 27.1 ± 1.2 | 0.001 ± 0.0005 |
| Dy | 0.077 ± 0.006 | 0.286 ± 0.015 | 0.617 ± 0.046 | 1.023 ± 0.071 | 1.036 ± 0.045 | 1.254 ± 0.054 | 1.253 ± 0.033 | 3.457 ± 0.053 | 0.024 ± 0.006 | 174.1 ± 5.8 | 0.025 ± 0.005 |
| Ho | 0.023 ± 0.002 | 0.080 ± 0.004 | 0.137 ± 0.012 | 0.246 ± 0.019 | 0.269 ± 0.013 | 0.350 ± 0.016 | 0.235 ± 0.008 | 0.642 ± 0.013 | 0.006 ± 0.002 | 35.4 ± 1.5 | 0.006 ± 0.001 |
| Er | 0.076 ± 0.006 | 0.275 ± 0.014 | 0.424 ± 0.038 | 0.690 ± 0.059 | 0.913 ± 0.041 | 1.097 ± 0.049 | 0.805 ± 0.025 | 1.886 ± 0.037 | 0.017 ± 0.004 | 89.1 ± 3.9 | 0.046 ± 0.007 |
| Tm | 0.014 ± 0.001 | 0.050 ± 0.003 | 0.062 ± 0.007 | 0.113 ± 0.011 | 0.142 ± 0.009 | 0.152 ± 0.011 | 0.103 ± 0.005 | 0.260 ± 0.008 | n. d. | 14.2 ± 0.9 | 0.006 ± 0.001 |
| Yb | 0.098 ± 0.007 | 0.349 ± 0.017 | 0.375 ± 0.033 | 0.599 ± 0.050 | 1.086 ± 0.049 | 1.307 ± 0.058 | 0.774 ± 0.026 | 1.682 ± 0.036 | n. d. | 80.9 ± 3.8 | 0.099 ± 0.011 |
| Lu | 0.016 ± 0.002 | 0.054 ± 0.004 | 0.050 ± 0.007 | 0.101 ± 0.013 | 0.163 ± 0.011 | 0.197 ± 0.013 | 0.094 ± 0.005 | 0.259 ± 0.008 | n. d. | 10.2 ± 0.8 | 0.020 ± 0.003 |

n.d. = not detected. Errors are 1σ errors on counting statistics only. "l" and "h" refer to pyroxene analyses with the lowest and highest REE abundances in the poikilitic or the initerstitial lithology.

Table 6.8

Representative REE abundances from ion microprobe analyses (in ppm) in RBT 04262.

| | Poikilitic Lithology | | | | Non-Poikilitic Lithology | | | | | | |
|---|---|---|---|---|---|---|---|---|---|---|---|
| | Pigeonite (l) | Pigeonite (h) | Augite (l) | Augite (h) | Pigeonite (l) | Pigeonite (h) | Augite (l) | Augite (h) | Maskelynite | Merrillite | Olivine |
| La | 0.008 ± 0.001 | 0.026 ± 0.002 | 0.059 ± 0.003 | 0.091 ± 0.006 | 0.031 ± 0.003 | 0.047 ± 0.004 | 0.050 ± 0.003 | 0.134 ± 0.004 | 0.182 ± 0.009 | 149.7 ± 3.7 | n. d. |
| Ce | 0.028 ± 0.002 | 0.077 ± 0.005 | 0.204 ± 0.008 | 0.329 ± 0.015 | 0.123 ± 0.009 | 0.173 ± 0.011 | 0.243 ± 0.009 | 0.856 ± 0.015 | 0.290 ± 0.012 | 358.7 ± 6.1 | n. d. |
| Pr | 0.004 ± 0.001 | 0.015 ± 0.002 | 0.058 ± 0.004 | 0.114 ± 0.009 | 0.038 ± 0.005 | 0.048 ± 0.006 | 0.072 ± 0.004 | 0.220 ± 0.006 | 0.037 ± 0.004 | 51.6 ± 2.1 | n. d. |
| Nd | 0.022 ± 0.007 | 0.131 ± 0.019 | 0.502 ± 0.033 | 0.999 ± 0.088 | 0.339 ± 0.048 | 0.458 ± 0.049 | 0.752 ± 0.038 | 2.171 ± 0.072 | 0.193 ± 0.014 | 250.0 ± 13.1 | n. d. |
| Sm | 0.015 ± 0.005 | 0.079 ± 0.012 | 0.236 ± 0.018 | 0.521 ± 0.056 | 0.125 ± 0.020 | 0.166 ± 0.022 | 0.248 ± 0.020 | 0.781 ± 0.033 | 0.035 ± 0.009 | 96.0 ± 7.5 | n. d. |
| Eu | 0.004 ± 0.001 | 0.031 ± 0.004 | 0.076 ± 0.006 | 0.136 ± 0.013 | 0.056 ± 0.006 | 0.087 ± 0.009 | 0.107 ± 0.007 | 0.333 ± 0.010 | 0.456 ± 0.016 | 35.5 ± 2.3 | n. d. |
| Gd | 0.044 ± 0.006 | 0.221 ± 0.014 | 0.407 ± 0.017 | 0.764 ± 0.043 | 0.445 ± 0.038 | 0.593 ± 0.024 | 0.633 ± 0.022 | 1.981 ± 0.044 | 0.060 ± 0.007 | 168.3 ± 6.1 | 0.003 ± 0.001 |
| Tb | 0.010 ± 0.001 | 0.055 ± 0.004 | 0.081 ± 0.004 | 0.119 ± 0.008 | 0.119 ± 0.009 | 0.141 ± 0.011 | 0.145 ± 0.005 | 0.384 ± 0.009 | 0.003 ± 0.001 | 25.9 ± 1.5 | 0.001 ± 0.0002 |
| Dy | 0.094 ± 0.008 | 0.502 ± 0.023 | 0.584 ± 0.022 | 1.119 ± 0.056 | 0.942 ± 0.059 | 1.080 ± 0.057 | 1.140 ± 0.027 | 3.215 ± 0.042 | 0.032 ± 0.006 | 174.7 ± 7.4 | 0.026 ± 0.005 |
| Ho | 0.020 ± 0.002 | 0.129 ± 0.006 | 0.119 ± 0.005 | 0.228 ± 0.014 | 0.242 ± 0.017 | 0.326 ± 0.013 | 0.209 ± 0.008 | 0.578 ±0.009 | 0.004 ± 0.001 | 32.7 ± 1.8 | 0.011 ± 0.002 |
| Er | 0.088 ± 0.008 | 0.361 ± 0.019 | 0.371 ± 0.018 | 0.633 ± 0.038 | 0.859 ± 0.059 | 0.983 ± 0.038 | 0.700 ± 0.019 | 1.679 ± 0.030 | 0.018 ± 0.004 | 91.8 ± 5.1 | 0.048 ± 0.009 |
| Tm | 0.013 ± 0.002 | 0.052 ± 0.004 | 0.053 ± 0.004 | 0.080 ± 0.007 | 0.125 ± 0.009 | 0.190 ± 0.012 | 0.096 ± 0.005 | 0.273 ± 0.008 | n. d. | 12.0 ± 1.1 | 0.009 ± 0.002 |
| Yb | 0.107 ± 0.010 | 0.541 ± 0.025 | 0.358 ± 0.018 | 0.547 ± 0.034 | 0.944 ± 0.081 | 1.183 ± 0.063 | 0.712 ± 0.031 | 1.565 ± 0.028 | n. d. | 59.1 ± 4.0 | 0.119 ± 0.004 |
| Lu | 0.017 ± 0.002 | 0.076 ± 0.005 | 0.040 ± 0.003 | 0.095 ± 0.010 | 0.143 ± 0.011 | 0.193 ± 0.014 | 0.084 ± 0.004 | 0.234 ± 0.008 | n. d. | 7.6 ± 0.9 | 0.030 ± 0.005 |

n.d. = not detected. Errors are 1σ errors on counting statistics only. "l" and "h" refer to pyroxene analyses with the lowest and highest REE abundances in the poikilitic or the initerstitial lithology.

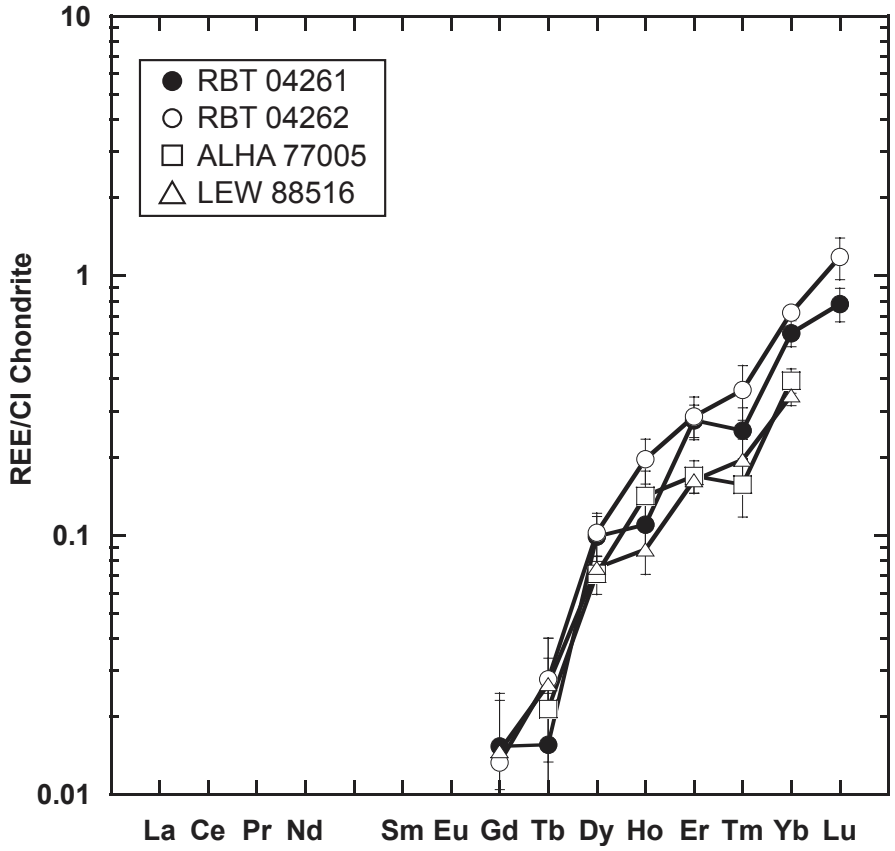


*Figure 6.11*- Chondrite-normalized REE abundances in olivine chadacrysts in RBT 04261 and RBT 04262. REE concentrations in olivine chadacryst in ALHA77005 and LEW 88516 (Harvey et al., 1993) are also shown for comparison. REE abundances are normalized to CI chondrites (Palme and Beer, 1993). Error bars indicate uncertainties (±1 $\sigma$ ) due to counting statistics only.

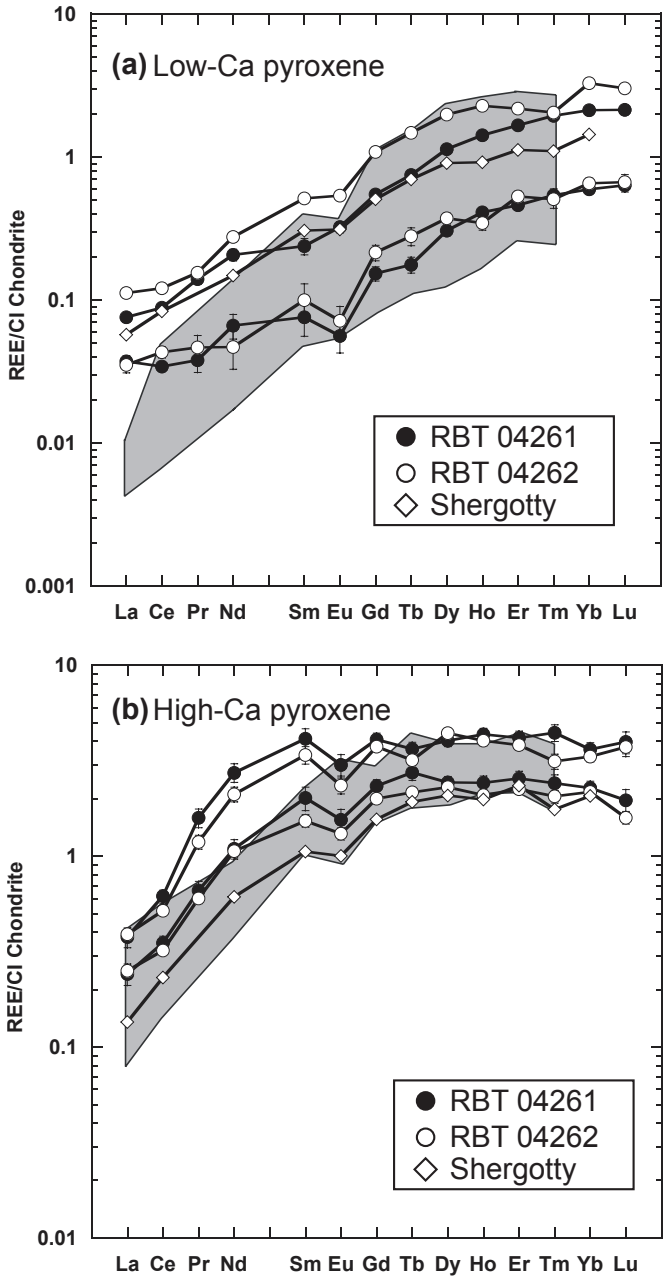


*Figure 6.12*- Chondrite-normalized REE abundances in (a) low-Ca and (b) high-Ca pyroxene oikocrysts in RBT 04261 and RBT 04262. Pyroxene oikocrysts with the highest and the lowest REE abundances are shown. Shaded areas indicate the range of REE concentrations in pyroxene oikocrysts of other lherzolitic shergottites (ALHA77005 and LEW 88516) (Harvey et al., 1993). Representative REE abundances in Shergotty low-Ca and high-Ca pyroxenes (Wadhwa et al., 1994) are also shown for comparison. REE abundances are normalized to CI chondrites (Palme and Beer, 1993). Error bars indicate uncertainties (±1 $\sigma$ ) due to counting statistics only.

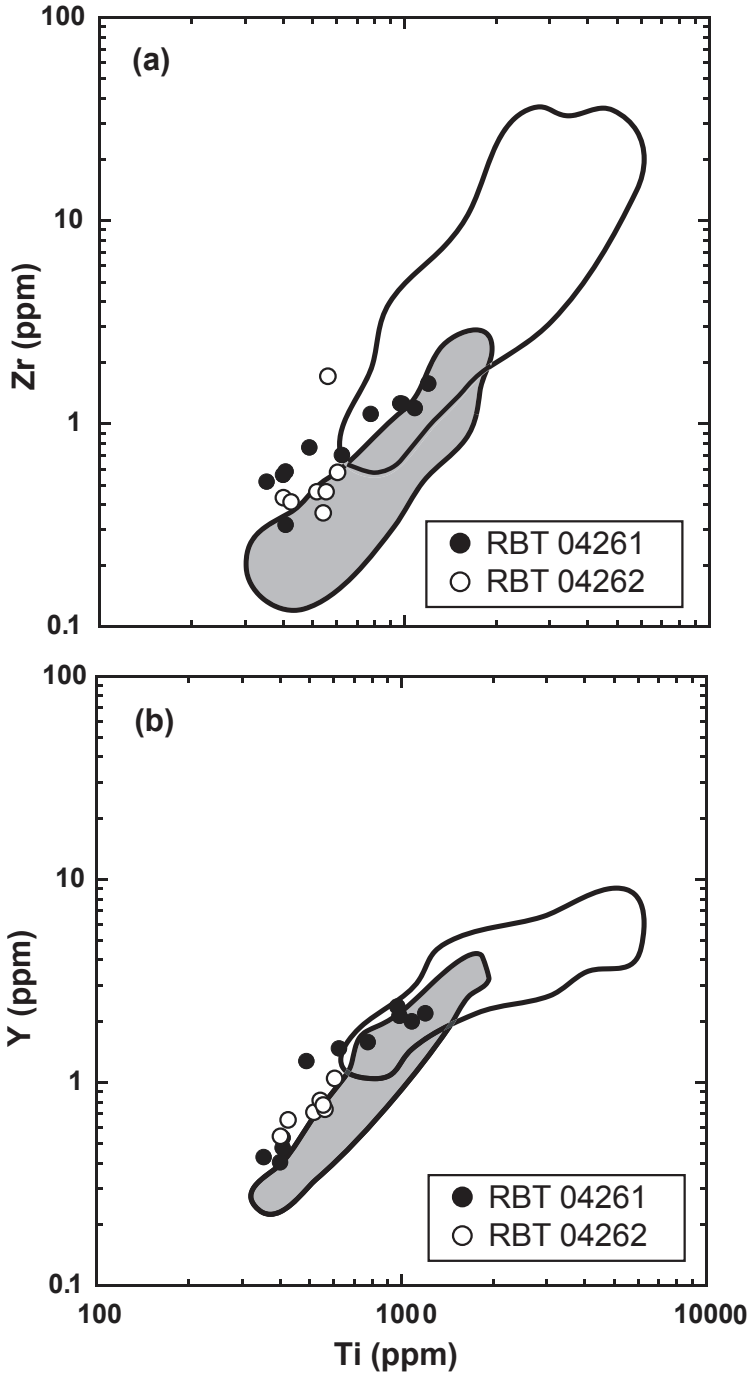


*Figure 6.13*- Abundances of Ti plotted versus (a) Zr and (b) Y concentrations in poikilitic low-Ca pyroxenes in RBT 04261 and RBT 04262. The outlined areas shaded in gray show the compositional ranges of poikilitic low-Ca pyroxenes in the lherzolitic shergottites (Harvey et al., 1993), while the white outlined areas show the compositional ranges of low-Ca pyroxenes in the basaltic shergottites (Wadhwa et al., 1994). Error bars (±1 $\sigma$ due to counting statistics) are typically smaller than the symbols.

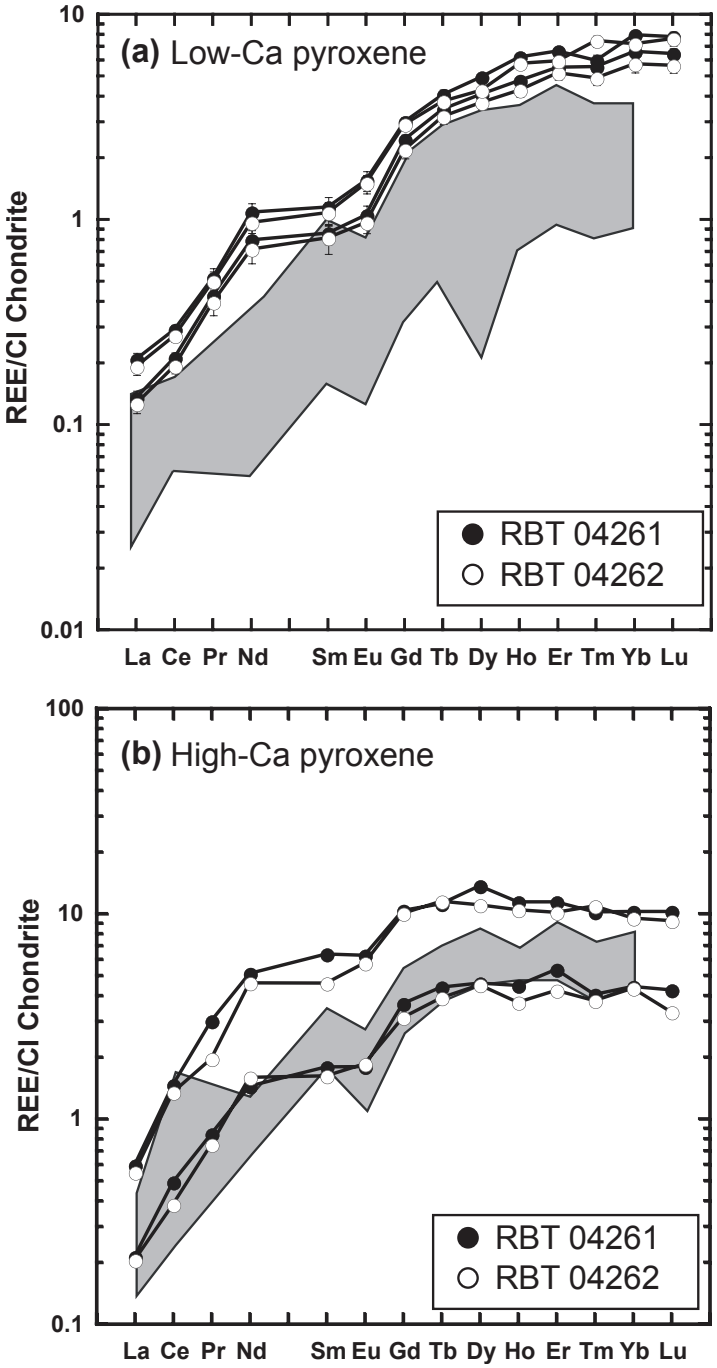


*Figure 6.14*- Chondrite-normalized REE abundances in (a) low-Ca and (b) high-Ca pyroxenes in the non-poikilitic areas of RBT 04261 and RBT 04262. Non-poikilitic pyroxenes with the highest and lowest REE concentrations are shown. Shaded areas indicate the range of REE abundances in non-poikilitic pyroxenes from other lherzolitic shergottites (ALHA77005 and LEW 88516) (Harvey et al., 1993). REE abundances are normalized to CI chondrites (Palme and Beer, 1993). Error bars indicate uncertainties (±1 $\sigma$ ) due to counting statistics only.

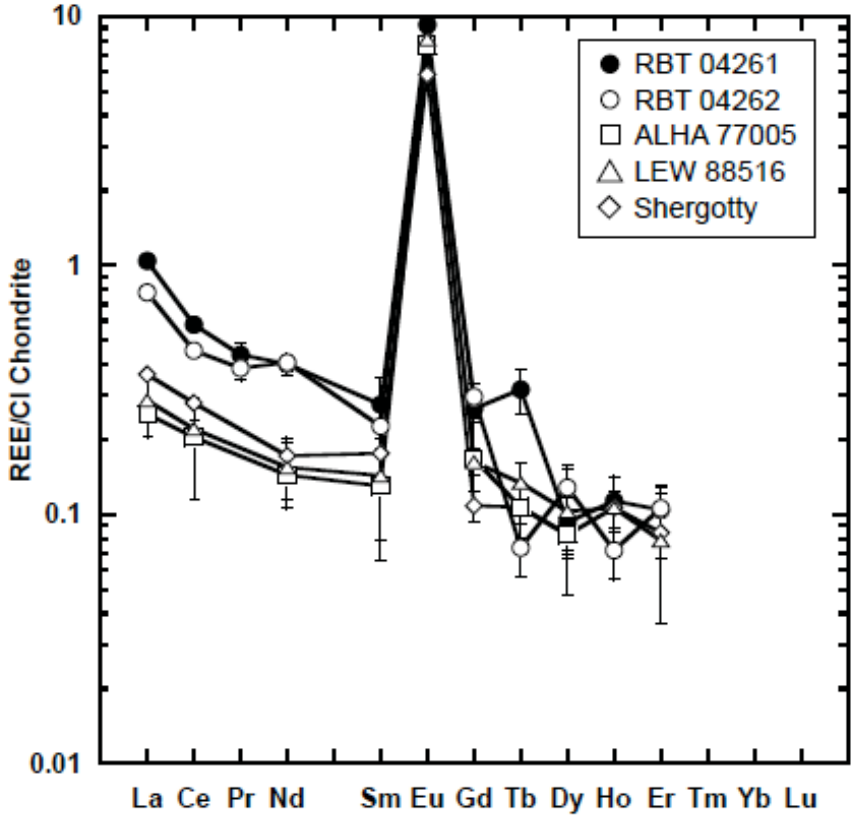


*Figure 6.15*- Chondrite-normalized REE concentrations in maskelynite of RBT 04261 and RBT 04262. The REE compositions of maskelynites in other lherzolitic shergottites (ALHA77005 and LEW 88516) (Harvey et al., 1993) and the basaltic shergottite Shergotty (Wadhwa et al., 1994) are also shown for comparison. REE abundances are normalized to CI chondrites (Palme and Beer, 1993). Error bars indicate uncertainties (±1 $\sigma$ ) due to counting statistics only.

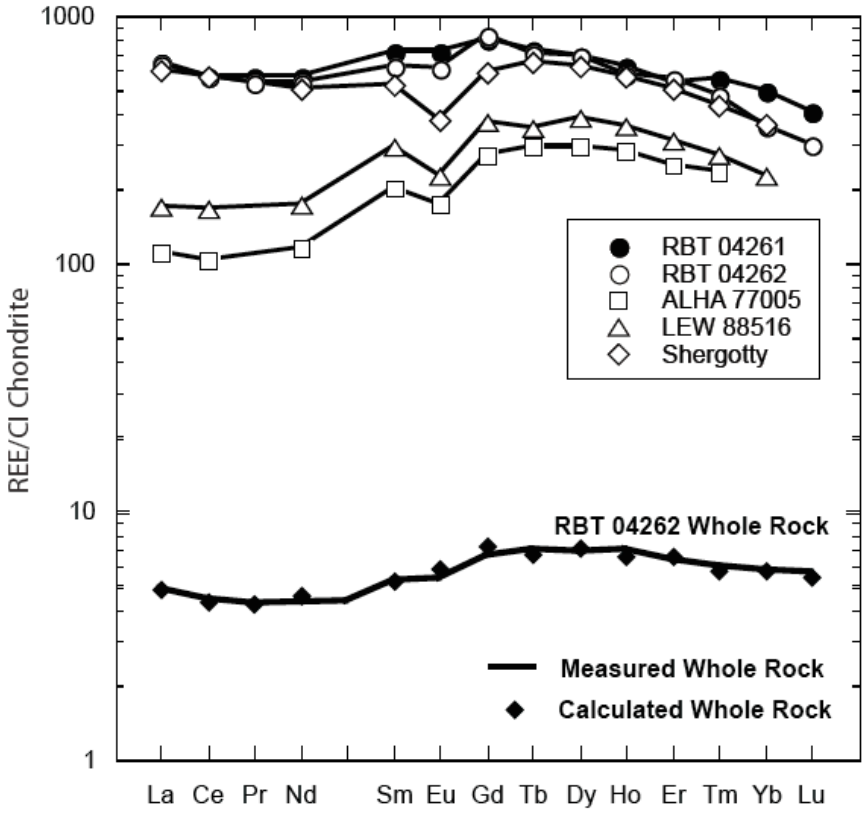


*Figure 6.16*- Chondrite normalized REE concentrations in merrillites of RBT 04261 and RBT 04262. REE compositions of merrillites in lherzolitic shergottites ALHA77005 and LEW 88516 (Harvey et al., 1993) and the basaltic shergottite Shergotty (Wadhwa et al., 1994) are shown for comparison. Also shown in this figure are the results of a mass balance calculation of REE abundances in the RBT 04262 whole-rock (filled black diamonds). Measured concentrations of the REE in the RBT 04262 whole-rock (Anand et al., 2008) are shown as the thick black line. REE abundances are normalized to CI chondrites (Palme and Beer, 1993).

*6.3.2.1 Olivine*

Olivine chadacrysts in RBT 04261 and RBT 04262 exhibit an overall depletion in REE abundances. Light rare earth elements in this mineral are present in such low concentrations that they were below the analytical detection limit of the ion microprobe. The C1-normalized REE abundances increase steeply from Gd (0.013-0.015 × CI) to Lu (0.78-1.18 × CI). Olivine chadacrysts in RBT 04261 and RBT 04262 exhibit, within error, almost identical REE abundances (Fig. 6.11). They are also indistinguishable from olivine chadacrysts in the lherzolitic shergottites ALHA77005 and LEW 88516.

*6.3.2.2 Pyroxenes*

Pyroxene oikocrysts in RBT 04261 and RBT 04262 have LREE-depleted patterns with negative Eu anomalies ($[Eu/Eu^*]_N$, where $Eu^*$ is the interpolated value between CI-normalized Sm and Gd abundances) in the range of 0.6-0.8 and 0.7-0.8 for low- and high-Ca pyroxenes, respectively (Fig. 6.12). The REE abundances in the low-Ca pyroxene oikocrysts are typically lower than those in the high-Ca pyroxene oikocrysts; the former shows a steeper LREE-depletion ($[La/Yb]_{CI} = 0.04$) than the latter ($[La/Yb]_{CI} = 0.11$). Both of the low- and high-Ca pyroxene oikocrysts in RBT 04261 and RBT 04262 are more enriched in LREE than those in other lherzolitic shergottites (e.g., $[La/Yb]_{CI} = 0.003$ and 0.02 for LEW 88516 low- and high-Ca pyroxene oikocrysts, respectively; Harvey et al., 1993) but are almost comparable to those in the enriched basaltic shergottites

(e.g., $[La/Yb]_{CI}$ = 0.04 and 0.07 for Shergotty low- and high-Ca pyroxenes, respectively; Wadhwa et al., 1994).

In addition to the REE, additional selected trace element abundances in the earliest formed pyroxenes (i.e., low-Ca pyroxene oikocryst) in RBT 04261 and RBT 04262 were also measured. Figure 6.13 shows the abundances of incompatible Zr and Y in the low-Ca pyroxene oikocrysts plotted versus their Ti concentrations. The Zr and Y abundances increase with increasing Ti contents in RBT 04261 and RBT 04262. The positive Zr-Ti and Y-Ti trends are also seen in low-Ca poikilitic pyroxenes in other lherzolitic shergottites and low-Ca pyroxenes of the basaltic shergottites, but the abundances of these incompatible elements are distinctly higher in the latter. The abundances of Ti, Zr, and Y in low-Ca poikilitic pyroxenes in RBT 04261 and RBT 04262 plot generally within the range of those in the other lherzolitic shergottites.

Non-poikilitic pyroxenes in RBT 04261 and RBT 04262 have LREE-depleted patterns with negative Eu anomalies ($[Eu/Eu^*]_N$ ~0.7-0.8) (Fig. 6.14). REE abundances in pyroxenes (high- and low-Ca) in the non-poikilitic areas are distinctly higher than those in pyroxenes in the poikilitic areas. The REE patterns of the non-poikilitic pyroxenes in RBT 04261 and RBT 04262 are similar but their abundances are slightly enriched relative to those of the non-poikilitic pyroxenes in other lherzolitic shergottite (ALHA77005 and LEW 88516).

*6.3.2.3 Maskelynite*

Maskelynite in RBT 04261 and RBT 04262 shows a LREE-enriched pattern, with most of the HREE present below the detection limit (Fig. 6.15).

This phase is also characterized by a large positive Eu anomaly ($[Eu/Eu^*]_N$~30-35). The LREE abundances are higher than those in lherzolitic shergottites, ALHA77005 and LEW 88516, and the basaltic shergottite, Shergotty.

*6.3.2.4 Merrillite*

While merrillite is present only in trace modal abundances in RBT 04261 and RBT 04262, it is the main carrier of the REE (La~190-680 × CI) (Fig. 6.16). Merrillites in both RBT 04261 and RBT 04262 exhibit relatively flat REE patterns with small negative Eu anomalies ($[Eu/Eu^*]_N$ ~0.83-0.95); the REE patterns of this mineral are almost indistinguishable in these two meteorites. The REE patterns of merrillites in RBT 04261 and RBT 04262 are similar to those in Shergotty but unlike the LREE-depleted pattern of merrillites in ALHA77005 and LEW 88516 (Fig. 6.16).

## 6.4 DISCUSSION

### 6.4.1 Are RBT 04261 and RBT 04262 Paired?

The initial characterization indicated that RBT 04261 and RBT 04262 are almost identical (Satterwhite and Righter, 2007); subsequent investigations were performed only on RBT 04262 (Anand et al., 2008; Beckett et al., 2008; Cartwright et al., 2008; Dalton et al., 2008; Greenwood, 2008; Lapen et al., 2008; Mikouchi et al., 2008). The results of our study demonstrate that textural features as well as the major and trace element mineral chemistries for RBT 04261 and RBT 04262 are so similar that these meteorites must be paired. One concern

regarding the parity of these two meteorites is their different cosmogenic radionuclide ages, suggesting different falls despite the fact that they were found <1 km apart. The reported $^{10}$Be exposure age and $^{10}$Cl terrestrial age of RBT 04261 are 3.0±0.6 Ma and <60 ka, whereas those of RBT 04262 are 2.0±0.5 Ma and 710±60 ka, respectively (Nishiizumi and Caffee, 2010). However, the ejection ages from Mars (i.e., the sum of exposure and terrestrial ages) for these two meteorites are identical within analytical errors (3.0±0.6 and 2.7±0.5 Ma for RBT 04261 and RBT 04262, respectively), suggesting that they were derived by the same impact event and probably from the same launch site. Hereafter, we will use the term RBT 04261/04262 to refer to these paired samples.

### 6.4.2 REE Budget

Since we have determined the modal abundances and REE compositions of the various mineral phases within RBT 04261/04262, it is possible to make a mass balance calculation of the REE abundances in the whole-rock and compare it with the measured whole-rock REE abundances to determine if all the phases that contribute to the REE budget have been analyzed. The most modally abundant phases (i.e., pyroxene, maskelynite, and olivine) are relatively depleted in REE, whereas one of the least abundant phases, merrillite, has the highest REE concentrations. Additional minor phases, such as chromite, are extremely poor in REEs and do not contribute significantly to the REE budget. As can be observed in Fig. 6.16, the measured whole-rock REE pattern of RBT 04262 is controlled by

the REE abundances in the merrillite. This is expected given the high abundances of REE in this phase.

The abundances of REE in the RBT 04262 whole rock were calculated using the modal abundances of the olivines, pyroxenes, maskelynite and merrillite in this meteorite given in Table 6.1 (converted to modal wt.%) and the representative REE abundances for these phases given in Table 6.8; as an approximation, the average of the REE concentrations of all pigeonites (poikilitic and non-poikilitic) was taken to be representative for low-Ca pyroxenes, and similarly the average of the REE concentrations of all augites was taken to be representative for high-Ca pyroxenes. Fig. 6.16 shows the calculated whole-rock REE abundances from this study along with the whole-rock concentrations reported by Anand et al. (2008). The close approximation of the calculated and measured whole-rock REE patterns indicates that all the phases that contribute significantly to the REE budget have been accounted for with the *in situ* analyses reported here.

### 6.4.3 Magmatic Processes Recorded by RBT 04261/04262

*6.4.3.1 Crystallization Sequence*

RBT 04261 and RBT 04262 exhibit cumulate textures similar to other lherzolitic shergottites. The crystallization sequence of RBT 04261/04262 is inferred from the textures and mineral chemistries. Since olivines and pyroxenes in the poikilitic areas show higher Mg# than those in the non-poikilitic area, the poikilitic lithology crystallized before the non-poikilitic lithology. This is consistent with the fact that poikilitic pyroxenes typically have lower abundances

of incompatible trace elements such as the REE than non-poikilitic pyroxenes (Figs. 6.12 and 6.14). Although it is unclear which mineral first appeared as a liquidus phase, textural context suggests the following crystallization sequence in the poikilitic lithology: chromite → olivine → low-Ca pyroxene → high-Ca pyroxene. Chromite is suggested to have been the first crystallizing phase because it occasionally occurs within olivine chadacrysts. The rounded and anhedral outlines of olivine chadacrysts (Fig. 6.3e, f) suggest partial absorption by coexisting melt to form low-Ca pyroxene. Such a texture is commonly observed in rocks that have experienced peritectic reactions: olivine + melt → pyroxene (Bard, 1986). High-Ca pyroxene rims formed after the low-Ca pyroxene cores. The high-Ca pyroxene rims enclose olivine chadacrysts that are less magnesian than those enclosed by the low-Ca pyroxene cores (Fig. 6.4). Moreover, the high-Ca pyroxene rims enclose maskelynite inclusions (Fig. 6.2). These observations suggest that, in the final stages of the formation of the poikilitic lithology, plagioclase started to crystallize.

The non-poikilitic lithology formed from an intercumulus melt. This melt had a more evolved composition than the parent magma of the poikilitic lithology, and was probably co-saturated with olivine, high- and low-Ca pyroxenes, and plagioclase. This is consistent with the observation that the two pyroxenes and plagioclase occur interstitially to each other (Fig. 6.3a, b). Moreover, the contrasting signatures of minor elements (decreasing $Al_2O_3$ and increasing $TiO_2$ with decreasing Mg#; Fig. 6.7a-d) for the non-poikilitic low-Ca pyroxenes suggest the co-crystallization of pyroxene and plagioclase (e.g., Bence and

Papike, 1970). Continuous crystallization substantially reduced the porosity in the cumulus pile and isolated small volumes of evolved, interstitial melt; then, more sodic plagioclase, ilmenite and merrillite crystallized. Some non-poikilitic olivines have euhedral outlines and these olivines are larger than other non-poikilitic olivines with sub- to anhedral outlines. Such euhedral olivines presumably co-crystallized with the poikilitic lithology. Because these olivines were not surrounded by pyroxene oikocrysts, they interacted and re-equilibrated with the fractionated intercumulus melt.

*6.4.3.2 Conditions for the Formation of RBT 04261/04262*

Subsolidus equilibration temperature ($T$) and oxygen fugacity ($fO_2$) were estimated by employing a two-pyroxene geothermometer (Lindsley, 1983), olivine-spinel geothermometer (Fabries, 1979), and olivine-orthopyroxene-spinel oxygen barometer (Wood, 1991). The $fO_2$ was additionally estimated using the Eu oxybarometer developed by Wadhwa (2001).

We assume that RBT 04261/04262 crystallized at near-surface conditions (~1 bar, Beckett et al., 2008; Mikouchi et al., 2008). The two-pyroxene geothermometer yields an equilibration temperature (~1,150 °C) for a pair of pigeonite ($En_{64}Wo_{11}Fs_{25}$) and augite ($En_{48}Wo_{35}Fs_{17}$) contacting each other at the rim of the poikilitic pyroxenes. Coexisting olivine-spinel-orthopyroxene grains (Fig. 6.3f) yield a subsolidus equilibration temperature (826±50 °C) and an oxygen fugacity ($\log fO_2$ = QFM-1.59±0.05) (Table 5.9). Based on the measured REE abundances in the poikilitic low-Ca pyroxene cores (i.e., with the lowest

REE abundances; Tables 6.7 and 6.8) and assuming that the REE pattern of the parent magma is parallel to that of the whole-rock (Anand et al., 2008) (see 6.4.3.3. for the reasoning for this assumption), $D_{Eu}/D_{Gd}$ values of 0.45±0.12 and 0.41±0.12 are calculated for RBT04261 and RBT04262, respectively (errors are from counting statistics on the pyroxene analyses only). Using the partition coefficient data of McCanta et al. (2004) for shergottite pigeonites, these values translate to $fO_2$ estimates of QFM-2.2 $^{+1.1}_{-0.9}$ and QFM-2.8 $^{+1.2}_{-0.8}$, respectively. These $fO_2$ estimates have large errors due to the relatively large uncertainties associated with the extremely low REE concentrations in the low-Ca poikilitic pyroxenes; nevertheless these are in agreement, within the uncertainties, with the $fO_2$ estimated using the olivine-orthopyroxene-spinel oxygen barometer. The distinctly higher temperature estimated by the two-pyroxene geothermometer as compared to the olivine-spinel geothermometer is commonly observed in terrestrial igneous rocks and is explained by the fact that the equilibrium exchange of Fe and Mg between spinel and olivine is much faster than the Ca-Fe-Mg exchange of pyroxenes (Fabries, 1979).

The liquidus and crystallization temperatures are difficult to determine, given the cumulate nature of RBT 04261/04262. As such, their whole-rock major element composition does not reflect the composition of their parent melt, although RBT 04261/04262 is interpreted to have crystallized in a nearly closed system following crystal accumulation (see 6.4.3.3. below). For example, Mg#s of melts in equilibrium with olivines in RBT 04261/04262 are calculated to be 0.3-0.4, assuming the exchange coefficient of Fe-Mg between olivine and melt of

0.3. These values are distinctly lower than the bulk rock Mg# (0.65) of RBT 04262 (Anand et al. 2008). Moreover, subsolidus re-equilibration has likely altered at least the major element compositions of the first crystallized minerals, such that they no longer record information about their initial crystallization conditions. The crystallization temperatures of pyroxenes, olivines and spinels are surely higher than the two-pyroxene equilibration temperature (~1,150 °C).

Table 6.9

Calculated temperature and oxygen fugacity of RBT 04262

| | olivine | orthopyroxene | chromite |
|---|---|---|---|
| Oxide wt% | | | |
| $SiO_2$ | 38.0 | 55.4 | 0.14 |
| $TiO_2$ | - | 0.11 | 3.30 |
| $Al_2O_3$ | - | 0.51 | 16.1 |
| $Cr_2O_3$ | 0.17 | 0.40 | 38.4 |
| $Fe_2O_3$ | - | - | 5.72 |
| FeO | 30.2 | 16.2 | 29.3 |
| MnO | 0.64 | 0.56 | 0.52 |
| MgO | 32.5 | 25.9 | 5.043 |
| CaO | 0.13 | 2.14 | 0.06 |
| $Na_2O$ | - | 0.03 | - |
| NiO | 0.09 | - | - |
| $V_2O_3$ | - | - | 0.63 |
| Total | 101.6 | 101.3 | 99.2 |
| | | | |
| Molar ratio | | | |
| Si | 1.009 | 1.989 | 0.005 |
| Ti | - | 0.003 | 0.083 |
| Al(IV) | - | 0.011 | 0.637 |
| Al(VI) | - | 0.011 | - |
| Cr | 0.004 | 0.011 | 1.021 |
| $Fe^{3+}$ | - | 0.000 | 0.145 |
| $Fe^{2+}$ | 0.671 | 0.486 | 0.824 |
| Mn | 0.014 | 0.017 | 0.015 |
| Mg | 1.287 | 1.388 | 0.253 |
| Ca | 0.004 | 0.082 | 0.002 |
| Na | - | 0.002 | - |
| Ni | 0.002 | - | - |
| V | - | - | 0.018 |
| Total | 2.989 | 4.000 | 3.003 |
| No. of oxygen | 4 | 6 | 4 |
| | | | |
| T (°C) | | 827 ± 50 | |
| $fO_2$ (log unit) | | QFM-1.59 ± 0.05 | |

*6.4.3.3 Parent Magma REE Composition and its Geochemical Reservoir*

The REE compositions of minerals in shergottites have been used to characterize the nature and evolution of their parent melts (e.g., Wadhwa et al., 1994). We reconstructed the REE compositions of the melts in equilibrium with the various minerals present in RBT 04261 and RBT 04262 using REE compositions of these minerals: low- and high-Ca pyroxene oikocrysts, maskelynite, and merrillite.

The REE concentrations of the melt in equilibrium with the minerals present in RBT 04261 and RBT 04262 can be determined using the relationship:

$$D_E = C_x / C_l$$

where $C_x$ and $C_l$ are the concentrations of a given element, $E$, in the crystal and liquid phases, and $D_E$ is the partition coefficient between the crystal and liquid phase for element $E$. The crystal/liquid partition coefficients used in this study are taken from Lundberg et al. (1990). For pyroxenes, the partition coefficients determined through ion microprobe measurements for low-Ca pyroxenes (i.e., $D_{IP}$) and the experimentally determined partition coefficient values for high-Ca pyroxenes (i.e., $D_{exp}$) are used. Previous studies (e.g., McKay et al., 1986) have shown that the partition coefficients for pyroxenes are strongly dependent on the pyroxene wollastonite content. The partition coefficient values in Lundberg et al. (1990) have been corrected for the wollastonite content of ALHA77005. Due to the close similarity between ALHA77005 and RBT 04261/04262 in terms of the wollastonite contents of the low- and high-Ca pyroxenes, it is reasonable to use these reported values to calculate the melt in equilibrium with these two phases.

For merrillite, the partition coefficient reported by Lundberg et al. (1990) for the Shergotty parent melt composition is used; note that Lundberg et al. (1990) referred to "merrillite" as "whitlockite". For maskelynite, the partition coefficient reported by Lundberg et al. (1990) for lunar plagioclase is used. Lundberg et al. (1990) reported that while absolute values of the plagioclase/melt distribution coefficients have a wide range (~factor of two), the REE patterns of these distribution coefficients are quite similar. Thus, the calculated REE pattern of the melt in equilibrium with the plagioclase is robust.

The calculated REE pattern of the melt in equilibrium with the low-Ca poikilitic pyroxene core reflects the REE pattern of the parent melt for RBT 04261/04262, because the pyroxene oikocrysts are among of the earliest REE-bearing phases to crystallize along with chromite and olivine chadacrysts. The crystallization of olivine and chromite does not significantly affect REE pattern of the parent melt since the REE are highly incompatible in these minerals. The REE patterns of the melts in equilibrium with the high-Ca poikilitic pyroxene, plagioclase (now maskelynite) and merrillite reflect those of more evolved melts at later stages during the crystallization history of RBT 04261/04262.

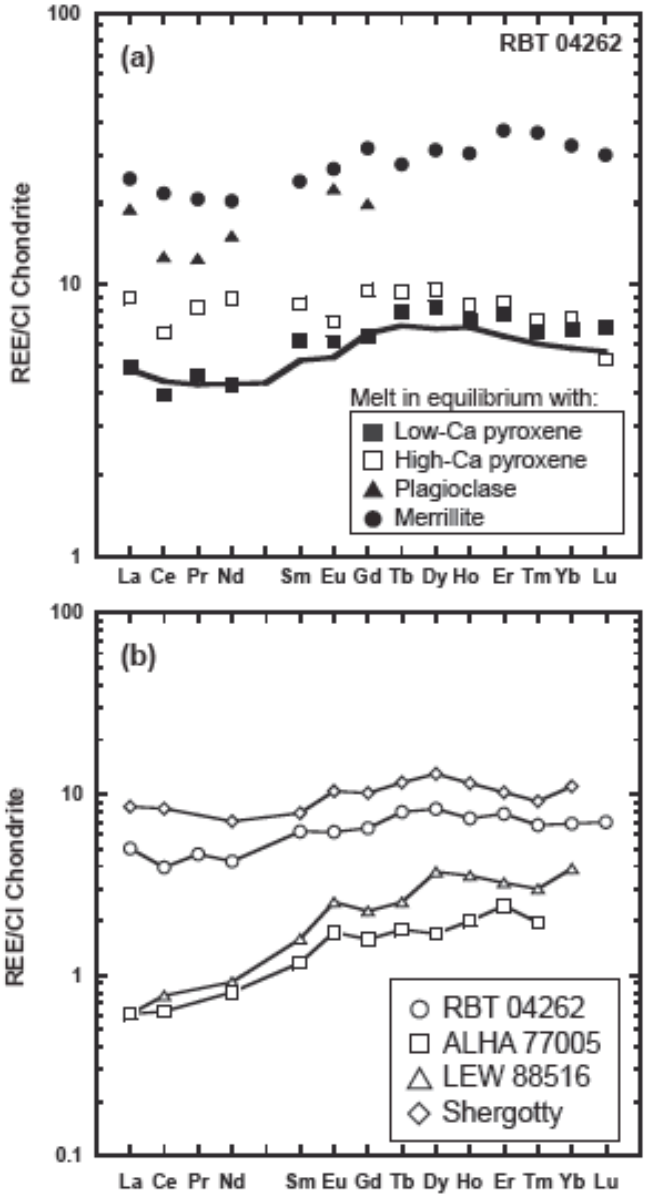


*Figure 6.17*- (a) Chondrite-normalized REE abundances in melts calculated to be in equilibrium with the low-Ca poikilitic pyroxene, high-Ca poikilitic pyroxene, plagioclase, and merrillite of RBT 04262. (b) Calculated chondrite-normalized REE concentrations in the parent melt (i.e., the melt in equilibrium with the low-Ca poikilitic pyroxene core) of RBT 04262. REE compositions of the calculated parent melts for the other lherzolitic shergottites (ALHA77005 and LEW 88516) (Harvey et al., 1993) and for the basaltic shergottite Shergotty (Wadhwa et al., 1994) are shown for comparison. REE abundances are normalized to CI chondrites (Palme and Beer, 1993).

Figure 6.17a shows the melts calculated to be in equilibrium with the REE compositions of low-Ca and high-Ca poikilitic pyroxenes, plagioclase (now maskelynite) and merrillite of RBT 04262; similar results are obtained for melts in equilibrium with minerals of RBT 04261 and are, therefore, not shown here. The calculated melt in equilibrium with the poikilitic pigeonite core composition (i.e., having the lowest REE abundances measured in this phase) in RBT 04262 has a relatively flat REE pattern almost identical to that of the whole-rock (Fig. 6.17a). Melts in equilibrium with later formed phases (i.e., poikilitic high-Ca pyroxene, plagioclase and merrillite) have REE patterns that are parallel but distinctly elevated relative to that of the whole-rock. These observations suggest that, following crystal accumulation, RBT 04261/04262 formed by progressive fractional crystallization in a nearly closed-system and that the poikilitic and non-poikilitic lithologies of RBT 04261/04262 originated from a single parent magma. This is additionally supported by the coherent trends observed in the distributions of minor elements in the poikilitic and non-poikilitic pyroxenes (Fig. 6.7).

The REE pattern estimated for the parent melt of RBT 04261/04262 suggests that it originated from a geochemically enriched reservoir. Figure 6.17b compares the REE patterns calculated for the parent melt of RBT 04262 with those of several basaltic and lherzolitic shergottites. The RBT 04262 parent melt has a REE pattern similar to those of the geochemically enriched basaltic shergottites (like Shergotty) but distinct from those of the depleted lherzolitic shergottites (like LEW 88516 and ALHA77005). Additionally, Lapen et al. (2008) and Shih et al. (2009) respectively reported initial $^{176}Lu/^{177}Hf$ and

$^{143}Nd/^{144}Nd$ ratios for RBT 04262 that are almost identical to those of Shergotty and Zagami. These geochemical observations suggest that RBT 04261/04262 originated from a relatively enriched source reservoir (similar to that for the other enriched shergottites like Shergotty and Zagami).

The enriched geochemical signatures of RBT 04261/04262 are consistent with the oxidation state of RBT 04261/04262 (QFM-1.6), because the enrichment and depletion of the shergottite geochemical reservoirs are strongly correlated with their oxidation states (Wadhwa, 2001; Herd et al., 2002). The oxidation state of RBT 04261/04262 (QFM-1.6) is in the $fO_2$ range of the enriched basaltic shergottites (~QFM -1 to -2 for Shergotty, Zagami and Los Angeles) but is distinctly higher than those of the depleted shergottites (~QFM -2.5 to -3.8 for DaG 476, Dhofar 019, SaU 005 and Y-980459) and the other lherzolitic shergottite (QFM -2.6 for ALHA7005) (Herd et al., 2002; Xirouchakis et al. 2002; Goodrich et al., 2003; Shearer et al., 2006; Usui et al., 2008).

### 6.4.4 Comparison with the Other Shergottites

RBT 04261/04262 clearly shows a close textural affinity to the other lherzolitic shergottites (ALHA77005, LEW 88516, NWA 1950, Y-793605 and GRV 99027), but some significant differences are noted in its geochemical characteristics. In fact, in many respects, RBT 04261/04262 is geochemically most similar to the enriched basaltic shergottites (e.g., Shergotty and Zagami).

Petrographic observations suggest that RBT 04261/04262 represents the most evolved magma among the lherzolitic shergottites. Olivine, pyroxene and

plagioclase have the lowest Fo, En and An components among those in the lherzolitic shergottites, respectively (Figs. 6.5, 6.6, and 6.8). Spinel also has the lowest Mg# among the lherzolitic shergottites. Plagioclase abundances in RBT 04261 (20.1 vol. %) and RBT 04262 (15.9 vol%) are distinctly higher than those of other lherzolitic shergottites (commonly <10 vol%). The high plagioclase abundances are probably not due to the sampling bias of large poikilitic pyroxenes in the studied PTSs, because another section for RBT 04262 also contains a relatively higher modal abundance (13 vol%) of plagioclase (Mikouchi et al., 2008). The high plagioclase abundances are related to the distinctly higher proportions of the non-poikilitic lithology (88 vol% and 79 vol% for RBT 04261 and RBT 04262, respectively) compared to those of the other lherzolitic shergottites (e.g., 39.3 vol% for GRV99027, Lin et al., 2005). Moreover, the pyroxene oikocrysts in RBT 04261 and RBT 04262 contain a lower modal abundance of olivine chadacrysts than those in the other lherzolitic shergottites (judging from photographs in the literatures: Harvey et al., 1993; Mikouchi and Miyamoto, 1997; Lin et al., 2005; Mikouchi, 2005). These observations suggest that the parent magma of RBT 04261/04262 had less normative olivine and more normative plagioclase than the parent magmas of the other lherzolitic shergottites.

Trace element chemistry is also distinct from the other lherzolitic shergottites, and shows some similarities to the enriched basaltic shergottites. The whole-rock composition of RBT 04262 is distinctly enriched in LREE relative to the other lherzolitic shergottites, but rather similar to those of the enriched basaltic shergottites (Anand et al., 2008). REE patterns of all the

analyzed minerals in RBT 04261/04262 are also enriched in LREE (with the exception of olivine, in which the LREE are present below the analytical detection limits) relative to those in the lherzolitic shergottites (Figs. 6.12, 6.14, 6.15 and 6.16). Finally, the REE pattern of the calculated parent melt of RBT 04261/04262 is somewhat LREE-enriched, and is quite distinct from the LREE-depletion in the parent melts estimated for the other lherzolitic shergottites but rather similar to that of the Shergotty parent melt. This LREE-enrichment in the calculated parent melt of RBT 04261/04262 cannot be explained by fractionation of common igneous minerals from the geochemically depleted magmas that produced the other lherzolitic shergottites. Thus, the magmatic source of RBT 04261/04262 is distinct from that of the other lherzolitic shergottites, and may be similar to the source of the enriched basaltic shergottites.

RBT 04261/04262 appears to be unique compared to other known lherzolitic shergottites. However, recently discovered lherzolitic shergottites (GRV 020090 and NWA 2646) show some similarities to RBT 04261/04262. Although limited datasets are available so far, these new meteorites exhibit relatively evolved magmatic compositions (e.g., as indicated by higher plagioclase abundances and lower Fo contents of their olivines) (Bunch et al., 2005; Lin et al., 2008). A new shergottite subgroup ("pyroxene-oikocrystic shergottite") has been proposed for these new shergottites including RBT 04261/04262, because they are not strictly "lherzolitic" due to high modal abundances of plagioclase (>10%; Mikouchi, 2009). Moreover, another recent shergottite find, NWA 4468, has a poikilitic pyroxene texture similar to the

lherzolitic shergottites, but likely exhibits a geochemically enriched signature (Irving et al., 2007; Borg et al., 2008). Systematic studies of these new shergottites along with RBT 04261/04262 could help clarify the petrogenesis of geochemically enriched mafic cumulates on Mars.

### 6.4.5 Relationship between Petrographic Types, Geochemical Reservoirs and Ejection Ages

Basaltic and olivine-phyric shergottites individually sampled both geochemically enriched and depleted reservoirs on Mars, but no definitive evidence of the presence of enriched lherzolitic shergottites has been reported prior to our study of RBT 04261/04262. A number of studies have addressed the relationship between the petrographic types and the geochemical reservoirs for shergottites (e.g., Wadhwa, 2001; Barrat et al., 2002; Borg et al., 2002; Herd et al., 2002; Borg and Draper, 2003; Treiman, 2003; Symes et al., 2008; Sarbadhikari et al., 2009). However, only a few investigations have attempted to combine them with chronological information (Nyquist et al., 2001, 2009; McSween, 2002). Here we summarize chronological relationships between the three types of shergottites and their two geochemical reservoirs.

Figure 6.18 shows a plot of the crystallization ages versus the ejection ages from Mars (hereafter referred to as Mars ejection age) for the shergottites. The crystallization ages were obtained based on Sm-Nd internal mineral isochrons, while the Mars ejection ages are based on the sums of terrestrial and mean cosmic-ray $^{3}$He, $^{21}$Ne and $^{38}$Ar exposure ages. Based on $^{207}$Pb-$^{206}$Pb isotopic systematics, Bouvier et al. (2005, 2008) have proposed an ancient crystallization

age (~4.1-4.3 Ga) for the shergottites, which is distinctly older than their Sm-Nd internal isochron ages. We will employ the Sm-Nd internal isochron ages in the following discussion of this section, because these Sm-Nd ages are consistent with Lu-Hf and Rb-Sr internal isochron ages (Nyquist et al., 2001) and because the old $^{207}Pb$-$^{206}Pb$ age is not based on mineral separates from individual shergottites but rather on whole-rocks and mineral leaching experiments of several different shergottites (Bouvier et al., 2005; 2008).

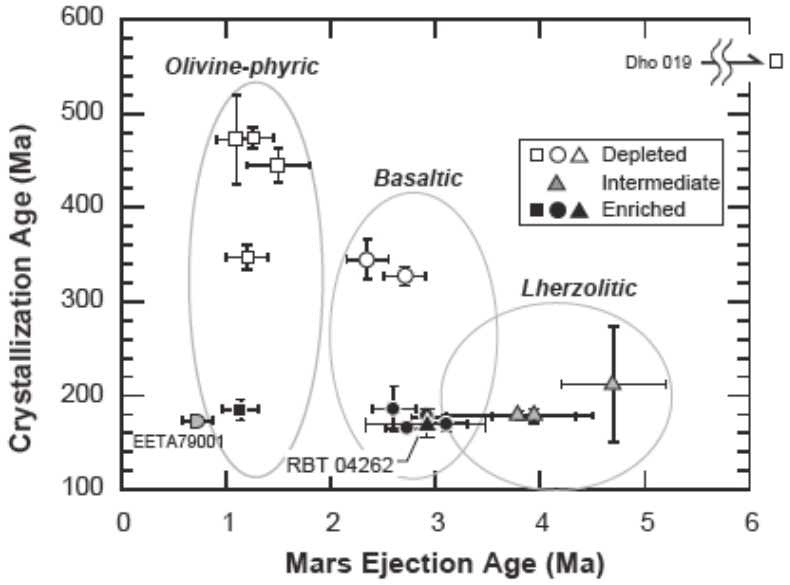


*Figure 6.18*- Mars ejection ages plotted versus Sm-Nd crystallization ages of the shergottites. All of the chronological data presented here, except for RBT 04262, have been taken from the compilations of Nyquist et al. (2001) and Christen et al. (2005). The Sm-Nd crystallization age and the Mars ejection age of RBT 04262 are from Shih et al. (Shih et al., 2009) and Nishiizumi et al. (2010), respectively. Symbols: squares, olivine-phyric shergottites; circles, basaltic shergottites; triangles, lherzolitic shergottites. White, gray, and black symbols indicate the depleted, intermediate and enriched shergottites, respectively.

Except for a few exceptions noted below, Figure 6.18 demonstrates a distinct relationship between chronological datasets, petrographic types and geochemical reservoirs. Shergottites (except for Dhofar 019 and RBT 04262) within each of the olivine-phyric, basaltic and lherzolitic subgroups have similar Mars ejection ages, which are distinct between the subgroups; specifically, the olivine-phyric, basaltic and lherzolitic shergottites have the youngest (<2 Ma), intermediate (~2-3 Ma) and the oldest (≥~4 Ma) Mars ejection ages, respectively. Among the olivine-phyric and basaltic shergottites, the geochemically enriched samples have crystallization ages distinctly younger than the depleted samples (except for EETA79001). On the other hand, the lherzolitic shergottites (with intermediate geochemical signatures) have crystallization ages almost identical to those of the enriched basaltic and olivine-phyric shergottites.

These observations provide constraints on the spatial location and mixing processes of the geochemical source reservoirs of the shergottites. The clustered Mars ejection ages for each of the three shergottite subgroups suggest that each subgroup had an individual launch site and that at least two of these launch sites are likely to have supplied both geochemically enriched and depleted samples. Thus, both enriched and depleted shergottites should have been located in the same geographic areas, although they clearly formed in different magmatic events (as recorded by their distinct crystallization ages).

Two contrasting models have been proposed regarding the location and mixing processes of the two geochemical source reservoirs for the shergottites: (1) assimilation of oxidized crust by mantle-derived, reduced magmas (Wadhwa,

2001; Herd et al., 2002), or (2) mixing of two distinct mantle reservoirs during melting (Borg and Draper, 2003; Symes et al., 2008; Treiman, 2003). In any model, the two geochemical reservoirs must be located close to each other such that the shergottite magmas sampled both reservoirs at the same launch site (Fig. 6.19). For model (1), the assimilated enriched reservoir occurs as domains in the crust, which must be traversed by ascending mantle magmas. Herd et al. (2002) proposed that the assimilated material may be the product of early and extensive hydrothermal alteration of the Martian crust, or it may be amphibole- or phlogopite-bearing basaltic rock within the crust. For model (2), both geochemical reservoirs reside in the mantle and were formed as a result of either crystallization of a magma ocean to produce geochemically depleted and enriched domains (Borg and Draper, 2003), or fluid-induced metasomatism that produced mantle heterogeneity (Treiman, 2003).

RBT 04262, the only enriched lherzolitic shergottite, also exhibits a unique chronological feature. It has a crystallization age of 174±14 Ma and a Mars ejection age of 2.9±0.6 Ma (Shih et al., 2009; Nishiizumi and Caffee, 2010;). As can be seen in Fig. 6.18, RBT 04262 does not plot in the field of lherzolitic shergottites but in the basaltic shergottite field. Therefore, we propose two possibilities for the relationship between RBT 04261/04262 and the other shergottites. One is that RBT 04261/04262 formed during the same magmatic event that produced the enriched shergottites and was then ejected from the same launch site as these shergottites; i.e., RBT 04261/04262 was not co-magmatic with the other lherzolitic shergottites. In this case, RBT 04261/04262 should be a

cumulate rock produced by fractionation from the same melts that formed the enriched basaltic shergottites. This model is consistent with the geochemically enriched signature of RBT 04261/04262. The other possibility is that all the enriched basaltic shergottites and all the lherzolitic shergottites, including RBT 04261/04262, formed in the same magmatic event. This scenario favors the oxidized, enriched crustal assimilation model (Fig. 6.19a) rather than the heterogeneous mantle model (Fig. 6.19b), because both geochemically enriched basaltic shergottite and the intermediate lherzolitic shergottites should be produced by the same magmatic event.

In either scenario, RBT 04261/04262 is possibly the first example of mafic cumulates derived from the launch site of the basaltic shergottites that originated as fractionated melts, suggesting that RBT 04261/04262 may be the cumulate counterpart to the enriched basaltic shergottites. New shergottites (GRV 020090, NWA 2646 and NWA 4468) may be additional examples of the geochemically enriched lherzolitic shergottites as currently represented by RBT 04261/04262 (Section 6.4.4). More comprehensive studies of these new meteorites as well as RBT 04261/04262 could provide more insights not only into the petrogenetic relationship between basaltic and lherzolitic shergottites but also into the origin of the geochemical source reservoirs of the shergottites on Mars.

The occurrence of both enriched and depleted members of the shergottites demands that both geochemical reservoirs had a close spatial association. Furthermore, if the distinct launch sites (as required by the distinct ejection ages) for each of the three shergottite subgroups were geographically widely

distributed, then these two geochemical reservoirs are required to have been geographically widespread as well. Although this conclusion does not allow us to distinguish between the two models discussed above (Fig. 6.19), it does suggest that the geochemical source reservoirs for the shergottites may be of regional or perhaps global extent on Mars.

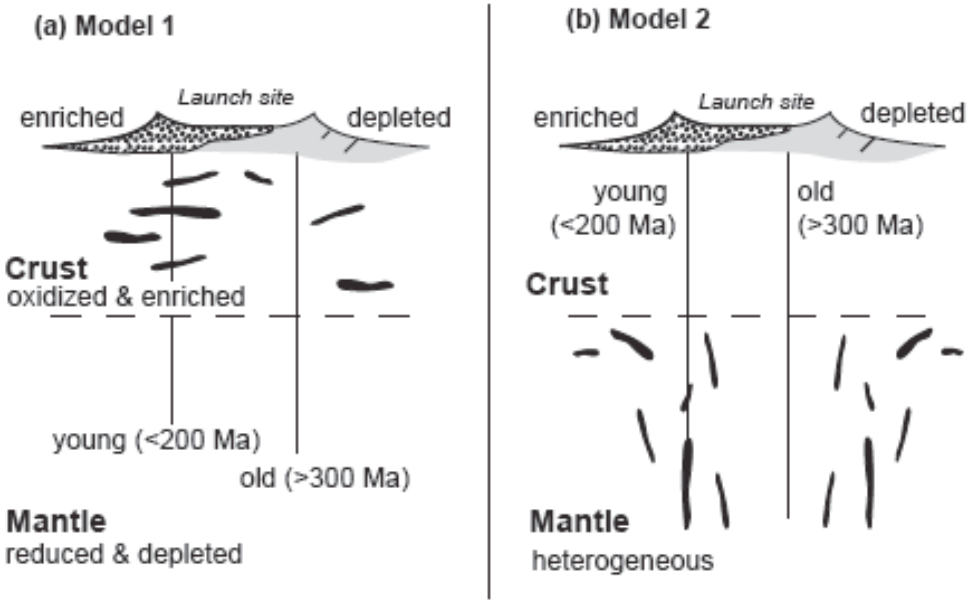


*Figure 6.19*- Two possible models for the location and mixing processes of shergottite geochemical source reservoirs. Any model is required to have a launch site from which both the geochemically enriched and depleted shergottites are supplied and needs to account for the fact that the depleted and enriched shergottites have distinct crystallization ages; the former are older (>300 Ma) than the latter (<200 Ma). (a) Model 1: Both enriched and depleted shergottites were generated from a reduced, depleted Martian mantle reservoir. The enriched shergottites interacted with oxidizing, geochemically enriched crustal materials (black) but the depleted ones did not. This model is modified after Herd et al. (2002). (b) Model 2: A heterogeneous Martian mantle where oxidized and enriched mantle domains (black) occur along with reduced, depleted mantle domains. Two possibilities were proposed for the occurrence in the Martian mantle of both depleted and enriched reservoirs; i.e., crystallization of the magma ocean (Borg and Draper, 2003; Symes et al., 2008), or fluid-induced mantle metasomatism (Treiman, 2003).

## 6.5 CONCLUSIONS

RBT 04261 and RBT 04262, which were initially classified as olivine-phyric shergottites, are lherzolitic shergottites. Both meteorites exhibit almost identical textures and mineral compositions, suggesting that they are paired. As is characteristic of lherzolitic shergottites, they consist of poikilitic and non-poikilitic lithologies. The poikilitic lithology is composed of pyroxene oikocrysts enclosing olivine and chromite chadacrysts. The non-poikilitic lithology includes olivine, pyroxene and plagioclase along with minor amounts of Ulv-rich chromite, ilmenite and merrillite. Olivine, pyroxene and chromite in the poikilitic lithology have more magnesian compositions than those in the non-poikilitic lithology.

Petrographic observations suggest that RBT 04261/04262 is the most evolved member of the lherzolitic shergottites. Olivine, pyroxene and plagioclase have the lowest Fo, En and An components, respectively. Modal abundances of plagioclase (now maskelynite) in RBT 04261/04262 are distinctly higher than those in other lherzolitic shergottites. The high proportions of plagioclase in these meteorites are related to the higher proportions of the non-poikilitic areas than in the other lherzolitic shergottites. Moreover, abundance of olivine chadacrysts in each pyroxene oikocryst is lower than in pyroxene oikocrysts from the other lherzolitic shergottites.

REE patterns of constituent minerals in RBT 04261/04262 are distinctly enriched in LREE relative to those in the other lherzolitic shergottites. These trace element signatures are similar to those observed previously for the enriched basaltic shergottites, and cannot be explained by crystal fractionation of common

igneous minerals from a melt generated from the intermediate geochemical source reservoir that gave rise to the parent magmas of the other lherzolitic shergottites. Thus, the magmatic source of RBT 04261/04262 is distinct from that of the other lherzolitic shergottites, but may be similar to that of the enriched basaltic shergottites.

The crystallization sequence of RBT 04261/04262 is inferred from textural observations and mineral chemistry. The poikilitic lithology crystallized as follows: chromite → olivine → low-Ca pyroxene → high-Ca pyroxene. The anhedral outlines of olivine chadacrysts suggest the chadacrystic olivines experienced peritectic reaction with coexisting melt to form poikilitic low-Ca pyroxene. The non-poikilitic lithology formed from an intercumulus melt; this melt was co-saturated with olivine, pyroxene and plagioclase. Continuous crystallization of these minerals produced highly fractionated melts from which albite-rich plagioclase, ilmenite and merrillite crystallized at the final stage of crystallization.

The REE pattern of the melt calculated to be in equilibrium with the core of the low-Ca pyroxene oikocryst is parallel to the REE patterns of the RBT 04262 whole-rock and merrillite. The parallelism of these REE patterns suggests that RBT 04261/04262 was produced by progressive fractional crystallization in a nearly closed system and that the poikilitic and non-poikilitic lithologies of RBT 04261/04262 originated from single parent magma. The REE pattern of the calculated parent melt for RBT 04261/04262 is similar to those of Shergotty and Zagami, suggesting that it originated from a geochemically enriched reservoir.

This is also consistent with the relatively oxidized magmatic conditions ($\log fO_2$ = QFM-1.6) for RBT 04261/04262.

Combination of petrographic, geochemical and chronological datasets for shergottites including RBT 04261/04262 suggests that each shergottite subgroup (basaltic, olivine-phyric, and lherzolitic) had a distinct launch site and that at least two of their launch sites (olivine-phyric and basaltic subgroups) included rocks that sampled both the geochemically enriched and depleted shergottites. Moreover, RBT 04261/04262, the first example of geochemically enriched mafic cumulates from Mars, was possibly derived from the launch site of the basaltic shergottites that originated in fractionated melts, suggesting that RBT 04261/04262 may be the counterpart to the enriched basaltic shergottites. These observations place constraints on the petrogenetic and geographic relationships between basaltic and lherzolitic shergottites and on the distribution and mixing processes for the geochemical source reservoirs of the shergottites on Mars.

# CHAPTER 7

# TRACE ELEMENT GEOCHEMISTRY OF NAKHLITE NORTHWEST AFRICA 5790: NEW INSIGHT INTO NAKHLITE PETROGENESIS ON MARS

## 7.1 INTRODUCTION

Our current understanding of the magmatic processes occurring on Mars, in part, rely on the geochemical evidence recorded in meteorites belonging to the shergottite-nakhlite-chassignite (SNC) meteorite group. The nakhlites, while the second most abundant of the SNC meteorite subgroup, are a relatively rare group of basaltic cumulate rocks, essentially pyroxenites, composed predominately of cumulate clinopyroxene phenocrysts with lesser abundant cumulate olivine contained within a fine-grained interstitial groundmass (Treiman, 2005, reference therein). Nakhlites are commonly thought to represent the remnants of a slowly cooling lava flow at or near the martian surface (e.g., Treiman, 1986). The extent and depth of the lava flow and resulting cumulate pile is still an open question. However, studies of nakhlite cooling rate suggest that nakhlites with the most protracted cooling history correspond to burial depths of 30 meters or greater (Mikouchi et al., 2003, 2006, 2012).

Presently, the SNC meteorite group consists of 63 individual samples with additional stones petrographically and geochemically paired with other samples. However, a majority of the 63 SNC meteorites are classified as shergottites with only 8 of those meteorites identified as nakhlites (13 when paired nakhlites are included). As such, each new nakhlite identified provides the opportunity to

evaluate and refine previous models for nakhlite formation and further develop an understanding of near surface conditions and magmatic dynamics on Mars. The most recently recovered nakhlite, Northwest Africa (NWA) 5790, was found in 2008 in the hot desert region of northern Africa. Initial investigations of NWA 5790 noted similarity in the broad mineralogy and geochemistry to the other nakhlites (Jambon et al., 2012). However, these same early studies also noted unique features of NWA 5790, such the highest modal abundance of interstitial groundmass (i.e., mesostasis), in addition to the lowest abundance of cumulate pyroxene phenocrysts, of any nakhlite. In addition, initial estimates of the cooling rate experienced by NWA 5790 suggests a shallower formation depth with burial depth estimates in the cumulate pile of less than 2 meters (Mikouchi et al., 2012). These features suggest that the petrogenetic history recorded in NWA 5790 may provide new insight into the broader formation of the nakhlite meteorite group.

In this study, we present the results of an investigation into the systematics of rare earth elements (REE) and additional trace elements, as well as petrographic observations and the major element composition, of individual mineral phases and in the bulk interstitial groundmass of NWA 5790. The geochemical and petrographic observations are used to infer information about the crystallization conditions of NWA 5790 (e.g., parent melt composition and redox conditions). Using the geochemical composition of NWA 5790 and its inferred petrogenetic history, as well as the comparative geochemistry of NWA 5790 to

other nakhlites, broader implications for the petrogenesis of the nakhlite group are discussed.

## 7.2 ANALYTICAL METHODS

### 7.2.1 Petrography and Major Element Composition Measurements

Petrography and mineral chemistry analyses were completed using a polished thin section of NWA 5790. Initial petrographic characterization was completed using an optical petrographic microscope. The determination of mineral phases and associated mineral chemistry was accomplished using a Cameca SX-100 electron microprobe at the University of Tennessee, Knoxville. The modal abundances of individual phases were determined by point counting and energy dispersive spectrometry (EDS) using the electron microprobe. Mineral chemistry was determined using wavelength dispersive spectrometry (WDS) with an accelerating potential of 15 KV. A 20 nA beam current with a 1 μm beam diameter was used for the analyses. Standard ZAF (PAP) corrections were used for all analyses and synthetic and natural mineral standards were measured throughout the analytical sessions. Typical detection limits of the ion microprobe analyses are <0.03 wt.% for $SiO_2$, $TiO_2$, $Al_2O_3$, MgO, CaO, $Na_2O$, and $K_2O$, and <0.05 wt.% for FeO, MnO, and $Cr_2O_3$.

### 7.2.2 Trace Element Measurements

The concentration of rare earth elements and selected additional trace elements were measured *in situ* using a Cameca IMS-6f ion microprobe at Arizona State University using the energy filtering techniques previously

described by Zinner and Crozaz (1986). Analyses utilized an O- primary beam with currents ranging from 2 to 10 nA, depending on the phase being measured, with an accelerating voltage of -12.5 KV (secondary ions accelerated using a +10KV accelerating voltage). A -75 V offset was used to minimize interferences from complex molecular ions. For measurements of the fine-grained mesostasis (groundmass), the primary beam was rastered with a current of 10 nA to obtain a bulk, average composition. Analyses times range from under 1 hour to approximately 2.5 hours depending on the elemental abundances of a given phase.

The elemental concentrations of REE and other trace elements were determined by comparison of the element to a reference element (Si in silicates, Ca in phosphates) and experimentally determined sensitivity factors. Several synthetic glass standards (e.g., NIST-610, NIST-612, and NIST-614) were measured at the start of each analytical session and were monitored periodically during the session. Deconvolution of isobaric interferences from monoxides that are not eliminated using energy filtering techniques was accomplished using previously determined monoxide to elemental ratios (Hinton, 1990) and measured light rare earth element ion signals of the sample.

## 7.3 RESULTS

### 7.3.1 Petrography and Major Element Composition

Figures 7.1 and 7.2 illustrate the typical petrographic characteristics observed in NWA 5790. Descriptions of the occurrence of individual phases are discussed below. The observed modal abundances of major constituent phase are

shown in Table 7.1 with major element chemistry of individual silicate and phosphate phases in Table 7.2.

*7.3.1.1 Pyroxene (augite)*

Pyroxene (augite) is the most abundant mineral phase observed in NWA 5790, constituting ~53% of the bulk mineralogy. The pyroxene occurs as large sub-mm to mm-size subheadral to euhedral phenocrysts (Fig 7.1) as well as within the fine-grained mesostasis (Fig 7.2). Individual phenocrysts are compositionally zoned from core to rim with occasional patchy zoning observed. An example of the compositional zoning with the pyroxene is observable in the back-scattered electron image in Figure 7.1a. The major element composition of the pyroxene phenocrysts ranges from $En_{36}Fs_{24}Wo38$ ((En) enstatite, (Fs) ferrosilite, (Wo) wollastonite) in the cores to $En_{11}Fs_{47}Wo_{42}$ in the rims (Fig 7.3). Pyroxenes within the fine-grained mesostasis are highly Fe-rich augites within a more limited composition range than the large pyroxene phenocrysts, ranging from $En_{11}Fs_{49}Wo_{41}$ to $En_3Fs_{52}Wo_{45}$.

*7.3.1.2 Olivine*

The olivine in NWA 5790 is observed primarily as isolated euhedral to subhedral phenocrysts, comprising approximately 3% of the bulk sample. Individual grains are large with some measuring in excess of 1.5 mm (Fig. 7.1). The olivine grains are compositionally zoned with homogenous cores of approximately $Fo_{35}$ (forsterite) that progress to $Fo_{24}$ at the grain rim. Occasionally lower Mg content is observed at the extreme edges of some olivine grains with values as low as $Fo_{18}$.

*7.3.1.3 Feldspar, Phosphate, and Mesostasis*

The mesostasis of NWA 5790 is a fine-grained, groundmass texture that is composed of feldspar, phosphates, olivine, pyroxene, and oxide grains. A majority of the phases that constitute the mesostasis occur as microcrysts and, consequently, are too small to obtain clean electron microprobe analyses. However, interspersed within the microcrysts of the groundmass are slightly larger grains around 20 μm or larger. The following major element chemistry descriptions, as well as the ion microprobe analyses for trace elements discussed in section 7.3.2, for constituent mesostasis phases are focused on these larger grains. A representative analysis of the bulk mesostasis chemistry is shown in Table 7.2.

Feldspar grains within the mesostasis include both plagioclase and K-feldspar (Fig 7.2). The plagioclase spans a limited composition range with values of $An_{19\text{-}13}Ab_{79\text{-}75}Or_{10\text{-}4}$. K-feldspar is much more sporadic in nature than the plagioclase. As such, only a single electron microprobe analysis was obtained with a composition of $An_2Ab_{18}Or_{80}$. Figure 7.4 shows the range of compositional variation observed within the feldspar grains of NWA 5790 in comparison with the feldspar values reported in other nakhlites.

Apatite occurs primarily as small grains (generally <10 μm), widely interspersed within the fine-grained mesostasis. In addition to the widespread microcrysts, isolated larger grains (i.e., >30 μm) occur sporadically throughout the mesostasis. Among the apatite large enough for electron microprobe analysis, the grains are nearly homogenous in composition.

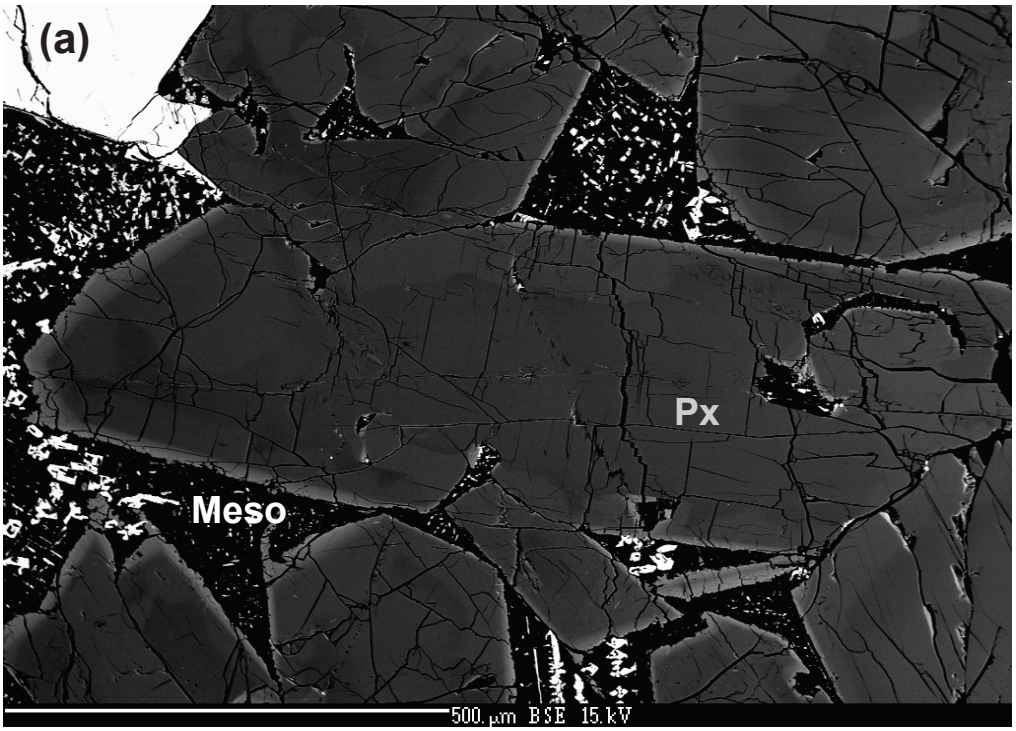


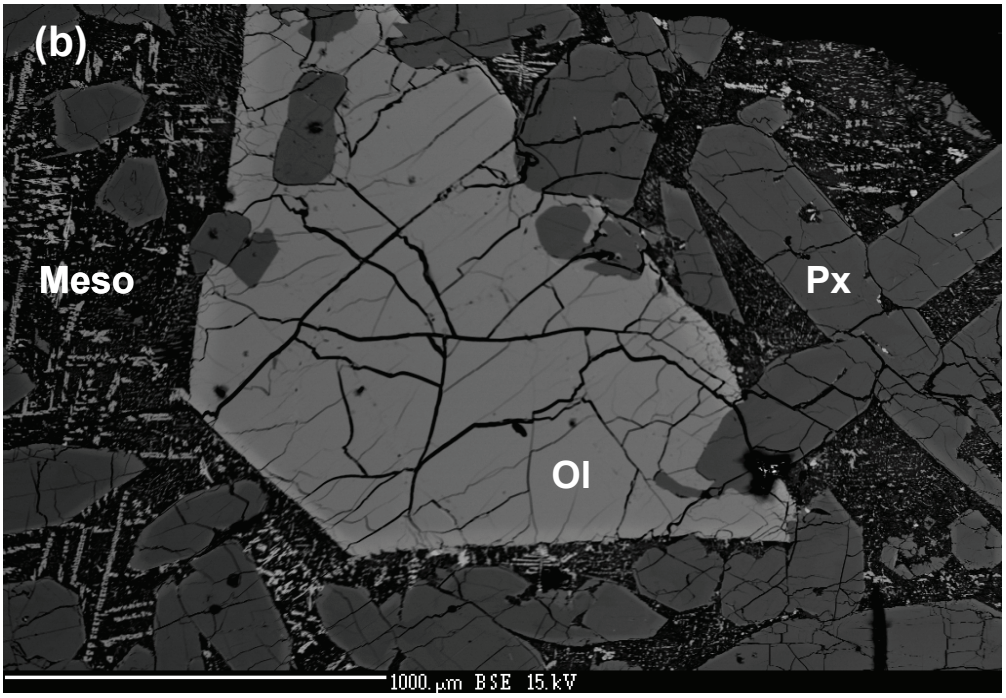


*Figure 7.1*- Back-scattered electron image of cumulate phases in Northwest Africa 5790 (Px: pyroxene, Ol: olivine, Meso: mesostasis).

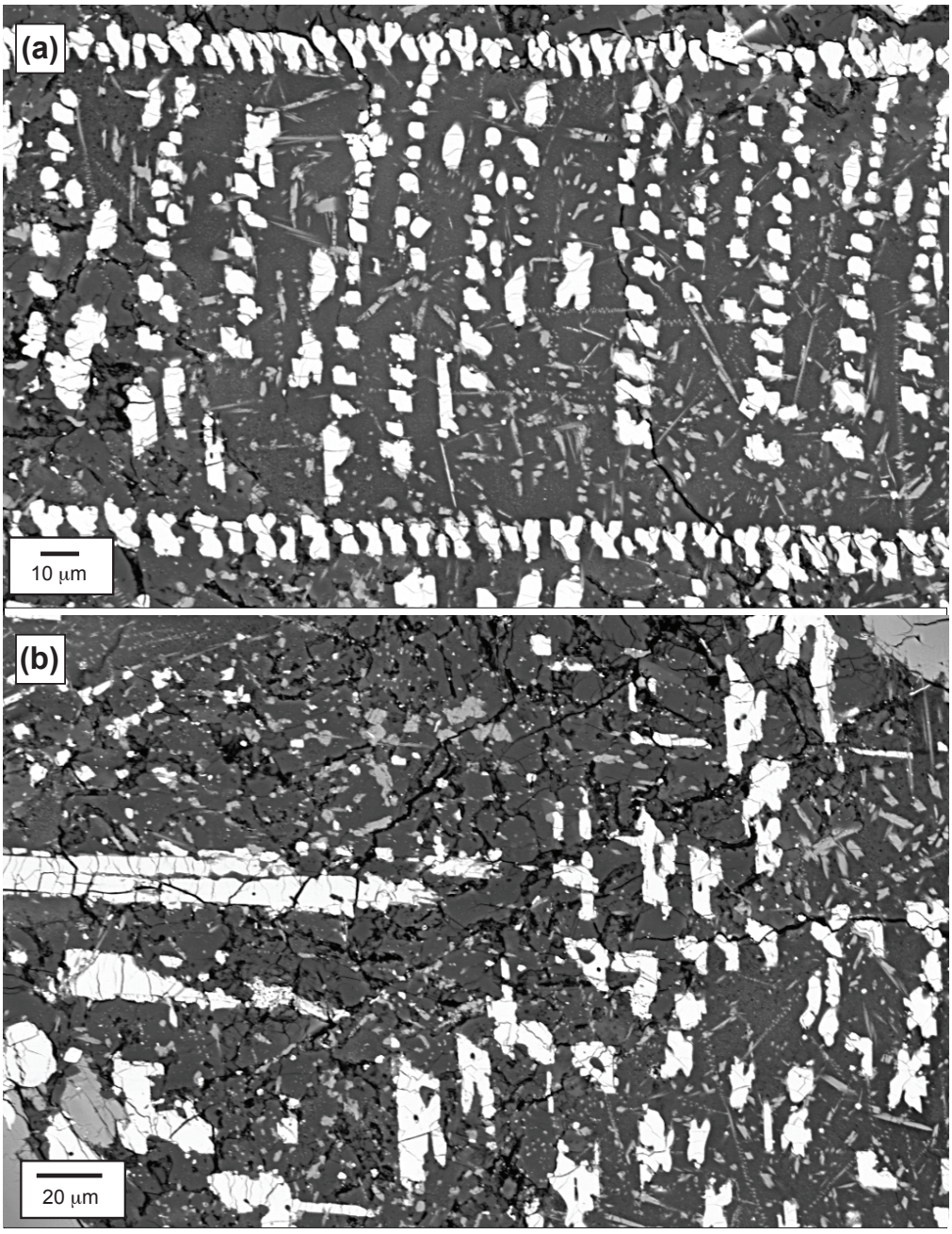


*Figure 7.2*- Back-scattered electron image of the fine-grained mesostasis region of Northwest Africa 5790.

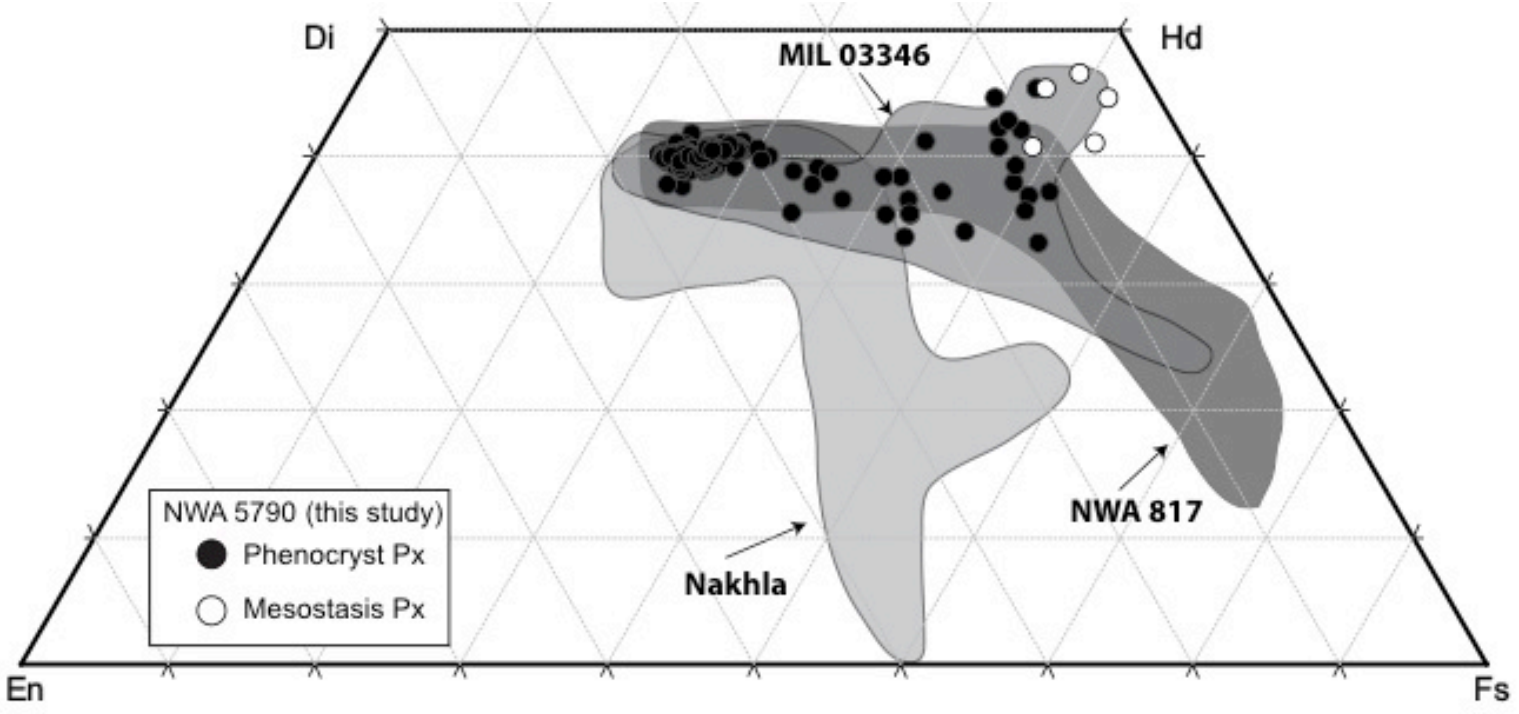


*Figure 7.3*- Pyroxene compositions of cumulate (phenocrysts) pyroxene and mesostasis pyroxene in Northwest Africa 5790 plotted on En-Fs-Wo composition diagram. Compositions for the nakhlites MIL 03346, NWA 817, and Nakhla are shown for comparison (Treiman, 1990; Harvey and McSween, 1991; Sautter et al., 2002; McKay and Schwandt, 2005; Day et al., 2006)

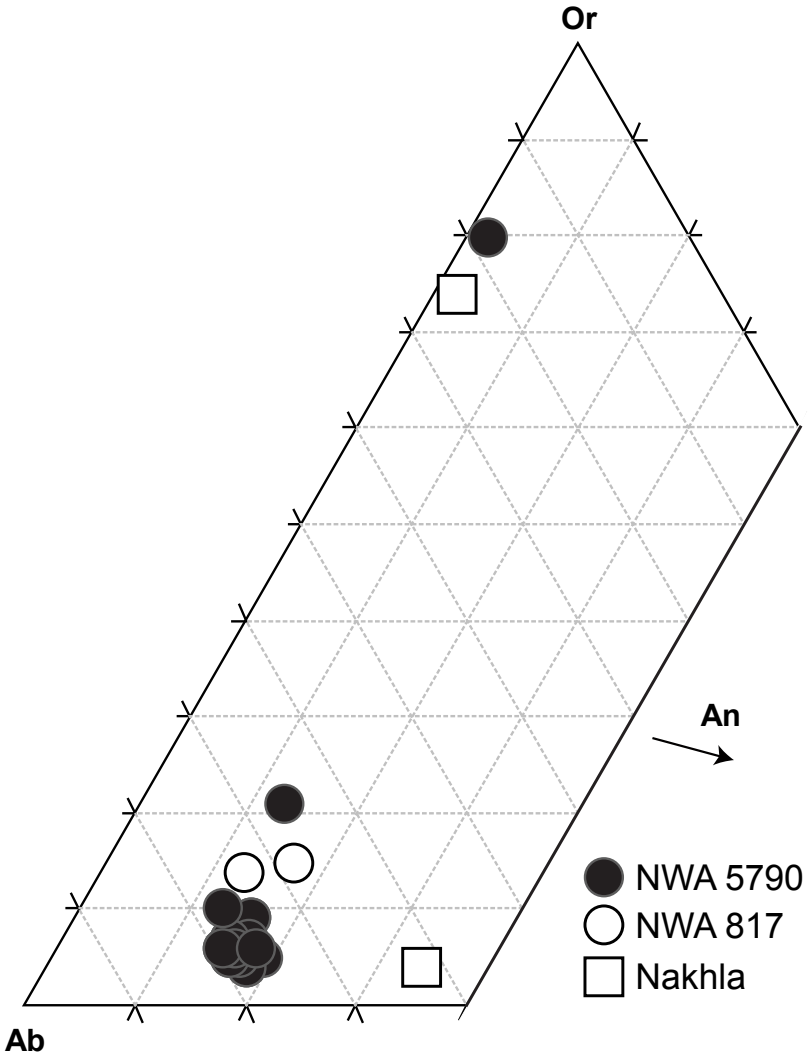


*Figure 7.4*- Compositions of the feldspar phases (plagioclase and K-feldspar) in Northwest Africa 5790. Shown for comparison are the compositions for the nakhlites NWA 817 and Nakhla (Bunch and Reid, 1975; Sautter et al., 2002)

Table 7.1

Mineralogical modal composition for NWA 5790 and nakhlite literature values (in modal %)

| Phase | NWA 5790 | Nakhla[a] | Lafayette[a] | Governador Valadares[a] | Yamato 000593/749/802[b] | NWA 817[c] | NWA 998[d] | MIL 03346[e] |
|---|---|---|---|---|---|---|---|---|
| Olivine | 2.9 | 11.6 | 15.7 | 10.1 | 12.2 | 10.0 | 10.0 | 1.1 |
| Pyroxene (augite) | 53.1 | 79.9 | 74.5 | 79.3 | 76.7 | 69.0 | 68.0 | 78.4 |
| Mesostasis | 44.0 | 8.5 | 9.8 | 10.6 | 10.5 | 20.0 | 19.0 | 19.8 |
| Orthopyroxene | - | - | - | - | - | - | 2.0 | - |
| Oxides[1] | - | - | - | - | 0.6 | 1.0 | - | 1.0 |
| Plagioclase[1] | - | - | - | - | - | - | - | 0.1 |

[1] Oxide and plagioclase phases reported as distinct to those observed in the mesostasis

[a] Friedman Lentz et al. (1999)

[b] Imae et al. (2003)

[c] Sautter et al. (2002)

[d] Treiman (2005)

[e] Day et al. (2006)

Table 7.2

Representative major element composition from electron microprobe analyses (in wt. %)

| | Augite | | | | | |
|---|---|---|---|---|---|---|
| Oxide | **Core** | **Rim** | **Olivine** | **Plagioclase** | **K-Feldspar** | **Mesostatsis** |
| $SiO_2$ | 50.82 | 48.86 | 32.57 | 64.40 | 64.29 | 57.63 |
| $Al_2O_3$ | 1.03 | 1.64 | <0.03 | 21.56 | 18.75 | 14.07 |
| MgO | 11.84 | 8.64 | 15.00 | <0.03 | <0.03 | 0.48 |
| CaO | 19.01 | 18.09 | 0.56 | 3.15 | 0.40 | 4.13 |
| MnO | 0.45 | 0.53 | 1.09 | <0.05 | <0.05 | 0.33 |
| FeO | 15.74 | 20.57 | 50.57 | 0.63 | 0.76 | 17.01 |
| $TiO_2$ | 0.37 | 0.62 | <0.03 | <0.03 | <0.03 | 0.43 |
| $Cr_2O_3$ | 0.17 | <0.05 | <0.05 | <0.05 | <0.05 | <0.05 |
| $Na_2O$ | 0.29 | 0.33 | <0.03 | 8.90 | 2.02 | 4.53 |
| $K_2O$ | <0.03 | <0.03 | <0.03 | 1.35 | 13.20 | 1.04 |
| Total | 99.72 | 99.28 | 99.83 | 99.98 | 99.42 | 99.65 |

### 7.3.2 Rare Earth Element Chemistry

Rare earth element abundances were measured *in situ* in individual grains of olivine, augite, and apatite, as well as the bulk mesostasis groundmass. Representative REE and additional trace element concentration in the minerals and mesostasis are presented in Tables 7.3 and 7.4. Feldspar grains (plagioclase and K-feldspar) are restricted to the mesostasis with grain sizes too small for analysis by ion microprobe.

*7.3.2.1 Pyroxene (Augite)*

Figure 7.5 shows the typical light rare earth element (LREE)-depleted patterns (CI-normalized La/Sm; i.e., $[La/Sm]_{CI}$ ~0.4) of the augite in NWA 5790. The augites also exhibit a slight decrease from the middle- to heavy (HREE) earth elements ($[Gd/Lu]_{CI}$ ~ 1.5) resulting in an overall concave downward REE pattern. All augites exhibit small, negative Eu anomalies ($[Eu/Eu^*]_{CI}$ ~0.9, where $Eu^*$ is the interpolated value between the CI-normalized Sm and Gd abundances). Primary zoning of the REEs are visible from the core to rim in individual augite grains. The range of REE abundances in the augite is moderate, ranging from La ~1.5 to 3.2 x CI-chondrite abundances.

The elemental abundances of several trace and minor elements (i.e., Ti, Y, and Zr), in addition to the REE, were measured in the augite phenocrysts. The abundances of these elements are shown in Figure 7.6a-b. Both Y and Zr show a coherent, positive trend when plotted against Ti indicative of the incompatible nature of all three elements. The augite data from NWA 5790 closely parallel the Zr-Ti and Y-Ti trends observed in the other nakhlites and fall within the

composition range they define. However, the core values in NWA 5790 (i.e., the lowest concentrations measured) are markedly higher than the core values of most other nakhlites.

*7.3.2.2 Olivine*

Olivine phenocrysts in NWA 5790 exhibit an overall depletion in REE abundances (Lu ~ 1.2 x CI) with a significant enrichment in HREEs ($[Gd/Lu]_{CI}$ ~0.08). The overall REE pattern of the NWA 5790 olivine is comparable with both the pattern and absolute abundances, particularly in terms of HREE, with the other nakhlites (e.g., NWA 817 and Nakhla) (Fig. 7.7).

*7.3.2.3 Phosphate (Apatite)*

Apatite is restricted to the occurrence of small grains in the fine-grained mesostasis; however, the phase has extremely high REE abundances in NWA 5790 (La ~1100 × CI) (Fig. 7.8). Only slight variation is observed in the absolute abundances of REE among different apatite grains. The apatite is LREE-enriched ($[La/Lu]_{CI}$ ~50) with significant negative Eu anomalies ($Eu/Eu^{*}$ ~0.3). The REE pattern closely parallels the apatite patterns observed in other nakhlites (e.g., Nakhla and NWA 998).

*7.3.2.4 Mesostasis*

Figure 7.9 shows the typical REE pattern of the fine-grained mesostasis region in NWA 5790. The mesostasis is significantly LREE-enriched ($[La/Lu]_{CI}$ ~5-6) with minimal variation of absolute abundances across the groundmass (La~ 90-100 × CI). The mesostasis pattern in NWA 5790 closely parallels the REE patterns observed in the mesostasis regions of other nakhlites (e.g., NWA 817 and

MIL 03346). In addition, the mesostasis REE pattern is similar to the whole-rock pattern measured for NWA 5790, although the absolute REE abundances observed in the mesostasis are approximately a factor of 2 higher than the whole-rock.

## 7.4 DISCUSSION

### 7.4.1 Distribution of Rare Earth Elements in NWA 5790

The measured REE abundances enable the characterization of the overall REE budget (i.e., the distribution of REE among the various constituent phases) in the bulk NWA 5790 sample. The highest overall concentrations of REE are found within the minor phosphate phase, apatite. The highly LREE-enriched nature of the apatite means this phase is one of the main sources of LREE, as well as a significant source of Eu and HREE in the bulk rock. The large positive Eu anomaly observed in plagioclase makes this phase an additional significant contributor to the overall Eu budget in the bulk rock. The occurrence of the apatite and plagioclase in the interstitial groundmass means that a majority of the LREE (~ 90-95 %) and Eu (~85%) reside within the fine-grained mesostasis with a lesser amount of HREE (~55%). Other phases found within the mesostasis (e.g., oxides) contain very minimal amounts of REE and do not contribute significantly to the overall REE budget. The cumulate augite phenocrysts (and to a lesser amount, the olivine) contribute only slightly to the overall LREE and Eu budget; however, they are the main reservoir for the remaining HREE inventory (~45%).

Table 7.3

Representative *in situ* REE abudnances (in ppm)

| | Augite | | | | | | | | | | | |
|---|---|---|---|---|---|---|---|---|---|---|---|---|
| | Core | | | Rim | | | Olivine | | | Apatite | | | Mesostasis | | |
| La | 0.375 | ± | 0.051 | 0.805 | ± | 0.060 | 0.005 | ± | 0.002 | 263.180 | ± | 3.373 | 23.394 | ± | 1.197 |
| Ce | 1.668 | ± | 0.116 | 3.504 | ± | 0.135 | 0.004 | ± | 0.002 | 674.524 | ± | 6.208 | 55.745 | ± | 1.475 |
| Pr | 0.344 | ± | 0.023 | 0.697 | ± | 0.054 | 0.004 | ± | 0.002 | 85.636 | ± | 1.955 | 7.882 | ± | 0.397 |
| Nd | 1.762 | ± | 0.111 | 3.850 | ± | 0.235 | 0.049 | ± | 0.008 | 250.914 | ± | 5.379 | 29.223 | ± | 1.236 |
| Sm | 0.576 | ± | 0.051 | 1.288 | ± | 0.156 | 0.011 | ± | 0.007 | 46.925 | ± | 2.677 | 8.465 | ± | 0.791 |
| Eu | 0.174 | ± | 0.022 | 0.406 | ± | 0.054 | 0.008 | ± | 0.004 | 3.743 | ± | 0.240 | 2.366 | ± | 0.208 |
| Gd | 0.657 | ± | 0.052 | 1.467 | ± | 0.131 | 0.034 | ± | 0.011 | 32.134 | ± | 1.068 | 6.999 | ± | 0.403 |
| Tb | 0.122 | ± | 0.012 | 0.267 | ± | 0.031 | 0.004 | ± | 0.001 | 6.422 | ± | 0.362 | 1.206 | ± | 0.102 |
| Dy | 0.766 | ± | 0.063 | 1.668 | ± | 0.155 | 0.046 | ± | 0.012 | 28.712 | ± | 1.408 | 6.028 | ± | 0.396 |
| Ho | 0.163 | ± | 0.017 | 0.333 | ± | 0.040 | 0.012 | ± | 0.003 | 6.099 | ± | 0.410 | 1.173 | ± | 0.100 |
| Er | 0.430 | ± | 0.047 | 0.957 | ± | 0.127 | 0.052 | ± | 0.012 | 16.823 | ± | 1.070 | 3.294 | ± | 0.287 |
| Tm | 0.059 | ± | 0.008 | 0.137 | ± | 0.025 | 0.016 | ± | 0.004 | 1.534 | ± | 0.107 | 0.416 | ± | 0.026 |
| Yb | 0.402 | ± | 0.044 | 0.889 | ± | 0.117 | 0.109 | ± | 0.019 | 6.515 | ± | 0.576 | 2.769 | ± | 0.265 |
| Lu | 0.052 | ± | 0.008 | 0.122 | ± | 0.023 | 0.029 | ± | 0.006 | 0.539 | ± | 0.040 | 0.406 | ± | 0.030 |

Errors are 1σ errors from counting statistics only.

Table 7.4

Additional trace element abundances (in ppm) in augite

| Analysis | Ti | Y | Zr |
|---|---|---|---|
| S1 | 2347.08 ± 11.317 | 4.858 ± 0.150 | 4.624 ± 0.258 |
| S2 | 2384.58 ± 15.125 | 5.072 ± 0.218 | 4.335 ± 0.317 |
| S3 | 1962.13 ± 9.010 | 3.902 ± 0.125 | 2.820 ± 0.168 |
| S4 | 2288.25 ± 10.781 | 4.148 ± 0.143 | 3.573 ± 0.209 |
| S5 | 2391.49 ± 11.379 | 5.479 ± 0.170 | 5.052 ± 0.257 |
| S6 | 1994.39 ± 9.617 | 4.747 ± 0.146 | 3.590 ± 0.200 |
| S7 | 1704.00 ± 8.671 | 3.216 ± 0.118 | 2.069 ± 0.148 |
| S8 | 2583.91 ± 12.244 | 5.179 ± 0.171 | 5.230 ± 0.270 |
| S9 | 1813.61 ± 10.053 | 3.512 ± 0.138 | 2.600 ± 0.187 |
| S10 | 1753.99 ± 10.107 | 3.728 ± 0.145 | 2.859 ± 0.200 |
| S11 | 2467.22 ± 12.110 | 5.195 ± 0.173 | 5.038 ± 0.269 |
| S12 | 2224.15 ± 11.490 | 4.891 ± 0.178 | 4.305 ± 0.338 |
| S13 | 1386.63 ± 11.363 | 2.730 ± 0.149 | 1.446 ± 0.132 |
| S14 | 2276.88 ± 10.745 | 4.601 ± 0.151 | 3.876 ± 0.218 |
| S15 | 2420.71 ± 11.276 | 4.600 ± 0.153 | 4.990 ± 0.251 |
| S16 | 1762.08 ± 9.851 | 3.547 ± 0.138 | 2.233 ± 0.172 |
| S17 | 2200.65 ± 11.720 | 4.391 ± 0.184 | 4.443 ± 0.308 |
| S18 | 2120.77 ± 11.647 | 4.890 ± 0.174 | 3.531 ± 0.233 |
| S19 | 2071.59 ± 11.993 | 3.883 ± 0.162 | 2.408 ± 0.201 |
| S20 | 2222.65 ± 11.838 | 3.507 ± 0.147 | 3.172 ± 0.220 |

Uncertainties are 1σ from counting error only.

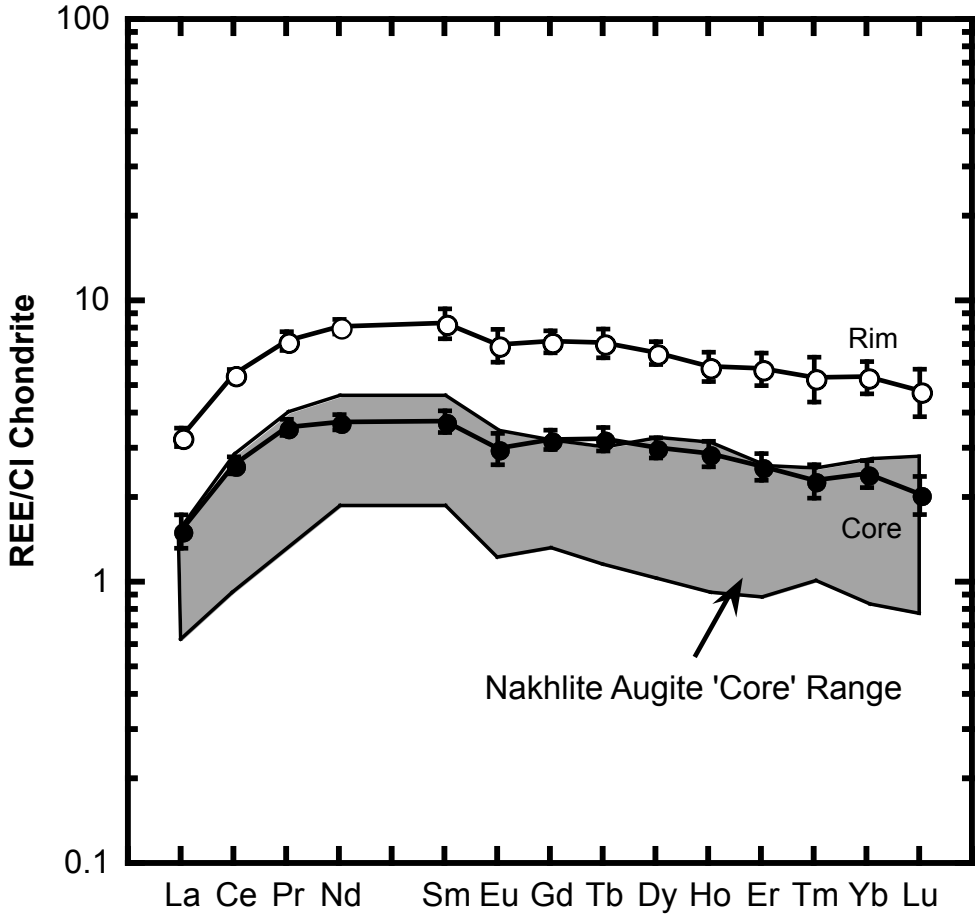


*Figure 7.5*- Range of CI-chondrite normalized REE abundances in the augite of NWA 5790. Filled and open circles represent the core and rim compositions, respectively. The shaded region indicates the range of core compositions observed in all other nakhlites (after Wadhwa and Crozaz, 1995; Wadhwa et al., 2004; Day et al., 2006).

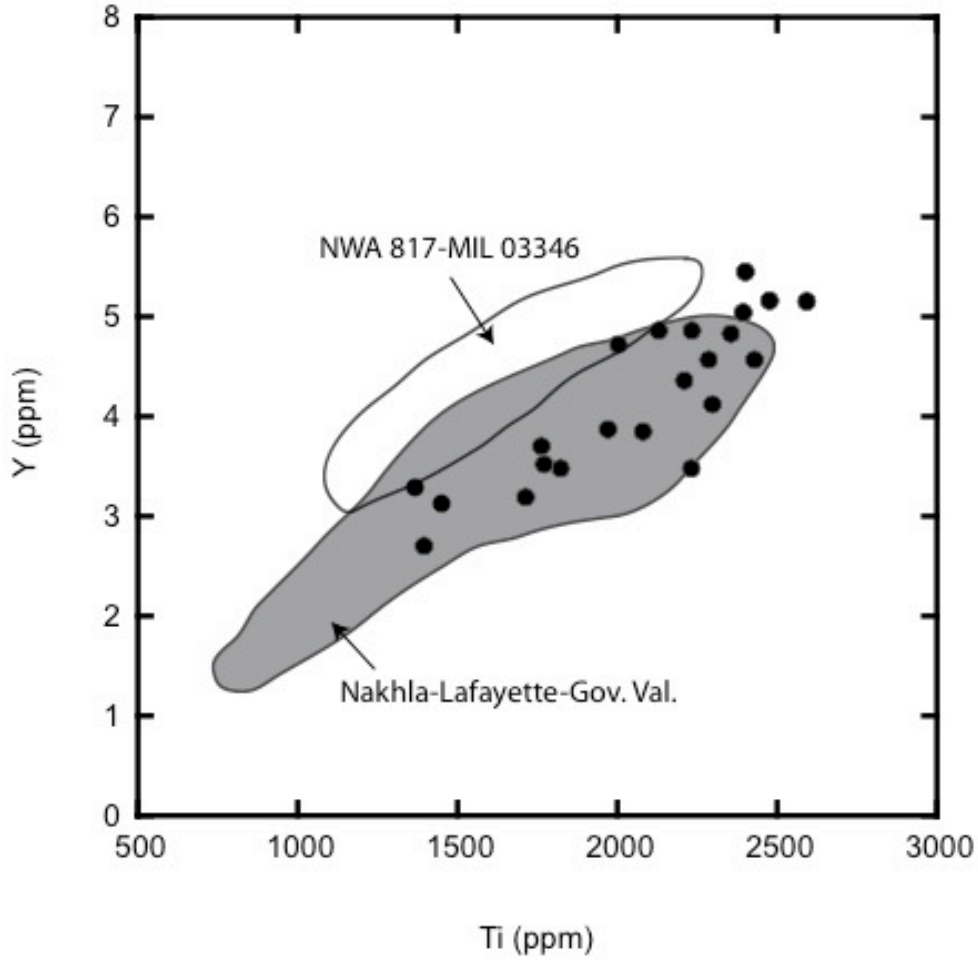


*Figure 7.6a*- Plot of Ti versus Y in augite of NWA 5790. Shown for comparison are the Ti-Y abundance range observed in Nakhla, Lafayette, Governador Valaderes (Gov. Val.), NWA 4801, and MIL 03346 (after Wadhwa and Crozaz, 1995; Wadhwa et al., 2004; Day et al., 2006)

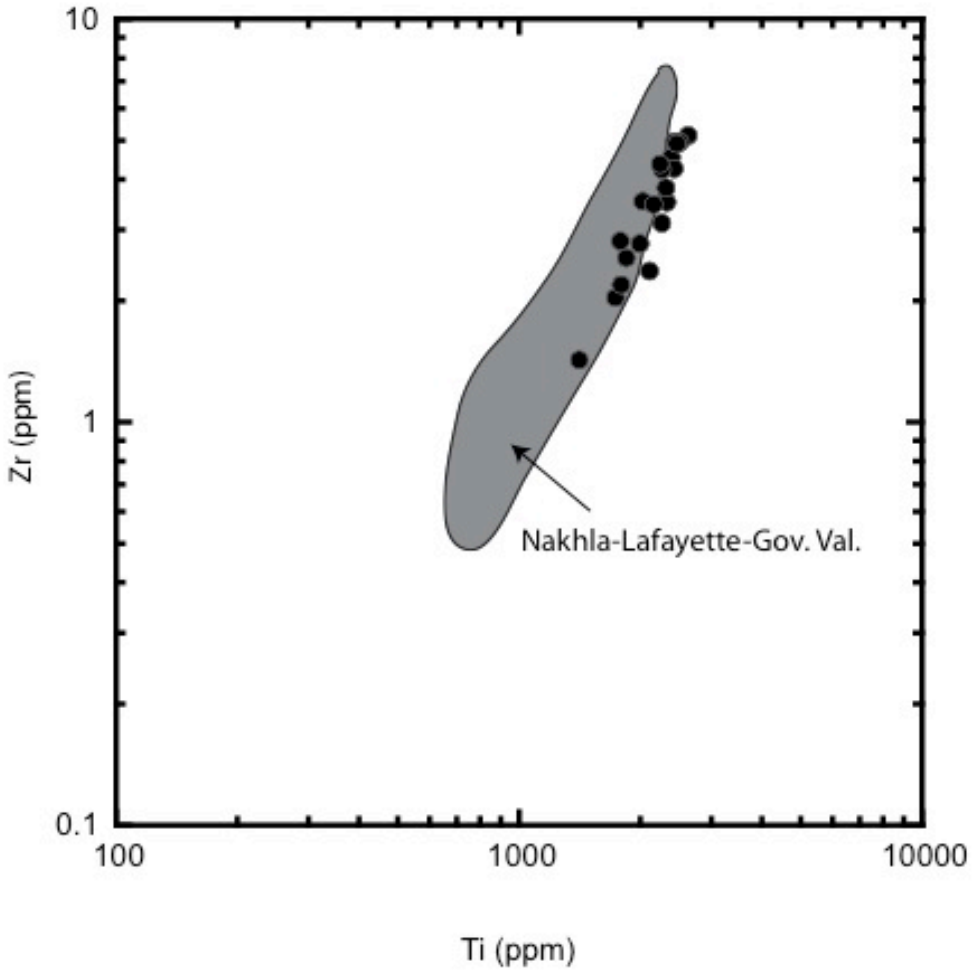


*Figure 7.6b*- Plot of Ti versus Zr in augite of NWA 5790. Shown for comparison is the Ti-Y abundance range observed in Nakhla, Lafayette, Governador Valaderes (Gov. Val) (after Wadhwa and Crozaz, 1995; Wadhwa et al., 2004)

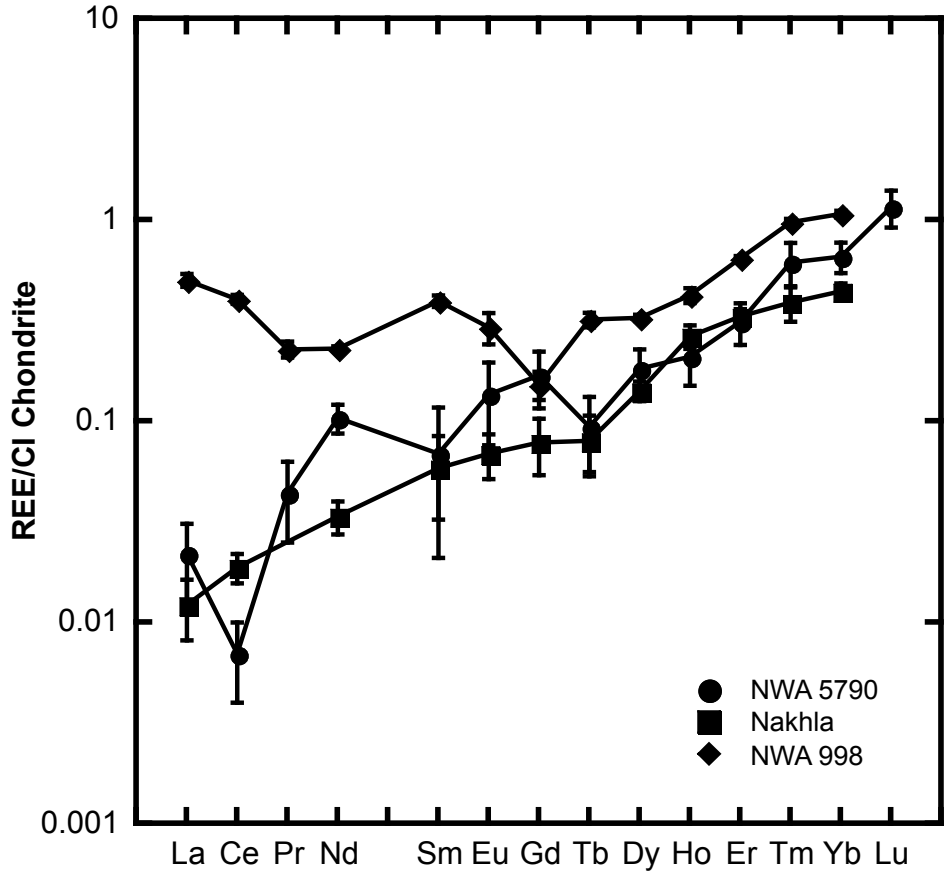


*Figure 7.7*- Representative CI-chondrite normalized REE abundances in the olivine of NWA 5790. Shown for comparison are the REE abundances observed in the nakhlites Nakhla and NWA 998 (after Wadhwa and Crozaz, 1995; Wadhwa et al., 2004).

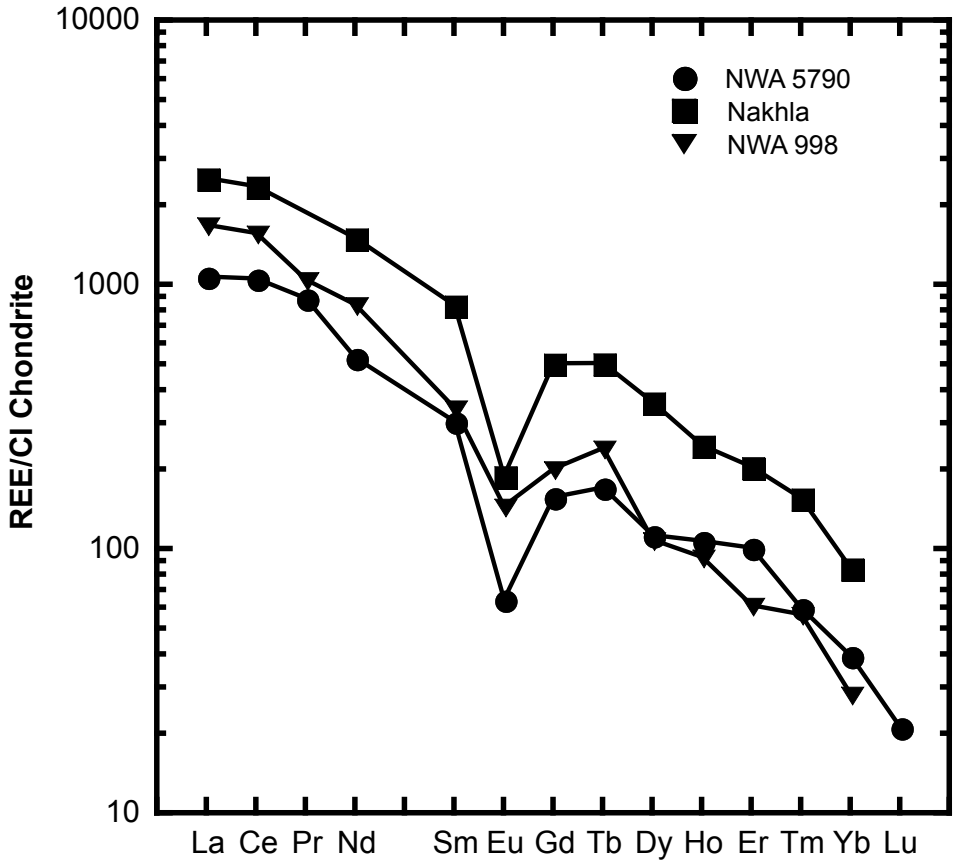


*Figure 7.8*- Representative CI-chondrite normalized REE abundances in the apatite of NWA 5790. Shown for comparison are the REE abundances observed in the nakhlites Nakhla and NWA 817 (after Wadhwa and Crozaz, 1995; Wadhwa et al., 2004).

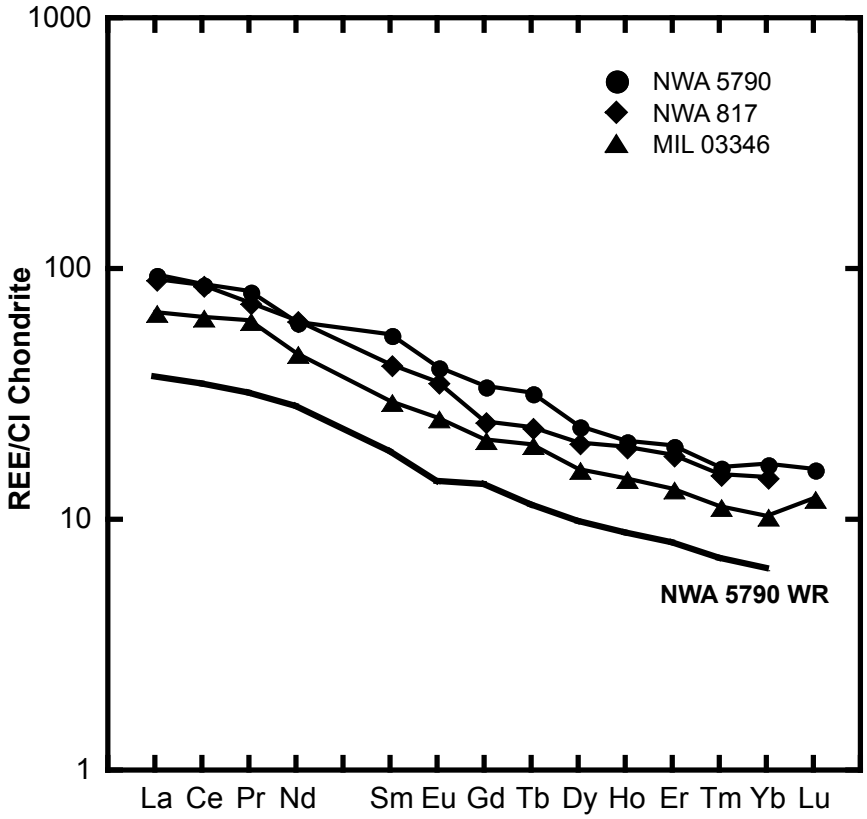


*Figure 7.9*- Representative CI-chondrite normalized REE abundances in the fine-grained mesostasis region of NWA 5790. Shown for comparison are the REE abundances observed in the nakhlites NWA 817 and MIL 03346 (after Wadhwa et al., 2004; Day et al., 2006). Also shown are the measured whole-rock REE abundances from Jambon et al. (2010).

Verification that all phases contributing to the REE budget have been analyzed can be accomplished by performing a mass balance calculation. In this calculation, the average REE abundances of each phase and the modal abundances of the phases (converted to wt. %) are used to generate a calculated whole-rock composition. For the purposes of this calculation, the bulk mesostasis composition and abundance is used instead of plagioclase and apatite individually due to the difficulty of modal abundance determinations of these minor phases in the fine-grained groundmass. Figure 7.10 shows the comparison of the calculated whole-rock composition to the measured bulk-rock of Jambon et al. (2010). The whole-rock composition calculated from the *in situ* analyses is indistinguishable from the measured whole-rock pattern. The strong agreement between the calculated and measured whole-rock indicates: (1) all the phases that are major REE contributors have been analyzed and (2) the petrographic determination of modal abundances has provided values representative of the bulk sample. The latter of these two implications is important as variation in estimates of modal occurrence can range by a moderate amount from study to study (This Study; Jambon et al., 2010)

### 7.4.2 Calculation of Parent Melt REE composition

The cumulate nature of nakhlites presents challenges in deciphering the parent melt composition from which the samples originated. This difficulty is particularly evident in trying to determine the major element composition of the parent melt (Treiman, 2005, references therein). Bulk chemistry techniques require a sample be representative of the bulk mineralogy in order to yield

accurate major element results. However, such representative samples, which require a large amount of material, are not readily available for nakhlites given the limited sample mass available for bulk chemistry techniques. Further attempts to constrain the major element composition of parent melts have been made utilizing trapped melt inclusions within olivine (e.g., Harvey and McSween, 1992; Treiman, 1993) and augite (e.g., Varela et al., 2001; Stockstill et al., 2005) phenocrysts with contradictory results among the different studies. While difficulty persists in determining the major element composition of the parent melt, the determination of the trace element composition of the parent melts has proven to be a more robust method to aid in deciphering the nature of the parent melt of individual nakhlites.

The use of *in situ* trace element measurements to determine the rare earth element composition of the parent melt of an individual nakhlite has been applied to a range of samples, such as Nakhla, Lafayette, Governador Valaderes, Yamato 000593, NWA 817, NWA 998, and Millers Range 03346 (Wadhwa and Crozaz, 1995; Wadhwa et al., 2004; Day et al., 2006. The calculation is accomplished using the core values (i.e., analyses that yield the lowest concentrations) of the augite *in situ* analyses. Geochemical modeling (e.g., Stockstill et al., 2005) and petrologic observations (Treiman 2005, references therein) suggest formation of augite phenocrysts early in the nakhlite crystallization sequence before the crystallization of other phases that would significantly modify the trace element composition of the parental liquid. Therefore, the calculation of the melt in equilibrium with the augite core should yield an estimate for the trace element

composition of the parent melt from which NWA 5790 formed. The concentration of a given trace element in the parent melt (i.e., the melt in equilibrium with the augite core) is determined using the relationship:

$$C_{E\,(Melt)} = \frac{C_{E\,(Augite)}}{D_E} \qquad \text{Eq. (7.1)}$$

where $C_E$ is the concentration of a given element, $E$, in the augite core or parent melt and $D_E$ is the experimentally determined partition coefficient for that element. $D$-values used for determining the parent melt composition in NWA 5790 are those determined experimentally by Oe et al. (2002) using synthetic samples of nakhlite pyroxene compositions.

The parallel nature of normalized trace element patterns of the parent melt and whole-rock composition in martian meteorites has long been suggested to indicate the evolution of the sample, after pyroxene crystallization, in a geochemically closed-system (e.g., Harvey and McSween, 1992; Wadhwa et al., 1994; Wadhwa and Crozaz, 1995). As shown in Figure 7.11, the parent melt of NWA 5790 is LREE-enriched and has a REE pattern that closely parallels the measured whole-rock composition of NWA 5790 (Jambon et al., 2010), as well as the parent melts of several other nakhlites calculated using augite core compositions (Wadhwa and Crozaz, 1995; Wadhwa et al., 2005; Day et al., 2006). Therefore, it follows that after the crystallization of augite, NWA 5790 continued to crystallize in closed-system conditions. While partition coefficients are not available for late stage crystallizing phases, such as apatite, a comparison of the bulk mesostasis shows a parallel pattern with both the whole-rock and the parent melt, providing further evidence for a geochemically closed-system throughout

the crystallization sequence. Similar REE patterns observed for the parent melts in the range of nakhlites indicates that all nakhlites formed from a geochemically similar source material, although the trace element abundances varies by a factor of 5 across the range of nakhlites with NWA 5790 having among the highest concentrations (see section 7.4.4.2 for further discussion on the implications of the observed abundances).

### 7.4.3 Estimation of Oxygen Fugacity Conditions ($fO_2$) of the Nakhlites

Estimations of the oxygen fugacity ($fO_2$) at the time of crystallization provide the opportunity to establish additional constraints on formation conditions. The redox conditions occurring during the formation of the nakhlites have only been generally constrained due to the limited number of samples that have been available. The earliest estimates of the oxygen fugacity conditions occurring during nakhlite crystallization were established using the Ti-Fe oxide oxybarometer, specifically on the type specimen Nakhla (Reid and Bunch, 1975; Delano and Arculus, 1980). Estimates from these early studies of Nakhla indicated relatively oxidizing conditions at the time of formation, but quantitative estimates were poorly constrained with estimates ranging from 1 log unit below the quartz-fayalite-magnetite buffer (i.e, QFM-1) by Reid and Bunch (1975) to almost QFM-3 by Delano and Arculus (1980). Several recent studies (e.g., Makishima et al., 2007; Szymanski et al., 2010) expanded the application of the oxide oxy-barometer to several additional nakhlites with all samples yielding similar $fO_2$ values that average around QFM to within 1 log unit below QFM.

An alternative method for estimation of the $fO_2$ utilizes the partitioning behavior of Eu from Gd in pyroxenes under various oxygen fugacity conditions (Wadhwa, 2001) with the Eu/Gd-oxybarometer, when utilized in nakhlite augites, particularly useful for understanding the early redox conditions of a given sample (Wadhwa et al., 2004). The initial use of the Eu/Gd-oxybarometer in nakhlites (e.g, Wadhwa et al., 2004) was limited to qualitative comparison to a single point calibration of Eu/Gd partitioning at $fO_2$ ~ QFM (Oe et al., 2002). However, even with the limited calibration data, all nakhlite augites analyzed by Wadhwa et al. (2004) indicated crystallization near $fO_2$ ~ QFM. Subsequent experimental work (e.g., Makishima et al., 2007) has expanded the $D_{Eu}/D_{Gd}$ versus $fO_2$ calibration curve to three points for nakhlite pyroxene composition. Following the methods described in Wadhwa et al. (2004), a $D_{Eu}/D_{Gd}$ value of 0.80±0.10 was calculated for NWA 5790, using the Eu/Gd ratio in the augite core composition measured in this study and the whole-rock composition determined by Jambon et al. (2010). Using the calibration curve determined by Makishima et al. (2007), this value corresponds to an oxygen fugacity for NWA 5790 at the time of crystallization of ~QFM+0.5(±1.0) (uncertainties from the errors in the Eu and Gd abundances only). The $fO_2$ conditions recorded in NWA 5790 are indistinguishable from previous estimates of nakhlite $fO_2$ conditions using Eu/Gd partitioning (e.g., Wadhwa et al., 2004). The agreement in $fO_2$ estimates across a range of nakhlites and between the estimates from augite Eu/Gd-oxybarometry and Fe-Ti oxide barometry suggest that oxygen fugacity conditions remained relatively constant (at ~ QFM) during the duration of nakhlite formation. However, it is important to

note that not all oxybarometers are in agreement with this scenario. Recent work by McCanta et al. (2009) utilized the partitioning behavior of Eu from Sm to estimate $fO_2$ conditions and noted a difference in the $fO_2$ estimates between those determined using the Fe-Ti oxide-oxybarometer and those calculated using Eu/Sm partitioning. McCanta et al. (2009) have suggested that this discrepancy may be recording a change in $fO_2$ conditions during the crystallization history of at least some of the nakhlites, while other nakhlites (e.g., MIL 03346) yield consistent $fO_2$ estimates. The discrepancy in the McCanta et al. (2009) estimates also extends to the estimates of the Eu/Gd-oxybarometer. The agreement between the Eu/Gd oxy-barometer estimates and the estimates using the Fe-Ti oxide-oxybarometer suggest a consistent, oxidizing formation environment for the nakhlites; however, the results of McCanta et al. (2009) may indicate the need for further refinement of the oxybarometer calibrations of one or more systems.

### 7.4.4 Geochemical Comparison: Evidence for an Evolving Melt

A comparison of the petrographic and geochemical characteristics among the limited number nakhlites provides the opportunity to develop an understanding of the comparative petrogenesis of the nakhlite group. A comparison of geochemical measurements of NWA 5790 indicate both a broad geochemical similarity to the other nakhlites , but also distinctive characteristics that provide new insight into the evolution of the parent melt from which the nakhlites originated. As discussed previously, the broad geochemical similarities appear to indicate a likely common geochemical source material for all the nakhlites. However, the distinct characteristics observed in NWA 5790 point to a

geochemically evolving melt during the crystallization of the nakhlite cumulate pile.

*7.4.4.1 Petrography*

In terms of petrography, nakhlites exhibit a significant variation in modal abundance of cumulate silicate phenocryst phases (augite and olivine) and the fine-grained groundmass mesostasis. As shown in Table 7.1, this variation ranges from 10% mesostasis and ~90% cumulate phases in Nakhla (Friedman Lentz et al., 1999) to as much as ~44% mesostasis and ~56% cumulate in NWA 5790 as observed in this work. Several studies (e.g., Mikouchi et al., 2003; Day et al., 2006) have suggested a stratigraphic profile for the nakhlite cumulate pile where the depth of a nakhlite in a cumulate pile is a function of an inferred cooling rate, based on the amount of mineral equilibration, as well as mesostasis and cumulate phenocryst abundance. Based on these parameters and a formation model of a nakhlite cumulate pile through crystal settling (Freidman-Lentz et al., 1999), the petrography of NWA 5790 indicates it likely formed in the upper limits of the nakhlite cumulate pile (based on the known nakhlites thus far).

*7.4.4.2 Comparative Major and Trace Element Chemistry*

The *in situ* analyses obtained for the various mineral phases, in particular the augite, provide indications that the augite phenocrysts crystallized from a relatively evolved geochemical melt. The trace element abundances in the cores of the augite phenocrysts in NWA 5790 yield among the highest absolute abundances of REE (Fig. 7.5), as well as other trace and minor elements such as Ti, Y, and Zr (Fig. 7.6a-b), observed in the nakhlites. The relative enrichment is

also observable in the calculated parent melt of NWA 5790, which utilizes the core values in the augite (Fig. 7.10). Other silicate phases, such as plagioclase and olivine, generally have trace element concentrations too low to observe relative enrichment. Further evidence for a more geochemically evolved melt can be observed in the major element composition of the silicates, in particular the augite. A comparison of the augite core compositions of NWA 5790 with the compositions observed in the other nakhlites indicates that the NWA 5790 augite cores are the most Fe-rich in composition. In a geochemically closed-system undergoing fractional crystallization, the cores of the augite would be expected to gradually evolve from Mg-rich to a more Fe-rich composition, while the parent melt would undergo an increase in incompatible trace element abundances. As such, the geochemical characteristics of the augite cores for NWA 5790 (i.e., Fe-rich and elevated trace element abundances) indicate a geochemically evolved parental melt, relative to most nakhlites with only NWA 817 showing similar, although slightly lower enrichments.

The bulk mesostasis in NWA 5790 also displays unique geochemical characteristics when compared with other nakhlites. The mesostasis has REE abundances higher than a majority of nakhlites with an analogous pattern and abundances to those observed in NWA 817 (Fig. 7.9). Comparing the REE abundances in NWA 5790 with the mesostasis in the nakhlites with the least modal abundance of mesostasis (e.g., Y-00593; Wadhwa et al., 2004), intermediate mesostasis modal abundance (e.g., MIL 00346; Day et al., 2006) to the most mesostasis-rich (NWA 5790; this study), there appears to be a positive

correlation with increasing REE abundances as a function of modal abundance of mesostasis. Following the cumulate pile model of Mikouchi et al. (2003) and Day et al. (2006), the positive correlation indicates the interstitial melts (represented by the mesostasis) sampled an increasingly more evolved melt towards the top of the cumulate pile, similar to the geochemical observations in the augite cores.

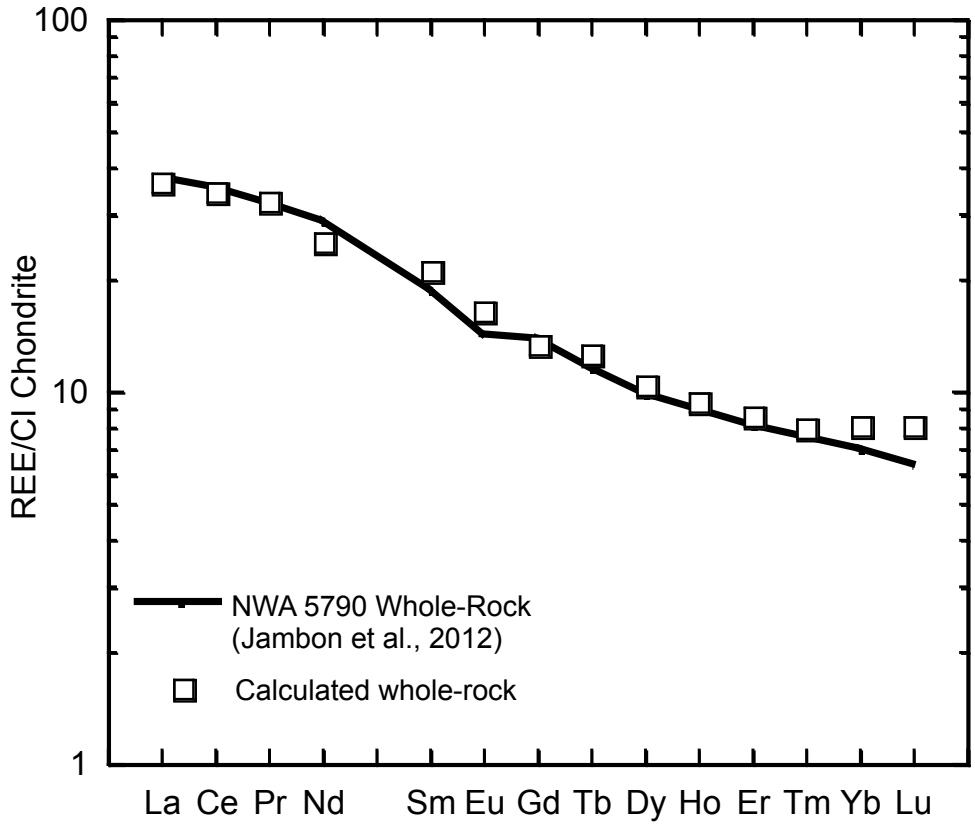


*Figure 7.10*- Comparison of calculated versus measured whole-rock REE abundances in NWA 5790. Solid line is the measured whole-rock composition reported by Jambon et al. (2010). Squares indicated the calculated whole-rock REE abundances (see text for details of the calculation).

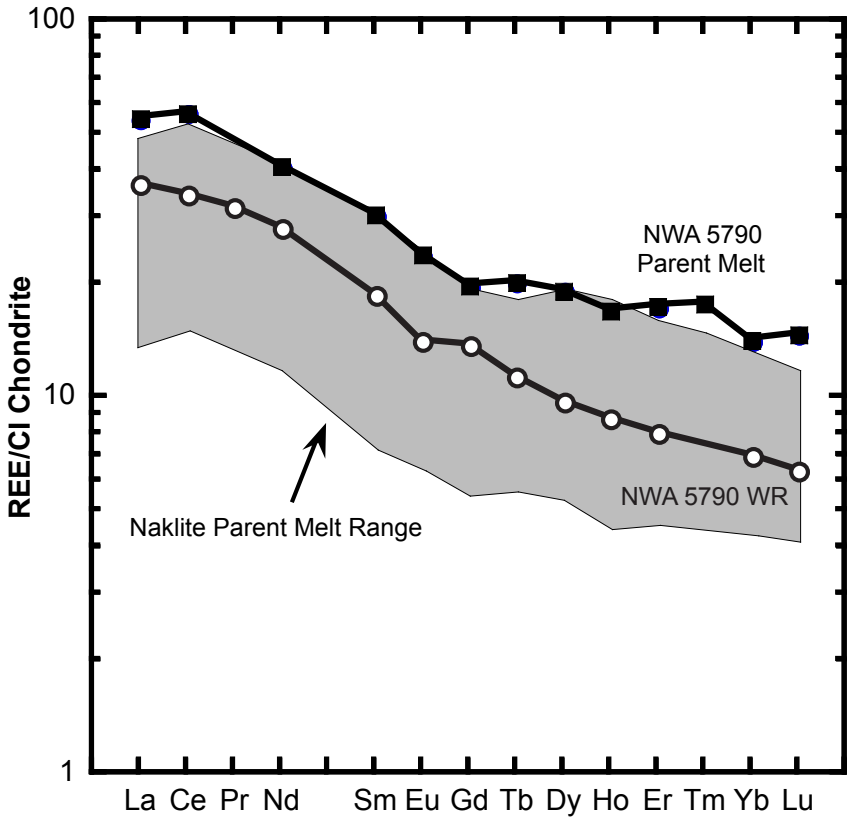


*Figure 7.11*- Calculation of the melt in equilibrium with the augite cores (i.e., parent melt) of NWA 5790 (solid squares) shown in comparison with the reported NWA 5790 whole-rock composition (open circles) (Jambon et al., 2010). The range observed for the parent melts calculated for other nakhlites is indicated by the gray shaded region (data from Wadhwa and Crozaz, 1995; Wadhwa et al., 2004; Day et al., 2006). D-values used for the parent melt calculation are from Oe et al. (2002) (see text for details of calculation).

## 7.5 CONCLUSIONS

The unique position inferred for NWA 5790 towards the upper limit of the nakhlite cumulate pile has provided a renewed look at the petrogenesis of the nakhlite cumulate pile from the perspective of the late stages of formation. First, the strong similarities in the overall REE pattern for NWA 5790 and those of the other nakhlites indicates that NWA 5790 and all nakhlites likely originated from a similar, if not identical, parent melt. The variations in the abundances observed within the parent melts suggest an evolving melt with NWA 5790 sampling the most evolved portion of the melt, as indicated from the augite cores and the bulk mesostasis REE compositions. Second, the parallelism of the normalized trace element pattern between the melt in equilibrium with the augite cores with that of the bulk mesostasis and the measured whole-rock strongly indicate the crystallization of NWA 5790 in a geochemically closed-system from the point of augite crystallization onward. Third, the redox conditions estimated using Eu/Gd partitioning are identical with previous estimates for nakhlites using the same Eu/Gd-oxybarometer system, as well as oxide oxybarometry. This observation indicates that the redox conditions during nakhlite formation remained consistent during the timespan encompassing augite formation.

REFERENCES

Albarède F., Scherer E., Blichert-Toft J., Rosing M., Simionovici A., and Bizzarro M. (2006) γ-ray irradiation in the early solar system and the conundrum of the $^{176}$Lu decay constant. *Geochim. Cosmochim. Acta* **70**, 1261-1270.

Amelin Y. (2008) U-Pb ages of angrites. *Geochim. Cosmochim. Acta* **72**, 221-232.

Amelin Y. and Irving A. J. (2007) Seven million years of evolution on the angrite parent body from Pb-isotopic data. *Workshop on the Chronology of Meteorites*. Lunar Planet. Inst., Houston. #4061 (abstract).

Amelin Y., Wimpenny J., and Yin Q.-Z. (2011) Angrite Lu-Hf whole rock data provide no direct support to accelerated decay of $^{176}$Lu by supernova irradiation. *Conference on Formation of First Solids in the Solar System.* Lunar Planet. Inst., Houston. #9014 (abstract).

Anand M., James S., Greenwood R. C., Johnson D., Franchi I. A., and Grady M. M. (2008) Mineralogy and geochemistry of shergottite RBT 04262. *Lunar Planet. Sci. XXXIX*. Lunar Planet Inst., Houston. #2173 (abstract).

Anders E. and Grevasse N. (1989) Abundances of the elements: Meteoritic and solar. *Geochim. Cosmochim. Acta* **53**, 197-214.

Bard J. P. (1986) Microtextures of igneous and metamorphic rocks. In *Petrology and structural geology*, pp. 248. D. Reidel Publishing Company, Dordrecht.

Barnes S. J. and Roeder P. L. (2001) The range of spinel compositions in terrestrial mafic and ultramafic rocks. *J. Petrol.* **42**, 2279-2302.

Barrat J. A., Jambon A., Bohn M., Gillet P., Sautter V., Gopel C., Lesourd M., and Keller F. (2002) Petrology and chemistry of the picritic shergottite North West Africa 1068 (NWA 1068). *Geochim. Cosmochim. Acta* **66**, 3505-3518.

Beckett J. R., C. M. M., and Stolper E. M. (2008) Phosphorus zoning in SNC olivines. *Lunar Planet. Sci. XXXIX*. Lunar Planet Inst., Houston. #1726 (abstract).

Bence A. E. and Papike J. J. (1972) Pyroxenes as recorders of lunar basalt petrogenesis: Chemical trends due to crystal-liquid interaction. *Proc. Lunar Planet. Sci. Conf.* **3**, 431-469.

Bizzarro M., Baker J. A., Haack H., Ulfbeck D., and Rosing M. (2003) Early history of Earth's crust-mantle system inferred from hafnium isotopes in chondrites. *Nature* **421**, 931-933.

Bizzarro M., Connelly J. N., Thrane K., and Borg L. E. (2012) Excess hafnium-176 in meteorites and the early Earth zircon record. *Geochim. Geophys. Geosyst.* **13**, Q03002, doi:10.1029/2011GC004003.

Blichert-Toft J., Boyet M., Télouk P., and Albarède F. (2002) 147Sm-143Nd and 176Lu-176Hf in eucrites and the differentiation of the HED parent body. *Earth Planet. Sci. Lett.* **204**, 167-181.

Borg L. E. and Draper D. S. (2003) A petrogenetic model for the origin and compositional variation of the Martian basaltic meteorites. *Meteorit. Planet. Sci.* **38**, 1713-1731.

Borg L. E., Gaffney A. M., and DePaolo D. J. (2008) Preliminary age of martian meteorite Northwest Africa 4468 and its relationship to the other incompatible-element-enriched shergottites. *Lunar Planet. Sci. XXXIX*. Lunar Planet Inst., Houston. #1851 (abstract).

Borg L. E., Nyquist L. E., Taylor L. A., Wiesmann H., and Shih C.-Y. (1997) Constraints on Martian differentiation processes from Rb-Sr and Sm-Nd isotopic analyses of the basaltic shergottite QUE 94201. *Geochim. Cosmochim. Acta* **61**, 4915-4931.

Borg L. E., Nyquist L. E., Wiesmann H., and Reese Y. (2002) Constraints on the petrogenesis of Martian meteorites from the Rb-Sr and Sm-Nd isotopic systematics of the lherzolitic shergottites ALHA77005 and LEW 88516. *Geochim. Cosmochim. Acta* **66**, 2037-2053.

Bouvier A. and Wadhwa M. (2010) The age of the Solar System redefined by the oldest Pb-Pb age of a meteoritic inclusion. *Nature Geoscience* **3**, 637-641.

Bouvier A., Blichert-Toft J., Vervoort J. D., and Albarede F. (2005) The age of SNC meteorites and the antiquity of the Martian surface. *Earth Planet. Sci. Lett.* **240**, 221-233.

Bouvier A., Vervoort J. D., and Patchett P. J. (2008) The Lu-Hf and Sm-Nd isotopic composition of CHUR: constraints from unequilibrated chondrites and implications for the bulk composition of terrestrial planets. *Earth Planet. Sci. Lett.* **273**, 48-57.

Bouvier A., Blichert-Toft J., Vervoort J. D., Gillet P., and Albarede F. (2008) The case for old basaltic shergottites. *Earth Planet. Sci. Lett.* **266**, 105-124.

Bouvier A., Brennecka G. A., Sanborn, M. E., and Wadhwa M. (2011) The formation of the angritic crust. *Mineralogical Magazine* **75**, 565.

Boyet M. and Carlson R. W. (2005) $^{142}$Nd evidence for early (>4.53 Ga) global differentiation of the silicate earth. *Science* **309**, 576-581.

Boyet M., Carlson R. W., and Horan M. (2010) Old Sm-Nd ages for cumulate eucrites and redetermination of the solar system initial $^{146}$Sm/$^{144}$Sm ratio. *Earth Planet. Sci. Lett.* **291**, 172-181.

Brennecka G. and Wadhwa M. (2012) Uranium isotope compositions of the basaltic angrite meteorites and the chronological implications for the early solar system. *Proc. Nat. Acad. Sci. USA* **109**, 9299-9303.

Bridges J. C. and Warren P. H. (2006) The SNC meteorites: basaltic igneous processes on Mars. *Journal. Geol. Soc. London* **163**, 229-251.

Bunch T. E., Irving A. J., Wittke J. H., and Kuehner S. M. (2005) Northwest Africa 2646: A Martian plagioclase-olivine clinopyroxenite akin to "lherzolitic shergottites". *Meteorit. Planet. Sci.* **40**, A25-A25.

Carmichael I. S. E. (1967) The iron-titanium oxides of salic volcanic rocks and their associated ferromagnesian silicates. *Contrib. Mineral. Petrol.* **14**, 36-64.

Cartwright J. A., Burgess R., Crowther S. A., and Gilmour J. D. (2008) Xenon isotope composition of shergottite RBT 04262. *Lunar Planet. Sci. XXXIX*. Lunar Planet Inst., Houston. #2000 (abstract).

Christen F., Eugster O., and Busemann H. (2005) Mars ejection times and neutron capture effects of the naklites Y000593 and Y000749, the olivine-phyric shergottite Y980459, and the lherzolite NWA1950. *Antarct. Meteorite Res.* **18**, 117-132.

Crozaz G. and McKay G. (1990) Rare earth elements in Angra dos Reis and Lewis Cliff 86010, two meteorites with similar but distinct magma evolutions. *Earth Planet. Sci. Lett.* **97**, 369-381.

Crozaz G., Floss C., and Wadhwa M. (2003) Chemical alteration and REE mobilization in meteorites from hot and cold deserts. *Geochim. Cosmochim. Acta* **67**, 4727-4741.

Dalton H. A., Peslier A. H., Brandon A. D., Lee C.-T., and Lapen T. J. (2008) Petrology and mineral chemistry of new olivine-phyric shergottite RBT 04262. *Lunar Planet. Sci. XXXIX*. Lunar Planet Inst., Houston. #2308 (abstract).

Day J. M. D., Taylor L. A., Floss C., and McSween H. Y. Jr (2006) Petrology and chemistry of MIL 03346 and its significance in understanding the petrogenesis of nakhlites on Mars. *Meteor. Planet. Sci*. **41**, 581-606.

Delano J. W. and Arculus R. J. (1980) Nakhla: Oxidation state and other constraints. *Lunar Planet. Sci. Conf XI.* **11**, 219-221 (abstract).

Eugster O. and Weigel A. (1995) Multiple break-up of the angrite parent asteroid: Asuka 881371 and other angrites. *Meteoritics*. **30**, 504 (abstract).

Eugster O., Weigel A., and Polnau E. (1997) Ejection times of martian meteorites. *Geochim. Cosmochim. Acta* **61**, 2749-2757.

Fabries J. (1979) Spinel-Olivine Geothermometry in Peridotites from Ultramafic Complexes. *Contrib. Mineral. Petrol.* **69**, 329-336.

Fletcher I. R. and Rosman K. J. R. (1982) Precise determination of initial εNd from Sm-Nd isochron data. *Geochim. Cosmochim. Acta* **46**, 1983-1987.

Floss C., Crozaz G., McKay G., Mikouchi T., and Killgore M. (2003) Petrogenesis of angrites. *Geochim. Cosmochim. Acta* **67**, 4775-4789.

Friedman Lentz R. C., Taylor G. J., and Treiman A. H. (1999) Formation of a martian pyroxenite: A comparative study of the nakhlite meteorites and Theo's Flow. *Meteor. Planet. Sci.* **34**, 919-932.

Gellissen M., Palme H., Korotev R. L., and Irving A. J. (2007) NWA 2999, a unique angrite with a large chondritic component. *Lunar Planet. Sci. XXXVIII*. Lunar Planet. Inst., Houston. #1612 (abstract).

Goodrich C. A. (2002) Olivine-phyric Martian basalts: A new type of shergottite. *Meteorit. Planet. Sci.* **2002**, B31-B34.

Goodrich C. A., Herd C. D. K., and Taylor L. A. (2003) Spinels and oxygen fugacity in olivine-phyric and lherzolitic shergottites. **38**, 1773-1792.

Greenwood J. P. (2008) Gypsum and jarosite in Roberts Massif 04262: Antarctic (?) weathering as a proxy for Martian weathering. *Lunar Planet. Sci. XXXIX*. Lunar Planet Inst., Houston. #2011 (abstract).

Gray C. M., Papanastassiou D. A., and Wasserburg G. J. (1973) The identification of early condensates from the Solar Nebula. *Icarus* **20**, 213-239.

Hans U., Kleine T., and Bourdon B. (2011) Strontium isotope anomalies in Ca-Al-rich inclusions and the Rb-Sr chronology of volatile depletion revisited. *Lunar Planet. Sci. XLII*. Lunar Planet. Inst., Houston. #2672 (abstract).

Harvey R. P. and McSween H. Y. Jr (1992) The parent magma of the nakhlite meteorites: Clues from melt inclusions. *Earth Planet. Sci. Lett.* **111**, 467-482.

Harvey R. P., Wadhwa M., McSween Jr H. Y., and Crozaz G. (1993) Petrography, mineral chemistry, and petrogenesis of Antarctic Shergottite LEW 88516. *Geochim. Cosmochim. Acta* **57**, 4769-4783.

Herd C. (2006) Insights into the redox history of the NWA 1068/1110 martian basalt from mineral equilibria and vanadium oxybarometry. *Am. Mineral.* **91**, 1616-1627.

Herd C. D. K., Borg L. E., Jones J., and Papike J. J. (2002) Oxygen fugacity and geochemical variations in the Martian basalts: Implications for Martian basalt petrogenesis and the oxidation state of the upper mantle of Mars. *Geochim. Cosmochim. Acta* **66**, 2025-2036.

Hinton R. W. (1990) Ion microprobe trace-element analysis of silicates: Measurement of multi-element glasses. *Chemical Geology* **83**, 11-25.

Hsu W. (1995) Ion microprobe studies of the petrogenesis of enstatite chondrites and eucrites. Ph.D. thesis, Washington University.

Ikeda Y. (1997) Petrology and mineralogy of the Y-793605 Martian meteorite. *Antarct. Meteorite Res.* **10**, 13-40.

Imae N., Ikeda Y., Shinoda K., Kojima K., and Iwata N. (2003) Yamato nakhlites: Petrography and mineralogy. *Antarct. Meteor. Res.* **16**, 13-33.

Irving A. J., Kuehner S. M., Rumble D., Bunch T. E., and Wittke J. H. (2005) Unique angrite NWA 2999: The case for samples from mercury. *Fall 2005 American Geophysical Union Meeting*. #P51A-0898 (abstract).

Irving A. J., Kuehner S. M., and Rumble D (2006) A fresh plutonic igneous angrite containing grain boundary glass from Tamassint, Northwest

Africa. *Fall 2006 American Geophysical Union Meeting*. #P51E-1245 (abstract).

Irving A. J. and Kuehner S. M. (2007) Plutonic angrite NWA 4801 and a model for the angrite parent body consistent with petrological and chronological constraints. *Workshop on the Chronology of Meteorites*. Lunar Planet. Inst., Houston. #4050 (abstract).

Irving A. J., Kuehner S. M., Korotev R. L., and Hupe G. M. (2007) Petrology and bulk composition of primitive enriched olivine basaltic shergottite Northwest Africa 4468. *Lunar Planet. Sci. XXXVIII*. Lunar Planet Inst., Houston. #1526 (abstract).

Jacobonsen S. B. and Wasserburg G. J. (1984) Sm-Nd isotopic evolution of chondrites and achondrites, II. *Earth Planet. Sci. Lett.* **67**, 137-150.

Jambon A., Barrat J-. A., Boudouma O., Fonteilles M., Badia D., Göpel C., and Bohn M. (2005) Mineralogy and petrology of the angrite Northwest Africa 1296. *Meteor. Planet Sci.* **40**, 361-375.

Jambon A., Barrat J-.A., Bollinger C., Sautter V., Boudouma O., Greenwood R. C., Franchi I. A., and Badia D. Northwest Africa 5790: Top sequence of the nakhlite pile. *Lunar Planet. Sci. Conf. XLI*. Lunar Planet. Inst., Houston #1696 (abstract).

Jolliff B. L., Hughes J. M., Freeman J. J., and Zeigler R. A. (2006) Crystal chemistry of lunar merrillite and comparison to other meteoritic and planetary suites of whitlockite and merrillite. *Am. Mineral.* **91**, 1583-1595.

Jurewicz A. J. G., Mittlefehldt D. W., and Jones J. H. (1991) Melting of the Allende (CV3) meteorite: Implications for origins of basaltic meteorites. *Science* **252**, 695-698.

Jurewicz A. J. G., Mittlefehldt D. W., and Jones J. H. (1993) Experimental partial melting of the Allende (CV) and Murchison (CM) chondrites and the origin of asteroidal basalts. *Geochimica et Cosmochimica Acta* 57:2123-2139.

Kinoshita N., Paul M., Kashiv Y., Collon P., Deibel C. M., DiGiovine B., Greene J. P., Henderson D. J., Jiang C. L., Marley S. T., Nakanishi T., Pardo R. C., Rehm K. E., Robetson D., Scott R., Schmitt C., Tang X. D., Vondrasek R., and Yokoyama A. (2012) A shorter $^{146}$Sm half-life measured and implications for $^{146}$Sm-$^{142}$Nd chronology in the Solar System. *Science* **335**, 1614-1617.

Kleine T., Hans U., Irving A. J., and Bourdon B. (2012) Chronology of the angrite parent body and implications for core formation in protoplanets. *Geochim. Cosmochim. Acta* **84**, 186-203.

Kuehner S. M., Irving A. J., Bunch T. E., Wittke J. H., Hupe G. M., and Hupe A. C. (2006) Coronas and symplectites in plutonic angrite NWA 2999 and implications for mecury as the angrite parent body. *Lunar Planet. Sci. XXXVII*. Lunar Planet Inst., Houston. #1344 (abstract).

Kuehner S. M. and Irving A. J. (2007) Grain boundary glasses in plutonic angrite NWA 4590: Evidence for rapid decompressive partial melting and cooling on mercury. *Lunar Planet Sci. XXXVIII*. Lunar Planet Inst., Houston #1338 (abstract).

Lapen T. J., Brandon A. D., Beard B. L., Peslier A. H., Lee C.-T., and Dalton H. A. (2008) Lu-Hf age and isotope systematics of the olivine-phyric shergottite RBT-04262 and implications for the sources of enriched shergottites. *Lunar Planet. Sci. XXXIX*. Lunar Planet Inst., Houston. #2073 (abstract).

Lin Y., Liu T., Shen W., Xu L., and Miao B. (2008) Grove mountains (GRV) 020090: A highly fractionated lherzolitic shergottite. *Meteorit. Planet. Sci.* **43**, A86-A86.

Lin Y. T., Guan Y. B., Wang D. D., Kimura M., and Leshin L. A. (2005) Petrogenesis of the new lherzolitic shergottite Grove Mountains 99027: Constraints of petrography, mineral chemistry, and rare earth elements. *Meteorit. Planet. Sci.* **40**, 1599-1619.

Lindsley D. H. (1983) Pyroxene thermometry. *Am. Mineral.* **68**, 477-493.

Ludwig K. R. (1991) ISOPLOT: a plotting and regression program for radiogenic isotope data. USGS Open File Report, 91-445.

Lugmair G. W. and Marti K. (1977) Sm-Nd-Pu timepieces in the Angra dos Reis meteorite. *Arth Planet. Sci. Lett.* **35**, 273-284.

Lugmair G. W., Galer S. J. G., and Carlson R. W. (1991) Isotope systematics of cumulate eucrite EET-87520. *Meteor. Planet. Sci*. **26**, 368 (abstract).

Lugmair G. W. and Galer S. J. G. (1992) Age and isotopic relationship among the angrites Lewis Cliff 86010 and Angra dos Reis. *Geochim. Cosmochim. Acta* **56**, 1673-1694.

Lundberg L. L., Crozaz G., and McSween H. Y. (1990) Rare earth elements in minerals of the ALHA77005 shergottite and implications for its parent magma and crystallization history. *Geochim. Cosmochim. Acta* **54**, 2535-2547.

Makishima J., McKay G., Le L., Miyamoto M., and Mikouchi T. (2007) Oxidation state of nakhlites as inferred from Fe-Ti equlibria and augite/melt europium partitioning. *Lunar Planet. Sci. Conf. XXXVIII*. Lunar Planet. Inst., Houston #1834 (abstract).

Markowski A., Quitté G., Kleine T., Halliday A. N., Bizzarro M., and Irving A. J. (2007) Hafnium-tungsten chronometry of angrites and the earliest evolution of planetary objects. *Earth Planet. Sci. Lett.* **262**, 214-229.

Marty B., Marti K., Barrat J., Birck J. L., Blichert-Toft J., Chaussidon M., Deloule E., Gillet P. Göpel C., Jambon A., Manhès G., and Sautter V. (2001) Noble gases in new SNC meteorites NWA 817 and 480. *Meteor. Planet Sci.* **36**, A122.

McCanta M. C., Rutherford M. J., and Jones J. H. (2004) An experimental study of rare earth element partitioning between a shergottite melt and pigeonite: implications for the oxygen fugacity of the martian interior. *Geochim. Cosmochim. Acta* **68**, 1943-1952.

McCanta M. C., Elkins-Tanton L., and Rutherford M. J. (2009) Expanding the application of the Eu-oxybarometer to the lherzolitic shergottites and nakhlites: Implications for the oxidation state heterogeneity of the martian interior. *Meteor. Planet. Sci.* **44**, 725-745.

McKay G. and Schwandt C. S. (2005) Mineralogy and petrology of new Antarctic nakhlite MIL 03346. *Lunar Planet. Sci. Conf. XXXVI*. Lunar Planet. Inst., Houston #2351 (abstract).

McKay G., Wagstaff J., and Yang S.-R. (1986) Clinopyroxene REE distribution coefficients for shergottites: The REE content of the Shergotty melt. *Geochim. Cosmochim. Acta* **50**, 927-937.

McKay G., Le L., Wagstaff J., and Crozaz G. (1994) Experimental partitioning of rare earth elements and strontium: Constraints on petrogenesis and redox conditions during crystallization of Antarctic angrite Lewis Cliff 86010. *Geochim. Cosmochim. Acta* **58**, 2911-2919.

McKay G., Miyamoto M., Mikouchi T., and Ogawa T. (1998) The cooling history of the Lewis Cliff 86010 angrite as inferred from kirschsteinite lamellae in olivine. *Meteor. Planet. Sci.* **33**, 977-983.

McSween Jr. H. Y. (2002) The rocks of Mars, from far and near. *Meteorit. Planet. Sci.* **37**, 7-25.

McSween Jr. H. Y. (2006) Mars. In *Meteorites, Comets, and Planets*, Vol. 1, Chapter 1.22. (ed. H. D. Holland and K. K. Turekian). Elsevier-Pergamon, Oxford. pp. 1-27.

The Meteoritical Bulletin: Entry for Northwest Africa 6291, accessed 08/28/2011, http://www.lpi.usra.edu/meteor/metbull.php?code=52026.

The Meteoritical Bulletin: Entry for angrites, accessed 09/01/2012, http://www.lpi.usra.edu/meteor/metbull.php?sea=&sfor=names&stype=contains&lrec=50&categ=Angrites&srt=name

Mikouchi T. (2005) Northwest Africa 1950: Mineralogy and comparison with Antarctic lherzolitic shergottites. *Meteorit. Planet. Sci.* **40**, 1621-1634.

Mikouchi T. and Miyamoto M. (1997) Yamato-793605: A new lherzolitic shergottite from the Japanese Antarctic meteorite collection. *Antarct. Meteorite Res.* **10**, 41-60.

Mikouchi T., Miyamoto M., and McKay G. A. (1996) Mineralogical study of angrite Asuka-881371: Its possible relation to angrite LEW 87051. *Am. Mineral.* **80**, 585-592.

Mikouchi T., Miyamoto M., McKay G. A., and Le L. (2001) Cooling rate estimates of quenched angrites: Approaches by crystallization experiments and cooling rate calculations of olivine xenocrysts. *Meteor. Planet Sci.* **36***,* A134-A145 (abstract).

Mikouchi T., Koizumi E., Monkawa A., Ueda Y., and Miyamoto M. (2003) Mineralogy and petrology of Yamato 000593: Comparison with other maritan nakhlite meteorites. *Antarct. Meteorite Res.* **16**, 34-57.

Mikouchi T., Miyamoto M., Koizumi E., Makishima J., and McKay G. (2006) Relative burial depth of nakhlites: An update. *Lunar Planet Sci. XXXVII*. Lunar Planet Inst., Houston. #1865 (abstract).

Mikouchi T., Kurihara T., and Miyamoto M. (2008) Petrology and mineralogy of RBT 04262: Implications for stratigraphy of the lherzolitic shergottite igneous block. *Lunar Planet. Sci. XXXIX*. Lunar Planet Inst., Houston. #2403 (abstract).

Mikouchi T., Miyamoto M., and McKay G. (2011) Kirschsteinite exsolution lamellae in olivine from young angrites: Implications for their thermal history. *Mineralogical Magazine*. **75**, 1469.

Mikouchi T., Makishima J., Kurihara T., Hoffman V. H., and Miyamoto M. (2012) Relative burial depth of nakhlites revisited. *Lunar Planet Sci. XLIII*. Lunar Planet Inst., Houston. #2363 (abstract).

Minster J-F., Birck J-L., and Allègre C. J. (1982) Absolute age of formation of chondrites studies by the $^{87}$Rb-$^{87}$Sr method. *Nature* **300**, 414-419.

Mittlefehldt D. W. and Lindstrom M. M. (1990) Geochemistry and genesis of the angrites. *Geochim. Cosmochim. Acta* **54,** 3209-3218.

Mittlefehldt D. W., McCoy T. J., Goodrich C. A., and Kracher A. (1998) Non-chondritic meteorites from asteroidal bodies. In *Planetary Materials: Reviews in Mineralogy 36*, 1st ed., edited by Papike J. J.: Washington, DC: Mineralogical Society of America. pp. 4-1 – 4-195.

Mittlefehldt D. W., Killgore M., and Lee M. T. (2002) Petrology and geochemistry of D'Orbigny, geochemistry of Sahara 99555, and the origin of angrites. *Meteor. Planet. Sci.* 37, 345-369.

Moynier F., Agranier A., Hezel D. C., and Bouvier A. (2010) Sr stable isotope composition of Earth, the Moon, Mars, Vesta, and meteorites. *Earth Planet. Sci. Lett.* **300**, 359-366.

Münker C., Weyer S., Scherer E., and Mezger K. (2001) Separation of high field strength elements (Nb, Ta, Zr, Hf) and Lu from rock samples for MC-ICPMS measurements. *Goechim. Geophys. Geosyst.* **2**, 1064, doi:10.1029/2001GC000183.

Nakashima D., Nagao K., and Irving A. J. (2008) Noble gases in angrites NWA 2999/4931, NWA 4590, and NWA 4801: Exposure ages and evidence of fissiogenic Xe. *71st Meeting of the Meteoritical Society.* #5078 (abstract).

Nyquist L. E., Bansal B., Wiesmann H., and Shih C.-Y (1994) Neodymium, strontium, and chromium isotopic studies of the LEW 86010 and Angra dos Reis meteorites and the chronology of the angrite parent body. *Meteoritics* **29**, 872-885.

Nyquist L. E., Bogard D. D., Shih C.-Y., Greshake A., Stoffler D., and Eugster O. (2001) Age and geologic histories of Martian meteorites. *Space Sci. Rev.* **96**, 105-164.

Nyquist L. E., Bogard D. D., Shih C. Y., Park J., Reese Y. D., and Irving A. J. (2009) Concordant Rb-Sr, Sm-Nd, and Ar-Ar ages for Northwest Africa 1460: A 346 Ma old basaltic shergottite related to "lherzolitic" shergottites. *Geochim. Cosmochim. Acta* **73**, 4288-4309.

Oe K., McKay G., Le L., Miyamoto M., and Mikouchi T. (2002) REE and Sr partition coefficients for Nakhla pyroxenes: Their relationship to other element abundances. *Lunar Planet. Sci. Conf. XXXIII*. Lunar Planet. Inst., Houston #2065 (abstract).

Okazaki R., Keisuki N., Imae N., and Kojima H. (2003) Noble gas signatures of Antarctic meteorites, Yamato (Y) 000593, Y000749, and Y000802. *Antarct. Meteor. Res.* **16**, 58-79.

Palme H. and Beer H. (1993) Abundances of the elements in the solar system. In *Landolt-Bornstein, Group VI*, Vol. 3 (ed. H. Voigt). Springer, Berlin. pp. 196-221.

Palme H. and Jones A. (2003) Solar system abundances of the elements. In *Treatise on Geochemistry, Vol. 1: Meteorites, comets, and planets*. (ed. A. M. Davis). Elsevier, Oxford. pp. 41-61.

Papike J. J., Karner J. M., and Shearer Jr. C. (2004) Comparative planetary mineralogy: V/(Cr + Al) systematics in chromite as an indicator of relative oxygen fugacity. *Am. Mineral.* **89**, 1557-1560.

Patchett P. J. and Tatsumoto (1980) Lu-Hf total-rock isochron for the eucrite meteorites. *Nature* **288**, 571-574.

Patchett P. J., Vervoort J. D., Söderlund U., and Salters V. J. M. (2004) Lu-Hf and Sm-Nd isotopic systematics in chondrites and their constraints on the Lu-Hf properties of the Earth. *Earth and Planet. Sci. Lett.* **222**, 29-41.

Paton C., Schiller M., and Bizzarro M. (2011) $^{84}$Sr anomalies in bulk-rock meteorites and acid-leachates of the Ivuna CI chondrite. *Conference on Formation of First Solids in the Solar System.* Lunar Planet. Inst., Houston. #9062 (abstract).

Podosek F. A., Zinner E. K., MacPherson G. J., Lundberg L. L., Brannon J. C., and Fehey A. J. (1991) Correlated study of initial $^{87}$Sr/$^{86}$Sr and Al-Mg isotopic systematics and petrologic properties in a suite of refractory inclusions from the Allende meteorite. *Geochim. Cosmochim. Acta* **55**, 1083-1110.

Prinz M., Keil K., Hlava P. F., Berkley J. L., Gomes C. B., and Curvello W. S. (1977) Studies of Brazilian meteorites, III. Origin and history of the Angra dos Reis achondrite. *Earth. Planet. Sci. Lett.* **35**, 317-330.

Prinz M., Weisberg M. K., and Nehru C. E. (1988) LEW 86010, a second angrite: Relationships to CAIs and opaque matrix. *19th Proceedings of the Lunar and Planetary Science Conference* 949-950.

Reid A. M. and Bunch T. E. (1975) The nakhlites part II: Where, when and how. *Meteoritics* **10**, 317-324.

Sanborn M. E., Wadhwa M., Hervig R., and Irving A. J. (2008) Rare earth element geochemistry of angrite Northwest Africa 2999. *Lunar Planet Sci. XXXIX*. Lunar Planet Inst., Houston. #1395 (abstract).

Sanborn M. E. and Wadhwa M. (2009) Rare earth element geochemistry of angrite Northwest Africa 4590 and Northwest Africa 4801. *Lunar Planet. Sci. XL*. Lunar Planet. Inst., Houston. #1345 (abstract).

Satterwhite C. and Righter K. (2007). In *Antarctic Meteorite Newsletter*, Vol. 30 (1), pp. 1-20.

Sautter V., Barrat J-. A., Jambon A., Lorand J. P., Gillet P., Javoy M., Joron J. L., and Lesourd M. (2002) A new martian meteorite from Morocco: the nakhlite Northwest Africa 817. *Earth Planet. Sci. Lett.* **195**, 223-238.

Scherer E., Münker C., and Mezger K. (2001) Calibration of the lutetium-hafnium clock. *Science* **293**, 683-687.

Scott E. R. and Bottke W. F. (2011) Impact histories of angrites, eucrites, and their parent bodies. *Meteor. Planet Sci.* **46**, 1878-1887.

Shearer C. K., Burger P. V., Papike J. J., Borg L. E., Irving A. J., and Herd C. (2008) Petrogenetic linkages among Martian basalts: Implications based on trace element chemistry of olivine. *Meteorit. Planet. Sci.* **43**, 1241-1258.

Shih C.-Y., Nyquist L. E., and Reese Y. (2009) Rb-Sr and Sm-Nd studies of olivine-phyric shergottites RBT 04262 and LAR 06319: Isotopic evidence for relationship to enriched basaltic shergottites. *Lunar Planet. Sci. XL*. Lunar Planet Inst., Houston. #1360 (abstract).

Shukolyukov A., and Lugmair G. W. (2008) Mn-Cr chronology of eucrite CMS 04049 and angrite NWA 2999. *Lunar Planet. Sci. XXXIX.* Lunar Planet. Inst., Houston #2094 (abstract).

Shukolyukov A., Lugmair G. W., and Irving A. J. (2009) Mn-Cr isotope systematics of angrite Northwest Africa 4801. *Lunar Planet. Sci. XL.* Lunar Planet. Inst., Houston. #1381 (abstract).

Söderlund U., Patchett P. J., Vervoort J. D., and Isachsen C. E. (2004) The $^{176}$Lu decay constant determined by Lu-Hf and U-Pb isotope systematics of Precambrian mafic intrusions. *Earth Planet. Sci. Lett.* **219**, 311-324.

Spivak-Birndorf L., Wadhwa M., and Janney P. E. (2009) $^{26}$Al-$^{26}$Mg systematics in D'Orbigny and Sahara 99555 angrites: implications for high-resolution chronology using extinct chronometers. *Geochim. Cosmochim. Acta* **73**, 5202-5211.

Stewart, B. W., Papanastassiou D. A., and Wasserburg G. J. (1994) Sm-Nd chronology and petrogenesis of mesosiderites. *Geochim. Cosmochim. Acta* **58**, 3487-3509.

Stockhill K. R., McSween H. Y. Jr., and Bodnar R. J. (2005) Melt inclusions in augite of the Nakhla martian meteorite: Evidence for basaltic parental melt. *Meteor. Planet. Sci.* **40**, 377-398.

Stöffler D. (2000) Maskelynite confirmed as diaplectic glass: Indications for peak shock pressures below 45 GPa in all martian meteorites. *Lunar Planet. Sci. Conf. XXXI*. Lunar Planet. Inst., Houston #1170 (abstract).

Suguira N., Miyazaki A., and Yanai K. (2005) Widespread magmatic activities on the angrite parent body at 4562 Ma ago. *Earth Planets Space* **57**, e13-e16.

Symes S. J. K., Borg L. E., Shearer C. K., and Irving A. J. (2008) The age of the martian meteorite Northwest Africa 1195 and the differentiation history of the shergottites. *Geochim. Cosmochim. Acta* **72**, 1696-1710.

Szymanski A., Brenker F. E., Palme H., and El Goresy A. (2010) High oxidation state during formation of the martian nakhlites. *Meteor. Planet. Sci.* **45**, 21-31.

Tanaka T., Togashi S., Kamioka H., Amakawa H., Kagami H., Hamamoto T., Yuhara M., Orihashi Y., Yoneda S., Shimizu H., Kunimaru T., Takahasi K., Yanagi T., Nakano T., Fujimaki H., Shinjo R., Asahara Y., Tanimizu M., Dragusanu C. (2000) JNdi-1: a neodymium isotopic reference in consistency with La Jolla neodymium. *Chemical Geology* **168**, 279-281.

Tera F., Eugster O., Burnett D. S., and Wasserburg G. J. (1970) Comparative study of Li, Na, K, Rb, Cs, Ca, Sr, and Ba abundances in achondrites and in Apollo 11 lunar samples. *Proc. Apollo 11 Lunar Sci. Conf.* **2**, 1637-1657.

Thrane K., Connelly J. N., Bizzarro M., Meyer B. S., and The L.-S. (2010) Origin of excess $^{176}$Hf in meteorites. *Astrophys J* **717**, 861-867.

Treiman A. H. (1986) The parental magma of the Nakhla achondrite: Ultrabasic volcanism on the shergottite parent body. *Geochim. Cosmochim. Acta* **50**, 1061-1070.

Treiman A. H. (1990) Complex petrogenesis of the Nakhla (SNC) meteorite: Evidence from petrography and mineral chemistry. *Lunar Planet. Sci. Conf. XX*. **20**, 273-280.

Treiman A. H. (1993) The parental magma of the Nakhla (SNC) achondrite inferred from magmatic inclusions. *Geochim. Cosmochim. Acta* **57**, 4753-4767.

Treiman A. H. (2003) Chemical compositions of Martian basalts (shergottites): Some inferences on basalt formation, mantle metasomatism, and differentiation in Mars. *Meteorit. Planet. Sci.* **38**, 1849-1864.

Treiman A. H. (2005) The nakhlite meteorites: Augite-rich igneous rocks from Mars. *Chemie der Erde* **65**, 203-270.

Treiman A. H. and Irving A. J. (2008) Petrology of martian meteorite Northwest Africa 998. *Meteor. Planet. Sci.* **43**, 829-854.

Treiman A. H., McKay G. A., Bogard D. D., Mittlefehldt D. W., Wang M. S., Keller L., Lipschutz M. E., Lindstrom M. M., and Garrison D. (1994) Comparison of the LEW 88516 and ALHA77005 Martian Meteorites - Similar but Distinct. *Meteoritics* **29**, 581-592.

Varela M. E., Kurat G., and Clocchiatti R. (2001) Glass-bearing inclusions in Nakhla (SNC meteorite) augite: Heterogeneously trapped phases. *Contrib. to Mineralogy and Petrology* **71**, 155-172.

Wadhwa M. (2001) Redox state of Mars' upper mantle and crust from Eu anomalies in shergottite. *Science* **291**, 1527-1530.

Wadhwa M. (2008) Redox conditions on small bodies, the Moon, and Mars. In *Oxygen in the Solar System: Reviews in Mineralogy 68*, 1st ed., edited by

MacPherson G. J.: Washington, DC: Mineralogical Society of America. pp. 493-510.

Wadhwa M. and Crozaz G. (1995) Trace and minor elements in minerals of nakhlites and Chassigny: Clues to their petrogenesis. *Geochim. Cosmochim. Acta* **59**, 3629-3645.

Wadhwa M. and Lugmair G. W. (1995) Age of the eucrite "Caldera" from convergence of long-lived and short-lived chronometers. *Geochim. Cosmochim. Acta* **60**, 4889-4893.

Wadhwa M., McSween H. Y., and Crozaz G. (1994) Petrogenesis of shergottite meteorites inferred from minor and trace element microdistributions. *Geochim. Cosmochim. Acta* **58**, 4213-4229.

Wadhwa M., Crozaz G. and Barrat J-. A. (2004) Trace element distributions in the Yamato 000593/000749, NWA 817, and NWA 998 nakhlites: Implications for their petrogenesis and mantle source on Mars. *Antarct. Meteorite Res.* **17**, 97-116.

Warren P. H., Kalleymeyn W. G., and Mayeda T. (1995) Consortium investigation of the Asuka=881371 angrite: Bulk-rock geochemistry and oxygen isotopes. *Proc. NIPR Symp. Antarctic Meteorites* **20**, 261-264.

Weisberg M. K., McCoy T. J, and Krot A. N. (2006) Systematics and evolution of meteorite classification. In *Meteorites and the Early Solar System II*, edited by Lauretta D. S. and McSween Jr. H. Y.: Tucson: The University of Arizona Press. pp. 19 – 52.

Wood B. J. (1991) Oxygen barometry of spinel peridotites. In *Oxide Minerals: Petrologic and Magnetic Significance*, Vol. 25 (ed. D. H. Lindsley). Mineralogical Society of America. Washington D. C. pp. 417-431.

Yanai K. (1994) Angrite Asuka-881371: Preliminary examination of a unique meteorite in the Japanese collection of Antarctic meteorites. *Proc. NIPR Symp. Antarctic Meteorites* **7**, 30-41.

Zinner E. and Crozaz G. (1986) A method for the quantitative measurement of are earth elements by ion microprobe. *Int. J. Mass Spectrom. Ion Processes* **69**, 17-38.

# APPENDIX A

## STATEMENT OF PERMISSION FROM CO-AUTHORS

Co-authors on the previously published article “Petrology and trace element geochemistry of Robert Massif 04261 and 04262 meteorites, the first examples of geochemically enriched lherzolitic shergottites” in Chapter 6 have granted their permission for use of the article in this dissertation. The list of co-authors includes: T. Usui, H. Y. McSween Jr., and M. Wadhwa.